



JOHANNES GUTENBERG  
UNIVERSITÄT MAINZ

**Human models for White Sutton syndrome:  
*POGZ* mutations change the transcriptome and induce  
defects in neural progenitor cell biology**

by

**Azza Soliman**

**Mainz, 2025**

**Human models for White Sutton syndrome:  
*POGZ* mutations change the transcriptome and induce  
defects in neural progenitor cell biology**

**Dissertation  
Zur Erlangung des Grades  
Doktor der Naturwissenschaften**

**Am Fachbereich Biologie  
Der Johannes-Gutenberg-Universität Mainz**

**Azza Soliman**

**Geb. am 31.01.1989 in Gizeh, Ägypten**

**Mainz, 2025**



Dekan:

1. Berichterstatter:

2. Berichterstatter:

Tag der mündlichen Prüfung: 23<sup>rd</sup> June 2025

## Table of Contents

Abstract .....	8
Zusammenfassung.....	10
List of abbreviations: .....	12
1 Introduction.....	13
1.1 Neurodevelopmental disorders (NDDs).....	13
1.2 Mechanisms of Neurodevelopmental disorders .....	14
1.3 POGZ & White Sutton Syndrome (WHSUS).....	18
1.4 POGZ.....	20
1.4.1 POGZ and Chromatin Remodeling.....	21
1.4.2 POGZ and Embryonic stem cell (ESC) identity .....	25
1.4.3 POGZ and Mitosis .....	26
1.4.4 POGZ and DNA double-strand breaks' (DSBs) Repair.....	27
1.4.5 POGZ and Sleep-related phenotypes .....	28
1.5 Variants of POGZ & Non sense mediated RNA decay .....	29
1.6 Induced pluripotent stem cells as a model for disease:.....	31
1.6.1 Common characteristics of iPSCs and ESCs.....	33
1.6.2 Induced pluripotent stem cells 'differentiation into disease specific cells .....	34
1.7 Human brain development and iPSCs .....	35
1.7.1 Brain development .....	35
1.7.2 Neurogenesis.....	36
1.8 Investigating Human Neuronal Differentiation and Brain Organogenesis via In Vitro Modeling.....	38
1.9 CRISPR/Cas genome editing .....	39
1.9.1 Non-Homologous End-Joining (NHEJ) .....	40
1.9.2 Homology Directed Repair (HDR).....	41
2 Aim of the project.....	42
3 Material and Methods.....	43
3.1 Material .....	43
3.1.1 Equipment .....	43
3.1.2 Disposable material .....	44
3.1.3 Chemicals and Media .....	45
3.1.3.1 Chemicals.....	45
3.1.3.2 Media.....	47
3.1.3.3 Media composition.....	47
3.1.4 Reagents, Kits, and Enzymes .....	49

3.1.4.1	Kits and reagents .....	49
3.1.4.2	Enzymes.....	49
3.1.5	Primers and Antibody.....	49
3.1.5.1	Primers.....	49
3.1.5.2	Primary antibodies .....	51
3.1.5.3	Secondary antibodies .....	52
3.1.6	Plasmids, gRNA and template constructs.....	52
3.1.6.1	Plasmids.....	52
3.1.6.2	gRNA constructs.....	52
3.1.7	Softwares and online tools.....	53
3.1.8	Cells.....	54
3.2	Methods .....	55
3.2.1	Cell culture conditions.....	55
3.2.1.1	Plate Coatings .....	55
3.2.1.2	Gelatine Coating .....	55
3.2.1.3	Matrigel Coating .....	55
3.2.1.4	Geltrex Coating .....	55
3.2.1.5	Poly-Ornithine/Laminin Coating.....	55
3.2.2	Cell culture.....	56
3.2.2.1	Fibroblasts .....	56
3.2.2.2	Induced Pluripotent Stem Cells (iPSCs) .....	57
3.2.2.3	Genome editing .....	59
3.2.2.4	Neural progenitor and stem cells (NPCs) .....	62
3.2.2.5	Neurospheres .....	64
3.2.2.6	Organoids .....	65
3.2.3	Cell culture methods .....	68
3.2.3.1	Cell pellet collection .....	68
3.2.3.2	PFA fixation of adherent cells.....	68
3.2.3.3	Cell counting.....	68
3.2.3.4	Karyotyping.....	69
3.2.4	Molecular methods .....	69
3.2.4.1	Immunofluorescence staining .....	69
3.2.4.2	Protein extraction.....	69
3.2.4.3	SDS gel-electrophoresis and Western Blot.....	70
3.2.4.4	DNA extraction .....	70
3.2.4.5	PCR amplification.....	71

3.2.4.6	Sequencing .....	71
3.2.4.7	Whole Exome Sequencing (WES) .....	72
3.2.4.8	Total RNA extraction .....	72
3.2.4.9	Retro-transcription of total RNA and cDNA synthesis.....	72
3.2.4.10	RT-qPCR .....	73
3.2.4.11	Quantification of Allele-Specific Expression by Pyrosequencing (QUASEP)...	74
3.2.4.12	Sendai Virus vector clearance .....	75
3.2.5	Click-iT™ EdU Flow Cytometry Assay: .....	76
3.2.6	Evaluation of NPCs differentiation by immunofluorescence staining (Differentiation Assay)	78
3.2.7	Evaluation of cell proliferation/ apoptosis by flow cytometry.....	78
3.2.8	RNA-sequencing .....	79
3.2.8.1	RNA-sequencing library preparation.....	80
3.2.8.2	Bioinformatics analysis of RNA-sequencing data .....	80
3.2.9	CUT& Tag sequencing (Cleavage Under Targets and Tagmentation) .....	81
3.2.9.1	RNA-sequencing library preparation.....	81
3.2.9.2	Bioinformatics analysis of CUT&Tag data.....	83
4	Results .....	86
4.1	Confirmation and characterization of cell type.....	86
4.1.1	Fibroblasts .....	86
4.1.1.1	Morphology .....	86
4.1.1.2	Immunofluorescent staining .....	86
4.1.2	iPSCs.....	87
4.1.2.1	CRISPR/Cas9 genome editing of female wildtype iPSCs.....	87
4.1.2.2	DNA sequencing of A2 wildtype and edited female iPSCs .....	88
4.1.2.3	Exome sequencing for the Off-target analysis of edited female iPSCs .....	89
4.1.2.4	DNA sequencing of wildtype and WHSUS male iPSCs.....	89
4.1.2.5	Morphology .....	89
4.1.2.6	Karyogram .....	91
4.1.2.7	Pluripotency (RT-qPCR) .....	91
4.1.2.8	Pluripotency (immunofluorescent staining).....	92
4.1.2.9	CRISPR/Cas9 editing of male WHSUS iPSCs.....	93
4.1.2.10	DNA sequencing of corrected male WHSUS iPSCs .....	93
4.1.3	NPCs.....	94
4.1.3.1	Morphology .....	94
4.1.3.2	RT-qPCR .....	94

4.1.3.3	Immunofluorescent staining .....	95
4.2	Characterization of <i>POGZ</i> mutant female iPSCs.....	96
4.2.1	<i>POGZ</i> mRNA expression of WT and edited female iPSCs and NPCs.....	96
4.2.2	Pyrosequencing to identify which allele transcript is expressed in WT and edited female NPCs (QUASEP analysis) .....	98
4.2.3	Protein expression of WT and edited female iPSCs and NPCs .....	98
4.2.4	Protein localization of WT and edited female iPSCs and NPCs .....	99
4.3	Characterization of <i>POGZ</i> mutant WHSUS male iPSCs.....	100
4.3.1	<i>POGZ</i> mRNA expression in WT male and WHSUS male iPSCs and NPCs.....	101
4.3.2	Pyrosequencing to identify from which allele <i>POGZ</i> was expressed in WT male and WHSUS male NPCs (QUASEP analysis) .....	101
4.3.3	<i>POGZ</i> protein expression of WT male and WHSUS male iPSCs and NPCs.....	102
4.3.4	Protein localization of in WT male and WHSUS male iPSCs and NPCs.....	103
4.4	Functional analyses of <i>POGZ</i> Wildtype and mutant iPSCs and iPSC-derived NPCs.....	104
4.4.1	Effect of <i>POGZ</i> <sup>+/-</sup> on cell proliferation & differentiation in 2D culture.....	104
4.4.1.1	Expression of proliferation & differentiation markers .....	104
4.4.1.2	Click iT EdU assay:.....	105
4.4.1.3	Neuronal differentiation assay of NPCs derived from iPSC lines .....	106
4.4.1.4	Investigation of proliferation, DNA damage and apoptosis markers in NPCs..	107
4.4.2	Effect of <i>POGZ</i> <sup>+/-</sup> on proliferation & differentiation in 3D culture .....	108
4.4.2.1	Neurospheres .....	108
4.4.2.2	Brain organoids.....	112
4.5	Transcriptomic profiling of <i>POGZ</i> wildtype and mutant NPCs .....	116
4.5.1	Cell pellets, RNA quality control and RNA sequencing.....	116
4.5.2	RNA-seq analysis.....	116
4.5.2.1	Sample clustering .....	116
4.5.2.2	Differentially expressed genes (DEGs): .....	117
4.5.2.3	Differentially expressed genes (DEGs) in female NPCs: .....	118
4.5.2.4	Differentially expressed genes (DEGs) in male NPCs: .....	120
4.5.2.5	Differentially expressed genes (DEGs) between female and male NPCs .....	121
4.5.2.6	Validation of RNA-Seq Data Using qPCR: .....	122
4.5.2.7	Inferring the differentiation status of WT and mutant NPCs .....	123
4.6	<i>POGZ</i> binding genes analysis via CUT&Tag sequencing: .....	124
4.7	Relationship between <i>POGZ</i> -regulated gene expression, <i>POGZ</i> binding.....	132
5	Discussion .....	136
5.1	Generation and validation of CRISPR/Cas9-mediated full/heterozygous <i>POGZ</i> knockout and patient iPSC-derived NPCs.....	137

5.1.1	Reprogramming of skin fibroblasts .....	137
5.1.2	CRISPR/Cas9 mediated genome editing in iPSCs:.....	139
5.1.3	Differentiation of induced pluripotent stem cells (iPSCs) into neural progenitor cells (NPCs)	141
5.1.4	Difference between studying in 2D and 3D cell culture models .....	142
5.1.4.1	Advantages and Limitations of 2D Models.....	143
5.1.4.2	The emergence of 3D Models: Neurospheres and Brain Organoids.....	143
5.1.4.3	Challenges and Future Directions.....	144
5.2	Functional analyses of <i>POGZ</i> wildtype/mutant iPSCs and iPSC-derived NPCs .....	145
5.2.1	Effect of missense <i>POGZ</i> mutations on its expression and cellular distribution in iPSCs and NPCs .....	145
5.2.2	<i>POGZ</i> variants effects in 2D culture models:.....	149
5.2.2.1	Effect on proliferation .....	149
5.2.2.2	Effect on cell survival:.....	153
5.2.2.3	Effect on neural differentiation:.....	154
5.2.3	<i>POGZ</i> variants effects in 3D culture models.....	156
5.2.3.1	Effect on proliferation .....	156
5.2.3.2	Effect on differentiation (migration):.....	157
5.2.3.3	Effect on brain organoids: .....	158
5.2.4	<i>POGZ</i> mutations change the transcriptome in the NPCs .....	160
5.2.5	<i>POGZ</i> regulation via DNA-binding (Cut&Tag):.....	166
	References.....	172
	Curriculum vitae .....	192
	Acknowledgments .....	

## Abstract

Intellectual disability (ID) and autism spectrum disorders (ASD) are complex neurodevelopmental conditions with high genetic heterogeneity. Studies indicate that 10%-40% of individuals with ID also have ASD, suggesting shared molecular mechanisms between these disorders [1-6]. Recent next-generation sequencing studies have highlighted a significant role of *de novo* mutations in ASD, particularly those with large effects [4, 7-10]. Among these, *POGZ* (Pogo Transposable Element with zinc finger “ZNF” domain) has emerged as a frequently mutated gene with potential loss-of-function effects in ASD patients [4, 10, 11]. However, the underlying molecular mechanisms and the pathogenic impact of *POGZ* mutations are not fully understood [12-16].

*POGZ* encodes a protein that mainly binds to heterochromatin protein 1 $\alpha$  and contributes to gene regulatory functions [13, 17]. Functionally, *POGZ* is critical for kinetochore assembly, sister chromatid cohesion, and mitotic chromosome segregation. *POGZ* deficiency can lead to premature mitotic exit, polyploidy, and potential cell death or genomic instability, which may disrupt neural development and brain function [18]. *POGZ* is thought to act as a transcriptional regulator, potentially influencing molecular networks that are critical for neuronal function [19-21].

This PhD study investigated the cellular and molecular mechanisms by which *POGZ* mutations contribute to neurodevelopmental disorders (NDDs) using human induced pluripotent stem cells (iPSCs) derived from patient and CRISPR/Cas9-mediated gene editing to introduce heterozygous *POGZ* mutations. These mutant iPSCs were differentiated into neural progenitor cells (NPCs) and neurons under both two-dimensional (2D) and three-dimensional (3D) culture conditions to analyze the effects of *POGZ* mutations on neural development.

Key findings of the study indicated that frameshift mutations in the N-terminus or the HP1-binding zinc finger-like (HPZ) domain of *POGZ* led to decreased *POGZ* protein expression without disrupting its nuclear localization. Using 3D neurospheres and brain organoids, it was found that *POGZ*-deficient cells exhibited impaired self-renewal of NPCs, alongside enhanced differentiation and increased neuronal migration. Additionally, analysis of the transcriptome via RNA sequencing revealed widespread changes in gene expression in NPCs carrying *POGZ* mutations. These alterations were significantly enriched for genes involved in mitotic chromatid segregation, DNA repair, nonsense-mediated decay, and

alternative splicing. Notably, the data revealed a transcriptomic signature characterized by the elevated expression of neuron-specific genes, suggesting an "accelerated differentiation" phenotype in mutant NPCs, mirroring the behavior observed in the 3D neurosphere models.

Furthermore, CUT&Tag sequencing was employed to identify direct targets of POGZ, providing evidence that POGZ directly regulated genes linked to synaptic function, chromosome segregation, and Wnt signaling. The overrepresentation of autism-associated risk genes among POGZ-regulated targets further suggested a potential link between POGZ dysfunction and the etiology of NDDs, including ASD.

This analysis emphasized the critical role of POGZ in regulating neural development at both the cellular and molecular levels. Understanding how *POGZ* mutations drive alterations in NPC behavior and gene regulation, is crucial for developing targeted therapeutic strategies for conditions associated with POGZ dysfunction. Ultimately, this study aimed to bridge the gap between genetic findings and pathophysiological mechanisms in NDDs, providing deeper insights into the developmental disruptions caused by *POGZ* mutations.

## Zusammenfassung

Intellektuelle Beeinträchtigung (ID) und Autismus-Spektrum-Störungen (ASD) sind komplexe neuroentwicklungsbedingte Erkrankungen, die durch genetische Heterogenität gekennzeichnet sind. Schätzungsweise 10 % bis 40 % der Menschen mit ID weisen ebenfalls ASD als Komorbidität auf, was auf gemeinsame molekulare Netzwerke und Signalwege zwischen diesen Störungen hindeutet [1-6]. Jüngste Studien zur Hochdurchsatz-Sequenzierung haben die bedeutende Rolle von *de novo* Mutationen, die oft zu Mutationen mit großen Auswirkungen führen, bei der Erhöhung des ASD-Risikos hervorgehoben [4, 7-10]. Trotz dieses möglichen Zusammenhangs bleiben die zugrunde liegenden molekularen Mechanismen der *POGZ*-Mutationen weitgehend unklar und ihre pathogene Wirkung ist noch nicht vollständig verstanden [12-16].

*POGZ* kodiert ein Protein, das hauptsächlich an das Heterochromatin-Protein 1 $\alpha$  bindet und zu genregulatorischen Funktionen beiträgt [13, 17]. *POGZ* spielt eine entscheidende Rolle bei der normalen Kinetochor-Assemblierung, der Kohäsion der Schwesterchromatiden und der Segregation von mitotischen Chromosomen. Ein Mangel an *POGZ* kann zu einem vorzeitigen Austritt aus der Mitose und zur Bildung polyploider Zellen führen, was potenziell zum Zelltod oder zu genomischer Instabilität führt und die Gehirnentwicklung stören sowie die neuronale Funktion beeinträchtigen kann [18]. Es wird angenommen, dass *POGZ* als Transkriptionsregulator wirkt und molekulare Netzwerke beeinflusst, die für die neuronale Funktion von entscheidender Bedeutung sind [19-21].

Diese Doktorarbeit untersuchte die zellulären und molekularen Mechanismen, durch die disruptive Mutationen im *POGZ*-Gen zu neuroentwicklungsbedingten Störungen (NDDs) beitragen. Dazu wurden menschliche induzierte pluripotente Stammzellen (iPSCs) als Modellsystem verwendet, die von Patienten abgeleitet wurden und CRISPR/Cas9-vermittelte Gen-Editierungstechniken eingesetzt, um heterozygote *POGZ*-Mutationen einzuführen. Diese iPSC-Linien mit heterozygoten *POGZ*-Mutationen wurden dann sowohl unter zweidimensionalen (2D) als auch dreidimensionalen (3D) Kulturbedingungen zu neuronalen Vorläuferzellen (NPCs) und Neuronen differenziert, um zu untersuchen, wie *POGZ*-Mutationen die neuronale Entwicklung beeinflussen.

Die Ergebnisse der Studie zeigten, dass Frameshift-Mutationen in *POGZ*, insbesondere im N-Terminus oder in der HP1-bindenden Zinkfinger-ähnlichen (HPZ) Domäne, zu einer

reduzierten POGZ-Proteinexpression führten, ohne die nukleäre Lokalisation zu beeinträchtigen. Durch die Verwendung von 3D-Neurosphären und Gehirnorganoiden wurde festgestellt, dass POGZ-defiziente Zellen eine beeinträchtigte Selbst-Erneuerung der NPCs, begleitet von verstärkter Differenzierung und erhöhter neuronaler Migration, zeigten. Darüber hinaus ergab die Analyse des Transkriptomts mittels RNA-Sequenzierung weitreichende Veränderungen in der Genexpression in NPCs mit *POGZ*-Mutationen. Diese Veränderungen waren signifikant angereichert für Gene, die an der mitotischen Chromatiden-Segregation, DNA-Reparatur, dem nonsense-vermittelten Abbau und alternativem Spleißen beteiligt sind. Bemerkenswert war ein Transkriptionsmuster mit erhöhter Expression von neuronenspezifischen Genen, was auf ein „beschleunigtes Differenzierungs“-Phänotyp bei mutierten NPCs hinweist, ähnlich dem Verhalten in den 3D-Neurosphären-Modellen.

Zudem wurde CUT&Tag-Sequenzierung eingesetzt, um direkte Zielgene von POGZ zu identifizieren. Diese Analysen lieferten Hinweise darauf, dass POGZ direkt Gene reguliert, die mit synaptischer Funktion, Chromosomensegregation und Wnt-Signalgebung in Verbindung stehen. Die Überrepräsentation von mit Autismus assoziierten Risikogenen unter den POGZ-regulierten Zielgenen deutet weiter auf einen möglichen Zusammenhang zwischen POGZ-Dysfunktion und der Ätiologie von NDDs, einschließlich ASD, hin.

Diese Analyse unterstreicht die entscheidende Rolle von POGZ in der Regulierung der neuronalen Entwicklung auf zellulärer und molekularer Ebene. Das Verständnis, wie *POGZ*-Mutationen zu Veränderungen im Verhalten von NPCs und in der Genregulation führen, ist entscheidend für die Entwicklung gezielter therapeutischer Strategien für mit POGZ-Dysfunktion assoziierter Erkrankungen. Ziel dieser Arbeit war es, die Lücke zwischen genetischen Erkenntnissen und pathophysiologischen Mechanismen bei NDDs zu schließen und tiefere Einblicke in die durch *POGZ*-Mutationen verursachten Entwicklungsstörungen zu bieten.

**List of abbreviations:**

iPSCs – induced pluripotent stem cells	UL – upper layer
ESCs – embryonic stem cells	OPCs - oligodendrocyte progenitor cells
NPC – neural progenitor cells	CNS – central nervous system
CRISPR - clustered regularly interspaced short palindromic repeats	ECMs - extracellular matrices
ICM - inner cell mass	SMAD – small mother against decapentaplegic
scRNA-seq - Single cell RNA-seq	lncRNA – long non-coding RNA
dpf - days post-fertilization	XCR – X-chromosome reactivation
PS - primitive streak	IVF – <i>in vitro</i> fertilization
EMT - epithelial-mesenchymal transition	ID – intellectual disabilities
hPSC – human pluripotent stem cell	NDD – neurodevelopmental disorder
LIF - Leukemia Inhibitor Factor	ASD – autism spectrum disorder
EpiSCs - epiblast stem cells	ADHD – attention deficit hyperactivity disorder
mESCs – mouse embryonic stem cells	FXS – fragile X syndrome
NEC - neuroepithelial cells	mTOR – mammalian target of Rapamycin
VZ - ventricular zone	QUASEP – quantification of allelespecific expression by pyrosequencing
vRG - ventricular radial glial cells	PTC – premature termination codon
aRG - apical radial glial cells	POGZ – pogo transposable element derived with ZNF domain
SVZ – subventricular zone	PABPC1 – poly(A) binding protein cytoplasmic 1
BPs – basal progenitors	WT – wild type
IFL - inner fiber layer	UTR– untranslated region
bIPCs - basal intermediate progenitor cells	uORFs – upstream open reading frames
oRG – outer radial glia	RBP – RNA binding proteins
PCW – post-conceptual weeks	
tRG – truncated radial glial cells	
NE – neuroepithelial cells	
CR – Cajal-Retzius	
SP – subplate cells	
MZ – marginal zone	
DL – deep layer	
NMD – nonsense mediated decay	
EJC– exon junction complex	

## 1 Introduction

### 1.1 Neurodevelopmental disorders (NDDs)

Neurodevelopmental disorders (NDDs) are a heterogeneous spectrum of early onset neuropsychiatric syndromes affecting central nervous system (CNS) development with a prevalence in children of more than 15% worldwide [22]. NDDs are typically characterized by reduced cognitive abilities and impaired adaptive behavior that resulted from abnormal brain development [23-25]. Despite the fact that NDDs involve disruptions in neurogenesis, glial and neuronal proliferation, migration, synapse formation, and myelination during early embryogenesis [26, 27], these disturbances lead to lasting behavioral and neurological impairments in individuals with NDDs, affecting both children and adults [28, 29].

NDDs typically encompass a diverse range of different neurologic conditions varying in severity. These include intellectual disability (ID), developmental delay (DD), autism spectrum disorder (ASD), cerebral palsy (CP), attention deficit/hyperactivity disorder (ADHD), bipolar disorder (BP), and epilepsy and schizophrenia [30] (Fig.1).

Although some NDDs exhibit traditional Mendelian inheritances, deciphering the genetic components of these NDDs poses a challenge due to their non-Mendelian characteristics. This means they are not necessarily following dominant, recessive, or X-linked inheritance patterns. These particular disorders involve the interaction of allelic variants in several genes [31, 32]. Therefore, the complexity of the NDDs is heightened by their polygenic nature and *de novo* mutations in multiple genes where often resulting in similar clinical phenotypes as revealed by whole-exome and whole-genome sequencing [33-35]. Nevertheless, it is approximated that around 40% of NDDs are monogenic in nature, predominantly caused by mutations in a single gene [36, 37]. This proportion escalates to about 50% specifically in the case of ID [38-40]. Due to the fact that numerous of these susceptible genes may not encode proteins exclusively expressed in the brain, with known functions in neurodevelopment, the understanding of disease pathogenesis remains severely limited.

To be noticed that males exhibit a higher prevalence of neurodevelopmental disorders (NDDs) compared to females, with male-to-female ratios ranging from 1.2:1 to 4:1, particularly in conditions like autism, ADHD, and tic disorders in children [41, 42]. Disorders such as ADHD, autism, and ID are more common in boys, though profound

autism shows no sex bias [43, 44]. Sex differences in NDDs extend to behavioral traits, potentially affecting treatment responses [45]. Several hypotheses explain this sex bias, including a "female protective effect" due to the additional X chromosome, which may offer resilience against autism through mechanisms like altered gene dosage and X-linked gene expression [46, 47]. Furthermore, sex chromosome aneuploidies (SCAs) like Turner syndrome and Klinefelter syndrome underscore how X chromosome imbalances disrupt gene dosage, increasing NDD risk [48]. Additionally, autosomal genes show sex-biased expression in disorders like ADHD and autism [49, 50].

## **1.2 Mechanisms of Neurodevelopmental disorders**

Genetic analyses are essential for uncovering potential candidate genes responsible for neurodevelopmental disorders (NDDs), which often manifest as a combination of psychiatric symptoms and physical anomalies, such as facial dysmorphology and cardiac abnormalities. The impairment of various molecular and cellular mechanisms contributes to the development of NDDs [51, 52]. These impairments include disruptions in critical processes like neuronal differentiation, migration, and synaptic development during early brain formation. These processes are tightly regulated by genetic and epigenetic mechanisms, and their disruption can lead to a wide range of cognitive, motor, and behavioral deficits. One such mechanism involves dysregulations in **neuronal differentiation**, where progenitor cells fail to develop into mature, functional neurons. Mutations in *MECP2* (encoding the methyl-CpG-binding protein 2, MeCP2) are associated with Rett syndrome [53]. Although Rett syndrome is a distinct condition from ASD, both conditions can share some behavioral features like sensory disturbances, highlighting the potential relationship between these disorders [54, 55]. MeCP2 functions as transcriptional repressor and activator (epigenetic modifier) [56, 57] in post-mitotic neurons [58]; therefore mutations in *MECP2* lead to impaired neuronal differentiation and synaptic maturation, resulting in severe intellectual disability, motor abnormalities, and autistic-like behaviors [59]. Neurons derived from induced pluripotent stem cells (iPSCs) of Rett syndrome patients show reduced dendritic spine density and altered electrophysiological properties, reflecting their impaired development [60].

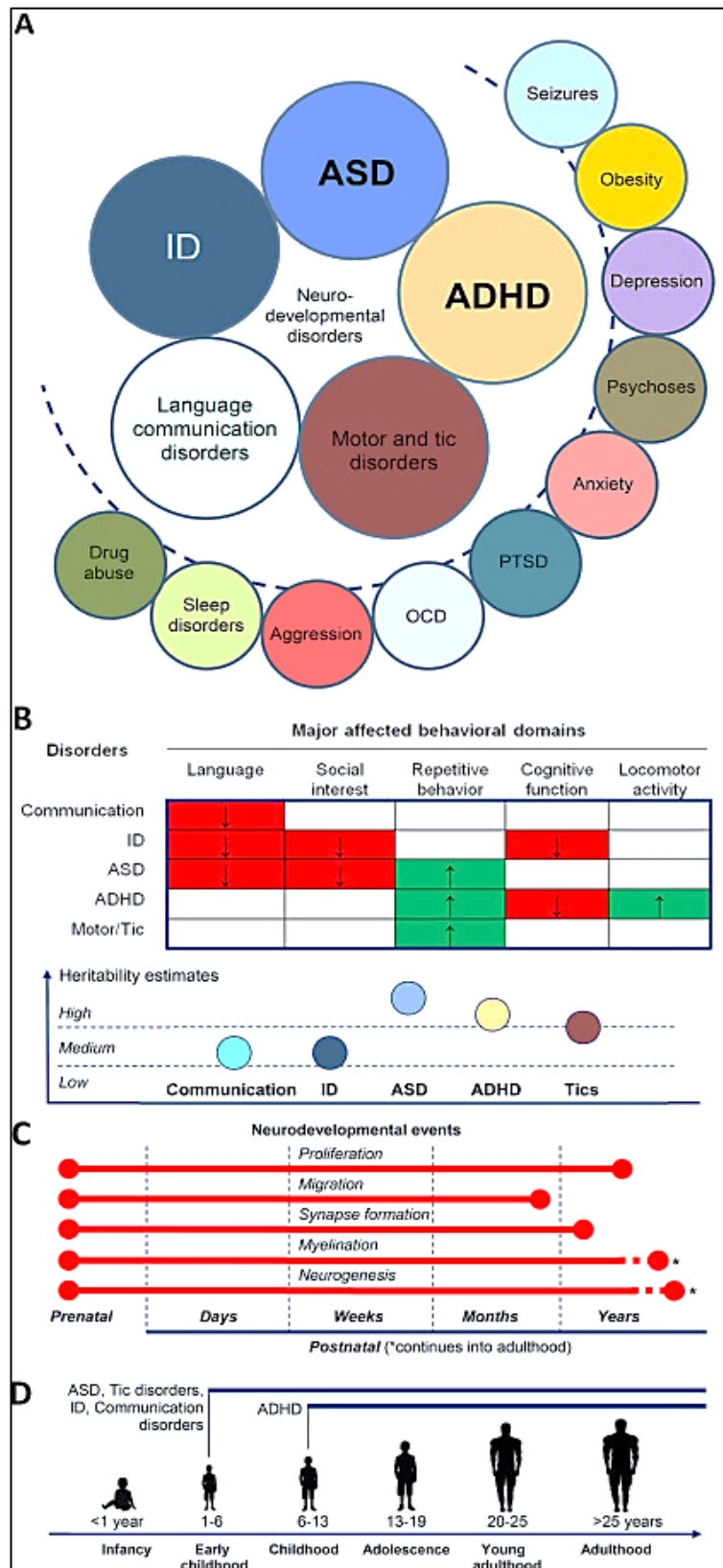


**Fig.1. The spectrum nature of Neurodevelopmental Disorders (NDDs).** Panel A depicts the spectrum of neurodevelopmental and associated disorders. Panel B illustrates the structure of phenotypic domains and heritability patterns in common NDDs (red—decreased, green—increased). ASD—Autism Spectrum Disorder, ID—Intellectual Disabilities, ADHD—Attention Deficit Hyperactivity Disorder, OCD—Obsessive Compulsive Disorder, PTSD—Post-Traumatic Stress Disorder. Panel C outlines the temporal progression of key neuronal processes relevant to neural development. Panel D showcases the typical onset timing of selected common neurodevelopmental disorders[61].

This dysfunction highlights how disruptions in neuronal differentiation can have wide-ranging effects on brain function.

Another essential mechanism implicated in neurodevelopmental disorders is **neuronal migration**, which refers to the movement of neurons from their site of origin to their final position in the brain. Disruptions in this process can lead to structural brain abnormalities and severe neurological impairments. Lissencephaly, for instance, is caused by mutations in the *LIS1* or *DCX* genes, which are crucial for proper neuronal migration[62]. In lissencephaly, neurons fail to reach their correct cortical layers, resulting in a smooth brain surface (lacking normal gyri and sulci) and causing severe cognitive and motor deficits. The improper layering of neurons in the cerebral cortex leads to profound developmental delays, epilepsy, and intellectual disabilities[63]. Similarly, in subcortical band heterotopia (double cortex syndrome), a related disorder also caused by *DCX* mutations, neurons migrate incompletely, resulting in a “double cortex” appearance, with cognitive impairment and seizures[64]. These disorders illustrate the critical role that precise neuronal migration plays in shaping the brain’s architecture and function.

Deficits in synaptic processes, which can disrupt communication between neurons and lead to the cognitive and behavioral symptoms observed in these disorders. Identifying novel disease-causing genes through genetic studies helps to elucidate these underlying mechanisms and advance our understanding of NDDs[51, 52, 65, 66]. **Synaptic dysfunction** is another major mechanism implicated in neurodevelopmental disorders, particularly in conditions associated with intellectual disability and autism spectrum disorder (ASD). For example, fragile X syndrome (FXS) results from an expanded CGG repeat in the *FMR1* gene that leads to the epigenetic silencing of the *FMR1* gene [67]. This genetic mutation leads to distinct facial features [68], ID, and reduced dendritic spine density. These effects are due to the absence of the fragile X mental retardation protein (FMRP), which regulates synaptic plasticity, leads to abnormal dendritic spine development and synaptic function [69-71]. FMRP acts as a negative regulator of mRNA translation in neurons[72] resulting in an excess of immature dendritic spines, resulting in impaired synaptic communication and contributing to the cognitive and behavioral symptoms of the disorder[73].The FXS phenotype shares common features with Angelman syndrome (AS) that is caused by the loss of one copy of the Ubiquitin Protein Ligase E3A (*UBE3A*) gene [74, 75] leading to similar ID and behavioral patterns [76, 77],

along with decreased dendritic spine density and impaired synaptic plasticity [78, 79]. These shared deficits emphasize the significance of synaptic processes in NDDs [69].

Similar to FXS and AS mouse models [80, 81], *Mecp2* knock out mice, a model of human Rett syndrome, [56, 82], showed also impairments in synaptic plasticity [83, 84]. Also, recently *SYNGAP1* (encoding the synaptic Ras-GTP activating protein 1) and *SNAP25* (encoding synaptosomal-associated protein 25) have been identified as ID risk genes where *SYNGAP1* regulates synaptic signaling and *SNAP25* regulates neurotransmission [85, 86].

Moreover, mutations in genes like *SHANK3*, NEUROLIGIN3 (*NLGN3*) and NEUROLIGIN4 (*NLGN4*), that are involved in **synaptic scaffolding**[69, 87], have been implicated in developmental delay , decreased socialization, and ASD [88, 89]. Animal models with *SHANK3* mutations show disrupted synaptic function at striatal synapses and cortico-striatal circuits and abnormal social behaviors, mimicking key aspects of ASD[90]. *NLGN3* and *NLGN4* were among the first genes associated with ASD [89]. Consistent with this, Neuroligin (*Nlgn*) knockout mice exhibit specific distinct transmission deficits (*Nlgn1* for excitatory, *Nlgn2* for inhibitory) [91] and social impairments (*Nlgn3* and *Nlgn4*), resembling key features of ASD [89, 92]. Other genes, that are participating in dopaminergic and serotonergic neurotransmission, have been associated with ADHD such as dopamine receptors D4 (*DRD4*) and D5 (*DRD5*), dopamine transporter DAT(*SLC6A3*), serotonin transporter (*SERT, SLC6A4*), and serotonin 1B receptor (*HTR1B*) [93, 94].

NDDs can also arise from defects in the maintenance and **repair of neuronal connections**. Spinal muscular atrophy (SMA), for example, is caused by mutations in the *SMN1* gene, which plays a critical role in motor neuron survival and function. The loss of motor neurons in SMA leads to progressive muscle weakness and motor deterioration[95]. Neuronal progenitors derived from SMA patient iPSCs provide a valuable model to study the disease, revealing defects in motor neuron differentiation and survival. These findings have paved the way for the development of targeted therapies, such as the FDA-approved drug nusinersen, which aims to restore SMN protein levels and improve motor function[96]. The success of SMA research illustrates the power of understanding the molecular mechanisms underlying NDDs in developing effective treatments.

Beyond individual mechanisms, many NDDs involve complex interactions between multiple pathways, such as autism spectrum disorder (ASD), which is associated with

alterations in neuronal connectivity, synaptic function, and gene regulation. Genetic studies have identified hundreds of risk genes involved in synaptic plasticity, transcriptional regulation, and chromatin remodeling[97]. Disruptions in these processes can lead to imbalances in excitatory and inhibitory signaling in the brain, which is thought to contribute to the characteristic social, communication, and behavioral deficits in ASD[98]. The involvement of genes encoding chromatin-modifying enzymes and epigenetic modifiers in ASD has become a crucial area of study. Notable genes include *CHD8* and *ADNP*, both critical for chromatin remodeling, as highlighted by De Rubeis et al. (2014) [97]. Such research supports the known association of *MECP2* as epigenetic modifier with Rett syndrome [56]. Other examples include *EHMT1*, which modifies histones and is linked to Kleefstra syndrome, and *KMT2C*, a histone methyltransferase whose mutations are associated with neurodevelopmental disorders and ASD [97, 99]. This complexity highlights the need for multifaceted therapeutic approaches that target different aspects of neuronal development and function. In conclusion, these examples, along with many others confirm the pivotal association of genetic causes in NDDs and their mechanistic pathobiology. In addition, understanding such disorders/mechanisms offer avenues for developing targeted therapies aimed at correcting or mitigating these developmental disruptions.

### **1.3 POGZ & White Sutton Syndrome (WHSUS)**

*POGZ* (Pogo Transposable Element with zinc finger “ZNF” domain) is another gene identified through genomic sequencing. It is one of the most recurrently mutated *de novo* genes with potential loss-of-function in ASD patients (Fig.2) [4, 10, 11]. The mutations in *POGZ* lead to a spectrum of NDDs called White-Sutton syndrome (WHSUS, OMIM: 616364)[100, 101]. *POGZ* mutations were initially identified in patients through large-scale cohort-based whole exome sequencing of individuals with NDDs[101]. This study revealed that *de novo* mutations in the *POGZ* have been found across six independent and diverse cohorts of individuals with NDDs, including conditions ranging from autism spectrum disorder to developmental delay[101]. WHSUS is inherited in an autosomal dominant manner, so insufficiency in just one allele of the responsible gene can result in the manifestation of the disease [102]. WHSUS phenotypic spectrum is widely diverse including developmental delay, autism spectrum disorder, other neuropsychiatric issues, with or without structural brain malformations, varying degrees of intellectual disability,

seizures, visual impairment, hearing loss, and gastrointestinal and urinary tract abnormalities (Fig.2) [103]. What has been noticed is that the severity of symptoms of WHSUS are variable depending not only on the type of the *POGZ* genetic variants but also the location of it and the possibility of undergoing nonsense-mediated RNA decay (NMD) [103]. Nonsense, frameshift (destroyed by NMD) and missense variants located in the first half of the protein (including ZF 1–8 and HPZ) are associated with milder phenotypes, while variants (NMD-escaping nonsense, frameshift and also missense) in the proline-rich domain and in its close proximity cause the most severe outcomes (Fig.3&7). The distal part of the protein, including CENPB, DDE and coiled coil domain, were associated with a mild-to-moderate disease severity (Fig.3). In the C-terminal end of *POGZ* (integrase domain-binding motif), no pathogenic variants have been identified yet (Fig.3). Missense variants seem linked to milder phenotypes ( $p=0.0421$ ), with behavioral anomalies rather than intellectual disability [17, 103], whereas nonsense and frameshift variants that evade NMD are more inclined to more severe phenotypes ( $p<0.0001$ ) causing intellectual disability and accompanying malformations of the gastrointestinal or urinary tract [100, 103]. Nevertheless, a distinct genotype-phenotype correlation was not being well established till Nagy *et al.*, [103] did it in terms of the disease severity. In Nagy *et al.*, it has been found that variants in the proline-rich region of the *POGZ* protein and the ones causing gain-of-function or dominant negative effect through escaping NMD, were significantly linked to more severe phenotypes ( $p=0.0004$ ) (Fig.7) [103]. Nonetheless, some observations highlight the potential for a distinct clinical profile associated with mutations in the *POGZ* gene [18, 100, 101]. Some physical traits, such as obesity and brachydactyly, may be exclusive to WHSUS when it is compared with symptoms of other intellectual disabilities including behavioral abnormalities, cognitive impairment, and certain physical characteristics such as Smith-Magenis syndrome (SMS, MIM#182290) [104, 105]. However, unlike WHSUS, SMS also manifests maladaptive behaviors and sensory issues highlighting the importance of considering SMS in the differential diagnosis [106, 107]. While the frequency of WHSUS remains undisclosed, previous studies suggest that alterations in the gene associated with WHSUS are estimated to occur in approximately 1 out of 700 patients diagnosed with ID, ASD, or both [108].



**Fig.2. Clinical images of individuals carrying *de novo* likely gene-disruptive (LGD) mutations in *POGZ* reveal common facial features, including a broad forehead, high nasal bridge, hypertelorism, and occasionally a thin upper lip. However, these facial characteristics are not highly distinctive or easily recognizable. The images depict various individuals at different ages, showing the progression of their facial features over time[109].**

#### **1.4 POGZ**

The *POGZ* gene is located on chromosome 1q21.3. Within the ENSEMBL database, there are 24 isoforms [110], with five corresponding to curated RefSeq/consensus CDS isoforms in human (GRCh38.p14). The longest transcript, identified by the ENSEMBL Transcript ID: ENST00000271715.7 and RefSeq: NM\_015100.4, consists of 19 exons, of which 18 are coding (exons 2–19). In GTEx database, only two isoforms, *POGZ* isoform 3 (17 exons) (GenBank: NM\_145796.4) and isoform 2 (18 exons) (GenBank: NM\_207171.2), exhibited high expression across most tissues. The longest annotated isoform (GenBank: NM\_015100.4) does not exhibit constitutive expression but shows higher expression in specific tissues, including the brain (particularly the cerebellum, pituitary gland, and cerebellar hemisphere), the thyroid, and female reproductive organs such as the uterus, ovaries, and cervix. Bulk tissue gene expression for *POGZ* exhibits constitutive expression across various tissues, with particularly high expression levels in the pituitary and cerebellum[17]. In adult tissues, *POGZ* isoforms 2 and 3 consistently displayed significantly increased expression in the cerebellum and pituitary gland compared to all other brain sub-tissues. The most abundantly expressed *POGZ* isoform 3 (GenBank: NP\_665739.3) differed from the longest annotated isoform by the exclusion of amino acids 112–189 encoded by two alternatively spliced exons. Additionally, *POGZ* isoform 2 (GenBank:

NP\_997054.1) exhibited the second-highest RNA expression pattern and differed from the longest isoform by the exclusion of amino acids 34–94. In Human brain, expression of POGZ peaks during the embryonal period around weeks 8–9 of gestation, gradually declines until birth, and persists at low levels into adulthood [17]. In mouse brain, POGZ is robustly expressed at embryonic day 13, followed by a gradual decline throughout brain development. Immunohistochemical examinations revealed enrichment of POGZ expression ranging from the ventricular zone to the cortical plate, so it's expressed in both neuronal progenitors and newly formed neurons, and more particularly pronounced in neurons during early developmental stages[111]. Nuclear expression was observed in Purkinje cells in the cerebellum at postnatal day (P) 7 and P15 but diminished by day 30. In primary mouse cultured hippocampal neurons, POGZ was predominantly localized in the nucleus but also detected in axons and dendrites, with partial presence at synapses [112].

*POGZ* gene encodes POGZ protein that is mainly a heterochromatin binding protein and characterized by eight zinc finger domains, which mediates DNA-binding and protein interaction (Fig.3). Followed by, an HP1-binding motif (HPZ domain), that associates with heterochromatin protein 1 (HP1), aiding in chromatin compaction, proline-rich domain (PRO), it is known for mediating interactions with other proteins, and this domain has been linked to more severe phenotypic outcomes when disrupted by genetic variants. The protein also contains a CENPB-like DNA Binding Domain (CENPB-DB) that is homologous to the centromere protein B (CENP-B) and is implicated in binding to specific DNA sequences at the centromere, suggesting a role in chromosomal stability and segregation during cell division. Following by, a transposase-derived DDE domain, that is implicated in chromatin remodeling. close to the C- terminal, coiled coil (CC) domain and integrase domain-binding motif (I domain) are located (Fig.3) [13, 17, 113, 114] .

#### **1.4.1 POGZ and Chromatin Remodeling**

POGZ serves as a regulator of chromatin remodeling, playing essential roles in chromosomal segregation and mitotic progression through kinetochore assembly[113]. POGZ interacts with heterochromatin protein 1 $\alpha$  (HP1 $\alpha$ )/(CBX5), that in turn leads to activation and the dissociation of aurora B kinase from chromosome arms during M phase[113]. POGZ binding to HP1 $\alpha$  depends mainly on its HPZ domain (amino-acid residues 791–850) (Fig.4), and a peptide composed exclusively of these residues is ample

for interaction with the HP1 $\alpha$  carboxy-terminal chromoshadow domain (CSD) [113]. POGZ also interacts with SP1 transcription factor, and chromodomain helicase DNA-binding protein 4 (CHD4) which suggests POGZ acts as a chromatin regulator [19-21]. In Matsumura *et al.*, chromatin immunoprecipitation (ChIP) assays showed that the *Jag2* promoter region was enriched with anti-POGZ antibodies, indicating POGZ binding to the *Jag2* promoter in cortical neural stem cells (NSCs) from E16.5 wildtype (WT) mice [115]. To investigate POGZ function, Sun *et al.*, performed CUT&Tag in FLAG-POGZ *Pogz*<sup>-/-</sup> mouse embryonic stem cells (ESCs)[116]. CUT&Tag identified 16,728 significantly enriched peaks, revealing POGZ localization primarily at proximal transcription start sites (TSS) and distal regions. Further analysis showed POGZ binding at distal regions enriched for poised and active enhancers. Approximately 10,000 genes were found to be POGZ targets. KEGG analysis indicated enrichment in pathways related to neurodegeneration, including Parkinson's and Huntington's diseases, aligning with the association of *POGZ* mutations with neurodevelopmental disorders[116]. Genome-wide binding profiles of POGZ were characterized using ChIP-seq and CUT&Tag experiments in another Sun *et al.*, study [117]. A few derepressed endogenous retroviruses (ERVs) showed significant POGZ enrichment, suggesting that POGZ regulates most ERVs indirectly. Notably, POGZ-bound ERVs like IAPEY and RLTR9E were among the youngest murine transposable elements, retaining

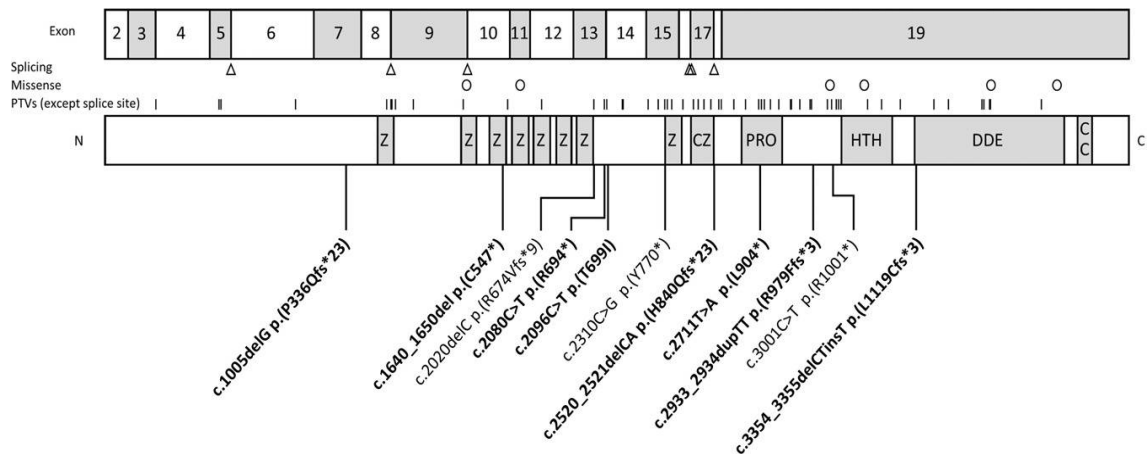


**Fig.3. Schematic structure of *POGZ* exons and its protein with putative functional domains.** The top panel shows the exonic structure of the *POGZ* gene, with the first exon being non-coding. The lower panel depicts the POGZ protein, which includes the following domains: zinc finger domains (Z), a chromobox 5 binding region with an additional zinc finger domain (CZ), a proline-rich domain (PRO), a helix-turn-helix centromere protein-B-like DNA-binding domain (HTH), a DDE superfamily endonuclease domain (DDE), and a coiled-coil domain (CC). Below the protein model are the variants identified in this study, with novel variants highlighted in bold. Above the protein model, previously reported protein-truncating variants (PTVs) are indicated by lines (excluding splice site variants), missense variants associated with WHSUS are represented by circles, and triangles denote variants predicted to affect splicing[114].

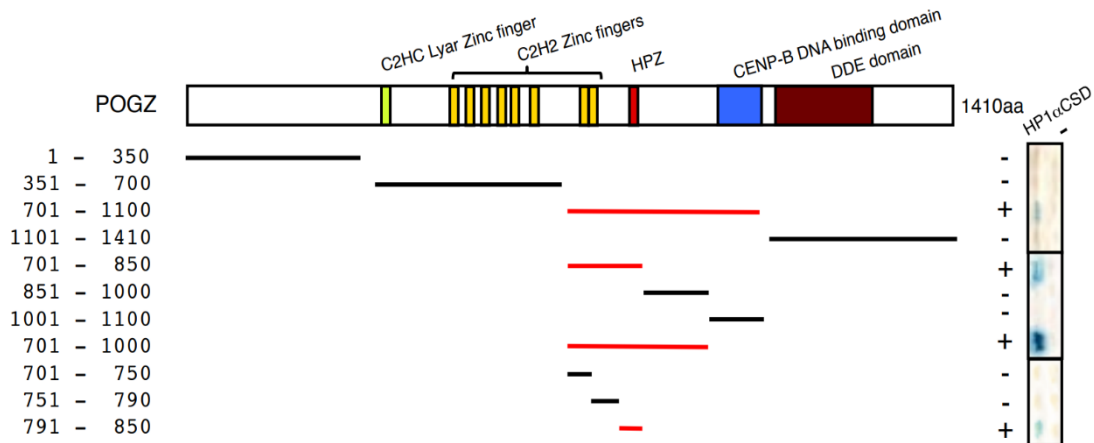


**Fig.4. Fragments of POGZ that yielded positive signals in the yeast two hybrid (Y2H)  $\beta$ -galactosidase assay with HP1 $\alpha$  CSD as bait (on the right) are highlighted in red. Specifically, the POGZ fragment encompassing amino acids 791 to 850 interacts with HP1 $\alpha$  CSD[113].**

transposition capability, indicating POGZ's functional specificity. In addition, POGZ binding signals were abundant at the *Dux* gene promoter which is a known positive regulator of 2-cell stage embryo-like (2C-like) state, a state where cells spontaneously transit back into the pluripotent state. *Dux* was significantly derepressed in *Pogz* knockout mouse ESCs, with increased chromatin accessibility revealed by ATAC-seq. DUX protein levels were higher in *Pogz* knockout ESCs compared to controls[117].

In Papadimitriou *et.al.*, it has been shown that POGZ binds to parts of euchromatin and facilitates the transcription and activation of chromatin at gene regulatory elements (REs). POGZ directly binds within 50kb of clustered synaptic genes leading to their activation to encode molecules related to synapse and axon guidance[111]. In this study, CUT&RUN (C&R) was performed in E13.5 WT mouse telencephalons using an anti-POGZ antibody. *Pogz*<sup>-/-</sup> embryos and IgG served as negative controls. The C&R analysis identified 2,023 consensus POGZ peaks. These peaks showed significantly reduced signals in *Pogz*<sup>-/-</sup> and IgG controls, confirming the validity of POGZ interactions. POGZ was found to occupy transcription start sites (29% of peaks) and distal intergenic regions (71%), suggesting its role as a transcriptional regulator. Notably, 4.7% of POGZ peaks overlapped with enhancers active in the E11.5 mouse embryonic brain, compared to only 0.06% overlap with non-brain enhancers, indicating POGZ's binding to brain-specific enhancers[111].

HOMER motif analysis revealed that POGZ C&R peaks were highly enriched for homeobox and ZNF motifs, which are known to bind telencephalic enhancers. *De novo* motif discovery also identified putative POGZ binding motifs. Genes near POGZ-occupied loci were enriched for GO terms such as "nuclear euchromatin" and "axonal growth cone,"

suggesting POGZ may regulate genes involved in euchromatin and axon growth. Overall, the C&R and immunostaining experiments from same study provide evidence that POGZ primarily binds euchromatic loci and regulatory elements[111].

Moreover, in the E13.5 mouse telencephalon, embryonic cerebral cortex, POGZ is involved in formation of a nuclear complex with Heterochromatin Protein 1 $\gamma$  (HP1 $\gamma$ )/ (CBX3) and Activity-dependent neuroprotector homeobox protein (ADNP), ADNP is an important gene associated with ASD. This complex co-occupies genomic loci where the relative binding levels of POGZ/ADNP at REs influences transcriptional output. In other terms, when POGZ occupies loci with decreased co-occupancy of ADNP and HP1 $\gamma$ , it functions as a transcriptional activator. Conversely, POGZ acts as a repressor when it exhibits high co-occupancy with ADNP and HP1 $\gamma$ . The study also identifies potential molecular targets of POGZ that are other autism risk genes and transposable elements then elucidates its function in ASD [111].

From literature and STRING Consortium 2023, many other genes are experimentally proven to interact with POGZ such as *PSIP1*(*LEDGF /p75*) via POGZ integrase binding domain[118], *CHAMP1*[119-121] and *MAD2I2*[119, 122](Fig.5). In addition to its interactions with different HP1 proteins mentioned earlier; *CBX1*(*HP1 $\beta$* )[113, 119], *CBX5*(*HP1 $\alpha$* )[113, 119], *CBX3*(*HP1 $\gamma$* ) [111, 113, 123, 124] (Fig.5). Therefore, disturbance in these genes might result in related disorders. *PSIP1* (PC4- AND SFRS1-INTERACTING PROTEIN 1) is a coactivator gene that aids in the differentiation of neuroepithelial stem cells and in safeguarding cells during stress-induced apoptosis [17, 125]. For *CBX1* (Chromobox protein homolog 1), it encodes a nonhistone protein involved in heterochromatin formation. This protein is predominantly found in heterochromatin regions and is associated with centromeres. It likely plays a role in regulating chromatin structure and gene expression through epigenetic mechanisms[126].The *CBX5* (chromobox protein homolog 5) binds histone H3 tails methylated at Lys-9 is removed from chromatin when Tyr-41 of histone H3 is phosphorylated. It interacts with the lamin-B receptor (LBR), influencing inner nuclear membrane and heterochromatin interaction and influencing the functional kinetochore[17, 114].

POGZ also interacts with *CHAMP1* (Chromosome alignment-maintaining phosphoprotein 1) that plays a crucial role in ensuring the proper alignment of chromosomes and their components during metaphase[127]. *CHAMP1* facilitates the attachment of microtubules

to the kinetochore during sister chromatid orientation and chromosome segregation [128]. It has been shown that CHAMP1 forms with POGZ a heterochromatin complex promoting homologous recombination (HR) repair[129]. Mutations in the *CHAMP1* gene lead to a neurodevelopmental disorder characterized by hypotonia, impaired language, and dysmorphic features. Individuals with this disorder exhibit symptoms such as microcephaly, low-set ears, delayed psychomotor development, intellectual disability, and autistic features[130, 131]. *MAD2L2* (Mitotic Arrest Deficient 2 like 2) regulates DNA synthesis via mediating between the error-prone DNA polymerase zeta catalytic subunit REV3L and the inserter polymerase REV1 and it encodes the MAD2B checkpoint [132, 133].

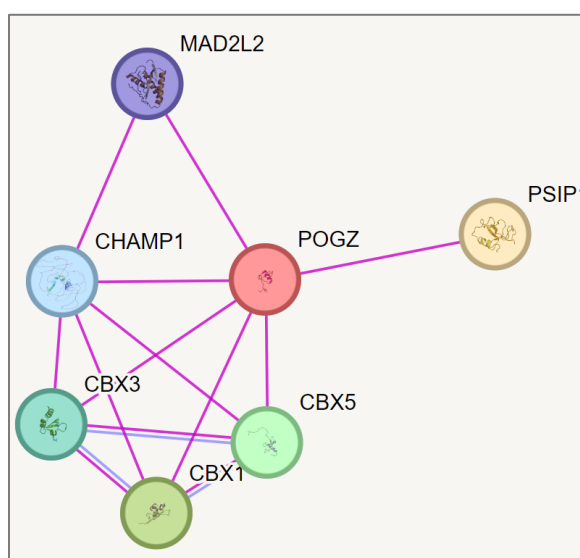


**Fig.5. STRING functional protein association networks of POGZ with predicted protein partners:** PSIP1(LEDGF /p75), CBX1, CBX5 CBX3 CHAMP1 and MAD2L2 that are experimentally proven. The edges indicate both functional and physical protein associations at high confidence (0.700) interaction score. Filled network nodes represent proteins with a known 3D structure. Edges represent protein-protein associations; purple lines represent experimentally determined data and light blue lines represent protein homology.

#### 1.4.2 POGZ and Embryonic stem cell (ESC) identity

POGZ maintains embryonic stem cell (ESC) identity and induces the expression of neural genes during ESC differentiation into neural lineages. In mouse embryonic stem cell (mESC), it was shown that POGZ shares binding motifs with NANOG/OCT4 core pluripotency factors. By using published NANOG/OCT4 ChIP-seq datasets, an extensive overlap was found between POGZ and NANOG/OCT4 peaks genome-wide indicating POGZ co-localizes with NANOG and OCT4 across the genome. In addition, double immunofluorescence staining demonstrated that POGZ co-localizes with NANOG in ESC nuclei, and co-immunoprecipitation (co-IP) experiments showed that POGZ can pull down endogenous OCT4. These findings indicate that POGZ plays a significant role in maintaining

ESC stemness, which aligns with observations that loss of POGZ compromises ESC stemness[116].

The same study showed that POGZ is predominantly localized to gene promoters and enhancers and acts as both a transcriptional activator and repressor in mESCs. Loss of POGZ dysregulates expression of genes important for differentiation, particularly neural genes via affecting chromatin accessibility and histone marks at local euchromatin loci. RNA-Seq analysis of early passage *Pogz*<sup>-/-</sup> mESCs (at passage 10) identified many of up-regulated differentially expressed genes (DEGs) that are involved in neural differentiation and axonogenesis, such as *App*, *En2*, *Insm1*, *Lama1*, *Meis1/2*, *Neurog3*, *Nefh*, *Nefl*, *Nefm*, *Ngfr* and *Nkx2.9*, indicating loss of POGZ reinforces ESC differentiation [116]. POGZ directly interacts with the SWI-SNF (esBAF) chromatin remodeler complex, regulating enhancer activities through epigenetic modifications like chromatin remodeling and histone modification. During mESC neural induction, POGZ mediates recruitment of esBAF/BRG1 and H3K27ac at enhancer regions of neural progenitor genes related to regulation of synapse function and axon development [116].

#### **1.4.3 POGZ and Mitosis**

It has been shown that POGZ is needed for formation of the kinetochore and spindle assembly checkpoints (SAC) during mitosis (M) [113]. In HeLa cells, it has been shown that the HP1 $\alpha$ -binding domain (HPZ) of POGZ which binds to HP1 plays a crucial role in proper mitotic progression and separation of HP1 $\alpha$  from chromosome arms. Furthermore, the function of POGZ is needed for the precise activation and separation of Aurora B kinase from chromosome arms during M phase. These observations show POGZ significance in mediating the dissociation of HP1 $\alpha$  and the activation of Aurora B kinase during mitosis. Knockdown of POGZ in HeLa cells resulted in significant phenotypic changes, including sister-chromatid cohesion defects, mis localization of the chromosomal passenger complex (CPC), cohesion and kinetochore protein assembly, causing premature mitotic exit, polyploidy, and potential cell death or genomic instability[113].

Another study showed late passage (>15 passages) *Pogz*<sup>-/-</sup> and *Pogz*<sup>+/-</sup> mouse mESCs displayed significant cell growth and proliferation defects showing POGZ depletion reduced number of cell division mitosis marker phospho-histone H3 (PHH3)-positive cells. In the same study, analysis of the apoptotic marker annexin-v by flow cytometry in *Pogz*<sup>-/-</sup> mESCs demonstrated that the loss of POGZ leads to a significant increase in cell death.

These findings indicate that POGZ plays a critical role in maintaining normal cell viability and is essential for proper mitotic progression [116].

Investigating apical and intermediate neural progenitors, reduced mitotic cells (pHH3+) were observed in *Pogz*-deficient mice (E15.5) with brain specific *Pogz* conditional knockout using the Cre-lox system, with loxP sites flanking exons 13–19[134]. Moreover, a cell-cycle progression studies showed accelerated cell-cycle exit with in utero electroporation of *Pogz* shRNA[134]. In adult mouse neurogenesis, *Pogz*-deficient mice had fewer immature neurons (DCX+) in the dentate gyrus. While proliferation (Ki67+ cells) was unaffected, there was a significant reduction in BrdU+ cells 21 days post-injection, indicating decreased cell survival. Thus, *Pogz* is crucial for proper cell-cycle progression and neurogenesis [134].

In Deng *et al* study, the role of POGZ in mitosis and neural stem cell (NSC) proliferation was investigated during the neural rosette stage[135]. On day 21, immunostaining of neural rosettes for mitosis marker PHH3 and cell proliferation marker MKI67 was performed. Both PHH3 and MKI67 levels were significantly reduced in *POGZ*<sup>-/-</sup> lines, with a moderate reduction in PHH3+ cells observed in the *POGZ*<sup>+/-</sup> line [135].

#### **1.4.4 POGZ and DNA double-strand breaks' (DSBs) Repair**

Recently, it has been shown that POGZ is also involved in DNA double-strand breaks (DSBs) repair as it facilitates the recruitment of HP1 to DNA DSBs in human cells (Fig.6) [136]. It has been found that radiomimetic antibiotic treated HeLa or U2OS cells have more  $\gamma$  H2AX positive cells where the cells were transfected with the small interfering RNAs (siRNAs) targeting *POGZ* 48h pre-treatment. This suggests POGZ depletion would interfere the phosphorylation of the histone variant H2AX on serine 139 ( $\gamma$  H2AX), which is a critical step in the initiation of the response to DSBs and their subsequent repair[136]. Therefore, *POGZ* deficiency delays the repair process of DSBs and increases cellular sensitivity to various DNA-damaging agents like cisplatin and talazoparib. Mechanistically, POGZ supports homology-directed DNA repair by anchoring the BRCA1/BARD1 complex at DSB sites in an HP1-dependent manner [136].

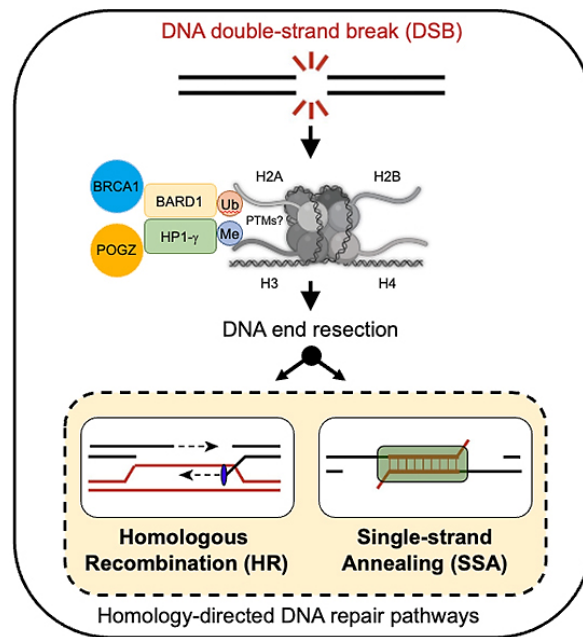


**Fig.6. The zinc finger protein POGZ promotes homologous recombination** across various cell types by anchoring the HP1-gamma-BARD1-BRCA1 complex at DNA double-strand breaks (DSBs)[136].

#### 1.4.5 POGZ and Sleep-related phenotypes

Subsequently, a recent report showed the genes linked to sleep-associated characteristics are among the targets of POGZ[137]. The report was elucidating that the intersecting molecular pathways that are disrupted due to POGZ loss of function and contribute to the development of sleep-related phenotypes in individuals with causative *POGZ* variants previously described[137]. They identified genes linked to sleep-related traits among POGZ regulatory targets in previously published data. Noteworthy those pathways are involved in circadian rhythm regulation, tau protein binding, and ATPase activator activity[137]. The enrichment of tau protein pathways in the intersecting gene list aligns with previous studies linking increased tau levels in interstitial and cerebrospinal fluid to wakefulness and sleep deprivation, indicating that tau protein is affected by sleep disturbances[138]. Tau-related abnormalities have also been observed in NDDs, including the rare genetic syndrome linked to *ADNP*, another chromatin remodeler associated with ASD and a key POGZ interactor[111]. Variants in the *ADNP* gene are associated with reduced microtubule-tau interactions, leading to tauopathies[139]. Moreover, the report shows that POGZ is implicated in circadian rhythm regulation, possibly through its interaction with the BAF complex (BRG1/BRM-associated factor) [116]. The BAF complex is important during the activation phase of the internal circadian clock [140]. This BAF complex acts as an ATP-dependent chromatin remodeler which is involved in regulating

gene expression and differentiation and is strongly linked to NDDs[141]. *POGZ* affects the ATPase activator activity pathway that has been linked to increased levels of norepinephrine in the brain, sustained neuronal excitability and sleep deprivation[142].

### **1.5 Variants of *POGZ* & Non sense mediated RNA decay**

As it was mentioned the severity of *POGZ*-associated disorders varies significantly among patients. One explanation for this diversity in phenotypes from mild to severe is the types and locations of variants in *POGZ* and the predicted occurrence of nonsense-mediated mRNA decay (NMD) and hence the molecular mechanisms of *POGZ* mutations' pathogenicity (Fig.7). In Nagy et al, It was observed that missense variants were more frequently linked to mild phenotypes, whereas truncating variants predicted to evade NMD were associated with more severe phenotypes[103]. Notably, variants located in the proline-rich region of the *POGZ* protein were correlated with the most severe phenotypes. Molecularly, frameshift and nonsense variants located in the first half of the protein (including ZF 1–8 and HPZ) before the amino acid residue 810, are predicted to undergo NMD and lead to haploinsufficiency[103] (Fig.7). In patients with complete deletion of the *POGZ* gene or deletion of exons 4–19, those variants are supposed to have similar effect that of NMD. With a complete gene deletion, mRNA synthesis from the deleted allele does not occur, while deletion of exons 4–19 results in a significantly truncated transcript, so likely undergoing NMD as well [103]. On the other hand, truncating frameshift and nonsense variants located after the amino acid residue 810, are notably associated with sever phenotypes(Fig.7). Meanwhile, all missense variants are expected to escape NMD but are associated with milder phenotype(Fig.7).

Not only the type of variants affects the severity but also the location of it. Mutations observed within the proline-rich region exhibited the most pronounced phenotypic severity. Conversely, zinc finger domains were predominantly linked to milder phenotypes. Even the analysis of variants outside the functional domains of *POGZ* showed that variants within the region spanning 1–850 residues were associated with milder phenotypes, while those within the region spanning 851–1014 residues exhibited the most severe phenotypes. Therefore, the severity of *POGZ*-related phenotype may be influenced by gain-of-function or dominant negative effects resulting from NMD evasion, along with the location of variants within the protein's proline-rich domain[103] (Fig.7). Some pathogenic/likely pathogenic variants have been reported in patients on ClinVar (Genomic

variation as it relates to human health) including mutations located at the very N-terminus like p. Asp3fs and p. Met1Val ([ClinVar/POGZ](#)) (Fig.8).

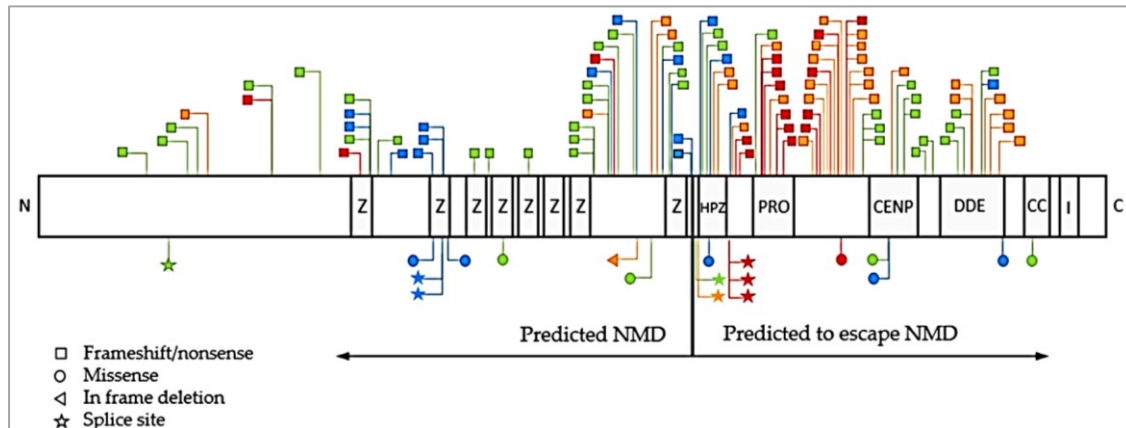


**Fig.7. Variants in POGZ domains are distributed across different regions.** NMD: nonsense-mediated RNA decay; CENP-binding: Centromere protein (CENP)-B-DNA-binding domain; DDE: originated from a transposase encoded by a pogo-like DNA transposon; Z: zinc finger domains 1-8; HPZ: HP1-binding zinc finger-like domain (zinc finger domain 9); CC: coiled coil domain; I: Integrase domain-binding motif. According to Nagy et al. severity score; Severity scores 1: blue, severity score 2: green, severity score 3: orange and severity score 4: red. Variants with inconsistent severity labeling (e.g., a red-labeled variant in the N-terminal domain or zinc finger 1 domain) originate from cohort 3, which had less detailed phenotypic information. [67].

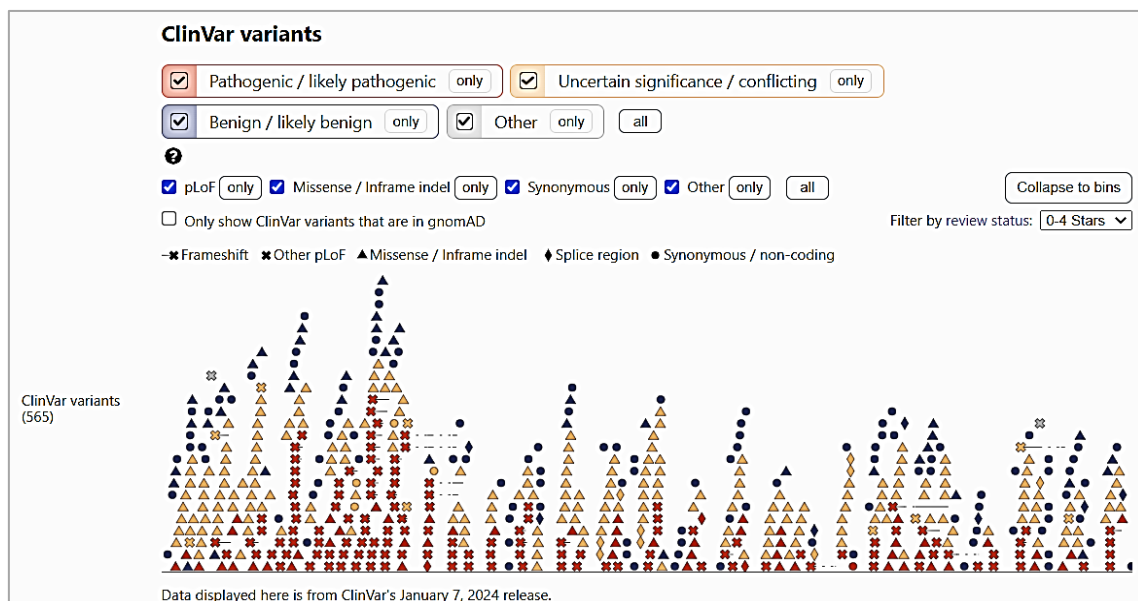


**Fig.8. Clinvar's data base on January 7, 2024 release showing different types of variants in POGZ domains that are distributed across the gene.**

### **1.6 Induced pluripotent stem cells as a model for disease:**

Reprogramming somatic cells into induced pluripotent stem cells (iPSCs) represents a transformative milestone in developmental biology. Initially demonstrated by Yamanaka in 2006, iPSCs are artificially induced pluripotent stem cells derived from various somatic cell sources through the expression of four key transcription factors known as OSKM: Octamer 3/4 (Oct3/4), Krüppel-like factor 4 (Klf4), SRY-box containing gene 2 (Sox2), and the proto-oncogene cytoplasmic Myc protein (c-Myc). This reprogramming process enables the reversal of terminally differentiated cells to a pluripotent state, rendering them capable of differentiating into any embryonic lineage[143] (Fig.9).

OCT4, a POU-type transcription factor, is crucial for embryonic development and stem cell pluripotency, with dysregulation potentially leading to tumor development[144]. KLF4, a member of the zinc-finger krueppel family of transcription factors, plays pivotal roles in cell proliferation, differentiation, and apoptosis regulation[145]. SOX2, belonging to the SRY-related HMG-box family, controls the expression of genes pivotal for embryonic development and cell fate determination, particularly mediating neural stem cell self-renewal [146]. c-MYC, a nuclear-phosphoprotein, is implicated in cell cycle progression, apoptosis, and cellular transformation, often being upregulated in cancers[147] (Fig.9). Prior to the advent of iPSCs, other cell types like lymphoblastoid cell lines and fibroblasts were utilized as disease models, each with its limitations. While lymphoblastoid cell lines offer patient-specificity, they fall short in modeling non-blood-related diseases, particularly neuronal disorders due to their mesodermal origin[148, 149]. Fibroblasts, although easily obtainable in a patient-specific manner through skin biopsies, present challenges in accurately modeling neuronal diseases due to their mesodermal origin[150]. Embryonic stem cells (ESCs) were initially considered the benchmark for disease modeling due to their pluripotency[151]. In contrast to fibroblasts and lymphoblastoid, ESCs lack patient-specificity, necessitating precise genome editing for disease-associated mutations. However, despite this capability, ESCs lack the genetic and epigenetic background specific to individual patients. The advent of iPSCs addressed these limitations, offering both pluripotency and patient-specificity by being generated from somatic cells of individual patients[152]. Since the pioneering work of Takahashi and Yamanaka, extensive efforts have been directed towards reprogramming diverse somatic cell sources to enhance efficiency and safety. iPSCs can now be derived from various

somatic tissues, including differentiated cells, somatic stem cells, senescent cells, and even biological waste materials and urine[153]. The choice of donor cells significantly impacts the characteristics of iPSCs, with studies indicating varying reprogramming efficiencies depending on the cell type of origin. Importantly, iPSCs retain an epigenetic memory from their original cells, which influences their differentiation potential and cellular behavior[154-156].

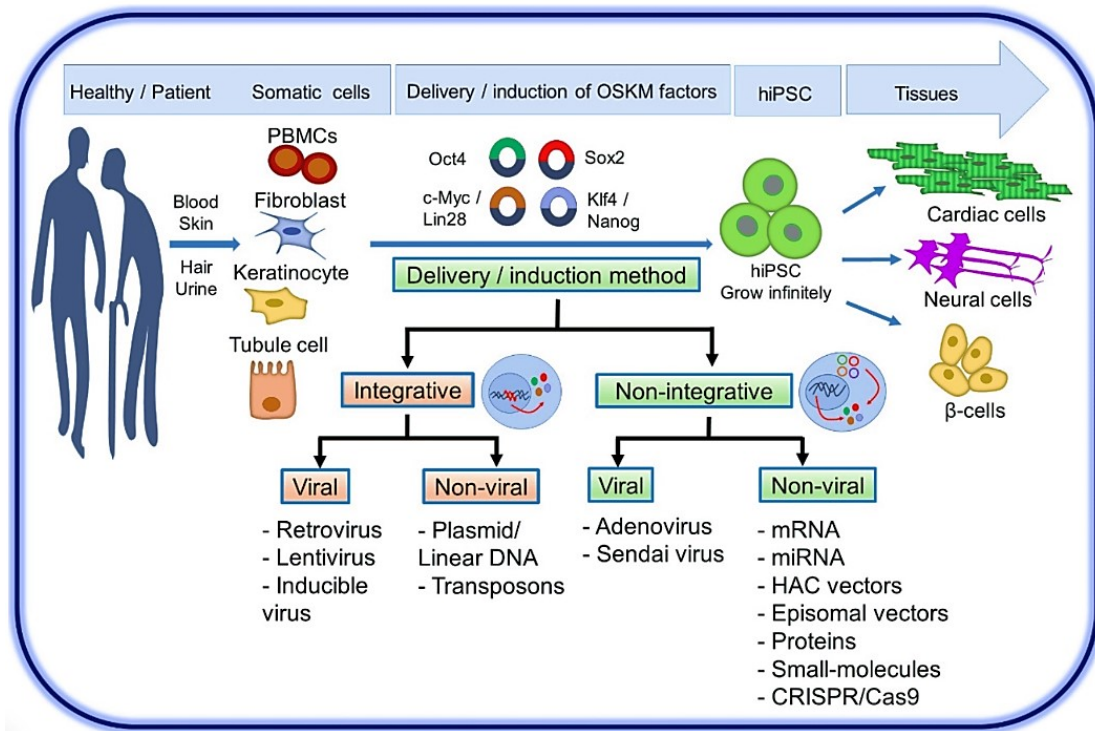


**Fig.9 Schematic diagram showing OSKM factors delivery or induction to reprogram somatic cells into pluripotent cells, followed by iPSC differentiation into cells from all three germ layers[157].**

Among the most commonly utilized cell sources for reprogramming are blood cells and skin fibroblasts, owing to standardized methods, easy accessibility, and the availability of biobanks containing iPSC lines from both healthy individuals and patients. These biobanks serve as invaluable resources for iPSC derivation, particularly for disease modeling and medical research endeavors[156, 158].

Advancements in iPSC technology have revolutionized the study of human development and diseases, offering unprecedented opportunities to investigate cellular and complex disease phenotypes in vitro[152]. By differentiating iPSCs into specific cell types or three-dimensional organoids, researchers can conduct comprehensive studies of human biology, disease mechanisms, and therapeutic interventions[152, 159, 160]. Additionally, iPSC-based models facilitate high-throughput toxicology screening and drug discovery, thereby accelerating the development of novel treatments. Moreover, the combination

of iPSC technology with advanced genetic engineering techniques such as CRISPR-Cas9 has unlocked promising avenues for personalized medicine and regenerative therapies. Through the precise manipulation of iPSCs, researchers can correct disease-causing genetic mutations and generate patient-specific cell lines for autologous cell-based therapy, offering new hope for individuals with a wide range of debilitating conditions[161, 162].

### **1.6.1 Common characteristics of iPSCs and ESCs**

In addition to their pluripotency and capacity for differentiation into all cell types except the placenta, both ESCs and iPSCs exhibit common features. They display remarkably similar patterns of chromatin methylation, promoter activity, and histone demethylation [163]. While their global DNA methylation patterns show substantial similarity, iPSCs possess a few distinct marks, suggesting incomplete reprogramming [164]. Despite these differences, their comparable epigenetic profiles lead to characteristic transcriptomic and proteomic profiles typical of stem cells, confirming iPSCs as stem cells post-reprogramming. Morphologically, both cell types grow as colonies of monolayer cells with well-defined borders and large nuclei comprising a majority of the cell volume. Furthermore, their doubling times remain consistent and can be expanded indefinitely due to telomerase activity [143]. To assess their potency and differentiability, both ESCs and iPSCs are subjected to tests such as the formation of embryoid bodies (EBs) and injection into immunosuppressed mice, where only stem cells can generate teratomas composed of cells from all three germ layers [163].

In the context of patient-specific iPSCs compared to ESCs, while iPSCs offer the advantage of patient-specificity, genome editing is often necessary to achieve isogenic controls. Unlikely, ESCs are typically edited to introduce specific patient mutations [165]. Studies have demonstrated significant differences in DNA methylation, gene expression, and differentiation efficiency among iPSCs derived from unrelated healthy individuals. Consequently, to effectively model diseases in vitro, it is imperative to utilize iPSC lines as controls that closely match the genetic profile of disease-specific lines. In recent years, numerous precise genome editing tools, including CRISPR/Cas, have been developed and widely adopted for this purpose.

### 1.6.2 Induced pluripotent stem cells 'differentiation into disease specific cells

Since the first successful isolation of human embryonic stem-like cells, totipotent non-committed inner cell mass (ICM) cells, in 1994[166] and later of human ESCs in 1998, researchers have been developing protocols to induce stem cells to differentiate into specific cell types[151]. Initially, protocols were established for neurons, cardiomyocytes, pancreatic  $\beta$ -cells, and blood cells, with the overarching goal of enabling allogeneic cell therapy in the long term [152] (Fig.10). With the advent of iPSCs, many of these protocols were adapted for patient-specific disease modeling, eliminating the need for gene editing as required with ESCs. This approach allowed scientists to identify disease-associated phenotypes in NDDs, such as in Rett syndrome in 2010[60] and fragile X syndrome (FXS) in 2015[167]. Using Rett syndrome (RTT) as an NDD genetic model, researchers developed a culture system using iPSCs from RTT patients' fibroblasts, which were able to generate functional neurons exhibiting various deficits compared to controls. This model not only uncovered early alterations in RTT neurons but also demonstrated its potential as a tool for drug screening, diagnosis, and personalized treatment before disease onset[60]. Other researchers developed a high-content imaging assay using iPSCs from FXS patients to identify compounds that could reactivate the silenced *Fmr1* gene, testing 50,000 compounds and finding several that induced weak expression of FMRP, setting the stage for further drug discovery efforts[167].

Contemporary research puts the focus now on generating three-dimensional (3D) organoids that mimic the cellular composition and heterogeneity of human organs, thereby improving translatability to clinical trials. Notable examples include cerebral organoids containing functional neurons, which exhibit cortical self-organization with regions expressing forebrain and hindbrain markers [168]. These neurons display spontaneous electrical activity. Despite that, 3D organoids face challenges like lack of vasculature, leading to limited growth and necrosis, and variability in formation, affecting reproducibility[169]. They also lack the full complexity of an in vivo brain and remain relatively immature, limiting their use in long-term studies[169, 170]. To enhance physiological relevance, organoids can be transplanted into mice to create human-mouse chimeras, where the human organoids become vascularized and interact with the host organism's hormonal, circulatory, nervous, and immune systems. The coming years will

shed light on the extent to which these advancements improve outcomes and facilitate translation to clinical trials [152].

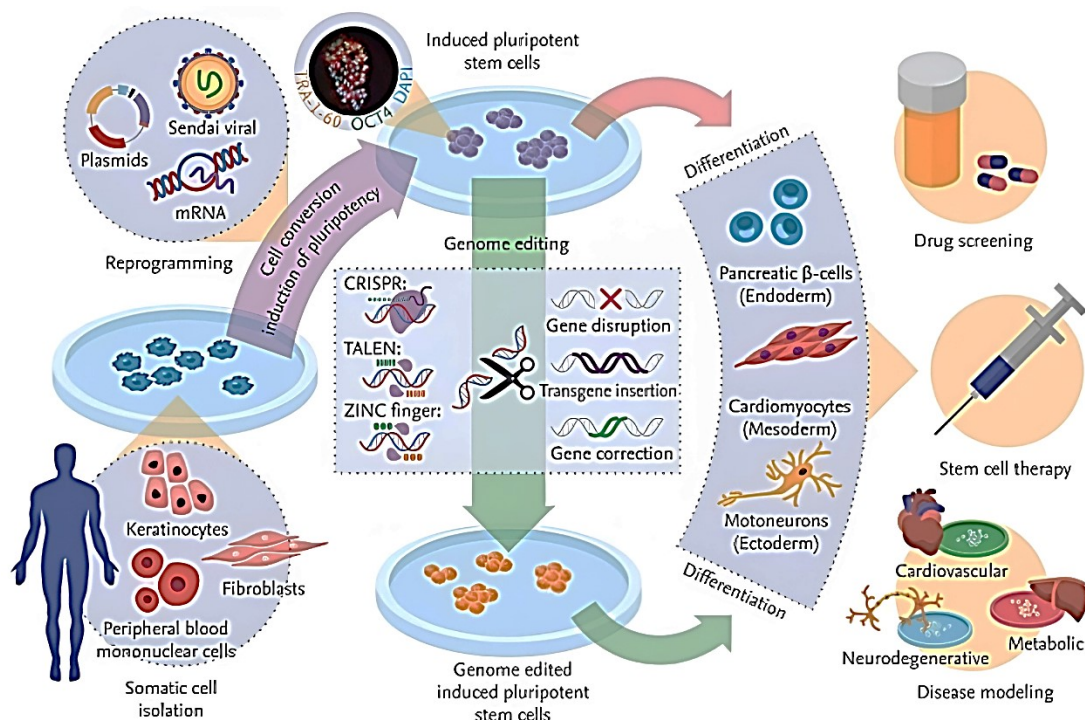


**Fig.10. Reprogramming specific somatic cells into induced pluripotent stem cells (iPSCs) and their clinical implications.** Somatic cells are isolated from a patient and then reprogrammed into iPSCs by introducing four reprogramming factors: octamer-binding transcription factor 4 (Oct4), sex determining region Y-box 2, Kruppel-like factor 4, and c-Myc. Genetic defects within iPSCs can be corrected using gene editing tools such as zinc finger nucleases (ZFNs), activator-like effector nucleases (TALENs), and the clustered regularly interspaced short palindromic repeats (CRISPR) system. Subsequently, iPSCs, whether edited or not, are differentiated into various target cells for applications in disease modeling, drug screening, and stem cell therapy[171].

## 1.7 Human brain development and iPSCs

### 1.7.1 Brain development

Following gastrulation, the human embryo undergoes complicated morphogenetic adjustments, ensuing in the formation of three germ layers: ectoderm, mesoderm, and endoderm. Neurogenesis, the process of nervous system development, initiates during neurulation, a critical stage where the neural plate undergoes invagination to form the neural tube, the precursor to the entire nervous system, including the brain and spinal cord. During early neurogenesis, the neural tube includes a layer of neuroepithelial cells (NECs) inside the ventricular zone (VZ). NECs primarily undergo symmetric division, expanding the pool of cortical neural progenitors and influencing the overall size of the developing brain[172-174]. As the neural tube develops further, a distinct population of progenitor cells called ventricular radial glial cells (vRG) emerges in the VZ. vRG cells play a pivotal function in cortical development, displaying a completely unique morphology

characterized by their cell bodies positioned within the VZ, apical processes extending toward the ventricular surface, and basal processes traversing the whole cortical thickness[172, 175]. These cells undergo both symmetric and asymmetric divisions, contributing to the expansion of the progenitor pool and generating intermediate progenitor cells (IPCs) or neurons respectively[176].

As neurogenesis progresses, additional layers of progenitor cells expand, specifically inside the subventricular sector (SVZ), a region adjacent to the VZ. Basal progenitors (BPs) inside the SVZ mostly induce neuronal differentiation, giving rise to the formation of internal and outer subventricular zones (iSVZ and oSVZ)[177, 178]. The oSVZ, particular to mammalian species with large cortices, contains basal intermediate progenitor cells (bIPCs) and outer radial glia (oRG), also called basal radial glia progenitors[179]. oRG cells constitute an essential cell population in cortical expansion, showing tremendous proliferative capacity and the ability to generate numerous neuronal subtypes. These cells make a contribution to the increased complexity and size of the human cortex, a defining characteristic of primate brains in comparison to other species[180]. Importantly, variations in the morphology and the nature of radial glial cells occur during mid-gestation, with vRG transitioning into truncated radial glia (tRG) and oRG maintaining their connections with the pial surface to facilitate neuronal migration of newborn neurons[181-183].

### **1.7.2 Neurogenesis**

Neurogenesis encompasses the transition of neural progenitor cells into neurons, a process that initiates during early human embryonic development, following neurulation around 4 weeks after conception (PCW), and typically persists until 23 PCW in most brain regions. Nevertheless, there are some age-related exceptions concerning the areas of the cerebellum or the hippocampus where neurogenesis continues the entire postnatal period [184]. Hence, the timing and duration of embryonic neurogenesis may vary across specific regions of the nervous system, implying the involvement of distinct regulatory mechanisms in nervous system development [185-187]. In humans, cognitive functions, including decision-making, perception and language, are directly connected with and controlled by the cerebral cortex, a brain region that allows primates to perform more complicated tasks, and displays significant disparities between them and rodents, which underlie primate-specific high-order cognitive traits [184, 188, 189]. With focus on neurogenesis in cortex, the initial phase of cerebral cortex development, referred to as

corticogenesis, entails the formation of the preplate or primordial plexiform layer, situated between the ventricular zone and the pia membrane of the dorsal telencephalon. This stage emerges around embryonic day (E) 33 in human [190, 191], primarily comprising early differentiated neurons termed pioneer neurons (Fig.11). These pioneer neurons encompass diverse populations such as Cajal-Retzius cells (CR), crucial for migration signaling, predecessor cells, and subplate cells (SP) [192-194]. The preplate region exhibits considerable dynamism, with post-mitotic neurons migrating within it from the SVZ and VZ regions. Subsequently, the preplate area evolves into the cortical plate, while the intermediate zone develops above the SVZ and VZ. During this transition, CR cells migrate above the cortical plate and beneath the pia membrane, forming the marginal zone (MZ). Concurrently, SP cells migrate beneath the preplate region and constitute the subplate (SP) between the intermediate zone and cortical plate [193, 195, 196].

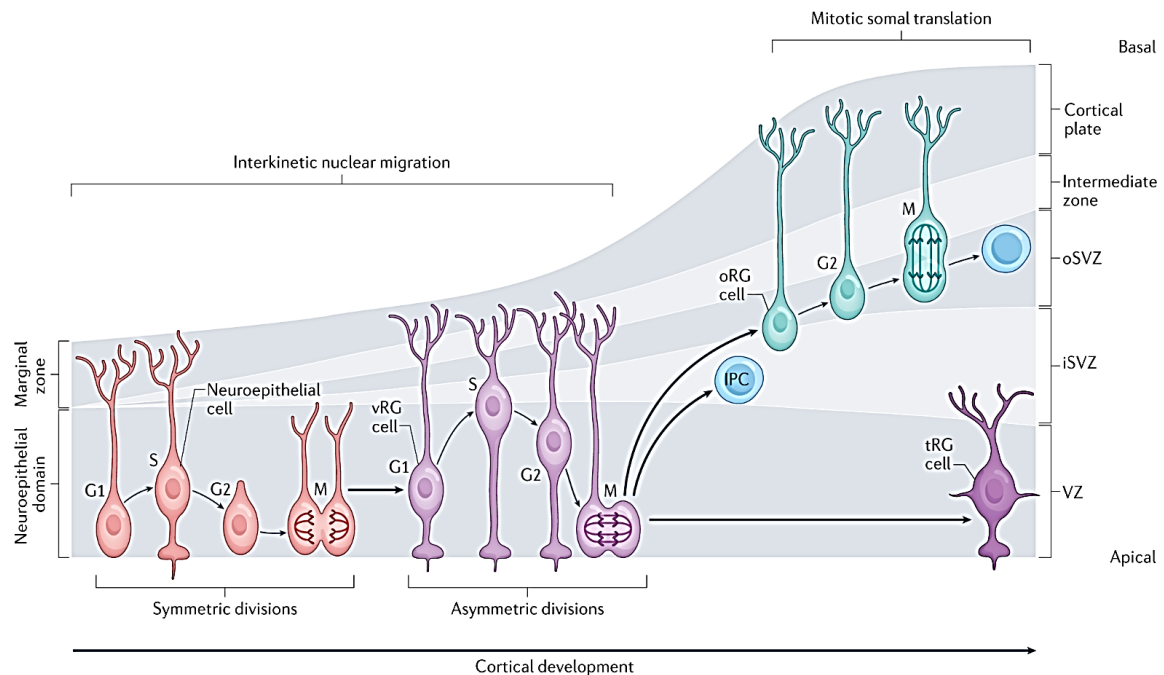


**Fig.11. Cortical neurogenesis in human.** Neuroepithelial cells (NE) transform into radial glial (RG) cells within the ventricular zone (VZ). RG cells then undergo either symmetric division to expand their population or asymmetric division to contribute to neurogenesis. RG can directly differentiate into neurons or give rise to intermediate progenitors, which undergo further proliferation before differentiating into neurons. The outer subventricular zone is enlarged in primates, leading to increased proliferation of progenitor cells and overall greater volume[197].

In the mature cortex, the MZ eventually evolves into the first layer and encompasses various cell types and dendrites from neurons located in other layers[193]. The SP region is transient and critical for neural circuit formation and axon guidance [198, 199]; a distinctive feature of humans and primates is the secondary expansion of the SP region[200]. Once the MZ and SP zones are established, the upper and lower boundaries

are delineated, prompting neurons to migrate towards the cortical plate from the VZ and SVZ, utilizing the basal projection of oRG cells as a scaffold. Neuronal migration persists until reaching the CP region, where signaling pathways induce neurons to cease migration, differentiate, and extend dendrites and synaptic connections [201]. The generation of the six cortical layers occurs through neuronal migration in an "inside-out" manner. Deep-layer (DL) neurons, located in the V and VI layers, are the earliest primate neurons generated [202]. Subsequently, the IV layer emerges, with neurons receiving inputs from the thalamus[203]. Finally, upper-layer (UL) neurons differentiate into layers II and III, characterized by corticocortical projections, primarily originating from oRG cells [179]. The capacity of precursor cells to differentiate into various neurons remains incompletely understood. Several models have been proposed to elucidate this unique ability: one model suggests early specification of progenitors into specific neuronal subtypes during development, while another proposes that homogeneous progenitors give rise to diverse neurons during the neurogenesis stage [204]. Recent scRNA-seq studies are beginning to provide initial evidence of the molecular mechanisms underlying precursor differentiation, suggesting a process of "priming" of the RG progenitor cells for differentiation into specific neuronal subtypes prior to cell division[205].

### **1.8 Investigating Human Neuronal Differentiation and Brain Organogenesis via In Vitro Modeling**

In vitro modeling approaches significantly facilitate in-depth research on human neuronal differentiation and brain organogenesis. Historically, the study of human brain development faced serious limitations due to limited access and limited availability of primary tissue samples. Nevertheless, recent stem cell technology has revolutionized to investigate main aspects of central nervous system (CNS) organogenesis using human-derived pluripotent stem cells (hPSCs)[206-208]. The ability to culture mammalian embryonic brain tissues in vitro since 1970, enables the formation of structures similar to in vivo brain regions such as the cortex, hippocampus, and neuromuscular junctions[209, 210]. The development of human pluripotent stem cells, including both embryonic stem cells (hESCs)[211] and induced pluripotent stem cells (hiPSCs)[212], has further pushed the advancement in this field. Techniques have been outlined for generating neurons from hPSCs in cultures in which growth factor combinations and small molecules can be utilized in the culture medium[213, 214]. Initially, the hPSCs were primarily differentiated into

neurons in two-dimensional (2D) neuronal cell cultures[215]. Although 2D cultures are suitable for large-scale studies, 2D cultures lack the intricate complex cellular interactions and extracellular matrix dynamics which are crucial during embryonic development [216, 217]. Additionally, they lack temporal dynamics to model processes such as circuit formation and gliogenesis occurring during later stages of human embryonic and neonatal development.

As a reaction to the existing limitations with hPSC for 2D culture, protocols for generating three-dimensional (3D) cell agglomerates from hPSCs, known as organoids, were developed in the early 2010s[206]. These organoids self-organize into complex neural structures resembling embryonic neural tissues, allowing for the study of complex cellular interactions and tissue architecture in vitro[206]. The optic cup organoids were the first series generated, that showed the practicability of reconstruction of particular brain regions in a dish[218].

Protocols for generating brain organoids typically fall into two categories: unguided and guided differentiation protocols. Unguided protocols where hPSCs exhibit inherent self-patterning and self-organization within an extracellular matrix (ECM), leading to differentiation into various neural structures. However, unguided differentiation often results in variability between experiments and undesirable false differentiation into non-neuronal cell types[219]. In comparison, specific signaling molecules and morphogens are used in guided differentiation to drive neural differentiation in a more controlled systematic manner, resulting in more reproducible outcomes[220-222]. Recent breakthroughs in organoid technology include ECM-free organoid development and modeling of post-natal developmental stages, allowing for a deeper-level investigation of both physiological and pathological aspects of neural development[221, 223, 224].

### **1.9 CRISPR/Cas genome editing**

CRISPR/Cas genome editing technique that has been used since 2012 [225] was inspired by the immune system in prokaryotes. In prokaryotes the CRISPR-Cas system has evolved as a protection mechanism against viruses[226]. This revolutionary system comprises two essential components: The Cas9 protein and the single guide RNA (sgRNA), which is composed from an endonuclease (nuclease) protein and a non-coding RNA (Fig.12). The Cas9 protein is the enzymatic core responsible for cutting the DNA with perfect precision at the target site. Different Cas9 proteins are produced, some of which have definite

features, while others are general. Originally, classical Cas9 was constricted in its range of activity by a specific PAM-sequence (protospacer adjacent motif) of NGG and induced a double-strand break (Fig.12). But upon being widened by alternative Cas9 proteins from different bacterial species, which perform with PAM-sequences of different kinds, this restriction was blurred, so the range of target loci for genome editing increased[227]. A long with it, diverse engineered Cas9 proteins come into the picture, which could initiate single strand nicks or are completely inactive and fused with silencers or activators to modulate gene expression[228, 229]. The sgRNA is composed of two subdomains, the so-called crRNA (crisprRNA) and the tracrRNA (trans-activating crRNA) that are vital for the processing of the Cas9 protein. It guides Cas9 into the target gene locus. While tracrRNA provides a secondary structure that binds the Cas9 enzyme and induces sgRNA and Cas9 interaction, crRNA carries a 20-nucleotide sequence that is specific to the provided sequence location[225]. The Cas9 protein and the guide RNA (sgRNA) assemble together to form a ribonucleoprotein complex with the ability to cut the DNA at a specific position. In the last few years, many labs and companies made their own platforms for rapid and effective design, cloning, and transfection of sgRNA, coupled with optimized Cas proteins. At first, protocols relied on plasmid-based transfection methods for delivering sgRNA and Cas, either through a single plasmid or two separate plasmids. These systems utilize cellular transcription and translation machinery. More recent approaches involve the use of pre-synthesized ready sgRNAs and Cas proteins, eliminating the need for cellular modifications. Following a double-strand break occurrence, cells have two repair pathways available: non-homologous end-joining (NHEJ) or homology-directed repair (HDR) pathways[230] (Fig.12).

### **1.9.1 Non-Homologous End-Joining (NHEJ)**

The NHEJ mechanism represents a non-specific mechanism for DNA repair that is prone to errors, often resulting in small insertions or deletions, without necessitating any homologous regions. The double strand break occurrence is followed by involvement of various proteins that participate in the recognition as well as in the repair process[231, 232]. In the first stage, the DNA-protein kinases will bind to the two ends of the DNA, positioning them close to each other and recruiting other enzymes necessary for subsequent steps. Often, mutations arise during end processing, where enzymes excise nucleotides if the two ends are incompatible or lack the requisite 3' hydroxyl or 5'

phosphate overhangs essential for ligation. The final step involves the ligation of the two DNA ends by the DNA ligase IV complex (Fig.12).

### 1.9.2 Homology Directed Repair (HDR)

HDR is the cell's precise mechanism for repairing double-strand breaks that unlike NHEJ, necessitates a template sequence (Fig.12). The homologous recombination template originates by using either the sister chromosome or, alternatively, co-transfection with the sgRNA and Cas protein to induce specific mutations or repair a mutation. Iyama & Wilson (2013) state that MRN protein complex is the first protein to bind the DNA ends and bringing them into proximity [232]. The following step involves the recruitment of enzymes which generate the 3' overhangs of single-stranded DNA by trimming from the 5' ends. Replication protein A (RPA) that is a DNA-binding protein then reacts with single-stranded DNA and then, gets assisted by other HDR proteins to search for a similar sequence. Upon finding a similar sequence (from the template), they form a displacement loop, enabling a DNA polymerase to synthesize new DNA by extending the 3' end (Fig.12). The cell can proceed with either the double-strand break repair (DSBR) or the synthesis-dependent strand annealing (SDSA) pathway. DSBR involves the second 3' end also forming a Holiday junction, typically leading to a crossover event. Conversely, SDSA results in repair without crossover, as the newly synthesized overhang dissociates from the Holiday junction and is then able to anneal to the remaining damaged 3' overhang. Finally, a ligase completes the pathway by sealing all remaining single-strand gaps (Fig.12).

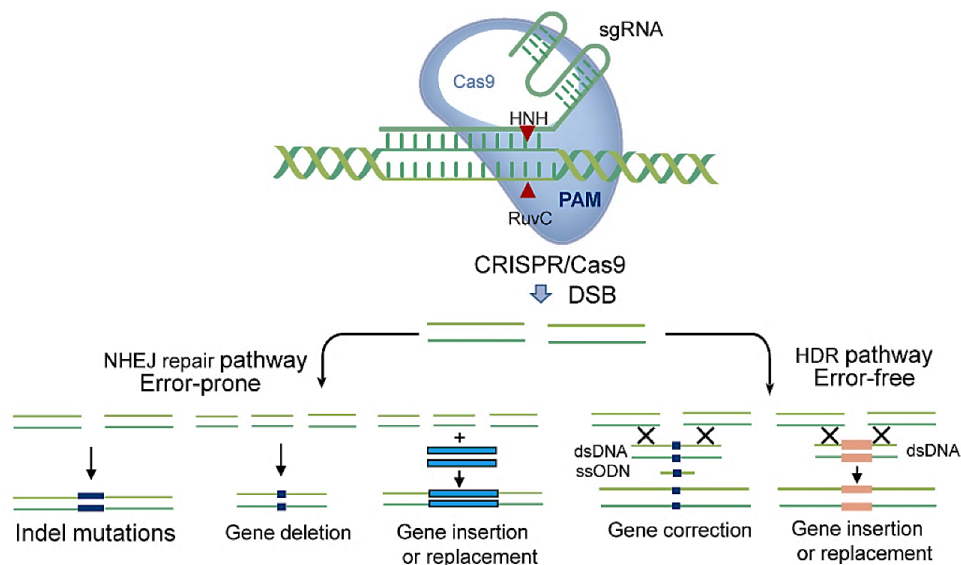


**Fig.12. CRISPR/Cas genome editing.** The sgRNA recognizes the target sequence and facilitates Cas9 completion. Cas9 induces a double-strand break via its active domains three bases adjacent to the PAM sequence. After induction of a double strand break, either the NHEJ pathway is used to ligate the two DNA strands frequently causing an Indel mutation or the HDR pathway is used to ligate the two DNA strands using a donor template [233].

## 2 Aim of the project

The aim of this PhD study is to investigate the cellular and molecular mechanisms by which mutations in the *POGZ* gene contribute to neurodevelopmental disorders (NDDs), specifically intellectual disability (ID) and autism spectrum disorders (ASD). Given the genetic complexity and overlap between these conditions, with *POGZ* identified as a key gene associated with ASD, the research seeks to understand the downstream effects of *POGZ* mutations and how these mutations disrupt brain development. To achieve this, patient-derived induced pluripotent stem cells (iPSCs) were used as a model system, with CRISPR/Cas9 gene editing to introduce heterozygous *POGZ* mutations.

These iPSCs were differentiated into neural progenitor cells (NPCs) and neurons under both two-dimensional (2D) and three-dimensional (3D) culture conditions, including neurospheres and brain organoids. The study investigated how *POGZ* mutations influence critical aspects of neural development, including NPC self-renewal, neuronal differentiation, and migration. By analyzing the 3D neurospheres and organoids, it aims to replicate a more in vivo-like environment, allowing the observation of changes in neural cell behavior and the formation of brain-like structures. This approach provided insights into how mutations in *POGZ* disrupt the formation of cortical layers, neuronal maturation, and migration patterns—key processes that may be altered in NDDs. Additionally, transcriptomic analysis via RNA sequencing was performed to identify changes in gene expression in *POGZ*-mutant NPCs, revealing disruptions in pathways such as mitotic chromatid segregation, DNA repair, and synaptic function. Through CUT&Tag sequencing, the study further identified direct targets of *POGZ* and showed how these genetic changes correlate with broader molecular disruptions seen in ASD and other NDDs. The overrepresentation of autism-associated risk genes among *POGZ* targets points to a mechanistic link between *POGZ* dysfunction and ASD pathophysiology.

Ultimately, this study aimed to bridge the gap between genetic findings and the biological mechanisms underlying NDDs by providing a deeper understanding of how *POGZ* mutations alter neural development and gene regulation. These insights could guide the development of targeted therapies for *POGZ*-related conditions, offering potential new treatments for these complex disorders.

### 3 Material and Methods

#### 3.1 Material

##### 3.1.1 Equipment

**Table 1 Laboratory equipment used during the PhD study**

Name	Manufacturer	Model	Function
Nanodrop™ OneC Spectralphotometer	ThermoFisher Scientific	ND-ONEC-W	DNA and RNA quantification
StepOnePlus™ Real-Time PCR System	ThermoFisher Scientific	4376600	Real time qPCR
PeqPower 300 V	Peqlab	300 V	Power supply for agarose chamber
Electrophoresis chamber	Peqlab	40-1214, 0-150V, 0-100mA ClassII	Agarose gel separation
Gel iX20 Imager	Intas Science Imaging	iX20	UV imaging of agarose gel
Agarose gel comb	VWR / PeqLab	20 wells 1.5 mm	Preparation of agarose gel
ChemiDoc™ MP Imaging System	Bio-Rad	170-8280	Visualization and imaging of western blots
PyroMark Q96 instrument	Qiagen	9001525	Pyrosequencing
The block for warming the samples			
The platform for the vacuum			
NextSeq	Illumina	NextSeq 2000	RNA-sequencing
Revolve Microscope	Echo	Revolve	Fluorescent microscope
Olympus SZX10 Stereo Microscope	Olympus	SZX10	Stereomicroscope
Leica BGV A3 Stereo Microscope (2011)	Leica	BGV A3	Stereomicroscope
Axiovert25 Inverted Microscope	Zeiss	Axiovert25	Inverted microscope
EVOS XL Microscope with photography	Life Technologies	EVOS XL	Inverted microscope
CO2 incubator	Binder		Cell incubator
CO2 incubator	ThermoForma	371	Cell incubator
Revco EXF	Binder Thermo Scientific	EXF	Cell incubator
ARPEGE140 Liquid nitrogen tank, LIQUIDE, Air Liquide	Arpege	ARPEGE 140	Cell vial long-term storage
Neubauer chamber	Brand		Cell counting
4D-Nucleofector	Lonza	AAF-1002B+AAF-1002X	iPSC electroporation
BD FACSAria™III Cell Sorter	BD	FACSAria™III	Cell sorter for electroporated cells
Liebherr Fridge and Freezer Combination & Freezer	Liebherr		Samples and reagents storage

RevcoExF	Thermo Fisher Scientific	8930	
Acco-Jet Pro	Brand	Pro	Pipette boy
ErgoOne Fast	Starlab	FAST	Pipette boy
Rollermixer SRT9D	Stuart	SRT9D	Roller for mixing solutions
HERASafe Heraeus Sterile Working Bench	Thermo Fisher Scientific	HERASafe	Sterile cell culture working bench
Advanced Primus 96 Thermocycler	PeqLab	96-well	Thermocycler
T100TM Thermal Cycler	BioRad	T100	Thermocycler
VV3	VWR	VV3	Vortexer
Vortex Genie 2™	Bender & Hobein AG	Genie 2	Vortexer
Scout™Pro 600g	Ohaus	DB-4726.5	Scales
Mini Star Table Centrifuge	MiniStar	Mini Star	Table centrifuge
Roth Table centrifuge	Roth	ROTILABO Uni-fuge	Table centrifuge
Perfect Spin P Centrifuge	PeqLab	PerfectSpin P	Table centrifuge for 96-well plates
Eppendorf centrifuge 5415D	Eppendorf	5415D	Centrifuge
Eppendorf centrifuge 5415C	Eppendorf	5415C	Centrifuge
Perfect Spin 24R Refrigerated microcentrifuge	PeqLab	Perfect Spin 24R	Centrifuge
Heraeus Megafuge 16R	Thermo Scientific	Megafuge 16R	Centrifuge

### 3.1.2 Disposable material

**Table 2 Laboratory disposables used during the PhD study**

Name	Manufacturer	Description
12-well cell culture plate Cell star	Greiner Bio-One	12 well plate
6-well cell culture plate Cell star	Greiner Bio-One	6 well plate
Safe-Seal Micro tube (1.5 ml)	Sarstedt	reaction tube,
Eppendorf microfuge tubes (1,5/2 ml)	Eppendorf	Reaction tube
Micro screw tube	Sarstedt	Tubes for aliquoting media supplements (e.g. N2, FGF, ...)
Cell Star tubes (15/50 ml) (PP, graduated, conical bottom, blue screw cap, sterile)	Greiner Bio-One	15 ml and 50 ml falcons
0.2 ml 8-Strip Non-flex PCR Tubes, with Flat Caps	StarLab	PCR tubes
Cryo vials (Self-sealing Cap)	StarLab	Cryo preservation / storage of frozen cells
TipOne filter Tips (10/20/200/1000 µl)	TipOne	Pipette tips

StarLab Filter Tips (10/20/200/1000 µl)	StarLab	Pipette tips
(Nonfiltered) Yellow Tips (200 µl)	StarLab	Pipette tips used in cell culture for removing media with glass pipettes and pump
SafeSeal SurPhob Tips, Low Binding (10 µl)	Biozym	Pipette tips for RT-qPCR
Rack for tubes (1.5/2ml)	NeoLab	Racks for microfuge tubes
NeoRack for falcons	Neolab	Racks for 15 ml and 50 ml falcons
Discovery Comfort Pipettes (10/20/200/1000 µl)	Discovery Comfort	Pipettes
Ergo One Pipettes (10/20/200/1000 µl)	StarLab	Pipettes
Eppendorf Research Pipettes (10/20/200/1000 µl)	Eppendorf	Pipettes
Pipettes (5ml, 10ml, 25ml with graduation)	Greiner Bio-One	glass pipettes
Steri Cup Quick Release, Millipore Express Plus 0,22 µM (Filter Bottles)	Merck Millipore	Bottles to sterile filter media
Superfrost Microscope slides	Thermo Scientific	Glass slides for immune florescence staining
Parafil" M"	Bernis	Laboratory film
Nitril gloves	StarGuard	Sterile gloves
PCR adhesive seal sheet	Thermo Scientific	Sealing of 96-well plates for RT-qPCR
Cell Culture Dish Cell Star	Greiner Bio-One	Petri dishes in cell culture
175cm <sup>2</sup> Cell Culture Flasks	Greiner Bio-One	Fibroblast/HEK culturing
TC Flask T75, Cell+	Sarstedt	Fibroblast/HEK culturing
Microtube TOUGH-TAGS	Diversified Biotech	Tube labelling
Microtube TOUGH-SPOTS	Diversified Biotech	Tube labelling
Multipette Plus manual handdispenser	Eppendorf	Automatic dispenser for QUASEP assay
Multichannel pipette (200 µl)	Thermo Fisher	Multichannel dispenser for PCR products during QUASEP assay

### 3.1.3 Chemicals and Media

#### 3.1.3.1 Chemicals

**Table 3 Chemicals used during the PhD study**

Name	Maufacturer
Acetic Acid	
Acrylamid	Carl Roth
Agar	Carl Roth
Ampicillin	AppliChem
APS	Sigma
Agarose	AppliChem
Ampuwa Spüllösung, 1000ml Plastipur	FRESENIUS KABI

Aqua ad iniectabilia Braun	BRAUN
Boraic acid	Carl Roth
Bromphenol blue	Carl Roth
BSA (Bovine serum albumin)	Carl Roth
CaCl <sub>2</sub>	Carl Roth
DPBS	Gibco LifeTechnologies
EDTA Disodium Salt 2-hydrate	AppliChem
99,99% Ethanol	Honeywell, Riedl-de Haen
99% Ethanol (for disinfection 70 % in water)	Martin & Werner Mundo oHG
Ethidiumbromide	Carl Roth
Glycerin	Carl Roth
Glycin	Carl Roth
HEPES	Carl Roth
Isopropanol	Carl Roth
Milk powder	Carl Roth
Meliseptol Foam Pure	Carl Roth (Braun)
Na <sub>2</sub> HPO <sub>4</sub>	Carl Roth
NaCl	Carl Roth
NaOH	Carl Roth
PFA	Carl Roth
PhosStop	Roche
Protease inhibitor	NEW ENGLAND BioLabs & AppliChem
Proteinase K	AppliChem
Poly-L-Ornithine-hydrobromide	SIGMA-Aldrich
ProLong <sup>TM</sup> Diamong	Thermo Fisher
ProLong <sup>TM</sup> Gold	Thermo Fisher
ProLong <sup>TM</sup> Glass Antifade	Thermo Fisher
SDS	Carl Roth
RNase AWAY (# 7002)	MiBp Molecular Bio Products
Terralin liquid	Schülke +
TRIS	Carl Roth
TEMED	Invitrogen
Triton-X 100	Carl Roth
Trytpone	Carl Roth
Tween20	Carl Roth
Urea	Carl Roth
β-mercaptoethanol	Carl Roth
Vectashield	Vector Laboratories
PyroMark Gold Q96 Enzyme	QIAGEN
PyroMark Gold Q96 Substrate	QIAGEN
PyroMark Gold Q96 dNTPs	QIAGEN
Binding buffer	(Generated in the diagnostics laboratory)
Annealing buffer	(Generated in the diagnostics laboratory)

### 3.1.3.2 Media

**Table 4 Media and compounds used for cell culturing during the PhD study**

Name	Manufacturer
Accutase	ThermoFisher Scientific
Advanced DMEM	Gibco LifeTechnologies
B27+VitA-supplement	Gibco LifeTechnologies
B27-supplement	Gibco LifeTechnologies
bFGF	Gibco LifeTechnologies
EFG	Gibco LifeTechnologies
CloneRTM 10x Cloning Supplement	Stemcell Technologies
DMEM (1x) high glucose	Gibco LifeTechnologies
DMEM	Gibco LifeTechnologies
DMEM with GlutaMAX™	Gibco LifeTechnologies
DMEM/F-12 GlutaMAX™	Gibco LifeTechnologies
DMSO	Carl Roth
DPBS	Gibco LifeTechnologies
ESC-qualified FBS	Gibco LifeTechnologies
FBS	Gibco LifeTechnologies
Gelatine	Sigma
Geltrex	Gibco LifeTechnologies
HBSS	SIGMA
IMDM	Gibco LifeTechnologies
KOSR	Gibco LifeTechnologies
Laminin	Sigma
Matrigel Matrix	Corning
mTeSRTM1	Stemcell Technologies
mTeSRTM1- supplement	Stemcell Technologies
N2-supplement	Gibco LifeTechnologies
MEM-NEAA	Gibco LifeTechnologies
Neural Induction Supplement	Gibco LifeTechnologies
Neurobasal Medium	Gibco LifeTechnologies
Opti-MEM	Gibco LifeTechnologies
Pen/Strep	Gibco LifeTechnologies
Poly-L-Ornithine-hydrobromide	SIGMA
Rock Inhibitor	Stemcell Technologies
RPMI 1640	Gibco LifeTechnologies
TrypLETExpress	Gibco LifeTechnologies

### 3.1.3.3 Media composition

**Table 5 Media composition and function for different cell types used during the PhD thesis**

Cell type	Media function	Media composition
Fibroblasts	Extraction	DMEM + 20% FBS + 1% Pen/strep
	Culturing	IMDM +1% Pen/Strep + 15% Fetal bovine serum (FBS)

	Freezing	Culturing Medium + 10% DMSO
iPSC reprogramming	Fibroblast	FRM: Fibroblast Reprogramming Medium: DMEM + 10% ESC-Qualified FBS + 1% MEM Non-Essential Amino Acids Solution (10 mM) + 0,1% $\beta$ -mercaptoethanol (55 mM)
	MEF cells	MEF medium = FRM
	iPSCs	iPSC Reprogramming Medium: DEMEM/F-12 (GlutaMAX™) + 20% KnockOut Serum Replacement (KOSR) + 1% MEM Non-Essential Amino Acids Solution (10 mM) + 0,1% $\beta$ -mercaptoethanol (55 mM) + 1% Pen/Strep + 0,4% bFGF (10 $\mu$ g/ml)
iPSCs	Coating	Matrigel Matrix or geltrex diluted in DMEM/F-12 (with GlutaMAX)
	Replating	PBS/EDTA: 500 ml DPBS + 301 $\mu$ l 0,8M EDTA solution 0,9g NaCl
	Culturing	mTeSRTM1 + mTeSRTM1 supplement + 1% Pen/Strep
	Freezing	iPSC culturing medium + 10 % DMSO + 25% KOSR
NPCs differentiation	Neural induction	NIM: Neural Induction Medium Neurobasal medium + 2% Neural induction supplement + 1% Pen/strep
	Neural expansion	NEM: Neural Expansion Medium: ~50 % Neurobasal medium + ~ 50% Advanced DMEM/F-12 + 2% Neural induction supplement + 1% Pen/strep
NPCs	Coating	Poly-Ornithine/Laminin
	Culturing	NM: Neural Medium DMEM/F-12 + 1% Pen/Strep + 2% Vitamin B27 + 1% N2-solution + 0,1% FGF2
	Replating	NM + 15-30% KOSR
	Freezing	NM + 10% KOSR + 10% DMSO
Neurons	Coating	Poly-Ornithine/Laminin
Neurons	Culturing	Neurobasal +: Neurobasal Medium + 1% Pen/Strep + 1% Glutamax + 2% Vitamine B27 with VitA
Neurospheres	Culturing	Neural Maintenance Medium (NMM): ~50 % Neurobasal medium + ~ 50% Advanced DMEM/F-12 (GlutaMAX™) + 2% Vitamin B27 + 1% N2- solution + 1% L-Glutamine (2 mM) + 0,1% FGF2 (10 ng/mL) +0,05% EGF (10 ng/mL) +1% MEM-NEAA + 1% Pen/strep
	Coating (migration assay)	Poly-Ornithine/Laminin

### 3.1.4 Reagents, Kits, and Enzymes

#### 3.1.4.1 Kits and reagents

**Table 6 Reagents and kits used during the PhD study**

Name	Manufacturer
CytoTune™-iPS 2.0 Sendai Reprogramming Kit	Thermofisher Scientific
High Pure RNA Isolation Kit	Roche
High Pure PCR Product Purification Kit	Roche
RNA Cleanup Kit	Monarch
PrimeScript™ RT Master Mix	TaKaRaBio
Revert Aid First Strand cDNA Synthesis Kit	Thermofisher Scientific
PyroMark Gold Q96 Reagents	QIAGEN
Reverse Transcription Kit with PrimeScript™ RT Master Mix	TaKaRaBio
NEBNext Ultra II Directional RNA library preparation kit	NEW ENGLAND BioLabs
P3 Primary Cell 4D-Nucleofector™ X Kit L	Lonza
PSC Neural Induction Kit	Thermofisher Scientific
Western Lightning® Plus-ECL, Enhanced Chemiluminescence Substrate	PerkinElmer
EnGen® sgRNA Synthesis Kit, <i>S. pyogenes</i>	New England Biolabs
EnGen® Mutation Detection Kit	New England Biolabs
Lipofectamine™ 2000 Transfection Reagent	Thermofisher Scientific
Lipofectamine™ 3000 Transfection Reagent	Thermofisher Scientific
Neural Tissue Dissociation Kit	Miltenyi Biotec
Click-iT™ EdU Alexa Fluor™ 488 Flow Cytometry Assay Kit	Thermofisher Scientific
TSA buffer	Bio-Techne

#### 3.1.4.2 Enzymes

**Table 7 Enzymes used during the PhD study**

Name	Manufacturer
FastStart™ Taq DNA Polymerase	Roche
Herculase II Fusion DNA Polymerases	Agilent
PrimeScript™ RT Master Mix	TaKaRaBio
SYBR® Premix Ex Taq™ II	TaKaRaBio
Proteinase K	NEW ENGLAND BioLabs & AppliChem
Enzyme	PyroMark Gold Q96 Reagents, QIAGEN
RNase A, DNase and protease free (10 mg/ml)	Thermo Fisher

### 3.1.5 Primers and Antibody

#### 3.1.5.1 Primers

**Table 8 Primers used during the PhD study.** Primers were ordered with a concentration of 100 µM and diluted with dH<sub>2</sub>O to 10 µM before used.

Name	Sequence (5' → 3')
<b>PCR</b>	
POGZ_c.Ex1_fw	ACCAATGGAGTCAAAGTTCTGA
POGZ_c.Ex1_r	AGAAGAGCTTTTGTTACCTGTGG
POGZ_intron.16_Fr	GGAGGGCATTCTTTCTTT

POGZ_intron.17_Rr	TCCTCCCCTTGCTCAACTAA
<b>RT-qPCR</b>	
POGZ_Ex.8&9_Fr	ACACTATCTGCCAGCACTGT
POGZ_Ex.8&9_Rv	GCTCACTTTCAAACGCCCAT
POGZ_Ex.16&17_Fr	ATCATGTTCCACGGAAGAGC
POGZ_Ex.16&17_RV	GATGCTGCTGGATCTGTGAG
POGZ_Ex.18&19_Fr2	ATAGCTCACTCAAGGCATGG
POGZ_Ex.18&19_Rv2	GCTGGGGCTAAGGGAGTTAG
GAPDH_for	CCACATCGCTCAGACACCAT
GAPDH_rev	AAATCCGTTGACTCCGACCTT
Klf4_for	CCCACATGAAGCGACTTCCC
Klf4_rev	CAGGTCCAGGAGATCGTTGAA
MAP2_For	GGAGGTGTCTGCAAGGATAGT
MAP2_Rev	GGTGGAGAAGGAGGCAGATT
NANOG_for	AAGGTCCCGGTCAAGAAACAG
NANOG_rev	CTTCTGCGTCACACCATTGC
Nestin_for	CCAGATCGCTCAGGTCCTG
Nestin_rev	AGCTGAGGGAAGTCTTGGAG
Oct4_for	GTGTTCAGCCAAAAGACCATCT
Oct4_rev	GGCCTGCATGAGGGTTTCT
PAX6_for	ACCCAAGAGCAAATTGAGGC
PAX6_rev	CCATTTGGCCCTTCGATTAGA
SOX2_for	TGGACAGTTACGCGCACAT
SOX2_rev	CGAGTAGGACATGCTGTAGGT
TAU_For	GTGCAAATAGTCTACAAACCAGT
TAU_Rev	CAATCTTCGACTGGACTCTGT
TUBB_For	TCGGACTTGCACTGGAG
TUBB_Rev	CAGGCCTGAAGAGATGTCCA
DCX_qPCR_Hu_Fr	TATGCGCCGAAGCAAGTCTCCA
DCX_qPCR_Hu_Rv	CATCCAAGGACAGAGGCAGGTA
CCND2_qPCR_Hu_Fr	AGTCCCATCTGCAACTCCTG
CCND2_qPCR_Hu_Rv	CGCAAGATGTGCTCAATGAA
MKI67_qPCR_Fr	GAAAGAGTGGCAACCTGCCTTC
MKI67_qPCR_Rv	GCACCAAGTTTTACTACATCTGCC
CHD8_qPCR_Fr	CACTGACTGCTTTCGGGTGGAA
CHD8_qPCR_Rv	GGTCTCCACATCTCGTTCAGTC
EIF1AX_qPCR_Fr	GGGAAATGGACGGCTAGAAGCA
EIF1AX_qPCR_Rv	TCCTGGTAGTCTCGGAGACCAA
NLGN3_qPCR_Fr	GTCTGGTTCACTGCCAACTTGG
NLGN3_qPCR_Rv	CCGTCAATTATCCGCTAAGTCCTC
PINK1_qPCR_Fr	GTGGACCATCTGGTTCAACAGG
PINK1_qPCR_Rv	GCAGCCAAAATCTGCGATCACC
SLC25A25_qPCR_Fr	GCATCGTTGGTGGCTTCACTCA
SLC25A25_qPCR_Rv	CCTCAGAGTCTCCTGGTCACTA
GABRA5_qPCR_Fr	CTGCTCTACACCATGCGCTTGA
GABRA5_qPCR_Rv	GAGCCGTTGGTCCAGACGTAAA
SLITRK3_qPCR_Fr	ACAGACGCCTTTGCTGGCACAT
SLITRK3_qPCR_Rv	TCACAGGTGCAGTCCAAGGAT
HNRNPR_qPCR_Fr	CTTAGCCAAGCCACCAGACAAG

HNRNPR_qPCR_Rv	CCTCTAATTGGAGGTGGCATGC
SLC5A6_qPCR_Fr	GGCTGCTTTGTCTAGGAATGGC
SLC5A6_qPCR_Rv	CATTCCAAGGCAGAAGAGTCCC
LPHN3_qPCR_Fr	GCTCTTGACAGAGCCTATGTCCA
LPHN3_qPCR_Rv	CACTCGTAGTCAGGTCTCTCCA
SLITRK1_qPCR_Fr	CCACAGCATCCGAAAATCGCAC
SLITRK1_qPCR_Rv	TAGCCACCTGAGGTCCAAAAGG
<b>PCR for Pyrosequencing (QUASEP)</b>	
Pyro_A2POGZ2D5_Ex.2.3_F2	[Btn]CATGGCGGACACCGACCT
Pyro_A2POGZ2D5_Ex.2.3_R	GCACTGGAGCCGAGACTGG
Pyro_385/20C34_POGZ.Ex.17_F	CTGGCCTGCACTTCATGTACCT
Pyro_385/20C34_POGZ.Ex.17_R	[Btn]GCTTGCCATAGCATCGC
<b>QUASEP</b>	
Pyro_A2POGZ2D5_Ex.2.3_Sq	CTCCTCCTCACATTCC
Pyro_385/20C34_POGZ.Ex.17_Sq	CACTTCATGTACCTTTGTTA
<b>SeV vectors clearance RT-PCR</b>	
SeV_For	GGATCACTAGGTGATATCGAGC
SeV_Rev	ACCAGACAAGAGTTTAAGAGATATGTATC
KOS_For	ATGCACCGCTACGACGTGAGCGC
KOS_Rev	ACCTTGACAATCCTGATGTGG
KLF4_For	TTCCTGCATGCCAGAGGAGCCC
KLF4_Rev	AATGTATCGAAGGTGCTCAA
c-MYC_For	TAACTGACTAGCAGGCTTGTCG
c-MYC_Rev	TCCACATACAGTCCTGGATGATGATG

### 3.1.5.2 Primary antibodies

**Table 9 Primary antibodies used during the PhD study**

Protein	Organism	Source	Identifier
POGZ	Rabbit	Abcam	ab171934
POGZ	Rabbit [EPR10612]	Abcam	ab167408
POGZ	Rabbit	Bethyl Laboratories	A302-510A
$\alpha$ -SERPINH1	Rabbit	Sigma-Aldrich	S5950
$\alpha$ -NANOG	Goat	R&D Systems	AF1997
$\alpha$ -TRA-1-60	Mouse	Millipore	4360
	Rabbit	Cell Signaling Technologie	9733
$\alpha$ -PAX6	Rabbit	BioLegend	901301
$\alpha$ -SOX2	Rabbit	Abcam	ab137385
$\alpha$ -NESTIN	Mouse	Merck	MAB5326
$\alpha$ -MAP2	Mouse	Sigma	M4403
KI-67 (D3B5)	Rabbit	Cell Signaling Technologie	9129
Phospho-Histone H3 (Ser10) PHH3	Rabbit Polyclonal	Cell Signaling Technologie	9701
Gamma H2AX	Mouse mAb/IgG1k	Millipore	05-636-I

	[JBW301]		
Cleaved Caspase-3 (Asp175) Cas3	Rabbit Polyclonal	Cell Signaling Technologie	9661

### 3.1.5.3 Secondary antibodies

**Table 10 Secondary antibodies used during the PhD study**

Protein	Organism	Source	Identifier
anti-Rabbit IgG, Alexa Fluor 488	Goat	Invitrogen	A11008
anti-Mouse IgG, Alexa Fluor 488	Goat	Invitrogen	A11017
anti-Mouse IgG, Alexa Fluor 488	Rabbit	Invitrogen	A11008
anti-Mouse IgG, Alexa Fluor 594	Goat	Invitrogen	A11012
anti-Goat IgG, Alexa Fluor 594	Rabbit	Invitrogen	A11079

### 3.1.6 Plasmids, gRNA and template constructs

#### 3.1.6.1 Plasmids

**Table 11 Plasmids used during the PhD study**

Name	Manufacturer/Website
pU6-(BbsI) sgRNA_CAG-925 Cas9-venus-bpA	Addgene #86986
gRNA_Cloning Vector	Addgene #41824

#### 3.1.6.2 gRNA constructs

**Table 12 gRNAs used during the PhD study.** Red: 5'-overhang referred to the T7 promoter sequence necessary for cloning required for cloning; Black: gRNA sequence targeting *POGZ* exon2; purple: reverse complement sequence of gRNA.

Name	Sequence
POGZ- sgRNA1_for	TTTCTTGGCTTTATATATCTTGTGGAAGGACGAAACACCGTGAGCCCGTCTAGACCTCGC
POGZ_sgRNA1_rev	GACTAGCCTTATTTAACTTGCTATTCTAGCTCTAAAACGCCATAGCATCGCCACAGAC
POGZ_sgRNA2_for	TTTCTTGGCTTTATATATCTTGTGGAAGGACGAAACACCGTGACCTTTGTTACCCTCTG
POGZ_sgRNA2_rev	GACTAGCCTTATTTAACTTGCTATTCTAGCTCTAAAACAGAGGGTAACAAAGGTACAC
POGZ_sgRNA3_for	TTTCTTGGCTTTATATATCTTGTGGAAGGACGAAACACCGTACCTCTGTGGGCGATGCTA
POGZ_sgRNA3_rev	GACTAGCCTTATTTAACTTGCTATTCTAGCTCTAAAACAGCATCGCCACAGAGGTAC

**Table 13 sgRNAs used during the PhD study.** EnGen® sgRNA sequences are only suitable for EnGen® sgRNA Synthesis Kit. Red: 5'-overhang append T7 promoter sequence; blue: 3'-overhang append overlap sequence; black: gRNA sequence.

\* referred to phosphorothioate linkages.

Name	Sequence
EnGen® sgRNA1 POGZ.Ex.2	TTCTAATACGACTCACTATAGGCGGACACCGACCTGTTTCAGTTTAAAGCTAGA

EnGen® sgRNA2 POGZ.Ex.2	TTCTAATACGACTCACTATAGCGACCTGTTTCATGGAATGTGGTTTAA GAGCTAGA
EnGen® sgRNA1_POGZ.Exo.17_FW	TTCTAATACGACTCACTATAGTCTGTGGGCGATGCTATGGCGTTTT AGAGCTAGA
EnGen® sgRNA2_POGZ.Exo.17_FW	TTCTAATACGACTCACTATAGTGTACCTTTGTTACCCTCTGGTTTAA GAGCTAGA
EnGen® sgRNA3_POGZ.Exo.17_FW	TTCTAATACGACTCACTATAGTACCTCTGTGGGCGATGCTAGTTTAA GAGCTAGA
EnGen® sgRNA4_POGZ.Exo.17_FW	TTCTAATACGACTCACTATAGTTGTTACCTCTGTGGGCGATGTTTAA GAGCTAGA
EnGen® sgRNA5_POGZ.Exo.17_RV	TTCTAATACGACTCACTATAGGCCATAGCATCGCCACAGGTTTAA GAGCTAGA
EnGen® sgRNA6_POGZ.Exo.17_RV	TTCTAATACGACTCACTATAGTCGCCACAGAGGGTAACAAGTTTT AGAGCTAGA
EnGen® sgRNA7_POGZ.Exo.17_RV	TTCTAATACGACTCACTATAGCTTCTCCTACTTACCCCGGTTTAA AGCTAGA
EnGen® sgRNA8_POGZ.Exo.17_RV	TTCTAATACGACTCACTATAGTCTCCTACTTACCCCGTGGCGTTTAA GAGCTAGA
EnGen® sgRNA9_POGZ.Exo.17_FW	TTCTAATACGACTCACTATAGTCCAGCAGCATCCTGCCACGGTTTAA GAGCTAGA
395/20 Pt_ Pogz_WT_Template	C*T*CTTTTTAGTGGGAATCAAGCTGGCCTGCACTTCATGTACCTTT GTTACCTCTGTGGGCGATGCTATGGCCAAGCATTTGGTATTCAACC CCTCTCA*C*A

### 3.1.7 Softwares and online tools

**Table 14** Software and online tools used during the PhD project

Name	Manufacturer/Website
Bioedit	mBio
Office	Microsoft
Prism	GraphPad
Pyro Q CpG	Qiagen
Intas gDS	Intas Science Imaging
ND_1000 3.5.1	Peqlab Biotechnologies
NCBI	www.ncbi.nlm.nih.gov
Genome Browser (UCSC In-Silico PCR)	www.genome.ucsc.edu
CRISPOR	http://crispor.gi.ucsc.edu/
Primer3web	https://primer3.ut.ee/
Ensembl	http://www.ensembl.org/index.html
ClinVar (NCBI)	https://www.ncbi.nlm.nih.gov/clinvar/
STRING	https://string-db.org/
Refseq	https://www.ncbi.nlm.nih.gov/refseq/
Fiji - ImageJ-win64	
GTE Portal	https://gtportal.org/home/
FlowJo	BD Biosciences
Adobe Illustrator	Adobe
EndNote X7	Clarivate

### 3.1.8 Cells

The main experiments of this work were performed with cells originating from three different fibroblast cell lines (Table 12). A male wildtype control cell line (1263/16), a male heterozygous carrier of a *POGZ* mutation (395/20). Also, a female wildtype control fibroblast cell line (1179/17) was reprogrammed into iPSCs which later were genome edited using CRISPR/Cas9 to generate two mutant iPSC lines. All were reprogrammed into iPSCs and later differentiated into NPCs.

**Table 15 Cell lines used during the PhD project**

Patient/ Donor	Donor age	Sex	Cells	Name	Cell type	mutation
395/20	9 years	Male	395/20	Fibro	Fibroblasts	Heterozygous Chr1 g.151379461G>GT(hg19) p.(Thr824AsnfsTer40)
			395/20 C34 iPSCs	C34	iPSCs	
			395/20 C34 NPCs	C34	NPCs	
1263/16	26 years	Male	1263/16	Fibro	Fibroblasts	Wild type
			1263/16 S21 iPSCs	S21	iPSCs	
			1263/16 S21 NPCs	S21	NPCs	
1179/17	~60 years	Female	1179/17	Fibro	Fibroblasts	Wild type
			1179/17 A2 iPSCs	A2	iPSCs	
			1179/17 A2 NPCs	A2	NPCs	
			1179/17 A2POGZ2D5 iPSCs	A2D5	iPSCs	Heterozygous Chr1 g.151414660GA>G(hg19) p.(Phe7SerfsTer29)
			1179/17 A2POGZ2D5 NPCs	A2D5	NPCs	
			1179/17 A2POGZ1A1 iPSCs	A2A1	iPSCs	Compound heterozygous Chr1 (-) g. 151414650- 151414656 delGAATGTG(hg19) p.Cys10LeufsX11
			1179/17 A2POGZ1A1 NPCs	A2A 1	NPCs	
						Chr1 (-) g. 151414653T>TT(hg19) p.Glu9fsX27

## **3.2 Methods**

### **3.2.1 Cell culture conditions**

Cells were maintained at 37°C in a humidified incubator with 5% CO<sub>2</sub>, unless stated otherwise. All procedures were performed in a sterile environment within a laminar flow hood.

#### **3.2.1.1 Plate Coatings**

To ensure proper cell adhesion and preservation of cell identity, plates were coated prior to culturing iPSCs and NPCs. Specific coatings were also applied for particular experimental procedures.

#### **3.2.1.2 Gelatine Coating**

Gelatin-coated plates were used during crucial steps, including fibroblast isolation from skin punch biopsies and iPSC reprogramming. A 2% gelatin stock solution was pre-warmed, diluted 1:20 with pre-warmed PBS, and sterile-filtered. For 6-well plates, 1 ml of the solution was added to each well, and the plates were incubated for 1 hour in a humidified incubator before use.

#### **3.2.1.3 Matrigel Coating**

Matrigel, a commercial 3D basement membrane extract derived from Engelbreth-Holm-Swarm (EHS) mouse sarcoma, mimics the laminin/collagen IV-rich extracellular matrix, commonly used for culturing stem and primary cells. Prior to use, Matrigel was thawed overnight at 4°C, aliquoted according to LOT-specific dilution factors, and stored at -20°C. For coating, the Matrigel aliquot was diluted into 50 ml of chilled DMEM/F-12, mixed, and incubated at 4°C for 1 hour. To coat 6-well plates, 2 ml of the solution was added per well, followed by incubation at 37°C for 1 hour in a humidified incubator before use.

#### **3.2.1.4 Geltrex Coating**

Geltrex is another 3D basement membrane extract, similar to Matrigel but with more consistent protein concentrations across batches due to a different manufacturing process. For coating 6-well plates, Geltrex was diluted 1:100 in 6 ml of pre-chilled DMEM/F-12. Each well received 1 ml of the diluted solution, and the plates were incubated at 37°C for 1 hour in a humidified incubator before use.

#### **3.2.1.5 Poly-Ornithine/Laminin Coating**

Poly-Ornithine/Laminin coating is a combination of Poly-L-Ornithine and Laminin, frequently used for culturing neuronal and neural stem cells due to its promotion of neural cell adhesion and differentiation. A Poly-Ornithine stock solution (500 µg/ml) was diluted 1:50 in pre-chilled borate buffer (150 mM, pH 8.35). For coating 6-well plates, 1.5 ml of

this solution was added to each well and incubated overnight at 37°C in a humidified incubator. On the following day, the Poly-Ornithine solution was removed, and the plates were washed three times with 2 ml of HBSS. After washing, the plates were incubated for 3 hours at 4°C with a 1 µg/ml Laminin solution in HBSS. The coated plates could be stored long-term at -20°C for up to 6 months. Prior to use, they were thawed for at least 1 hour at 37°C in a humidified incubator.

### **3.2.2 Cell culture**

#### **3.2.2.1 Fibroblasts**

Human Dermal fibroblasts from the A2-, S21- and C34-line were used in the thesis. Fibroblasts were previously isolated from healthy control (thesis, Dr. Stephan Käseberg), while fibroblasts from a patient individual (C34-line) were isolated during the study.

##### **3.2.2.1.1 Isolation**

Dermal fibroblasts were isolated from a 4 mm skin punch biopsy, following a published protocol with slight modifications adjustments [234](). The biopsy was obtained through a medical procedure at the Human Genetics Department in Mainz and delivered to the research lab in pre-chilled Fibroblast Extraction Medium (FEM: DMEM + 20% FBS + 1% Pen/Strep). Under sterile conditions in a laminar flow hood, the biopsy was divided into 20-25 equal pieces using a stereomicroscope. These pieces were evenly distributed in a gelatin-coated six-well plate (see gelatin coating), containing 800 µl of FEM, and incubated at 37°C with 5% CO<sub>2</sub> in a humidified incubator. To prevent drying, 200 µl of FEM was added every other day. One week after processing, the FEM volume was increased to 2 ml per well and replaced every alternate day. After 3-4 weeks, when fibroblasts had migrated from the tissue and reached full confluency, cells were detached and reseeded in two T75 flasks using the splitting protocol (). Upon reaching confluency again, cells were transferred to three T175 flasks. Fibroblasts were stored in fibroblast freezing medium (IMDM + 15% FBS + 1% Pen/Strep + 10% DMSO) at a concentration of 1 million cells/ml following the freezing protocol (). Each cryovial was filled with 1 ml of the cell suspension, stored for 24-48 hours at -80°C, and then transferred to liquid nitrogen for long-term storage.

##### **3.2.2.1.2 Thawing**

Cells were thawed by immersing the cryovial partially in 37°C water or warming it by hand. After thawing, cells were transferred to a 15 ml conical tube containing pre-warmed fibroblast culture media and centrifuged for 4 minutes at 200g. The supernatant was

discarded, and the cell pellet was resuspended in fresh pre-warmed media, then transferred to a T75 flask. This thawing method was adapted for other cell types by adjusting the media and culture plates to suit the specific cells.

#### 3.2.2.1.3 Culturing

Human dermal fibroblasts were cultured in T75 or T175 flasks with fibroblast culture media (IMDM + 15% FBS + 1% Pen/Strep). The cells were monitored every other day and incubated at 37°C with 5% CO<sub>2</sub> in a humidified environment. Regular checks were performed to detect any potential Mycoplasma contamination.

#### 3.2.2.1.4 Splitting

Once fibroblasts reached 80%-90% confluency, they were detached and replated at a 1:2 to 1:10 splitting ratio, depending on experimental requirements. Cells were washed with PBS and incubated with TrypLE enzyme for 5 minutes at 37°C to detach them. The cells were collected in pre-warmed fibroblast culture media and resuspended to form a single-cell suspension. Cell counting was done using a Neubauer chamber, and the desired number of cells was transferred to a new flask containing fresh fibroblast culture media.

#### 3.2.2.1.5 Freezing

After cells were counted as outlined in the splitting section (), fibroblasts were centrifuged at 200g for 4 minutes. The supernatant was discarded, and the pellet was resuspended in fibroblast freezing medium (IMDM + 15% FBS + 1% Pen/Strep + 10% DMSO) at a concentration of 1 million cells/ml. One ml of the cell suspension was aliquoted into cryovials, which were stored in insulated boxes at -80°C for 24-48 hours. The cryovials were then transferred to liquid nitrogen for long-term storage.

### 3.2.2.2 Induced Pluripotent Stem Cells (iPSCs)

The iPSCs used in this study were generated by transducing human dermal fibroblasts using the CytoTune™-iPS 2.0 Sendai Reprogramming Kit, following a feeder-dependent reprogramming approach. The reprogramming was previously performed in the laboratory (thesis, Dr. Stephan Käseberg).

#### 3.2.2.2.1 Thawing

The thawing procedure for iPSCs followed the fibroblast thawing protocol () with slight modifications. After thawing, the cells were transferred into a 15 ml tube containing DMEM/F-12. The pellet was then resuspended in iPSC culture media (mTeSR1 + 1% Pen/Strep) and seeded into 6-well plates that had been pre-coated with Matrigel or Geltrex ().

#### 3.2.2.2.2 Culturing and cleaning of spontaneously differentiated cells

iPSCs were cultured in 6-well plates coated with Matrigel or Geltrex ( ) in iPSC culture media (mTeSR1 + 1% Pen/Strep). The media was refreshed daily with pre-warmed media. Spontaneous differentiation can occur during extended culturing or after procedures like reprogramming and electroporation, leading to the loss of pluripotency. To ensure the use of undifferentiated iPSCs for experiments, differentiated cells were manually removed. This was done in a sterile environment under a laminar flow hood, where differentiated cells were identified under a stereomicroscope and removed by scraping them with a flame-polished, angled, and sharpened Pasteur pipette. After removing the differentiated colonies, cell debris was washed away with DMEM/F-12, and the wells were replenished with fresh culture media.

#### 3.2.2.2.3 Splitting

Once iPSC colonies reached 70-80% confluence, they were re-plated in new 6-well plates coated with Matrigel or Geltrex. Cells were detached using a homemade, enzyme-free solution of PBS-EDTA (500 ml PBS, 0.9 g NaCl, 250  $\mu$ l 1M EDTA). Cells were washed twice with PBS-EDTA and incubated for 2 minutes at room temperature in 1 ml of PBS-EDTA. After incubation, PBS-EDTA was replaced with mTeSR1, and cells were scraped off with a cell scraper. The resulting cell clumps were resuspended in mTeSR1 until clumps of 50-500 cells were achieved, which were then seeded in a new Matrigel or Geltrex-coated 6-well plate.

For procedures requiring single-cell suspensions, such as electroporation or differentiation, a different splitting method was used. iPSCs were washed with PBS and incubated with 1 ml of TrypLE enzyme or Accutase for 5 minutes at 37°C. Cells were then collected with PBS or DMEM/F-12 and resuspended into a single-cell solution. After counting the cells with a Neubauer chamber, the desired number of cells was centrifuged at 200g for 4 minutes before proceeding with the further experiments.

#### 3.2.2.2.4 Colony picking

Colony picking was performed to ensure the clonal derivation of iPSCs during fibroblast reprogramming and to rescue heavily differentiated iPSC lines. The process took place under sterile conditions in a laminar flow hood. The cells were treated similarly to the splitting procedure, using PBS-EDTA. After incubation, 2 ml of mTeSR1 was added, and individual iPSC colonies were detached by simultaneously scraping and aspirating with a

200 µl pipette (with the tip cut to increase the surface area for scraping). The colonies were then transferred into a Matrigel or Geltrex-coated 12-well plate.

#### 3.2.2.2.5 Freezing

For freezing, iPSCs were handled as in the splitting procedure with PBS-EDTA. After incubation with PBS-EDTA, DMEM/F-12 was added, and cells were detached using a cell scraper. The cells were centrifuged at 200g for 4 minutes, and the supernatant was discarded. The cell pellet was resuspended in iPSC freezing medium (mTeSR1 + 20% KOSR + 10% DMSO + 1% Pen/Strep). The cell solution was aliquoted into cryovials and stored for 24-48 hours in insulated boxes at -80°C, then transferred to liquid nitrogen for long-term storage.

#### 3.2.2.3 Genome editing

Genome editing of iPSCs was performed to either introduce mutations in *POGZ* in the wildtype female A2 line or to correct the *POGZ* mutation (Chr1g.151379461G>GT (hg19)) present in the patient-derived C34 line. The guide RNAs (gRNAs) used for introducing *POGZ* mutations in the A2 iPSCs were previously designed using the crispr.mit.edu tool and were cloned into the gRNA cloning vector (gRNA Cloning Vector, a gift from George Church, Addgene plasmid #41824)[235]. The Cas9 protein was delivered via the CAG-Cas9-Venus plasmid (pU6-(BbsI) sgRNA\_CAG-925 Cas9-Venus-bpA, a gift from Ralf Kuehn, Addgene plasmid #86986)[236]. Along with the cloned gRNAs, EnGen® sgRNAs were also used later on to streamline the protocol for introducing or correcting *POGZ* mutations. To correct the mutation found in C34 iPSCs, a wildtype sequence template was used to enable homology-directed repair. A dsDNA break was introduced by the gRNA, and the template sequence was utilized to insert the correct *POGZ* sequence. The cloning of gRNAs and the genome editing procedure of iPSCs via electroporation were performed following the method described in Dr. Stephan Käseberg's thesis. Clones that carried the intended mutation were expanded and used for further experiments.

##### 3.2.2.3.1 Bacterial Culture

Bacterial cells (*Escherichia coli*) were used to produce and amplify plasmids, which were later utilized for the transfection of eukaryotic cells.

##### 3.2.2.3.2 Cloning of gRNA Constructs

For CRISPR/Cas9 genome editing, it was necessary to generate gene-specific gRNA constructs. To achieve this, a 20 bp target sequence was designed using an online tool (crispr.mit.edu), which identifies potential gRNAs within a given sequence and evaluates

their predicted specificity and efficiency. From the results, the two highest-rated gRNAs were selected and ordered as oligonucleotides. The gRNA cloning process began with annealing the gRNA oligo to its reverse complement sequence, followed by the extension of the 5' overhangs to create double-stranded DNA. This was done by combining 1  $\mu$ L of both the forward and reverse oligos with 4  $\mu$ L of Phusion buffer, 0.4  $\mu$ L of dNTPs, 13.4  $\mu$ L of water, and 0.2  $\mu$ L of Phusion polymerase. The reaction mixture was incubated in a thermal cycler as outlined in Table 16. Meanwhile, the gRNA cloning vector was linearized by mixing 1  $\mu$ g of vector DNA with 5  $\mu$ L of CutSmart<sup>®</sup> buffer, 1  $\mu$ L of AflIII restriction enzyme, and water to a total volume of 50  $\mu$ L. This mixture was incubated for 15 minutes at 37°C.

**Table 16** Cycler program used for gRNA annealing and extension.

Temperature	Time
98°C	30 s
72°C	5 min
4°C	forever

#### 3.2.2.3.3 Transformation

In the transformation process, cloned constructs were introduced into chemically competent *E. coli* cells using heat shock transformation. The plasmid was added to the competent cells and incubated on ice for 30 minutes, followed by a 90-second heat shock at 42°C and a subsequent 2-minute incubation on ice. Afterward, 250  $\mu$ L of LB medium was added to the bacterial suspension, which was then incubated for 30 minutes at 37°C with shaking. The suspension was plated on LB-agar plates containing either Ampicillin or Kanamycin, depending on the plasmid. After overnight incubation at 37°C, individual colonies became visible on the plates.

#### 3.2.2.3.4 Mini-Prep

For Mini-Prep, single colonies were selected after transformation and grown in 3 mL of LB-medium overnight at 37°C. The next day, 1 mL of the bacterial culture was centrifuged to form a pellet, which was resuspended in buffer P1. Buffers P2 and P3 were then added sequentially for cell lysis and neutralization, followed by centrifugation to separate the supernatant containing DNA. The DNA was precipitated with 100% ethanol and washed with 70% ethanol. The resulting DNA pellet was air-dried, reconstituted in 50  $\mu$ L of water, and the concentration was measured using a Nanodrop<sup>™</sup> spectrophotometer.

#### 3.2.2.3.5 Maxi-Prep

For Maxi-Prep, the remaining 2 mL of bacterial culture were expanded in 200 mL of LB-medium overnight at 37°C. DNA was extracted using the "EndoFree Plasmid Maxi Kit,"

following the manufacturer's protocol with slight modifications. The bacterial pellet was resuspended in buffers P1, P2, and P3, then filtered. After several wash and elution steps, DNA was precipitated with isopropanol, washed with ethanol, and resuspended in buffer TE. DNA concentration was measured using a Nanodrop™ spectrophotometer and adjusted to 1 mg/mL for further use.

#### 3.2.2.3.6 Sequencing

After Mini-Prep or Maxi-Prep, plasmids were sequenced to verify correct incorporation of cloned gRNA fragments and to ensure no mutations occurred during cloning. For sequencing, 5 µL of plasmid DNA (80-100 ng/µL) were mixed with 5 µL of a plasmid-specific primer. Samples were sent to "Eurofins Genomics" for sequencing, and results were analyzed using "BioEdit" software.

#### 3.2.2.3.7 sgRNA synthesis using EnGen® sgRNA Synthesis Kit

To make the synthesis of gRNAs simpler and quicker, EnGen® sgRNA Synthesis Kit, *S. pyogenes* was used. First, the sequences of some of the top-rated gRNAs generated by (crispr.mit.edu) checked for presence of "G" at the 5' end. If there were no "G's" at the 5' end, one was added. Then, To the 5' ends; T7 promoter sequence: **TTCTAATACGACTCACTATA** and to the 3' ends; 14 nucleotides overlap sequence: **GTTTTAGAGCTAGA** were appended to the gRNA's sequences (Table 12). The sgRNAs were synthesized by mixing 2 µl nuclease-free water, 10 µl EnGen 2X sgRNA Reaction Mix, *S. pyogenes*, 5 µl Target-specific DNA Oligo (1 µM), 1 µl DTT (0.1 M) and 2 µl EnGen sgRNA Enzyme Mix. The reaction mixture was plus spun and incubated at 37°C for 30 minutes. Subsequently, the mixture was transferred on ice where the volume was brought to by adding 30 µl of nuclease-free water. For DNase treatment, 2 µl of DNase I (RNase-free) was added to the mixture and incubated at 37°C for 15 minutes. The synthesized sgRNAs were then purified using Monarch RNA Cleanup Kit (50 µg) or High Pure RNA Isolation Kit. The concentrations were measured using "Nanodrop™ One Spectralphotometer" and gRNAs were stored at -20°C.

#### 3.2.2.3.8 Electroporation

iPSCs were electroporated using the Lonza 4DNucleofector X Unit. Initially, 800,000 cells were pelleted and resuspended in 100 µL of electroporation buffer P3, with 2.5 µg each of Cas9 and gRNA plasmids added. The cell-plasmid mixture was then electroporated using program CB-150. Following electroporation, 100 µL of RPMI was added, and the mixture

was incubated for 10 minutes at 37°C before transferring to a Matrigel-coated 6-well plate containing 2 mL of mTeSR1 with ROCK inhibitor (10  $\mu$ M). On day 1 post-electroporation, the media was fully replaced with mTeSR1 without ROCK inhibitor. On day 2, GFP-positive cells were FACS-sorted as single cells into a Matrigel-coated 96-well plate containing mTeSR1 plus 10% CloneR. After obtaining a single-cell suspension, iPSCs were resuspended in 300  $\mu$ L of mTeSR1 with 10% CloneR and sorted using a FACS Aria flow cytometer. Excess cells were discarded, and the media was refreshed with 100  $\mu$ L of mTeSR1 plus 10% CloneR 48 hours post-electroporation, followed by an additional 25  $\mu$ L 24 hours later. By day 4 post-sorting, the media was replaced with mTeSR1, with feeding every other day. The first colonies appeared typically after seven days, and once they covered at least 50% of the well by days 10-14, one well from the 96-well plate was split into a Matrigel-coated 12-well plate using PBS/EDTA. The cells were then expanded according to standard iPSC culture protocols.

#### **3.2.2.4 Neural progenitor and stem cells (NPCs)**

Neural progenitor and stem cells (NPCs) were utilized in this study as the initial cell line differentiated to model human neurodevelopment. NPCs were derived from various iPSC clones and lines. Successfully differentiated NPCs were maintained as stable lines, retaining their stem cell properties and their ability to differentiate into neurons up to passage 20.

##### **3.2.2.4.1 Differentiation of iPSCs into NPCs**

NPCs were differentiated by following an approach that was developed using a commercial PSC Neural Induction Medium (NIM, Gibco)[237]. On day -1, iPSCs were detached with PBS/EDTA and seeded on Matrigel- or Geltrex-coated 6-well plates at varying densities. On day 0, cells at 15-25% confluency were selected for NPC differentiation, and the medium was switched from mTeSR1 to NIM (Neurobasal + 2% Neural Induction Supplement + 1% Pen/Strep). The medium was gradually replaced according to the differentiation protocol. By day 7, cells reached full confluency and were replated following the manufacturer's instructions. Cells were incubated with Accutase for 7 minutes at 37°C, resuspended, filtered using a 100  $\mu$ m strainer, and centrifuged at 300g for 4 minutes. The resulting cell pellet was resuspended in Neural Expansion Media (NEM: 49% Neurobasal, 49% Advanced DMEM, 2% Neural Induction Supplement, 1% Pen/Strep) with ROCK inhibitor (5  $\mu$ M) and plated in Geltrex-coated 6-well plates at a density of

500,000 cells per well. After 24 hours, the medium was replaced with NEM without ROCK inhibitor, and cells were cultured with medium changes every other day.

To remove false differentiated cells, an adjusted protocol was used. After washing with PBS, cells were incubated with Accutase for 3-4 minutes at room temperature, followed by a PBS wash to remove detached cells containing mis differentiated cells. The remaining cells were further incubated with Accutase for 4 minutes at 37°C and replated as described. Once NPCs were free of false differentiated cells, they were cultured on poly-Ornithine/Laminin-coated plates with neuronal medium (NM: DMEM/F-12 + 1% N2 supplement + 2% B27 supplement + 1% Pen/Strep) and supplemented with FGF2 (20 ng/ml).

#### 3.2.2.4.2 Culturing

Successfully differentiated NPCs were cultured on poly-Ornithine/Laminin-coated dishes in neuronal medium (NM) supplemented with FGF2 (20 ng/ml). NPCs were limited to a maximum of 20 passages to avoid cellular changes due to extended culturing.

#### 3.2.2.4.3 Splitting

NPCs were replated once they reached confluence, usually 5-7 days after seeding. Cells were washed with PBS and incubated with TrypLE™ Express for 5 minutes at 37°C. Detached cells were collected in NM supplemented with 15-30% KOSR, resuspended thoroughly, and centrifuged at 200g for 5 minutes. The pellet was resuspended in NM with FGF2 (20 ng/ml) and seeded into poly-Ornithine/Laminin-coated 6-well plates at (100-200x10<sup>3</sup> cells/well).

#### 3.2.2.4.4 Freezing

For long-term storage, NPCs were frozen and kept in liquid nitrogen. After detaching and centrifuging the cells according to the splitting protocol, the cell pellet was resuspended in NM supplemented with 10% KOSR and 10% DMSO at a concentration of 1 million cells/ml. One ml of this cell suspension was transferred into cryovials and stored at -80°C for 48 hours before being moved to liquid nitrogen for long-term storage.

#### 3.2.2.4.5 Thawing

The thawing procedure for NPCs was adapted from the fibroblast thawing protocol () with slight modifications. After thawing, cells were transferred into a 15 ml tube containing NM supplemented with 15-30% KOSR. The cell pellet was resuspended in NM with FGF2 (20 ng/ml) and seeded into poly-Ornithine/Laminin-coated 6-well plates.

### 3.2.2.5 Neurospheres

3D neurosphere models were utilized to provide the possibility to study the effect of *POGZ* mutations on proliferation, neurogenesis and neuronal migration in more representative spatial cellular physiological environment.

#### 3.2.2.5.1 Generation of Neurospheres

Following Zhou et al., protocol[238] , once Monolayer NPCs reached confluence, they were washed with PBS once then incubated with TrypLE™ Express for 5 minutes at 37°C and dissociated into single cells. Detached cells were collected in NM supplemented with 15-30% KOSR, resuspended thoroughly, and centrifuged at 200g for 5 minutes. The pellet was resuspended in NMM media and counted to have a total of  $1.152 \times 10^6$  cells/mL were plated into a 96-well V-bottom plate in NMM media (12000 cells in 150  $\mu$ l per well) then incubated at 37°C with 5% CO<sub>2</sub> in a humidified environment. Medium change was done every other day and the neurospheres were maintained for either 3 or 5 according to upcoming experiment. Eleven batches were generated in total but some got skipped because of neurospheres poor quality.

#### 3.2.2.5.2 Immunofluorescence staining of floating neurospheres

The protocol of Sasaki et. al was used for the immunofluorescence staining of floating neurospheres in culture plates[239]. This protocol highlighted differences in the staining and washing procedures compared to conventional methods. Neurospheres were transferred from a culture plate to a 12-well plate using a 200–1000  $\mu$ L pipette and left undisturbed for 3 minutes to allow gravity precipitation. The medium was then carefully aspirated by tilting the plate and slowly drawing the liquid with a pipette. This washing process, followed by 3 minutes of gravity precipitation, was repeated three times. The protocol avoided centrifugation, as it could damage the sphere structure. To minimize the loss of neurospheres, the aspirated medium was kept aside for reuse in case all spheres were accidentally aspirated. After ensuring the spheres were at the bottom of the well, they were fixed with 4% PFA for 20 minutes at room temperature, followed by three PBS washes. The spheres were then permeabilized with 0.025% Triton X-100 for 5 minutes, washed again with PBS, and blocked in PBS containing 3.3% sheep serum for 30 minutes, followed by additional PBS washes.

The neurospheres were incubated with primary antibodies against SOX2 and NESTIN (1:500) in PBS for 1 hour at room temperature or overnight at 4°C. After PBS washes, the spheres were incubated with secondary antibodies, including Alexa Fluor 488 and Alexa

Fluor 594-conjugated IgGs, both at 1:200 dilutions. Finally, nuclear staining was performed using mounting medium (Vectashield with 0.5% DAPI), and the spheres were visualized under a fluorescence microscope. Unlike traditional methods using cryostat sections, this protocol simplified the process while still providing clear neurosphere structures.

#### 3.2.2.5.3 Neurospheres' Proliferation assay

After 5 days of culturing, five days old neurospheres were visualized and imaged using an inverted EVOS XL microscope under phase contrast. The diameter of neurospheres was measured using FIJI software.

#### 3.2.2.5.4 Neurospheres' migration assay

Neurospheres were cultured for 3 days then they were transplanted using cut 1mL tip and plated into neuronal differentiation medium (Neurobasal+) on into poly-Ornithine/Laminin-coated 6-well plates (5-6 neurospheres per well) and incubated at 37°C with 8% CO<sub>2</sub> in a humidified environment. On day 2 of neuronal differentiation, neurospheres were visualized and imaged using an inverted EVOS XL microscope. NPCs migration was evaluated by measuring the mean of the distances from the edge of the neurosphere to the nucleus of the most distant cells in all directions using FIJI software.

### 3.2.2.6 Organoids

Human brain organoids were generated from different iPSCs with slight modifications to the Lancaster protocol[168], according to an established in-house method provided from collaborators in Erlangen (Karow group). The protocol includes four different phases: the generation of Embryoid Bodies from Human iPSCs, the Neural Ectoderm differentiation, the Matrigel embedding and the neuroepithelial bud expansion, and the final neuronal tissue differentiation by using an orbital shaker. The protocol lasts at least for 30 days to obtain ventricle-like structures with mature neurons, and the generated cerebral organoids can be cultured for more than one year. Those 3D brain organoids model will provide the possibility to study effect of POGZ mutation on neurogenesis and neuronal migration in a more physiological condition, where newborn neurons markers as MAP2 positive can be used to measure neural maturation efficiency.

#### 3.2.2.6.1 Generation of Organoids

All iPSC lines were cultured in colonies using mTeSR medium on Matrigel-coated dishes in a 5% CO<sub>2</sub> environment at 37°C until they reached 80-90% confluency. Accutase was employed to create single-cell suspensions. After centrifugation, the cells were resuspended in organoid formation medium containing 4 ng/ml of low bFGF and 5 μM

ROCK inhibitor. The organoid formation medium comprised DMEM/F12 + GlutaMAX-I, 20% KOSR, 3% FBS, 0.1 mM MEM-NEAA, and 0.1 mM 2-mercaptoethanol. A total of 12,000 cells in 150  $\mu$ L of organoid formation medium were reaggregated in low-attachment 96-well plates for at least 48 hours. After 72 hours, half of the medium was replaced with 150  $\mu$ L of fresh organoid formation medium lacking bFGF and ROCK inhibitor. On day 5, a neural induction medium composed of DMEM/F12 + GlutaMAX-I, 1% N2 supplement, 0.1 mM MEM-NEAA, and 1  $\mu$ g/ml Heparin was added to the embryoid bodies (EBs) in the 96-well plates to facilitate their growth and neural differentiation. This neural induction medium was refreshed every two days until day 12 or 13, when the aggregates were transferred to droplets of undiluted Matrigel. The embedded organoids were then placed in a petri dish containing organoid differentiation medium devoid of vitamin A. The organoid differentiation medium consisted of a 1:1 mixture of DMEM/F12 + GlutaMAX-I and Neurobasal medium, 0.5% N2 supplement, 0.1 mM MEM-NEAA, 100 U/ml penicillin, 100  $\mu$ g/ml streptomycin, 1% B27 +/- vitamin A supplement, 0.025% insulin, and 0.035% 2-mercaptoethanol. Three to four days later, the medium was replaced with organoid differentiation medium containing vitamin A, and the plates were transferred to an orbital shaker set at 30 rpm within the incubator. The medium was changed twice a week.

#### 3.2.2.6.2 Fixation and cryosectioning of organoids

For fixation, organoids were transferred from petri dishes to 1.5 ml tubes on days 30 and 50. The organoids were washed with PBS and fixed in 4% paraformaldehyde for 30 minutes, with fixation time extended to one hour depending on the size of the organoids. Afterward, the organoids were washed three times for 10 minutes with PBS and incubated in 30% sucrose in PBS for cryoprotection. For cryosectioning, the organoids were embedded in Neg-50™ Frozen Section Medium on dry ice. Frozen organoids were then cryosectioned into 20  $\mu$ m sections using a cryostat. The sections were placed on SuperFrost Plus™ Object Slides and stored at -20°C until needed.

#### 3.2.2.6.3 Immunostaining of organoids

Organoid sections were post-fixed in 4% paraformaldehyde (PFA) for 15 minutes, followed by three washes with 1x PBS for 5 minutes each. The sections were then briefly rinsed with a blocking solution containing 4% Sheep serum and 0.25% Triton-X in 1x PBS, and subsequently incubated in the same blocking solution for at least one hour at room temperature. Overnight incubation at 4°C was performed with primary antibodies (anti-

MAP2 1:300 and anti-SOX2 1:300) diluted in an antibody solution containing 4% Seep serum and 0.1% Triton-X in 1x PBS. After three washes with PBS containing 0.5% Triton-X, secondary antibodies were applied (1:500), diluted in the antibody solution, and incubated for one hour at room temperature. The sections were then washed three times for five minutes each with PBS, with the final wash performed using PBS with 0.5% Triton-X. Slides were counterstained with DAPI at a dilution of 1:1000 in PBS for 5 minutes, washed again with PBS, and mounted with Aqua PolyMount. Throughout the staining process, the slides were maintained in a humidified chamber in the dark.

#### 3.2.2.6.4 Image analysis of organoids

The number of the ventricle zone-like structures (VZLS) formed per organoids were counted and compared to those of control organoids within each batch. To quantify the ventricle zone-like structures (VZLS) area in each organoid section, the total organoid area was measured using FIJI, excluding regions occupied by cysts. The area occupied by VZLS was also measured, and the proportion of the organoid area covered by VZLS was calculated. These values were averaged across different sections from the same organoid and then normalized to the average value of the control organoids within each batch.

For quantifying the neural area positive for SOX2 or MAP2 in organoid sections, the total organoid area (excluding cyst-covered regions) and the SOX2 or MAP2 positive area were measured using FIJI. The neural area was defined as the area positive for either SOX2 or MAP2 (SOX2+MAP2). The proportions of SOX2-positive area relative to the neural area and MAP2-positive area relative to the neural area were then calculated.

#### 3.2.2.6.5 Dissociation of organoids

At day 30, the organoids were treated with Neural Tissue Dissociation Kit according to the manufacture protocol to generate single-cell suspensions from neural tissues. Briefly, selected organoids were cut into smaller pieces, washed with medium, and rinsed three times for 5 minutes with 1x PBS. The organoid fragments were then transferred to a tube containing enzyme mix P (prepared according to the manufacturer's protocol) and incubated at 37°C for 10 minutes. After this, the pieces were gently triturated using a 1000 µL pipette tip and incubated for an additional 10 minutes at 37°C with enzyme mix A (as per the manufacturer's instructions). The tissue was further triturated using 1000 µL and 200 µL pipette tips and incubated for 5 minutes at 37°C. The resulting cell suspension was filtered through a 30 µm filter and centrifuged at 300 x g for 5 minutes. After a second

filtration through a 20 µm filter and subsequent centrifugation, the cell pellet was resuspended in neural differentiation medium (Neurobasal+) and cultured on plates coated with poly-L-ornithine and mouse laminin and incubated at 37°C with 8% CO<sub>2</sub> in a humidified environment. After 24 hours, the cells were fixed with 4% paraformaldehyde (PFA) for 15 minutes at room temperature. Immunocytochemistry was performed to detect MAP2, and the proportion of MAP2+ neurons was subsequently analyzed using a fluorescence microscope.

### **3.2.3 Cell culture methods**

To ensure reproducibility across different cell lines and types, standardized protocols were developed for sample collection and preparation

#### **3.2.3.1 Cell pellet collection**

Cell pellets were collected for subsequent genomic DNA or total RNA extraction from each cell type described above. Cells were harvested 16-18 hours after a complete media change to collect them during their exponential growth phase. To detach the cells from the culture plates, the media was first removed, followed by a PBS wash. After the wash, PBS was added back, and cells were manually detached using a plastic cell culture scraper. The detached cells were collected by adding additional PBS, then pelleted in a 15 ml tube by centrifugation for 4 minutes at 200g. The cell pellet was resuspended in fresh PBS, transferred to a 1.5 ml tube, and centrifuged for 5 minutes at 4500 rpm. The resulting cell pellet was then snap-frozen and stored at -80°C until further use.

#### **3.2.3.2 PFA fixation of adherent cells**

Adherent cells were fixed using a 4% paraformaldehyde (PFA) solution in PBS before proceeding with immunostaining. For imaging experiments, cells were seeded on coverslips and grown in 12-well plates, with the coverslips coated similarly to the wells of 6-well plates, if required by the specific cell type. Cells were fixed upon reaching confluency. When cells became ready for processing, the media was removed, and cells were gently washed twice with PBS. PFA was then added to the wells of the 12-well plate and incubated for 15-20 minutes. Following fixation, cells were washed three times with PBS and stored at +4°C in fresh PBS until further processing.

#### **3.2.3.3 Cell counting**

Cells were counted after the splitting procedure, either for replating or freezing. Following single-cell dissociation, 10 µl of the cell suspension was pipetted into a Neubauer counting

chamber. Cells within the four corner squares of the chamber were counted. The cell concentration was then calculated using the following formula:

$$\text{Concentration of cells } \left( \frac{\text{cells}}{\text{ml}} \right) = \frac{\text{cell count}}{\text{number of squares counted}} \times 2,5 \times 10\,000$$

#### **3.2.3.4 Karyotyping**

Karyotype analysis was conducted following iPSC reprogramming and genome editing by electroporation to rule out any chromosomal aberrations. Once the iPSCs reached confluency, they were processed at the diagnostics laboratory of the "Institute of Human Genetics" at the University Medical Centre Mainz by technician Denise Seyler. As the procedure was performed externally, the complete protocol details are not provided here.

### **3.2.4 Molecular methods**

#### **3.2.4.1 Immunofluorescence staining**

Immunofluorescence method was utilized to detect specific protein expression in cells. Cells grown on coverslips and previously fixed with paraformaldehyde (PFA) solution were used for staining. After three washes with PBS, the cells were incubated with a blocking solution (PBS, 5% BSA, 0.3% Triton) for 30 minutes at room temperature. This was followed by overnight incubation at +4°C with the primary antibody diluted in blocking solution.

The next day, cells were washed three times with wash buffer (PBS, 0.3% Triton) for 10 minutes each. They were then incubated in the dark for 1 hour with the secondary antibody diluted in blocking solution. From this point on, cells were handled in the dark as much as possible. After incubation, cells were washed three times in wash buffer for 10 minutes at room temperature, followed by a brief rinse with deionized water before being transferred to glass slides. Coverslips were mounted using 10 µl of mounting medium (Vectashield with 0.5% DAPI). Images were captured using the Echo Revolve fluorescent microscope and analyzed with Fiji software.

#### **3.2.4.2 Protein extraction**

Protein isolation was performed from fresh cell pellets using Magic Mix (48% urea, 15 mM Tris pH 7.5, 8.7% glycerin, 1% SDS, 143 mM β-mercaptoethanol) supplemented with protease and phosphatase inhibitors. The pellet was resuspended in an appropriate volume of Magic Mix and processed through a QIAshredder. After centrifugation at 12,000 rpm for 2 minutes, the supernatant was transferred to a fresh tube and stored at -80°C. Protein concentration was not measured.

### 3.2.4.3 SDS gel-electrophoresis and Western Blot

SDS gel electrophoresis was utilized to separate proteins by size from previously isolated cell samples. The separating gel was prepared and overlaid with a collecting gel once polymerized (Table 17). For electrophoresis, 10  $\mu\text{L}$  of the protein solution was mixed with 5  $\mu\text{L}$  of loading dye (Magic Mix with bromophenol blue) and incubated at 95°C for 5 minutes. The denatured protein solution, along with a size marker, was loaded onto the gel and separated at 199 V for approximately 50 minutes. The gel was subsequently transferred to a PVDF membrane using a blotting chamber, stacking filter paper, the membrane, the gel, and additional filter paper with the “Trans Blot Turbo Transfer Pack.” The transfer was conducted at 1 A for 30 minutes. Following transfer, the membrane was incubated with blocking buffer (PBS, 0.1% Tween, 5% milk powder/BSA) for 1 hour on a shaker. After removing the blocking buffer, the membrane was incubated overnight with the primary antibody (Table 17) diluted in blocking buffer. The following day, the membrane was washed three times for 10 minutes with PBS-T (PBS, 0.1% Tween) and then incubated for 1 hour with the secondary antibody (Table 8) diluted in blocking buffer. After three additional washing steps, the membrane was exposed to the “Western Lightning Plus ECL, Enhanced Chemiluminescence Substrate” and imaged using the “ChemiDoc Imaging System.” Images were prepared and analyzed with “ImageJ /FIJI” software.

**Table 17 Composition of separating and stacking gel for SDS gel-electrophoresis.**

Gel	Acrylamid (30%)	H2O	Tris buffer	SDS (10%)	APS (10%)	TEMED
Separating	1,7 mL	1,9 mL	1,3 mL (1,5 M; pH 8,8)	50 $\mu\text{L}$	50 $\mu\text{L}$	2 $\mu\text{L}$
Stacking	330 $\mu\text{L}$	1,4 mL	250 $\mu\text{L}$ (0,5 M; pH 6,8)	20 $\mu\text{L}$	20 $\mu\text{L}$	2 $\mu\text{L}$

### 3.2.4.4 DNA extraction

Genomic DNA was extracted from cell pellets that were frozen and stored at -80°C. The extraction process utilized self-made buffers and a protocol previously established by Dr. Stephan Kaseberg (Thesis, Dr. Stephan Kaseberg). The procedure was performed at room temperature. Initially, the cell pellet was resuspended in 300  $\mu\text{L}$  of SE-buffer (composed of 0.439 g NaCl, 0.841 g Na-EDTA, and 100 ml water). Once resuspended, 30  $\mu\text{L}$  of proteinase K (15 mg/ml) and 30  $\mu\text{L}$  of 10% SDS solution were added to the mixture, and the cells were lysed by incubating the mixture overnight at +37°C. The following day, 100  $\mu\text{L}$  of 5M NaCl solution was added to the cell lysate, and the samples were vortexed for 15 seconds.

Samples were then centrifuged at 6000g for 15 minutes. The supernatant, containing the genomic DNA, was transferred to a new 1.5 ml tube, while the pellet of cell debris was discarded. To precipitate the DNA, 600 µl of 100% ethanol was added to the supernatant, and after vigorous shaking, the samples were centrifuged for 20 minutes at 14,000g. The supernatant was discarded, and the pellet was washed twice with 1 ml of 70% ethanol, followed by centrifugation for 5 minutes at 14,000g after each wash. After the second ethanol wash, the pellet was air-dried to remove any residual ethanol and resuspended in 20 µl of deionized water (dH<sub>2</sub>O). The concentration of the genomic DNA was measured using the Nanodrop™ One Spectral Photometer. The DNA was stored at -20°C for future use.

#### 3.2.4.5 PCR amplification

The isolated DNA was amplified using a standard PCR protocol of Herculase II Fusion DNA Polymerase kit. A total of 50-100 ng of DNA was combined with 5 µL of 5× Herculase II reaction buffer, 0.5 µL of dNTPs, 1.25 µL each of forward and reverse primers, then diluted with dH<sub>2</sub>O to achieve a final volume of 50 µL. The amplification was carried out using a cycler program tailored to the specific primer and the anticipated product length (Table 18). To verify successful amplification, 5 µL of the PCR product was analyzed on a 1.5% agarose gel containing EtBr.

**Table 18 Standard Cycler program used for DNA amplification.** X stands for the primer specific melting temperature and Y for the product length specific elongation time.

1. Initial denaturation	95°C	2 min
2. Denaturation	95°C	30 s
3. Primer annealing	X°C	30 s
4. Elongation	72°C	Y s
5. Loop	Go to step 2	34X
6. Final elongation	72°C	5 min
7. Store	4°C	Forever

#### 3.2.4.6 Sequencing

The amplified DNA was subjected to sequencing after eliminating residual PCR components using the “High Pure PCR Purification Kit,” following the manufacturer’s guidelines. For sequencing preparation, 5 µL of the PCR product was combined with 5 µL of the primer. The resulting sample was then sent to “Eurofins Genomics” for sequencing. The results were made available online and analyzed using “BioEdit” software.

#### **3.2.4.7 Whole Exome Sequencing (WES)**

Whole Exome Sequencing was conducted to identify any off-target mutations following CRISPR/Cas9 genome editing. This procedure took place in the diagnostics laboratory of the “Institut für Humangenetik” at the University Medical Center Mainz, conducted by trained technicians. Consequently, the detailed protocol is not provided.

#### **3.2.4.8 Total RNA extraction**

Total RNA was extracted using the High Pure RNA Isolation Kit (Roche) according to the manufacturer's protocol for isolating RNA from cultured cells. The procedure was carried out at room temperature (RT). First, the cell pellet was resuspended in 200 µl of PBS, followed by the addition of 400 µl of Lysis/Binding buffer to each sample. The samples were then vortexed for 15 seconds, and the resulting lysates were transferred to the provided filter tubes. The tubes were centrifuged for 30 seconds at 8000g, after which the flowthrough was discarded.

To remove genomic DNA, the filter was treated with 10 µl of DNase I, diluted in 90 µl of DNase incubation buffer, and incubated for 15 minutes at RT. Following DNA digestion, the filter was washed with 500 µl of wash buffer 1 and centrifuged for 30 seconds at 8000g. The process was repeated using wash buffer 2. An additional washing step was performed by applying 200 µl of wash buffer 2 to the filter and centrifuging the samples at 13,000g for 2 minutes. After washing, the filter was transferred to a fresh 1.5 ml tube, and the RNA was eluted by adding 50 µl of elution buffer to the filter, followed by centrifugation for 1 minute at 8000g. RNA concentration was measured using the Nanodrop™ One Spectral Photometer, and the isolated RNA was stored at -80°C for future analysis.

#### **3.2.4.9 Retro-transcription of total RNA and cDNA synthesis**

For gene expression analysis, total RNA was reverse transcribed into cDNA using two comparable protocols: PrimeScript™ RT Master Mix and the RevertAid First Strand cDNA Synthesis Kit. In the case of the PrimeScript™ RT Master Mix, 500 ng of total RNA was used, and the volume was adjusted to 8 µl with water. Then, 2 µl of the 5x master mix was added to the reaction mixture, and the samples were incubated according to the cycler program outlined in Table 19. Following the completion of the program, the cDNA samples were diluted with dH<sub>2</sub>O to achieve a final RNA concentration of 5 ng/µl for further analysis.

**Table 19** Cycler program used for cDNA synthesis by using the PrimeScript™ RT Master Mix

Temperature	Time
37°C	15 min
85°C	5 second
4°C	forever

For the RevertAid First Strand cDNA Synthesis Kit, 500 ng of total RNA was used per reaction. To this, 1 µl of Oligo (dT) primers, 1 µl of Random Hexamer primers, and dH<sub>2</sub>O were added, bringing the total volume to 12 µl. The following components were then added: 4 µl of 5x Reaction Buffer, 1 µl of RiboLock RNase Inhibitor (20 U/µl), 2 µl of 10 mM dNTP Mix, and 1 µl of RevertAid M-MuLV RT (200 U/µl), making a final volume of 20 µl. The mixture was incubated according to the conditions specified in Table 20. After the cycler program, the resulting cDNA samples were diluted with dH<sub>2</sub>O to achieve a final RNA concentration of 5 ng/µl for subsequent analyses.

**Table 20** cycler program used for cDNA synthesis by using the RevertAid First Strand cDNA Synthesis Kit

Temperature	Time
25°C	5 min
42°C	60 min
70°C	5 min
4°C	forever

#### 3.2.4.10 RT-qPCR

Quantitative reverse transcription polymerase chain reaction (RT-qPCR) was utilized in this thesis to detect and quantify RNA levels during the reverse transcription and PCR processes, allowing for the assessment of gene expression in the samples. The reaction mix was prepared by combining 4 µL of cDNA with 7.5 µL of TB Green® Premix Ex Taq™ II, 2.5 µL of dH<sub>2</sub>O, and 1 µL of a primer pair mix, which included both forward and reverse primers. Each PCR reaction was conducted in a well of a 96-well plate, with all cDNA samples measured in technical triplicates to minimize the impact of technical variability. After preparation, the 96-well plate was loaded into the StepOnePlus System, and the RT-qPCR reaction was carried out following the conditions specified in Table 21. The provided software was used to organize the experimental design, set up the sample loading scheme, and perform the initial analysis of the results, which allowed for gene expression quantification based on amplification curves and cycle threshold (Ct) values.

**Table 21 PCR program for RT-qPCR experiment**

Stage	Temperature	Time
Initial denaturation	95°C	15 min
Denaturation	95°C	15 seconds
Primer annealing	60°C	30 seconds
Elongation	72°C	40 seconds
Loop from denaturation to elongation 34 times		
Final elongation	72°C	5 min
Calculation of Melt curve		

Ct values were analysed by using Microsoft Excel and R-Studio applying the  $\Delta\Delta C_t$ -method's protocol [240]. *GAPDH* was used as a control for the reference gene.

#### **3.2.4.11 Quantification of Allele-Specific Expression by Pyrosequencing (QUASEP)**

The Quantification of Allele-Specific Expression by Pyrosequencing (QUASEP) assay was employed to investigate allele-specific expression by quantifying the relative expression of genomic variants. Primers specific to the genomic variant of interest were designed using the PyroMark Assay Design 2 software. The first step of the QUASEP assay involved amplifying the region of interest where the genomic variant is located. A primer pair generated by the software was used for this purpose, with one primer biotinylated to prepare for the subsequent reaction. PCR was conducted to amplify the target region, using cDNA samples measured in technical triplicates to account for any potential technical errors. For a single PCR reaction (50  $\mu$ L total volume), 10  $\mu$ L of cDNA were combined with 5  $\mu$ L of 5 $\times$  Herculase II reaction buffer, 0.5  $\mu$ L of dNTPs, 1.25  $\mu$ L each of forward and reverse primers, 31.5  $\mu$ L of dH<sub>2</sub>O, and 0.5  $\mu$ L of Herculase II fusion DNA polymerase. The PCR reaction was performed according to the protocol outlined in Table 22. The same PCR reaction mix and cycling program were used across all QUASEP assays discussed in the thesis.

**Table 22 Thermocycler program for QUASEP PCR reactions**

Stage	Temperature	Time
Initial denaturation	94°C	2 min
Denaturation	94°C	15 seconds
Primer annealing	60°C	30 seconds
Elongation	72°C	45 seconds
Loop from denaturation to elongation 34 times		
Final elongation	72°C	5 min
Store of the samples	4°C	Forever

The amplification of the target region was confirmed by loading 7.5  $\mu$ L of the PCR products onto a 1.5% agarose gel containing ethidium bromide (EtBr). The presence of a single DNA

fragment, with a length corresponding to the target region, indicated successful amplification. Once confirmed, the remaining 42.5  $\mu\text{L}$  of PCR product was used for the Pyrosequencing reaction. Pyrosequencing was performed according to the manufacturer's protocol using the Pyromark machine. The experiment design and sample loading scheme were generated using Pyro Q CpG software. To prepare the samples, 42.5  $\mu\text{L}$  of the PCR product was mixed with 40  $\mu\text{L}$  of self-made binding buffer and 4  $\mu\text{L}$  of Streptavidin-Sepharose beads in a 96-well plate. The 96-well plate was gently vortexed to prevent Streptavidin-Sepharose bead precipitation during the preparation of the remaining reagents. In a separate 96-well pyrosequencing plate, 40  $\mu\text{L}$  of self-made annealing buffer was mixed with 2  $\mu\text{L}$  of sequencing primer. Samples were processed using a Vacuum Prep tool. The mixture containing the PCR products, binding buffer, and Streptavidin-Sepharose beads was aspirated, leaving a dry pellet. This pellet was incubated sequentially for 5 seconds in 70% ethanol, denaturation buffer (0.2M NaOH), and wash buffer (10mM Tris-Acetate, pH 7.4). The pellet was then resuspended in the prepared annealing buffer solution in the 96-well pyrosequencing plate and incubated for 2 minutes at 80°C. The Pyrosequencing cartridge was prepared by mixing the Pyromark Gold Q96 Reagents, including the enzyme, single nucleotide solutions, and the substrate mix. The required volumes and pipetting scheme were calculated by the Pyro Q CpG software. Both the pyrosequencing plate and the loaded cartridge were placed in the machine for the sequencing reaction. After pyrosequencing, the results were analyzed using Pyro Q CpG software, with the relative allele-specific expression levels presented as percentage values.

#### **3.2.4.12 Sendai Virus vector clearance**

To detect the presence of viral vectors in iPSC samples, an RT-PCR reaction was performed using cDNA. Two separate PCR reactions were carried out, each with different primer pairs targeting specific genes from the viral vectors used in the reprogramming process (KOS, KLF4, and c-Myc), and the Sendai Virus genome sequence (SeV). In one PCR reaction, SeV and KOS primers were used together, while KLF4 and c-Myc primers were combined in a second reaction. Each PCR reaction had a total volume of 25  $\mu\text{L}$ , consisting of 10  $\mu\text{L}$  cDNA, 2.5  $\mu\text{L}$  of 10x buffer, 1  $\mu\text{L}$  of each primer pair (Table 8), 0.5  $\mu\text{L}$  of dNTPs, 0.2  $\mu\text{L}$  FastStart™ Taq DNA Polymerase, and 1  $\mu\text{L}$  of GC-rich supplement, with water added to make up the final volume. The cycler program recommended by StemCell was followed, as outlined in

Table 23. To confirm successful amplification, 12.5  $\mu$ L of the PCR products were loaded onto a 1.5% agarose gel with EtBr and analyzed via gel electrophoresis.

**Table 23** cyclor program used for the SeV vector RT-PCR

Stage	Temperature	Time
Initial denaturation	94°C	2 min
Denaturation	94°C	30 seconds
Primer annealing	55°C	30 seconds
Elongation	72°C	30 seconds
Loop from denaturation to elongation 34 times		
Final elongation	72°C	5 min
Store of the samples	4°C	Forever

### 3.2.5 Click-iT™ EdU Flow Cytometry Assay:

Measuring cell proliferation is essential for assessing cell health, genotoxicity, and evaluating anti-cancer drugs, with the most accurate method being the measurement of DNA synthesis. Traditionally, this was done using radioactive nucleosides like  $^3$ H-thymidine, later replaced by antibody-based detection of bromo-deoxyuridine (BrdU). The Click-iT® EdU Flow Cytometry Assay offers a more efficient alternative. EdU (5-ethynyl-2'-deoxyuridine), a thymidine analog, is incorporated into DNA during synthesis and detected via a copper-catalyzed click reaction between an alkyne group in EdU and an azide conjugated to a fluorescent dye, such as Pacific Blue™, Alexa Fluor® 647, or Alexa Fluor® 488 (Fig 13). Standard flow cytometry can then be used to measure the percentage of cells in the S-phase of the cell cycle. The EdU labeling of cells began by plating cells at a density of  $1 \times 10^6$  and allowing them to recover overnight before any further treatment. It was important to ensure optimal cell growth before proceeding. A 2X working solution of EdU (20  $\mu$ M) was prepared in complete NPC medium and prewarmed. An equal volume of the 2X EdU solution was then added to the cell culture media to reach a final concentration of 10  $\mu$ M. Cells were incubated with 2ml EdU containing media (10  $\mu$ M) for 1h.

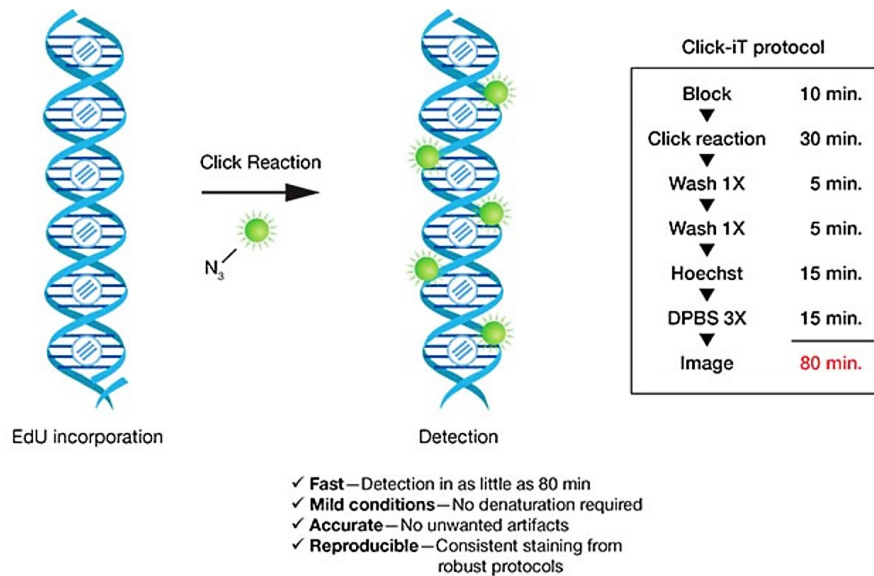


**Fig.13. EdU staining with Click-iT® EdU Assay kit allows for detecting newly synthesized DNA without the need for DNA denaturation.** Click-iT EdU Assay kit is compatible with standard fluorophores. The protocol is available for applications such as flow cytometry, imaging, microplates, high-content screening, and colorimetric immunohistochemistry.

At 1 hr time point, the EdU-containing media was removed, the cells were washed once with PBS, and harvested using 1 mL of TrypLE enzyme, followed by 5-6 minutes of incubation at 37°C. Afterward, 1 mL of 1% BSA/PBS was added, and the cells were pelleted by centrifugation at 1000g for 4 minutes.

For fixation, the cells were resuspended in 0.5 mL of 4% paraformaldehyde (PFA) and incubated for 15 minutes at room temperature. The cells were then pelleted (1000g for 4 minutes), the PFA was aspirated, and the cells were washed once with 1% BSA/PBS before pelleting and aspirating the supernatant. The cell pellet can be stored in 0.5 mL of 1% BSA/PBS at 4°C and be processed the next day. Permeabilization was carried out by removing the wash solution and adding 1 mL of 0.5% Triton X-100 in PBS to the pellet, resuspending the cells, and incubating for 15 minutes at room temperature.

For the click detection of EdU-labeled cells, it is essential to thaw the fluorescent azide and 10X Reaction Buffer Additive beforehand according to the manufacturer protocol. The required volumes of Click-iT components are calculated according to the following table 24 for 10 reactions. The total volume for the reaction was 5 ml. The reaction cocktail was prepared, protected from light, and used within 15 minutes. The cell pellet was dislodged, and 500 µl of the reaction cocktail is added to each sample, mixing well. The cells were incubated at room temperature for 30 minutes in the dark. Afterward, the cells were pelleted and washed once with 1 mL of 1% BSA/PBS.

For staining cells for DNA content, the cells were resuspended in either 300  $\mu$ L of DAPI (0.1 $\mu$ g/ml) containing 1% BSA/PBS, followed by 15 minutes of incubation in the at the room temperature. The cells were pelleted and washed once with 1 mL of PBS then pelleted and resuspended in 300  $\mu$ L PBS. At this stage, the cells were ready for analysis on flow cytometer. The cells were not only analyzed for Edu labeling for the S-phase but also for DAPI for other cell cycle phases.

**Table 24 Click-iT reaction cocktail preparation:**

Reaction Components	Location	Preparation	10x reaction
PBS, D-PBS, or TBS	10X stock, at 4°C	Dilute 10X stock 1:10 in dH2O	4.38mL
CuSO4	Ready to use, 4°C	-	100 $\mu$ L
Fluorescent Azide	Aliquots at -20°C	-	25 $\mu$ L
1X Reaction Buffer Additive	10X aliquots at -20°C	Dilute 10X stock 1:10 in dH2O	500 $\mu$ L
Total Volume			5mL

### 3.2.6 Evaluation of NPCs differentiation by immunofluorescence staining (Differentiation Assay)

Population of Map2+ neurons were quantified in terms of % of % positive area/total region of interest (ROI) area where ROI was total DAPI+ cells area using Fiji. A threshold was selected based on no fluorescence background to be used as negative control then measured the area occupied by DAPI+ cells (ROI) relative to total background area then the MAP2+ over the total ROI area. Four biological replicates were used per cell line. In each replicate, 3 coverslips were stained for each cell line and 5-10 images were taken per coverslip. Average of % positive area/total ROI area of the images belong to the same coverslip was calculated. Some coverslips were excluded due to poor immunostaining quality.

### 3.2.7 Evaluation of cell proliferation/ apoptosis by flow cytometry

An accelerated procedure was used for the detection of Ki67, PHH3,  $\gamma$ -H2AX and Cas3 in fixed cells by flow cytometry following the protocol of Saponin-Based Permeabilization of Firsanov et. al[241] with some modifications. Firstly, the NPCs were plated at a density of  $1 \times 10^6$  and allowing them to recover overnight before any further steps. On next day, the medium was removed, then PBS/EDTA solution was used to rinse the cells, followed by treatment with 1 ml TrypLE enzyme for 4-5 minutes at 37°C. Cell detachment was checked under an inverted microscope. After detachment, 1ml NPCs medium was added to inactivate the trypsin, then the cells were centrifuged at 600  $\times$  g for 6 minutes at room

temperature (RT), and washed with 600  $\mu$ L PBS. The cells were vortexed then pelleted by centrifugation at 600 $\times$  g for 6 minutes at 4°C.

Next, cells were fixed in a cold freshly prepared 4% formaldehyde in PBS for 10 minutes at 4°C. Then, 300  $\mu$ L of cold PBS (also precooled to 4°C) was added to the cell suspension, vortexed, and pelleted by centrifugation. The cells pellet was washed by adding 600  $\mu$ L of cold PBS, vortexed, and centrifugated. For permeabilization, 750  $\mu$ L of permeabilization solution (Perm) containing 0.1% saponin and 1–10% FCS in PBS was added to the pellet. The cells were incubated for 30 minutes at 4°C, with the tube gently tapped several times during the incubation. The cells were pelleted by centrifugation, the supernatant is aspirated, and 100  $\mu$ L of primary antibody diluted 1:250 in Perm according to table 25, was added. The cells were vortexed for 3 seconds and incubated for 20 minutes at 37°C, with occasional gentle tapping of the tube.

Following incubation, 600  $\mu$ L of Perm was added to the cell suspension in antibody solution, vortexed, and centrifuged. The supernatant was aspirated, and the cells were washed by adding 600  $\mu$ L of Perm to the pellet, followed by vortexing and centrifugation. The supernatant was aspirated. Next, 100  $\mu$ L of secondary Alexa Fluor -conjugated antibody, diluted 1:400 in Perm, was added (Table 25). The cells were vortexed for 3 seconds and incubated for 20 minutes at 37°C.

The previous wash steps were repeated twice, and 300  $\mu$ L of cold PBS was added to the cell suspension. For DNA counterstaining, 300  $\mu$ L of 0.5  $\mu$ g/mL DAPI in 0.1% Triton X-100 and 3 were added. The cells were vortexed and kept in the dark for 20 minutes at RT before analysis. Flow cytometry was then performed for detection.

**Table 25 Primary and secondary antibodies combinations used for flow cytometry:**

Primary antibodies combination	Dilution	Secondary antibodies combination	Dilution
Mouse $\gamma$ -H2AX + Rabbit Cas3	1:250 + 1:250	Goat anti-mouse Alexa Fluor 488 + Goat anti-rabbit Alexa Fluor 647	1:400 + 1:400
Mouse Ki67 + Rabbit PHH3	1:250 + 1:250	Goat anti-mouse Alexa Fluor 488 + Goat anti-rabbit Alexa Fluor 647	1:400 + 1:400

### 3.2.8 RNA-sequencing

RNA-sequencing was conducted to compare the transcriptome of NPCs obtained from wildtype A2, mutant A2D5 female lines and wildtype S21, mutant C34 male lines. The sequencing for those different NPCs was carried out by StarSEQ GmbH lab in Mainz.

The RNA sequencing analyses were conducted with assistance from Dr. Hristo Todorov and Dewi Hartwich.

### **3.2.8.1 RNA-sequencing library preparation**

For all lines the library for RNA-seq experiments was prepared by StarSEQ GmbH lab using total RNA samples (Minimum and maximum required amounts were 100 ng and 4 µg respectively) following the manufacturer's instructions of NEBNext Ultra II Directional RNA library preparation kit. The sequencing was performed by using a NextSeq 2000 as a paired-end 150 bp run and an expected output of 50 million reads per sample.

### **3.2.8.2 Bioinformatics analysis of RNA-sequencing data**

#### **3.2.8.2.1 RNA-sequencing data pre-processing**

Quality control of raw sequencing reads was performed using FastQC (v0.11.5). Reads were then subjected to adapter trimming and quality filtering using TrimGalore (v0.6.6). Trimmed reads were subsequently mapped to the human reference genome (GRCh37, Ensembl annotation) using STAR (v2.7.5). Aligned reads were quantified at the gene level using Subread's featureCounts (v2.0.1).

#### **3.2.8.2.2 Differential expression and downstream analysis**

Differential expression analysis was performed using the DESeq2 R package (v1.42.1) with default settings. Sample-to-sample variability was investigated using a principal component analysis (PCA) with the top 500 most variable genes as implemented in the plotPCA() function from DESeq2. Genes with an adjusted p-value <0.05 (Benjamini-Hochberg correction) were considered as differentially expressed. Volcano plots were generated using ggplot2 (v3.5.1). Differentially expressed genes (DEGs) from different pairwise comparisons were overlapped with autism risk genes included in the SFARI database (<https://gene.sfari.org/>). Intersections were visualized using Venn diagrams produced with the VennDiagram R package (v1.7.3). A GO term analysis of DEGs was performed with the clusterProfiler R package (v4.10.1). To gain insight into the differentiation status of WT and mutant NPCs, a set of neuron- and NPC-specific genes was obtained from the study by Burke et al., 2020[242]. The expression pattern of these genes was investigated using a PCA. To extract features that were important for explaining the observed PCA pattern, loadings of genes on the first principal component were calculated. Loadings represent correlations between the original variables and the multivariate dimensions in the PCA. Loadings were calculated with the following formula:

$$A = V\sqrt{L}$$

where  $V$  is the matrix of eigenvectors,  $L$  is a diagonal matrix with the corresponding eigenvalues and  $A$  corresponds to the loading matrix.

#### 3.2.8.2.3 Validation of RNA-Seq Data Using qPCR:

To validate the RNA-Seq results, qPCR was performed for selected DEGs. RNA was extracted from the same cell samples used for RNA-Seq analysis using the RNA extraction kit mentioned in 3.2.4.8, following the manufacturer's protocol. The RNA quality and concentration were assessed using a NanoDrop spectrophotometer. cDNA synthesis was carried out using the protocols in 3.2.4.9 according to the manufacturer's instructions.

Specific DEGs, such as *NLGN3* and *PINK1*, which exhibited significant upregulation or downregulation in both female and male NPCs and *MKI67*, *CHD8* and *SLC25A25* only in female NPCs and *CCND2*, *HNRNPR* and *SLC5A6* only in male NPCs in the RNA-Seq data, were selected for validation. Primers for each gene were designed using Primer3, ensuring an optimal amplicon size of 100-150 bp for efficient amplification. *GAPDH* was used as housekeeping genes for normalization. The primer efficiency was tested before were all used primers had efficiencies between 90 and 110%.

qPCR reactions were performed in triplicate for each target gene using the qPCR protocol with the SYBR Green Master Mix mentioned 3.2.4.10. Data were analyzed using Excel and GraphPad Prism]. The qPCR results were compared with the RNA-Seq fold changes to assess the consistency between the two methods, confirming the reliability of the RNA-Seq data.

### 3.2.9 CUT& Tag sequencing (Cleavage Under Targets and Tagmentation)

CUT& Tag experiments were conducted to identify and compare POGZ-DNA interactions of NPCs obtained from wildtype A2, mutant A2D5, and A2A1 female lines and wildtype S21, mutant C34 male lines. The CUT&Tag experiments were done in collaboration with Dr. Joan Barau and Jessica Lesimann; PhD, at Institute of Molecular Biology "IMB" Mainz. The sequencing for those different NPCs was carried out by the IMB Genomics facility in Mainz. The CUT&Tag sequencing analyses were conducted with assistance from Dr. Hristo Todorov.

#### 3.2.9.1 RNA-sequencing library preparation

CUT&Tag experiments were conducted on freshly collected NPCs, which were cultured and derived from iPSCs (wildtype A2, mutant A2D5, and A2A1 female lines and wildtype S21, mutant C34 male lines). CUT&Tag was performed following the protocol by Kaya-

Okur and Henikoff (2020) using concanavalin A (ConA) beads with minor modifications[243]. The procedure starts with formation of the Tn5-adaptor complex, Mosaic end adapter A (ME-A) and B (ME-B) oligonucleotides were annealed with their respective reverse oligonucleotides. Oligos were diluted to 200  $\mu$ M in annealing buffer (10 mM Tris pH 8, 50 mM NaCl, 1 mM EDTA) and mixed to a final concentration of 100  $\mu$ M. The mixture was heated at 90–95°C for 3–5 minutes, then cooled to room temperature over 45 minutes. 16  $\mu$ L of the annealed oligos were mixed with 100  $\mu$ L of 5.5  $\mu$ M pA-Tn5 fusion protein and incubated for 1 hour at room temperature before being stored at –20°C. Followed by preparation of 10  $\mu$ L of ConA beads slurry per sample (up to 400,000 cells) in 500  $\mu$ L Binding Buffer (20 mM HEPES-KOH pH 7.5, 10 mM KCl, 1 mM CaCl<sub>2</sub> and 1 mM MnCl<sub>2</sub>). Washing twice by separating on a magnet, aspirating, and resuspending in fresh Binding Buffer. After the final wash, the beads were resuspended in ~100  $\mu$ L per experiment. For each reaction, the cells (NPCs) were resuspended and washed twice by Dig-wash buffer that was wash buffer supplemented with 0.05% Digitonin (20 mM HEPES pH 7.5, 150 mM NaCl, 0.5 mM spermidine and add 1 Roche Complete Protease Inhibitor EDTA-Free tablet). After gently centrifuging the cells at 600g for 5 minutes, the supernatant was discarded. 200,000 cells were bound to 15  $\mu$ L ConA beads (Polysciences, 86057-10) and incubated at room temperature rotating for 10 min. The beads were separated on a magnet and the liquid was aspirated. The bead-cell mixture was resuspended in 25  $\mu$ L antibody buffer per experiment (1:50 POGZ [EPR10612] (ab167408) and IgG (Abcam, ab37415)) in 0.2 mL tube strips then incubated overnight at 4°C on Nutator. On the next day, secondary antibody Anti-Rabbit IgG (Antibodies-online, ABIN101961) was used at 1:100 in Dig-wash buffer and 50  $\mu$ L per sample was added. The mixture was incubated on a nutator for 30–60 min at room temperature or overnight at 4°C. After incubation, the mixture was cleared on a magnet, the liquid was removed, and washed once with Dig-wash buffer.

All other steps followed the original protocol by Kaya-Okur and Henikoff (2020), the pA-Tn5 adaptor complex (IMB in-house PPCF production, batch 5, 06-2023) was diluted to 1:200 in Dig-300 buffer, and 100  $\mu$ L was added per sample. The samples were incubated on a nutator at room temperature for 1 hour. Following incubation, the samples were rinsed and washed once with Dig-300 buffer. After a quick spin, tubes were placed on a magnet stand to clear liquid. 150  $\mu$ L Cold tagmentation buffer (10 mM MgCl<sub>2</sub> in wash

buffer) was added, and samples incubated at 37°C for 1 hour. Tagmentation was stopped by adding 5 µL 0.5M EDTA, 1.5 µL 10% SDS, and 1.25 µL Proteinase K, followed by 1-hour incubation at 55°C. DNA was extracted using a column prep kit and eluted in 25 µL of buffer. PCR mix was prepared using Q5 polymerase and 14 PCR cycles were used for library amplification. After the PCR tubes were cooled, 1.3 volumes (65 µL) of SPRI beads were added to the PCR tubes and mixed. The samples were incubated for 5–10 minutes, placed on a magnet to clear, and the supernatant was removed. The beads were washed twice with 200 µL of 80% ethanol, and residual liquid was removed. The beads were resuspended in 25 µL of water, incubated for 5 minutes, and the clear supernatant was transferred to a new tube. Experiments were done in triplicate, and pooled samples were sequenced on the NextSeq 2000 High Output, PE, 2×150 cycles for dual index reads.

### **3.2.9.2 Bioinformatics analysis of CUT&Tag data**

#### **3.2.9.2.1 Preprocessing, alignment and peak calling**

Initial quality control was conducted on raw FASTQ files using FastQC (v0.11.9). Adapter sequences and low-quality bases were removed from the raw sequencing reads using BBDuk (v38.86) with the following parameters: ktrim=r, k=23, mink=11, hdist=1, tpe, tbo, minlen=25, zipllevel=2, overwrite=true, qtrim=rl, trimq=10. Post-trimming quality checks were performed again using FastQC. Trimmed reads were then aligned to the human reference genome (GRCh37) using Bowtie2 (v2.5.1) with parameters optimized for CUT&RUN and CUT&Tag data. The alignment was performed using paired-end mode, with the following options: --local, --very-sensitive, --no-mixed, --no-discordant, -l 10, and -X 700. Aligned SAM files were converted to BAM format using Samtools (v1.2), with only mapped reads retained (-F 0x04). The resulting BAM files were then coordinate-sorted and indexed using Samtools. To generate coverage tracks, BAM files were further processed using bamCoverage (from deepTools v3.5.1), with a bin size of 10 bp and normalization using CPM (Counts Per Million). Peak calling was performed using SEACR (v1.3) on the processed BAM files. BAM files were first converted to BEDPE format using bedtools (v2.30.0), and pairs of reads with fragment lengths under 1000 bp were retained. The resulting BED files were processed to create BedGraph files using bedtools genomecov. SEACR was run in stringent mode, using IgG control files for peak calling.

#### **3.2.9.2.2 Consensus peak set generation**

To generate consensus peak sets from individual replicates, first peak files were concatenated into a single file using the cat command. The concatenated files were sorted

by chromosome coordinates using `sort -k1,1 -k2,2n -k3,3n`. After sorting, the concatenated peak files were merged using `bedtools merge (v2.31.1)`. Overlapping peaks within a 10 bp distance were merged, and the mean signal values for the 4th and 5th columns (representing total and maximum signal) were calculated. This generated a unified set of merged peaks for each condition. To assess how many of the merged peaks were present in each of the original replicates, `bedtools intersect` was used with the `-c` option, which counts the number of replicates that contain each peak. Peaks with a complete overlap (fraction of overlap = 1.0) were considered. Peaks present in two or more replicates were retained for downstream analyses. Consensus peaks from WT and HET samples were further filtered to exclude peaks overlapping with KO samples, using `bedtools intersect` with the `-v` option. This process ensured that only unique peaks specific to the WT and HET conditions were retained. The filtered consensus peaks were stored as new `.bed` files for further analysis.

#### 3.2.9.2.3 Visualization of signal density across peak regions

Signal matrices of read density around peaks regions were computed using `computeMatrix` from `deepTools (v3.5.1)` with options: `--skipZeros -a 3000 -b 3000 --referencePoint center`. To visualize the signal intensities across different peak regions, `plotHeatmap` from `deepTools` was used.

#### 3.2.9.2.4 Peak annotation and downstream analysis

Consensus peaks were annotated to genomic regions using the `Chipseeker R package (v1.38.0)`. POGZ-bound genes in male and female WT samples were overlapped with differentially expressed genes from the RNA-seq data and the significance of the overlap was evaluated using a chi-squared test, comparing observed versus expected frequencies. Furthermore, the intersection of POGZ-bound genes in female and male WT samples with autism risk genes included in the SFARI database was determined. To obtain an expected value for the overlap, a Monte Carlo simulation was performed. In 1000 iterations, a set of genes having the same size as the set of POGZ-bound genes, was randomly sampled and the intersection with genes in the SFARI database was determined. The observed value was then compared statistically against this null distribution using the cumulative distribution function of the normal distribution (one-sample z-test). GO term analysis for POGZ-bound genes was performed with the `clusterProfiler R package (v4.10.1)`.

#### 3.2.9.2.5 Differential occupancy analysis

Peak occupancy across the genome was analyzed using the DiffBind R package (v3.12.0). To remove potential false positives, peaks overlapping genomic blacklisted regions were excluded using the `dba.blacklist()` function. Peaks were counted using the `dba.count()` function. The data were normalized using the `dba.normalize()` function to account for differences in library sizes and sequencing depth. Sample correlations were visualized using a correlation heatmap produced with the `ph heatmap` package (v1.0.12). PCA was conducted to assess the variance between samples and plotted using the `dba.plotPCA()`. Differential peak occupancy between HET and WT groups was determined using DiffBind's differential analysis pipeline. The contrast between experimental groups was defined using the `dba.contrast()` function, with the WT group set as the baseline for comparison. Differential analysis was performed using the `dba.analyze()` function, which utilizes DESeq2 (v1.42.1). Significant differentially bound sites were identified using a false discovery rate (FDR) threshold of 0.05. Volcano plots were generated using `ggplot2` (v3.5.1). Differentially bound regions were annotated to genomic features using the `ChIPseeker` package (v1.38.0). To investigate the relationship between differential binding and gene expression, DEGs from the RNA-seq analysis were overlapped with genes showing differential binding. Overlaps between DEGs and differentially occupied genes were visualized using an UpSet plot generated with the `UpSetR` package (v1.4.0).

## 4 Results

### 4.1 Confirmation and characterization of cell type

Prior to conducting any further experiments, all cells were characterized to verify their cell type.

#### 4.1.1 Fibroblasts

As previously mentioned, three different sets of fibroblasts were used. The wildtype (WT) male and the wildtype (WT) female fibroblasts were isolated from a skin biopsy by former students of the lab and were available at the beginning of this project. Additionally, as part of this research, the WHSUS male patient fibroblasts were isolated and cultured from a skin biopsy as described in the methods section.

##### 4.1.1.1 Morphology

All WT male and female fibroblast cell lines grew as monolayers with an elongated morphology, as previously confirmed by former students of the lab. The WHSUS male patient fibroblasts showed a similar morphology with a steady growth rate (Fig 14A).

##### 4.1.1.2 Immunofluorescent staining

To confirm the cellular identity of the WHSUS male patient fibroblasts, an immunofluorescent staining was performed. The fibroblasts showed expression of the collagen protein SERPINH1, which is a fibroblast marker, which is localized in the cytoplasm. (Fig 14B).

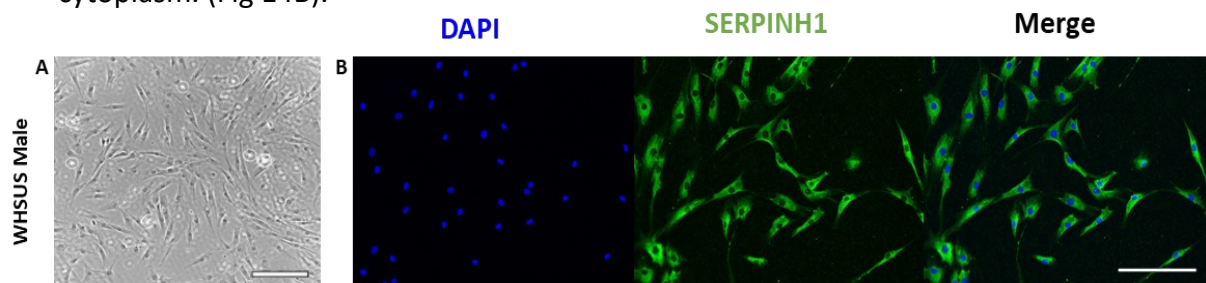


**Fig.14. Morphology and immunofluorescent staining of the WHSUS male fibroblasts.** A. White light pictures of fibroblasts show an elongated morphology. Scale bar: 100  $\mu$ M. B. Fibroblasts show expression of the collagen protein SERPINH1. The nuclei were stained with DAPI. Scale bar: 50  $\mu$ M.

#### 4.1.2 iPSCs

Completely characterized female wildtype and male wildtype fibroblasts were reprogrammed into iPSCs A2 and S21, respectively, by former students of the lab. During the course of this work, WHSUS male fibroblasts were reprogrammed into iPSCs C34 using same protocol. Approximately three to four weeks after viral transfection with non-integrating *CytoTune™-iPS 2.0 Sendai* Reprogramming Kit, iPSC colonies began to emerge within the fibroblast culture, and these colonies were expanded. To introduce mutations in female A2 iPSCs, CRISPR/Cas genome editing was done generating A2D5 (female heterozygous) and A2A1 (female compound heterozygous). Later, sequencing of all lines was confirmed via sanger sequencing. The characterization of the previously reprogrammed cells A2 (female WT), S21 (male WT), C34 (WHSUS male) along with A2 mutant iPSCs, A2D5 (female heterozygous) is shown in the following results:

##### 4.1.2.1 CRISPR/Cas9 genome editing of female wildtype iPSCs

After confirming a stable undifferentiated stemness status that was done by former students, the A2 female iPSCs underwent CRISPR/Cas9 genome editing to introduce protein truncating mutations into the first coding exon of *POGZ* that presents in all isoforms to ensure complete allele deletion via non-homologous end-joining (NHEJ). In addition, the edited iPSCs would have the same genetic background (isogenic) to A2. Electroporation was conducted to introduce either two distinct gRNA plasmids or two distinct ready sgRNA generated by EnGen® sgRNA Synthesis Kit. Each gRNA plasmid /sgRNA was electroporated together with a Cas9-GFP plasmid (Fig.15). GFP<sup>+</sup> cells were sorted by FACS and expanded. The cells were screened for the presence of their introduced *POGZ* mutations, their karyotype and pluripotent status, as previously described.

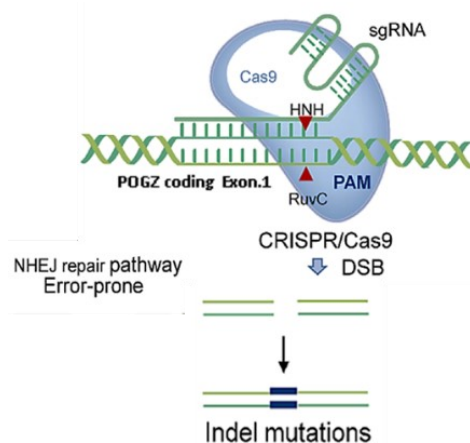


**Fig.15. CRISPR strategy to induce frameshift mutations in the first coding exon of *POGZ*.** iPSCs were electroporated with plasmids encoding the Cas9 protein and either gRNA1 or gRNA2, aiming for DSB repair via NHEJ.

#### 4.1.2.2 DNA sequencing of A2 wildtype and edited female iPSCs

*POGZ* first coding exon was initially sequenced, where the gRNAs bind and cause double strand breaks with nuclease activity of the Cas9 protein. The sequencing showed a heterozygous 1 bp deletion in the A2D5 iPSCs (c.41del) and a compound heterozygous 1 bp insertion (c.29\_30insT) and 7 bp deletion (c.26\_32del GAATGTG) in the A2A1 iPSCs (Fig.16) (Table 26). Those mutations are present early in the N-terminus region and are supposed to cause a frameshift, resulting in a premature stop codon (PTC). The heterozygous 1 bp deletion mutation in A2D5 iPSCs leads to change of phenylalanine to Serine at position 7 and termination of the protein at position 29 that is still in the first coding exon. In A2A1 iPSCs, the 1 bp insertion mutation leads change of Cysteine at position 10 to Leucin and termination of the translation at position 11 (p.Cys10LeufsX11) and 7 bp deletion leads to change of Glutamic acid at position 9 to Arginine and termination of the translation at position 27 (p.Glu9ArgfsX27). Both mutations in A2A1 iPSCs terminate in the in the first coding exon (Table 26).

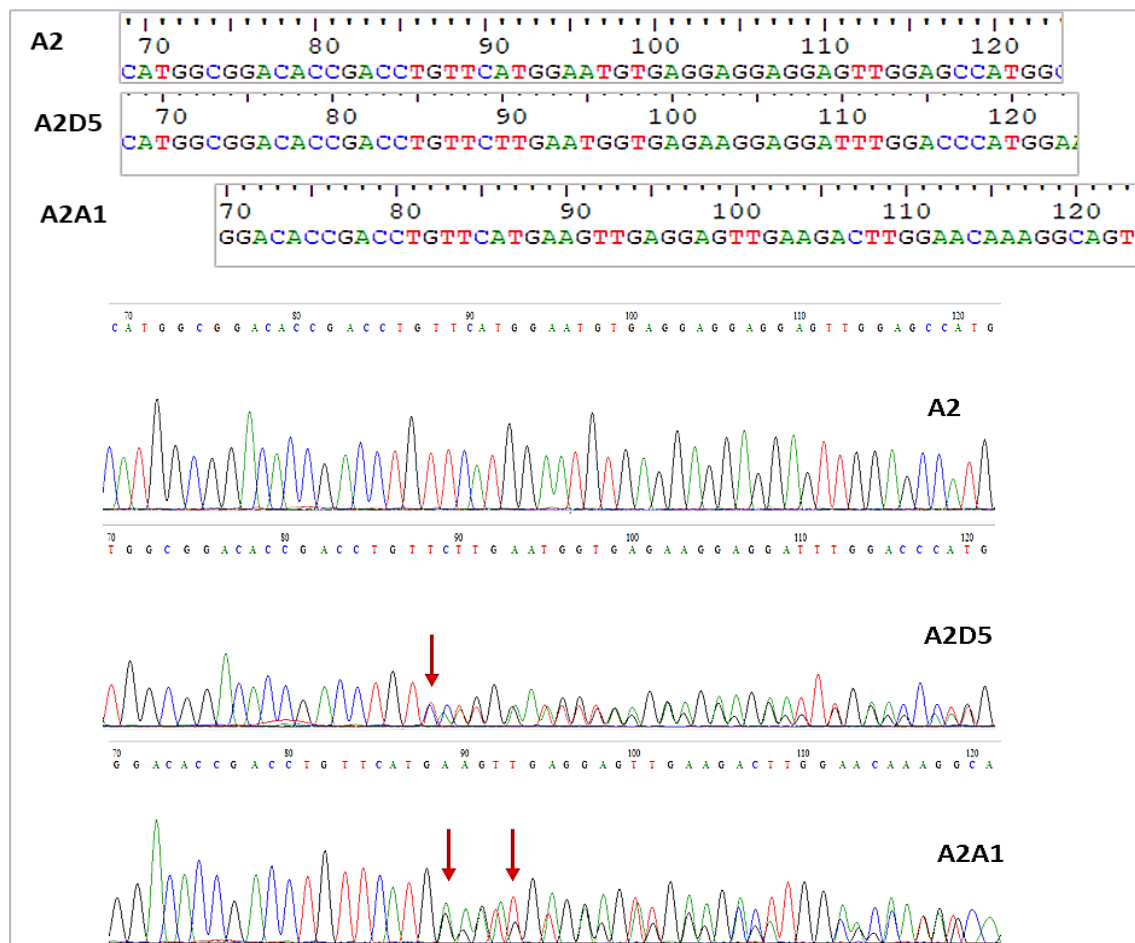


**Fig.16. Electropherogram showing the sequencing result for a chosen part of *POGZ* coding Exon 1. The red arrows mark the peak showing the 1 bp deletion in the A2D5 iPSCs; and the 7 bp deletion and the 1bp insertion in the A2A1 iPSCs. A2 iPSCs DNA shows the wildtype sequence of this chosen part of *POGZ* coding Exon 1.**

**Table 26 The mutations of female iPSC lines; A2D5 (*POGZ*<sup>+/-</sup>) and A2A1 (*POGZ*<sup>-/-</sup>) and their corresponding mutant POGZ proteins**

Cell line ID	DNA	Protein	Mutation
A2 ( <i>POGZ</i> <sup>WT/WT</sup> )	WT	Full WT protein	Wildtype
A2D5 ( <i>POGZ</i> <sup>+/-</sup> )	Chr1 g.151414660GA>G(hg19)	p. (Phe7SerfsTer29)	Heterozygous
A2A1 ( <i>POGZ</i> <sup>-/-</sup> )	Chr1 (-) g. 151414650-151414656 delGAATGTG(hg19) Chr1 (-) g. 151414653 T>TT (hg19)	p. Glu9ArgfsX27 p. Cys10LeufsX11	Compound heterozygous

These mutant iPSCs were generated using CRISPR/Cas9-mediated knockout; WT, wildtype; X, nonsense; ins, insertion; del, deletion; fs, frameshift; Ter, termination.

#### 4.1.2.3 Exome sequencing for the Off-target analysis of edited female iPSCs

To exclude any mutations can be caused by CRISPR/Cas 9 except of *POGZ*, whole exome sequencing (WES) was conducted with A2, A2D5 and A2A1 iPSCs. All three samples revealed a similar number of variants and upon assessing the predicted off-target effects (Guide design resources — Zhang Lab, n.d.) with up to 5 mismatches for the used gRNAs, A2, A2D5 and A2A1 showed no differences.

#### 4.1.2.4 DNA sequencing of wildtype and WHSUS male iPSCs

*POGZ* exon 17 was sequenced to confirm the presence of the *POGZ* mutation in the C34 iPSCs that was initially detected in the WHSUS patient's DNA derived from peripheral blood. As expected, the sequencing revealed the heterozygous 1 bp insertion (c.2470dup) in the C34 iPSCs (Fig 17) (Table 27). This mutation was present in the HPZ domain of *POGZ* and is supposed to cause a frameshift, resulting in a premature stop codon (PTC). This frameshift mutation leads to change of the threonine at 824 to asparagine and termination of the protein at amino acid at 864 in exon 19 (p.(Thr824AsnfsTer40)) (Table 27). Also, *POGZ* wildtype sequence was confirmed in male iPSCs, S21, to be used as a control.

#### 4.1.2.5 Morphology

All iPSC lines showed consistent growth, formed densely packed colonies with well-defined edges, and grew as monolayers (Fig.18; a representative picture of the WHSUS (C34) male iPSCs). Single cells within these colonies displayed a round morphology, with the nucleus occupying roughly 90% of the whole cell volume.

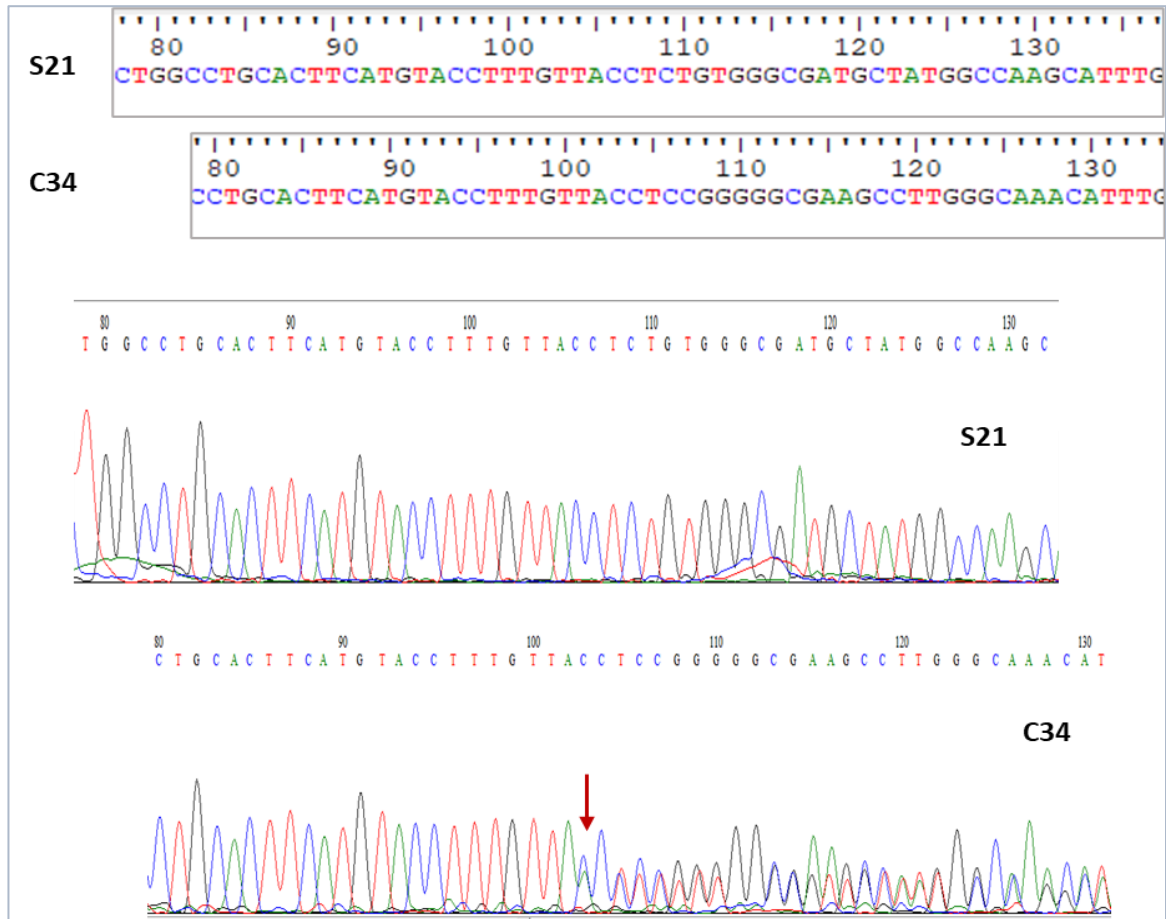


**Fig.17. Electropherogram showing the sequencing result for a chosen part of *POGZ* Exon 17.** The red arrows mark the peak showing the 1bp insertion in the WHSUS, C34 iPSCs. S21 iPSCs DNA shows the wildtype sequence of this a chosen part of *POGZ* Exon 17.

**Table 27 The mutation of WHSUS male iPSC line; C34 (*POGZ*<sup>+/-</sup>) and its corresponding mutant *POGZ* protein.**

Cell line ID	DNA	Protein	Mutation
S21 ( <i>POGZ</i> <sup>WT/WT</sup> )	WT	Full WT protein	Wildtype
C34 ( <i>POGZ</i> <sup>+/-</sup> )	Chr1 g.151379460G>GT (hg19)	p. (Thr824AsnfsTer40)	Heterozygous

These mutant iPSCs were generated using CRISPR/Cas9-mediated knockout; WT, wildtype; X, nonsense; ins, insertion; del, deletion; fs, frameshift; Ter, termination.

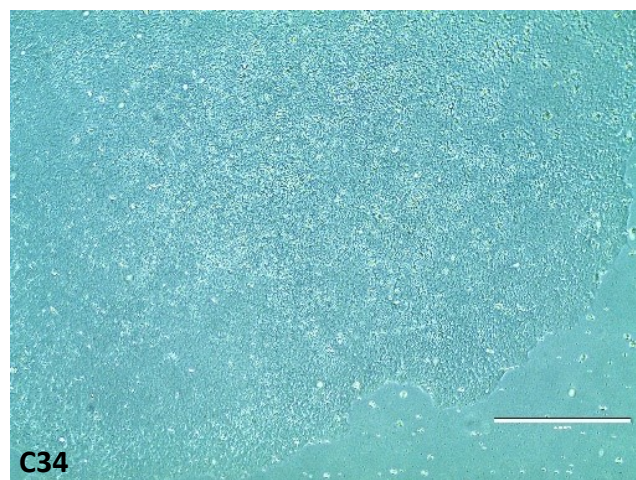


**Fig.18. Morphology of WHSUS male iPSCs (C34).** White light pictures of iPSCs show densely packed colony growing as monolayers. Single cells appear round with big nuclei. Scale bar: 400  $\mu$ M.

#### 4.1.2.6 Karyogram

To ensure the absence of any potential chromosomal abnormalities that could occur during the reprogramming or genome editing, karyotyping was performed on all iPSCs (Fig.19). The iPSC clones derived from the female wildtype fibroblasts, A2 showed a typical female karyotype of 46, XX; the iPSC clones derived from the male wildtype and male WHSUS patient fibroblasts, S21 and C34, respectively, showed a regular male karyotype of 46, XY. Similarly, the two iPSC clones resulting from the genome editing of A2 female iPSCs, A2D5 and A2A1 also showed a typical female karyotype of 46, XX. Importantly, none of the iPSCs used in the study displayed any form of chromosomal abnormality when examined at any of the time points.

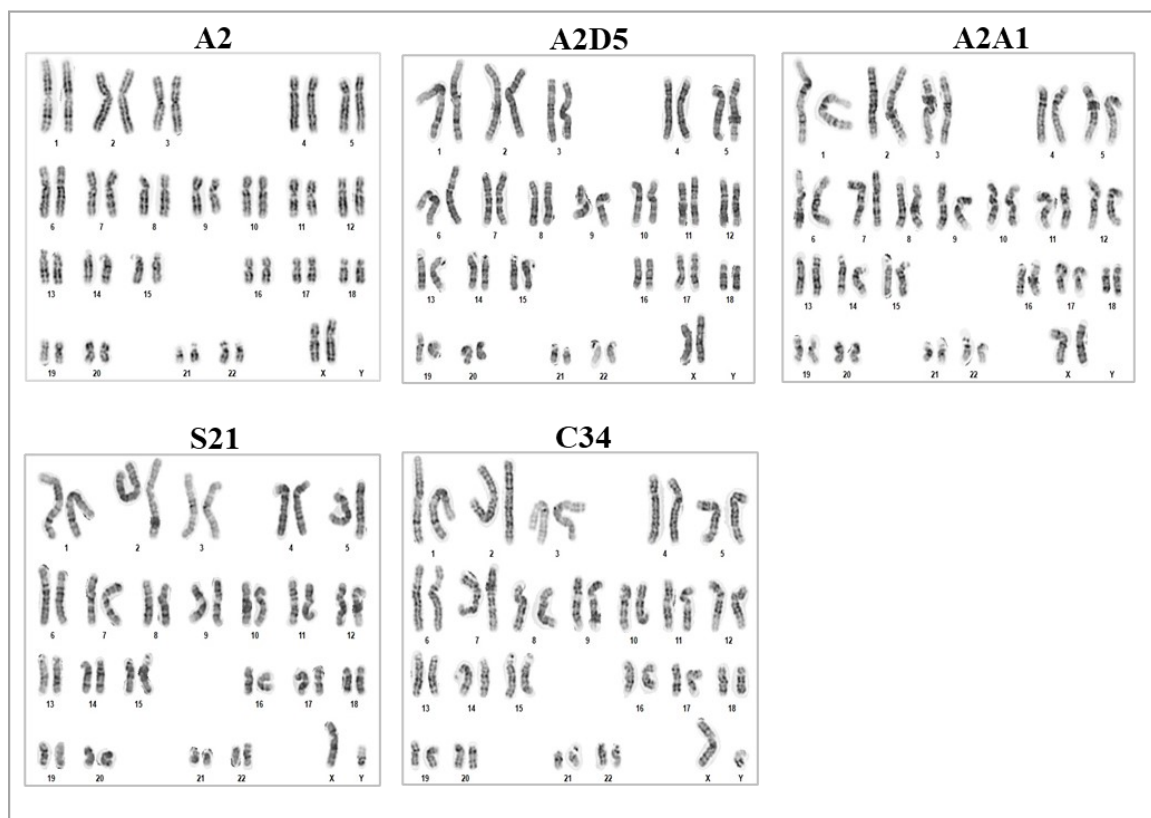


**Fig.19 Karyogramm of the iPSCs used in this study.** iPSCs showed a normal male karyotype of 46, XY by G-banding analysis for S21 and C34, and a normal female karyotype of 46, XX by G-banding analysis for A2, A2D5 and A2A1.

#### 4.1.2.7 Pluripotency (RT-qPCR)

The pluripotency of the A2 and S21 iPSCs was confirmed prior this study. To confirm the pluripotency of the WHSUS male iPSC line C34, RT-qPCR analysis of the pluripotency markers *KLF4*, *NANOG*, *OCT4*, and *SOX2* was performed. Normalizing Ct values to *GAPDH*

as housekeeping gene and comparing them to values of the corresponding fibroblasts. The C34 iPSCs showed a consistent expression pattern of all four genes in all iPSC samples.

#### 4.1.2.8 Pluripotency (immunofluorescent staining)

To confirm the pluripotency of the iPSC lines on protein level, an immunofluorescent staining was conducted against the pluripotency markers NANOG and TRA-1-60 (Fig. 20). NANOG is a nuclear localized transcription factor responsible for self-renewal, while TRA-1-60 is a membrane surface protein exclusively expressed in pluripotent stem cells. Results revealed that all iPSCs expressed both proteins. The NANOG staining colocalized with the nuclear counterstaining of DAPI, while the TRA-1-60 staining was more dispersed and localized outside of the nuclei.

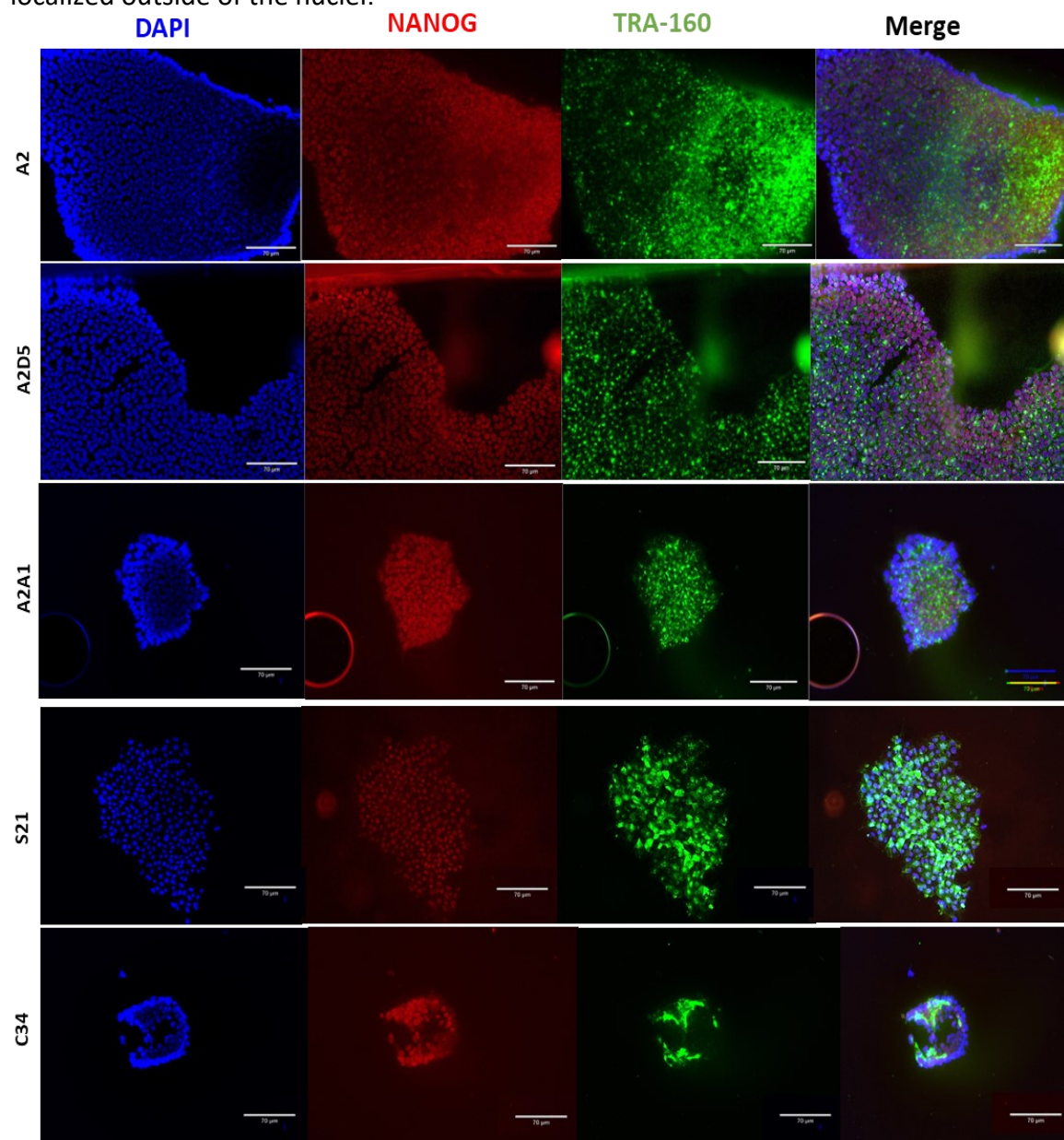


**Fig.20. Immunofluorescent staining of the iPSCs.** All cells show protein expression of the pluripotency markers NANOG and TRA-1-60. Scale bar: 70 µM.

#### 4.1.2.9 CRISPR/Cas9 editing of male WHSUS iPSCs

The male WHSUS patient iPSCs, C34, was used to correct *POGZ* mutation using CRISPR/Cas9 to have wildtype isogenic control. After a stable undifferentiated stemness status was confirmed, the C34 male WHSUS patient iPSCs underwent CRISPR/Cas9 genome editing to correct the mutation. Electroporation was conducted to introduce nine distinct ready sgRNA generated by EnGen® sgRNA Synthesis Kit. Each sgRNA was electroporated paired with a Cas9-GFP plasmid and a template of around 100 bp of *POGZ* Exon17 wildtype sequence (Fig.21). GFP<sup>+</sup> cells were sorted by FACS and expanded. The cells were analyzed for their *POGZ* mutation correction, their karyotype and pluripotent status, as previously described.

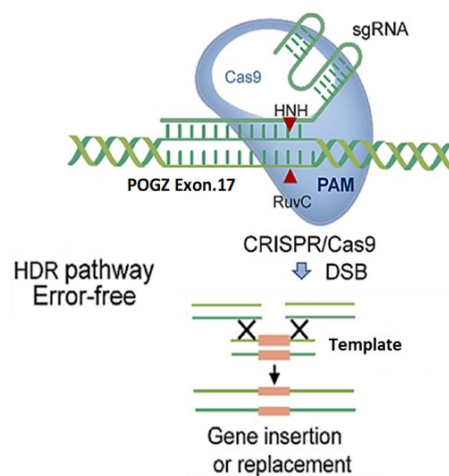


**Fig.21. CRISPR strategy to correct mutation in exon17 of *POGZ* using a template.** iPSCs were electroporated with plasmids encoding the Cas9 protein and gRNA1 to gRNA9, aiming for DSB repair via HDR and the template.

#### 4.1.2.10 DNA sequencing of corrected male WHSUS iPSCs

The sequencing of *POGZ* exon 17 in crisped WHSUS iPSCs, C34, showed unfortunately, that the mutation was not corrected and remained the same as in C34 with all nine gRNAs used. Therefore, the wildtype male iPSC line, S21, was used as control for C34 in all upcoming experiments.

### 4.1.3 NPCs

Comprehensively characterized iPSCs were used for the differentiation into NPCs. The NPCs presented here were generated using the protocol of the ThermoFisher commercial Kit.

#### 4.1.3.1 Morphology

NPCs were cultured as monolayer where they showed a slightly elongated cell morphology. Cells were passaged as single cells suspension where they showed consistent growth rate after passaging. Spontaneous differentiation of NPCs into a more neuronal like morphology was minimal.

#### 4.1.3.2 RT-qPCR

To confirm successful NPC differentiation, the expression of iPSCs and NPCs markers was analyzed by RT-qPCR (Fig.22). All of the NPCs showed a similar expression profile of the selected genes. The pluripotency genes were downregulated on a log<sub>2</sub> scale between 2-fold (*KLF4*) and 8- to 10-fold (*NANOG* and *OCT4*) respectively, while NPC marker genes were upregulated 2-3-fold (*NESTIN*) or even up to 10-fold (*PAX6*). The only gene showing almost no changes in its expression level was *SOX2*, with an upregulation in the NPCs of about 0.5-1-fold compared to the respective iPSCs. This small fold change in *SOX2* expression may not be dramatic because *SOX2* continues to play a critical role in both maintaining pluripotency and supporting early neural differentiation of NPCs.

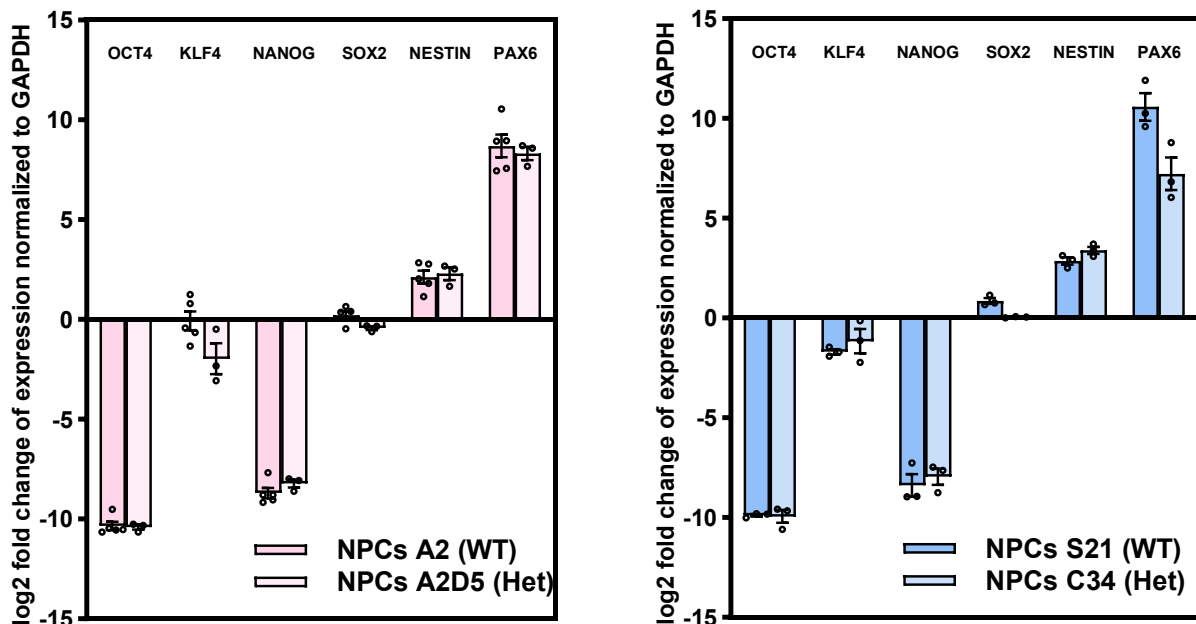


**Fig.22. RT-qPCR of the NPCs.** Female (left) and male (right) NPCs showed a decreased mRNA expression of *KLF4*, *NANOG* and *OCT4*, an almost unchanged expression of *SOX2* and an increased expression of *NESTIN* and *PAX6* relative to the iPSCs they were differentiated from. *GAPDH* was used for normalization. n=5(A2); n=3(A2D5); n=3(S21); n=3(C34). Values are mean  $\pm$  SEM.

#### 4.1.3.3 Immunofluorescent staining

For further characterization of the NPCs an immunofluorescent staining against the neuronal stem cell markers NESTIN, SOX2 and PAX6 was performed ((Fig.23-24). All NPCs showed protein expression of all three markers. The transcription factor SOX2 overlaid with the DAPI counterstaining of the nuclei, while the transcription factor PAX6 showed slightly diffuse staining, extending from the nuclei into the adjacent cytoplasm. As expected, the intermediate filament protein NESTIN was detected in the cytoplasm.

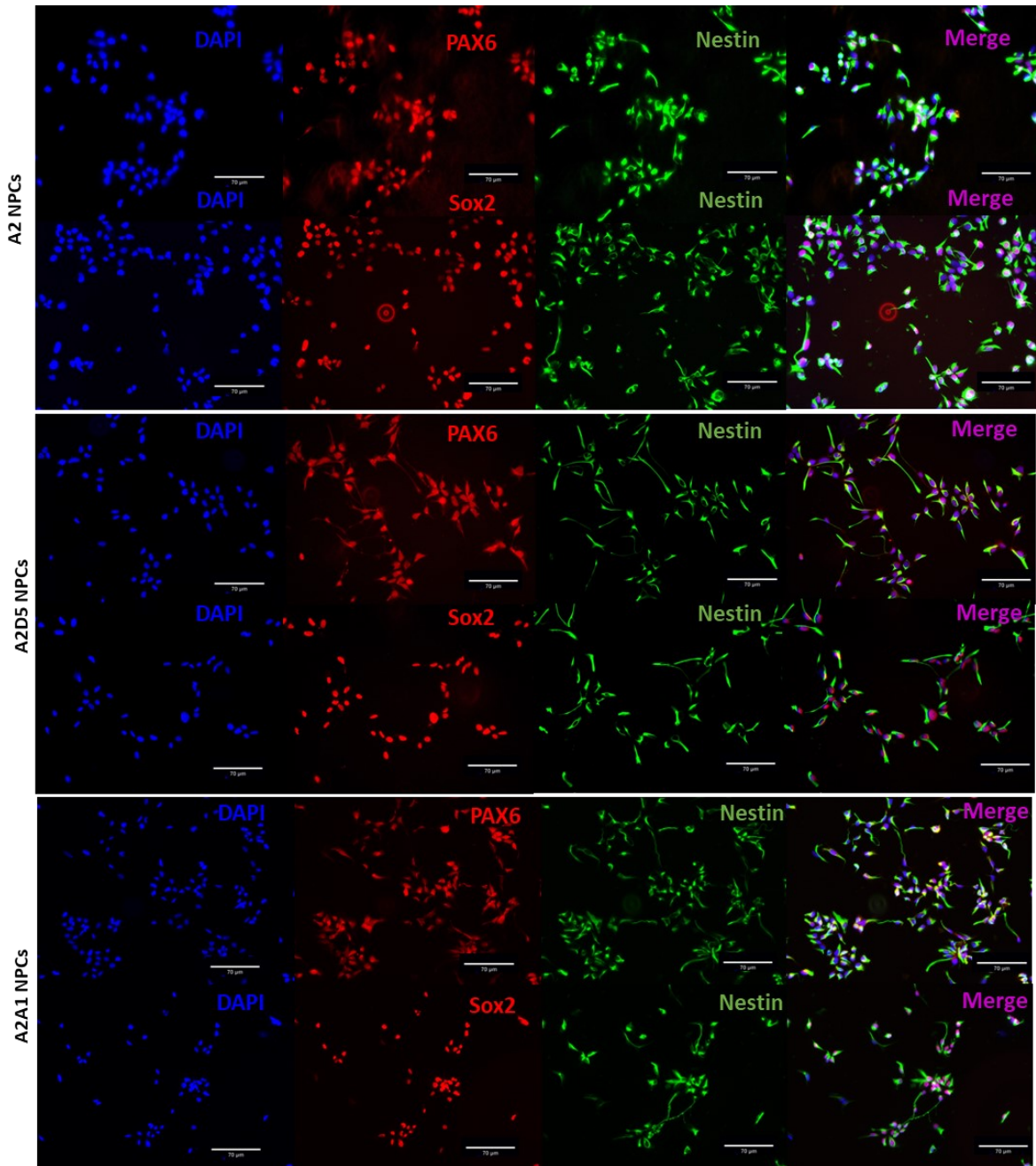


**Fig.23. Immunofluorescent staining of female NPCs.** All cells show protein expression of the neuronal stem cell markers; PAX6, NESTIN and SOX2. Scale bar: 70μM.

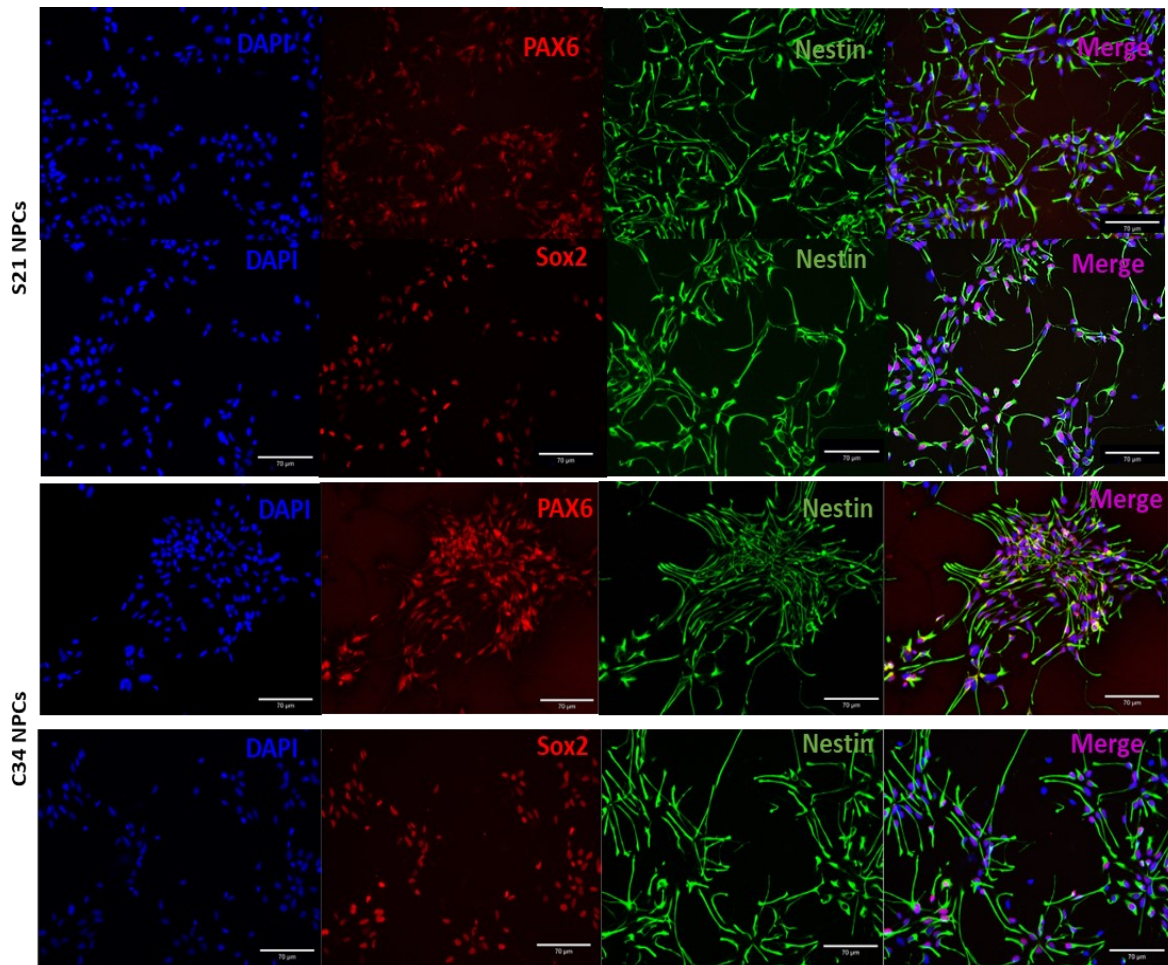


**Fig.24. Immunofluorescent staining of male NPCs.** All cells show protein expression of the neuronal stem cell markers PAX6, NESTIN and SOX2. Scale bar: 70 µM.

## 4.2 Characterization of *POGZ* mutant female iPSCs

Female mutant iPSCs A2D5 and A2A1 were generated from A2 wildtype female iPSCs using CRISPR/Cas9 genome editing. Since the wildtype and CRISPRed cell lines originate from the same iPSC clone, they have the same genetic background (isogenic). It is therefore more likely that any phenotypic differences between mutant and wild-type cells are due to the introduced mutation and not to differences in the (epi)genetic background, which could be individual-specific polymorphisms or (epi)genetic changes introduced by the reprogramming. For the same purpose, the male WHSUS patient iPSCs, C34, underwent CRISPR/Cas9 genome editing to try to correct *POGZ* mutation to have wildtype isogenic control but it was not successful.

### 4.2.1 *POGZ* mRNA expression of WT and edited female iPSCs and NPCs

The frameshift mutations in the A2D5 and A2A1 were expected to cause an early stop codon that might lead to non-sense mediated mRNA decay (NMD). To verify if the mutated mRNAs were subject to NMD, a RT-qPCR was performed and the amount of *POGZ* mRNA

quantified. Three different primer pairs that amplify different regions of *POGZ* mRNA were used with similar results. Both A2D5 and A2A1 iPSC lines surprisingly showed a similar *POGZ* mRNA expression profile relative to A2 iPSCs (Fig.25). Results showed no significant reduction in *POGZ* expression indicating that the mutated *POGZ* transcripts were not cleared by NMD in both A2D5 and A2A1 iPSCs. In the A2D5 and A2A1 NPCs, the mutant *POGZ* transcripts also showed similar *POGZ* expression profiles relative to A2 NPCs with no sign of undergoing NMD (Fig.26). As mentioned in the methods section, all primer pairs used were initially tested for their efficiency.

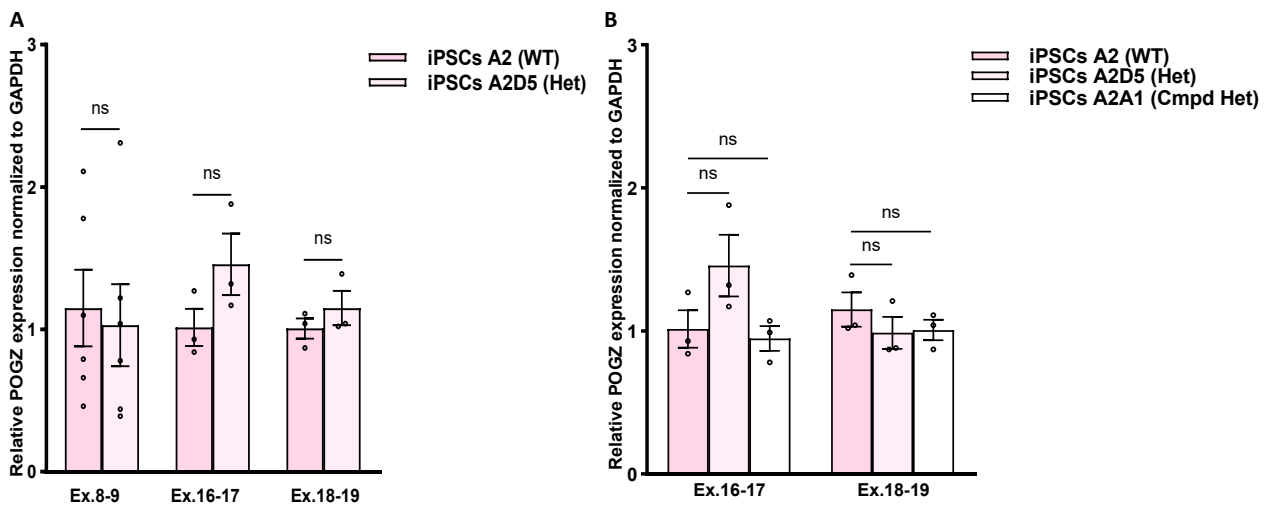


**Fig.25. Expression of *POGZ* mRNA in female iPSCs by RT-qPCR.** A: A2D5 (Het) was compared to A2 (WT) iPSCs using 3 different primer pairs. B: A2D5 (Het) and A2A1(cmpd Het) were compared to A2 (WT) iPSCs using 2 different primer pairs. RT-qPCR analysis showed that mRNA levels do not differ significantly between iPSC lines. *GAPDH* was used for normalization. For all samples n=3; except for Ex.8-9 pair: n=6 (A2); n=5 (A2D5). ns; non-significant, Ex.; Exon, WT; wildtype, Het; heterozygous, cmpd Het; compound heterozygous. Significances were calculated using unpaired t-tests. Values are mean ± SEM.

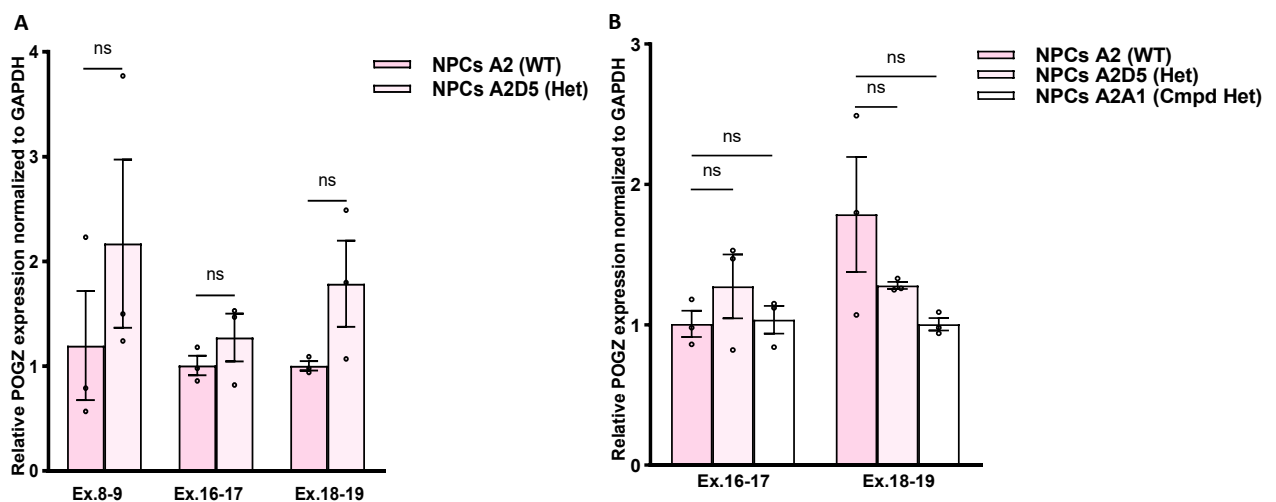


**Fig.26. Expression of *POGZ* mRNA in female NPCs by RT-qPCR.** A: A2D5 (Het) was compared to A2 (WT) NPCs using 3 different primer pairs. B: A2D5 (Het) and A2A1(cmpd Het) were compared to A2 (WT) NPCs using 2 different primer pairs. RT-qPCR analysis showed that mRNA levels do not differ significantly between NPC lines. *GAPDH* was used for normalization. For all samples n=3. ns; non-significant, Ex.; Exon, WT; wildtype, Het; heterozygous, cmpd Het; compound heterozygous. Significances were calculated using unpaired t-tests. Values are mean ± SEM.

#### 4.2.2 Pyrosequencing to identify which allele transcript is expressed in WT and edited female NPCs (QUASEP analysis)

RT-qPCR demonstrated no significant difference in *POGZ* expression between wildtype and mutant NPCs, which may be explained by several mechanisms. One potential explanation is that the mutant allele evaded NMD, leading to comparable expression levels from both the wildtype and mutant alleles. Alternatively, the mutant allele may have undergone downregulation via NMD, with compensatory upregulation of the wildtype allele maintaining overall expression levels.

To detect from which allele the *POGZ* transcripts were expressed in the mutant NPCs, pyrosequencing of the cDNA was performed. In A2D5 NPCs, the mutant allele transcript was expressed in 40.53% while the WT allele transcript in 59.63% which confirms that the mutant mRNA does not undergo NMD. Meanwhile, the A2 NPCs showed as expected 100% expression of WT allele transcript (Fig.27).

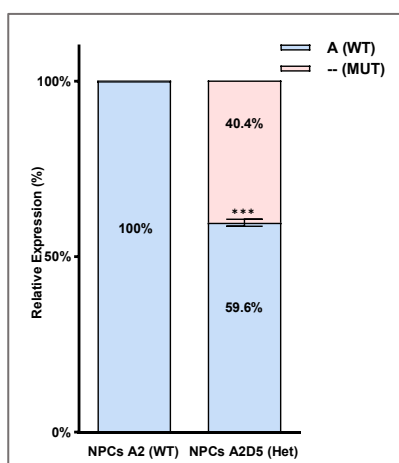


**Fig.27. QUASEP analysis of the mutant allele of *POGZ* in female NPCs.** A QUASEP assay was used to quantify the expression of mutant allele (--) in the NPCs relative to wildtype allele (A) in A2 (WT) and in A2D5 (Het) NPCs. Blue areas mark wildtype allelic expression; Pink areas mark mutant allelic expression; n=5 for all samples. Significances were calculated using paired t-tests \*\*\*P<0.001. Values are mean  $\pm$  SEM.

#### 4.2.3 Protein expression of WT and edited female iPSCs and NPCs

The frameshift mutations in A2D5 and A2A1 iPSCs were expected to cause an early stop codon leading to truncating the protein translation in the first coding exon (p. Phe7SerfsX29 in A2D5 and p. Cys10LeufsX11 and p. Glu9ArgfsX27 in A2A1). To investigate how the mutations affect *POGZ* protein levels, Western Blot experiments were performed with an N-terminal and a C-terminal *POGZ*-specific antibody. The N-terminal antibody (abcam#171934) binds to amino acids 1-562 of human *POGZ* and can detect the wildtype but not N-terminus truncated *POGZ* protein if it is expressed in the mutant NPCs. Meanwhile, the C-terminal antibody (Bethyl#A302-510A) binds to amino acids 1360-1410

of human POGZ, so it can detect both the wildtype and N-terminus truncated POGZ protein if it is present in the mutant NPCs. Using the N-terminal antibody (abcam#171934), wildtype POGZ appeared in A2 iPSCs at 155 kDa and lighter POGZ bands (67%) at the same size in A2D5 iPSCs (Fig.28A). In the NPCs, the N-terminal antibody showed similar results to iPSCs (Fig. 28B). To check if an alternative translation start site initiation might produce a shorter truncated protein lacking the N-terminus, a C-terminal antibody (Bethyl Catalog # A302-510A) was used. In the NPCs including A2A1, the outcome of the C-terminal antibody was comparable to the N-terminal with lighter POGZ bands (24%) in A2D5 at the same size and (11%) in A2A1 at a bit smaller size indicating that it might be POGZ lacking the N-terminal end of the protein (Fig.28C)

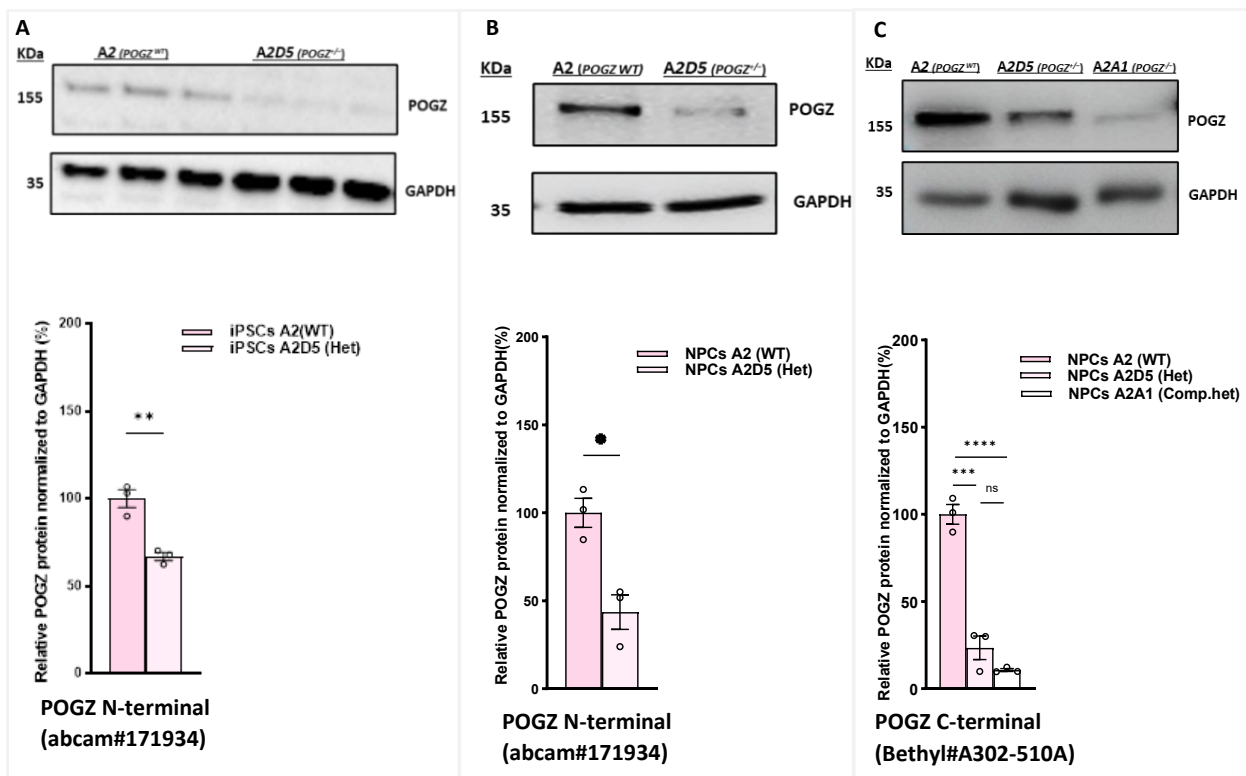


**Fig.28. Western Blot with antibodies detecting the N- or C-terminal part of POGZ in both female iPSCs and NPCs.** A2 iPSCs (A) or NPCs B&C) were used as control GAPDH was used as a loading control. WT; wildtype, Het; heterozygous, compd Het; compound heterozygous. For all samples n=3. Significances were calculated using unpaired t-tests \*P<0.1, \*\*P<0.01, \*\*\*P<0.001, \*\*\*\*P<0.0001. Values are mean  $\pm$  SEM.

#### 4.2.4 Protein localization of WT and edited female iPSCs and NPCs

It has been shown that *POGZ* mutations, particularly those resulting in the loss or truncation of the CENP-DB domain, can disrupt POGZ's nuclear localization[244]. To determine whether the *POGZ* mutation present in A2D5 mutant cells affects the subcellular localization of the protein, immunostaining was conducted using N-terminus antibody(abcam#171934) that binds to amino acids 1-562 of human POGZ protein. While

western blot analysis confirmed reduced POGZ protein expression in *POGZ*<sup>+/-</sup> iPSCs and NPCs relative to wildtype controls, immunocytochemistry revealed clear colocalization of DAPI and POGZ, confirming nuclear localization in both mutant and control iPSCs and NPCs. This suggests that the heterozygous *POGZ* mutation in N-terminus region does not impair the nuclear localization of POGZ (Fig.29), with the wildtype allele primarily contributing to the protein detected by immunocytochemistry. This supports recent findings by Matsumura *et al.* [244] which reported that ASD-associated *de novo* *POGZ* mutations, particularly those that eliminate or truncate the CENP-DB domain, disrupt nuclear localization. This implies that the effect of *POGZ* mutations on its nuclear localization is mutation-specific and may vary depending on the type and precise location of the mutation.

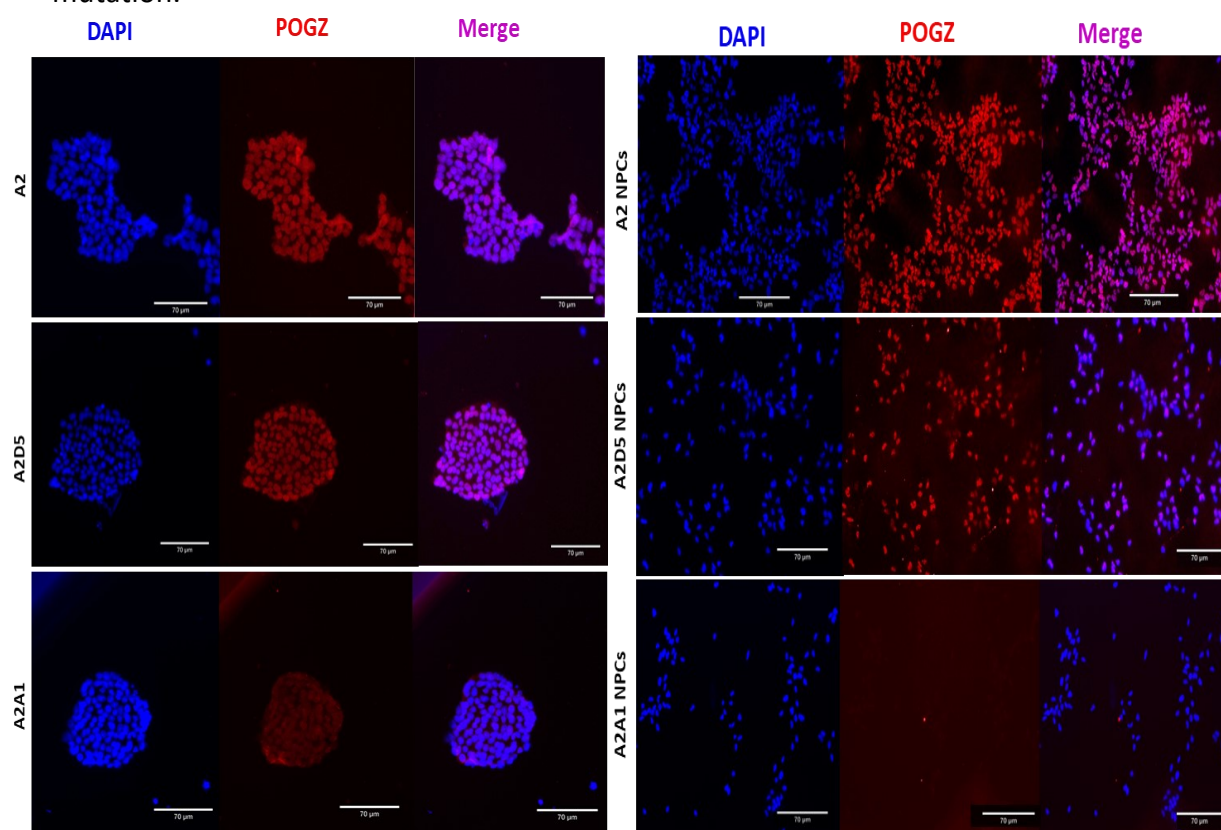


**Fig.29. Subcellular localization of POGZ protein in female iPSCs and NPCs.** POGZ was stained in A2 WT, A2D5 *POGZ*<sup>+/-</sup> and A2A1 *POGZ*<sup>-/-</sup> using N-terminal POGZ antibody (abcam#171934) for iPSCs (Left) and N-terminal POGZ antibody (abcam#ab167408) for NPCs (Right). Scale bar: 70 μM.

### 4.3 Characterization of *POGZ* mutant WHSUS male iPSCs

The male WHSUS patient iPSCs (C34) were generated from reprogrammed fibroblasts isolated from a patient's skin biopsy. Although it would have been preferable to use an isogenic control, S21 male wildtype iPSCs were used as control due to unsuccessful trials to correct the *POGZ* mutation of WHSUS iPSCs.

#### 4.3.1 *POGZ* mRNA expression in WT male and WHSUS male iPSCs and NPCs

The frameshift mutation in the C34 WHSUS male cell line, was expected to cause a frameshift followed by an early stop codon that might lead to non-sense mediated mRNA decay as a surveillance mechanism to get rid of these mutated mRNAs. A RT-qPCR was performed to quantify the amount of *POGZ* mRNA. The same four primer pairs previously used to amplify distinct regions of *POGZ* mRNA in female cells were utilized in this experiment. The C34 iPSCs showed a similar *POGZ* expression level as the S21 WT iPSCs (Fig.30A) suggesting that the mutated *POGZ* mRNA did not undergo NMD in C34 iPSCs. Similar results were obtained with RNA from the NPCs (Fig.30B).

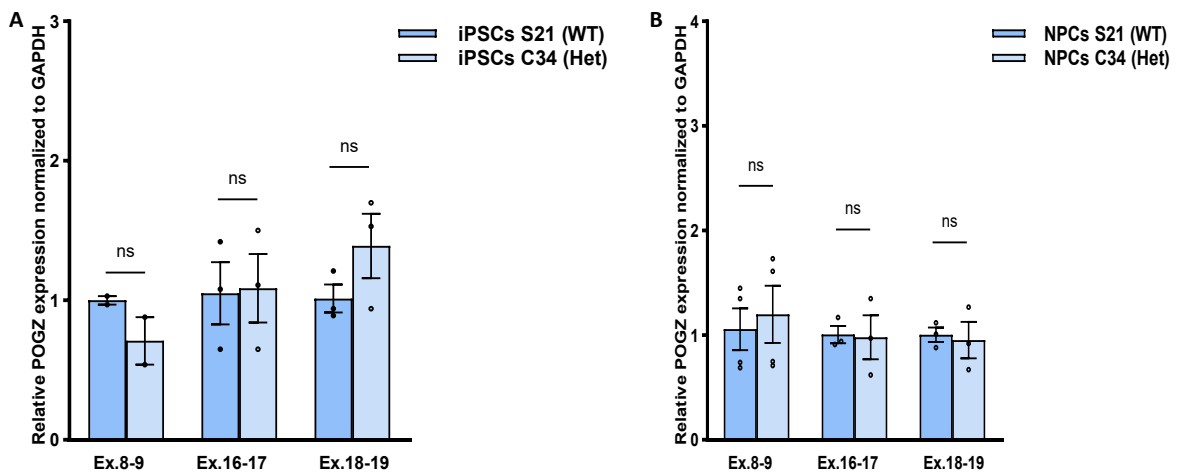


**Fig.30 Expression of *POGZ* mRNA in male iPSCs (A) and NPCs(B) by RT-qPCR.** A: C34 (Het) iPSCs was compared to S21 (WT) iPSCs using 3 different primer pairs. B: C34 (Het) NPCs was compared to S21 (WT) iPSCs using same primer pairs. RT-qPCR analysis showed that mRNA levels do not differ significantly between iPSCs and between NPCs. *GAPDH* was used for normalization. For all samples n=3; except for Ex.8-9 primers in iPSCs: n=2 and in NPCs n=4. ns; non-significant, Ex.; Exon, WT; wildtype, Het; heterozygous. Significances were calculated using unpaired t-tests. Values are mean  $\pm$  SEM.

#### 4.3.2 Pyrosequencing to identify from which allele *POGZ* was expressed in WT male and WHSUS male NPCs (QUASEP analysis)

To detect from which allele, *POGZ* was expressed in the mutant WHSUS male NPCs and if there was any expression compensation by the WT allele, pyrosequencing of cDNA was performed. In C34 WHSUS NPCs, the mutant *POGZ* allele transcript was expressed in 61.33% while the WT allele transcript in 38.67% which indicates that the mutant mRNA was expressed at higher levels than the WT allele and did not undergo NMD. As expected, the S21 NPCs showed 98.44% expression of WT allele transcript (Fig.31).

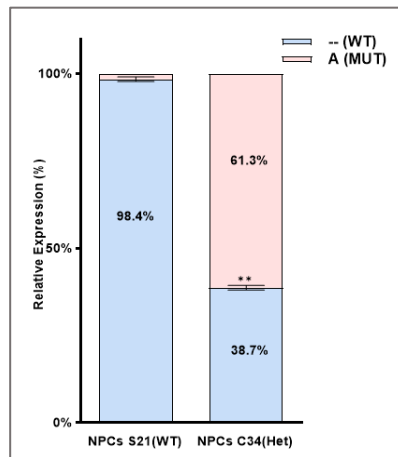


**Fig.31 QUASEP analysis of the mutant allele of *POGZ* in male NPCs.** A QUASEP assay was used to quantify the expression of mutant allele (A) in the NPCs relative to wildtype allele (--) in S21 (WT) and in C34 (Het) NPCs. Blue areas mark wildtype allelic expression; Pink areas mark mutant allelic expression; n=3 for all samples. Significances were calculated using paired t-tests; \*\*P<0.01. Values are mean  $\pm$  SEM.

### 4.3.3 *POGZ* protein expression of WT male and WHSUS male iPSCs and NPCs

As shown in 4.3.1, the mRNA from the mutated C34 allele did not undergo NMD. Therefore, the production of a truncated *POGZ* protein lacking the C-terminal was expected. To investigate how the mutation affects the protein level and if a truncated protein was produced, a Western Blot was performed with three different antibodies specific for *POGZ*. As it was mentioned the N-terminal antibody (abcam#171934), that binds to amino acids 1-562 of human *POGZ*, can detect the wildtype protein but not the N-terminus truncated one. While the C-terminal (Bethyl#A302-510A) antibody that binds to amino acids 1360-1410 of human *POGZ*, can detect wildtype, N-terminus truncated if present but not C-terminus truncated *POGZ* protein. Using the N-terminal antibody (abcam#171934), wildtype *POGZ* appeared in S21 iPSCs at 155 kDa. In the patient C34 iPSCs, this band also appeared, weaker than this in the S21 iPSCs suggesting this band represents full length *POGZ* that is produced from the wildtype allele (Fig.32A). In the NPCs, the N-terminal antibody (abcam#171934) showed significant less full length *POGZ* protein (48.8%) in C34 NPCs compared to S21 NPCs (Fig.32B). When the C-terminal antibody (Bethyl # A302-510A) was used in NPCs, the outcome was comparable to the N-terminal antibody (abcam#171934) with significant less *POGZ* band (33.8%) in C34 compared to S21 NPCs (Fig.32C). To check if there is a shorter truncated protein, another N-terminal antibody (Bethyl # A302-509A) that binds to amino acids 150-200 of human *POGZ* was used. A truncated *POGZ* protein band appeared only in C34 NPCs but not in S21 NPCs at smaller size but it was not quantified (Fig.32D). For the full-length *POGZ* protein,

the N-terminal antibody (Bethyl # A302-509A) produced results consistent with previous antibodies. C34 NPCs exhibited significantly reduced POGZ expression (47.8%) compared to S21 NPCs at the expected size of 155 kDa (Fig.32D). Additionally, a smaller molecular weight band was observed exclusively in C34 NPCs, suggesting that this unique band may represent a truncated POGZ protein lacking its C-terminal region (Fig.32D).

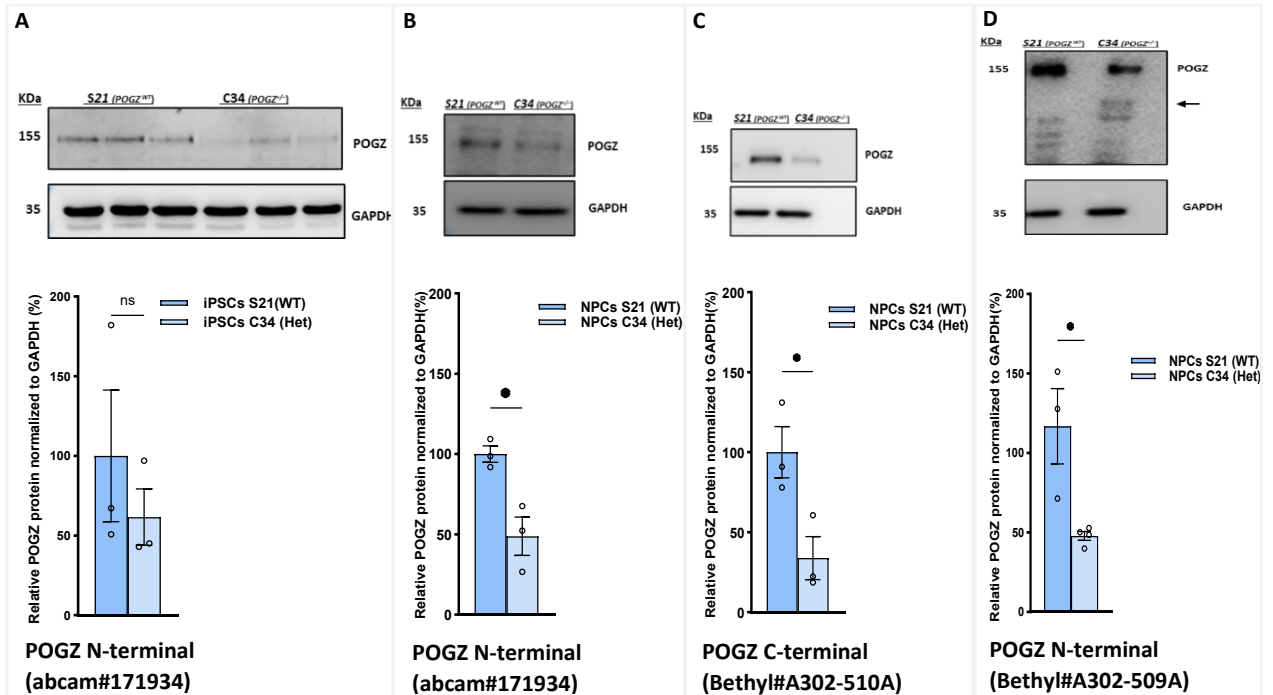


**Fig.32. Western Blot with antibodies detecting the N- or C-terminal part of POGZ in both male iPSCs and NPCs.** S21 iPSCs (A) or NPCs B, C&D) were used as control. GAPDH was used as a loading control. In (D) an arrow marks a truncated POGZ protein band in C34 (Het) NPCs (not quantified). WT; wildtype, Het; heterozygous. For all samples n=3. Significances were calculated using unpaired t-tests; \*P<0.1. Values are mean ± SEM.

#### 4.3.4 Protein localization of in WT male and WHSUS male iPSCs and NPCs

As it was mentioned that C34 cells carry a *POGZ*<sup>+/-</sup> mutation in the HPZ domain that leads to the truncation of the protein at amino acid 842 located in exon 19 affecting CENP-DB domain (Fig.3). As previously discussed, *POGZ* mutations that result in the elimination or truncation of the CENP-DB domain have been reported to impair nuclear localization[244], it was important to assess whether the *POGZ* mutation in WHSUS C34 mutant cells affects its subcellular localization. An immunostaining was performed using the N-terminus antibody (abcam #171934), which specifically binds to amino acids 1-562 of the human POGZ protein to detect both the wildtype and C-terminus truncated protein.

Despite western blot analysis confirming reduced POGZ protein levels in *POGZ*<sup>+/-</sup> WHSUS iPSCs and NPCs compared to wildtype controls, the immunocytochemical staining revealed colocalization of DAPI and POGZ in the nucleus of both mutant and control cells. This

suggests that the heterozygous *POGZ* mutation in HPZ domain does not disrupt the nuclear localization of the POGZ protein (Fig.33). This again supports that the impact of *POGZ* mutations on subcellular localization may vary depending on the specific type and position of the mutation.

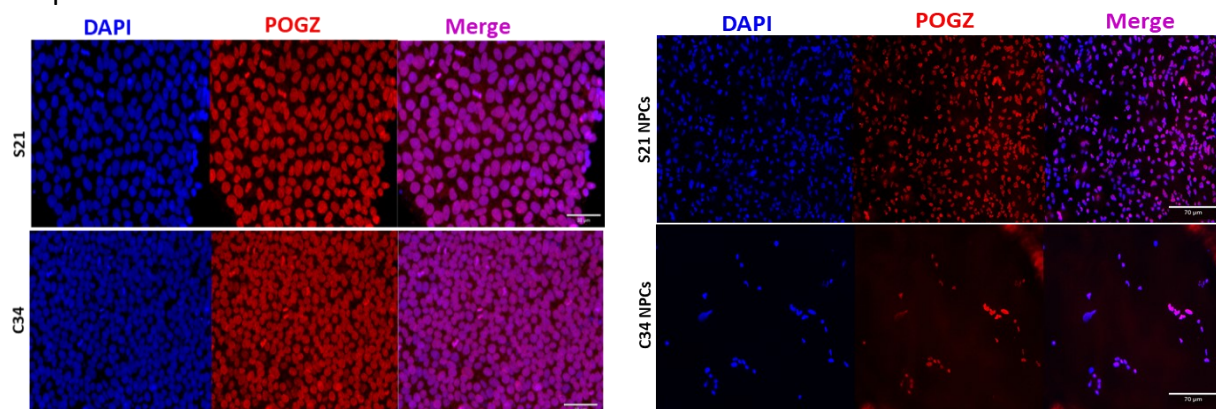


**Fig.33. Subcellular localization of POGZ protein in male iPSCs and NPCs.** POGZ was stained in S21 (WT) and C34 (*POGZ*<sup>+/-</sup>) using N-terminal POGZ antibody (abcam#171934) for iPSCs (Left) (Scale bar: 30  $\mu$ M) and N-terminal POGZ antibody (abcam#ab167408) for NPCs (Right) (Scale bar: 70  $\mu$ M).

#### 4.4 Functional analyses of *POGZ* Wildtype and mutant iPSCs and iPSC-derived NPCs

##### 4.4.1 Effect of *POGZ*<sup>+/-</sup> on cell proliferation & differentiation in 2D culture

###### 4.4.1.1 Expression of proliferation & differentiation markers

To check the effect of heterozygous *POGZ* in N-terminus and in HPZ domain on the proliferation and differentiation status of the mutant female and male NPCs, expression of proliferation and differentiation markers was measured in NPCs in undifferentiating conditions. A2D5 mutant NPCs showed a tendency of higher expression of *DCX* markers (p-value= 0.123) for immature neurons compared to A2 WT NPCs (Fig.34A). The p-value of *DCX* expression, indicated a trend toward significance, though it did not reach the conventional threshold. The mature neurons marker (*MAP2*) (p-value= 0.628) and the proliferation marker *CCDN2* (p-value= 0.316) were not differentially expressed between A2D5 and A2 NPCs (Fig.34A). In the male NPCs, this higher expression tendency of *DCX* (p-value= 0.357) was less in the C34 mutant NPCs compared to S21 WT (Fig.34B). Higher *MAP2* expression (p-value= 0.167) in C34 NPCs indicated a trend toward significance. Oppositely to female NPCs, C34 mutant NPCs showed a significant decrease in *CCDN2* expression (p-value= 0.009) compared to S21 WT (Fig.34B).

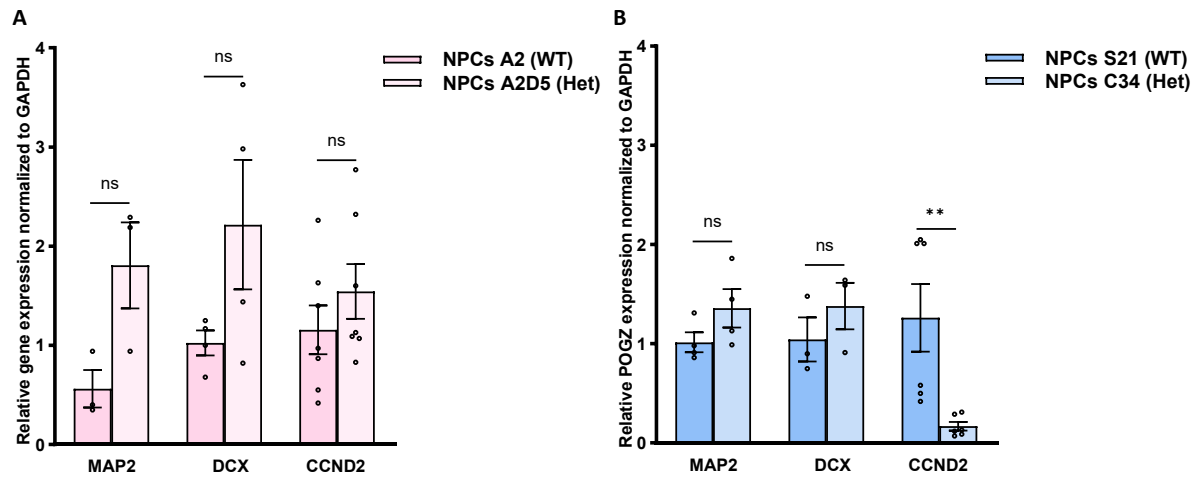


**Fig.34. Expression of proliferation & differentiation markers mRNA in female (A) and male (B) NPCs by RT-qPCR.** A: A2D5 (Het) was compared to A2 (WT) NPCs; showing a trend of significance of *DCX* expression (n=4; p-value= 0.123), and insignificant expression change of *MAP2*(n=3) & *CCND2* (n=6) relative to A2. B: C34 (Het) was compared to S21 (WT) NPCs; showing a significant decrease in *CCND2* expression (n=6; p-value= 0.009), a trend of significance of *MAP2* expression of (n=4, p-value= 0.167), and insignificant expression change of *DCX* (n=3) relative to S21. *GAPDH* was used for normalization; ns; non-significant, WT; wildtype, Het; heterozygous. Significances were calculated using unpaired t-tests; \*\*P<0.01. Values are mean  $\pm$  SEM.

#### 4.4.1.2 Click iT EdU assay:

To assess the effects of the *POGZ* mutations on the cell's ability to proliferate, Click iT-Edu assay was performed. This assay is an efficient method for measuring DNA synthesis and cell proliferation. It uses EdU, a thymidine analog, which is incorporated into DNA during the active DNA synthesis S-phase of the cell cycle. The incorporated EdU is subsequently detected through a copper-catalyzed click reaction between alkyne group in EdU and an azide conjugated to a fluorescent dye. Flow cytometry is then used to quantify the percentage of proliferating cells. The experiment was done following Click-iT™ EdU Cell Proliferation Imaging Kit, Alexa Fluor™ 488 protocol followed by measuring the cells in S-phase of cell cycle by flow cytometry. Compared to the respective wildtype controls, the mutant NPC lines, female A2D5 and male C34 did not show any significant differences in EdU incorporation across S-phase (Fig. 35 A-B) (p-values=0.541 and 0.223 respectively) or any of the other cell cycle phases (for G2-phase; p-values=0.835 and 0.591 and for G1-phase; p-values=0.177 and 0.150 respectively (Fig. 35 A-B) .

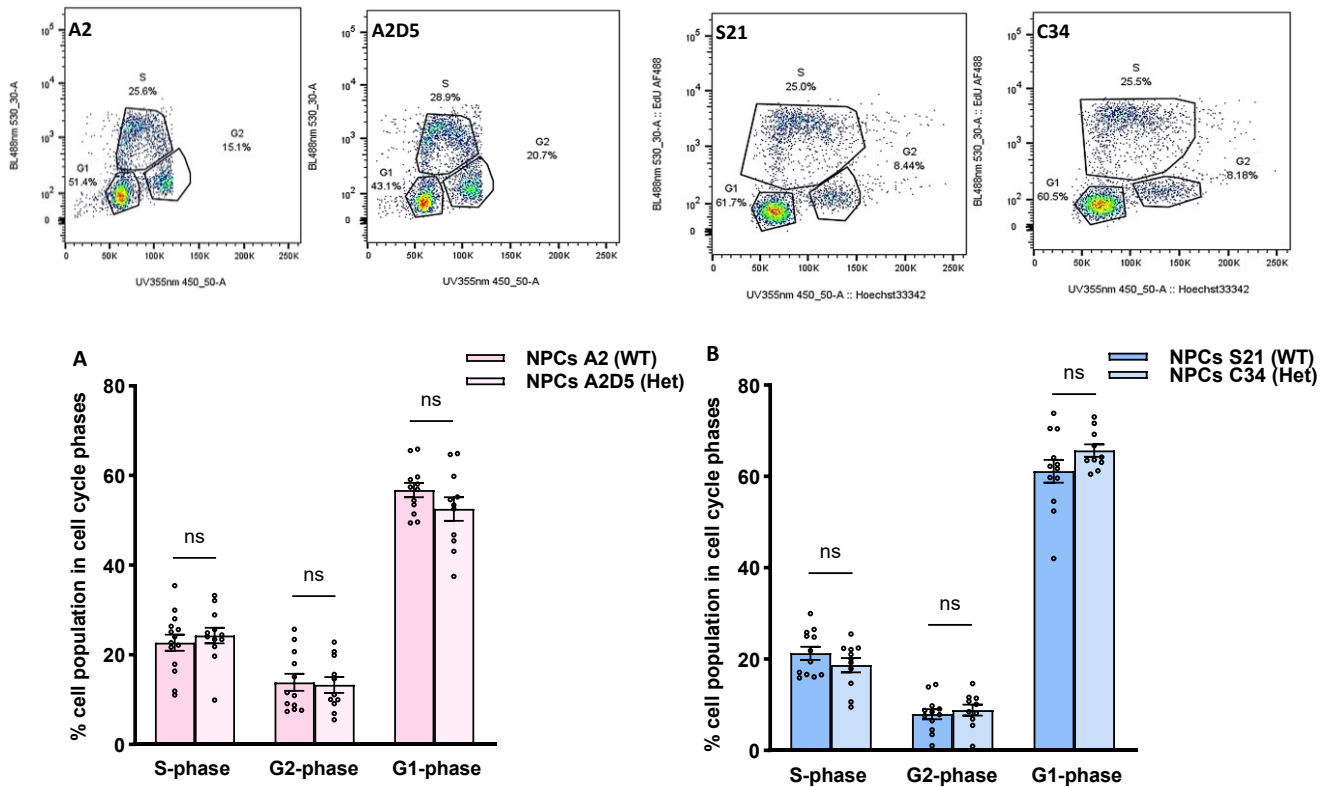


**Fig.35. Click IT EdU assay in female and male NPCs by flowcytometry.** Upper panel: biparametric dot plots of A2, A2D5, S21 and C34 NPCs showing phases of cell cycle. Lower panel: Quantification of % cell population in different cell cycle phases in female (A) and male (B) NPCs shows mutant NPC lines, female A2D5 and male C34 did not show any significant differences in EdU incorporation across S-phase or any of other cell cycle phases; A2(WT) (S-phase: n=14; G2- & G1-phase: n=12), A2D5(Het) (S-phase: n=12; G2- & G1-phase: n=11), S21(WT) (S- & G2- & G1-phase: n=12), C34(Het) (S-phase: n=11; G2 & G1-phase: n=10). ns, non-significant, WT; wildtype, Het; heterozygous. Significances were calculated using unpaired t-tests. Values are mean  $\pm$  SEM.

#### 4.4.1.3 Neuronal differentiation assay of NPCs derived from iPSC lines

To investigate potential differentiation defects in the NPCs carrying heterozygous *POGZ* mutations, neuronal differentiation assays were carried out. In these assays, NPCs were induced to differentiate into neurons for 2 days, and the proportion of MAP2-positive (MAP2+) neurons was assessed using immunostaining with a MAP2 antibody, which marks mature neurons. Results showed that in this early-stage of neuronal differentiation, female A2D5 mutant NPCs showed a significantly higher number of MAP2+ cells ( $p$ -value=0.0354) compared to its A2 control. This suggests an accelerated or enhanced differentiation process. However, this increase in the MAP2+ cells observed in the female mutant was absent in the WHSUS C34 male NPCs ( $p$ -value=0.620) when compared to the S21 control. These results suggest that the functional consequences of *POGZ* mutations on neuronal differentiation may depend on the location of mutation and which domain got affected and hence influencing neural cell behavior (Fig.36).

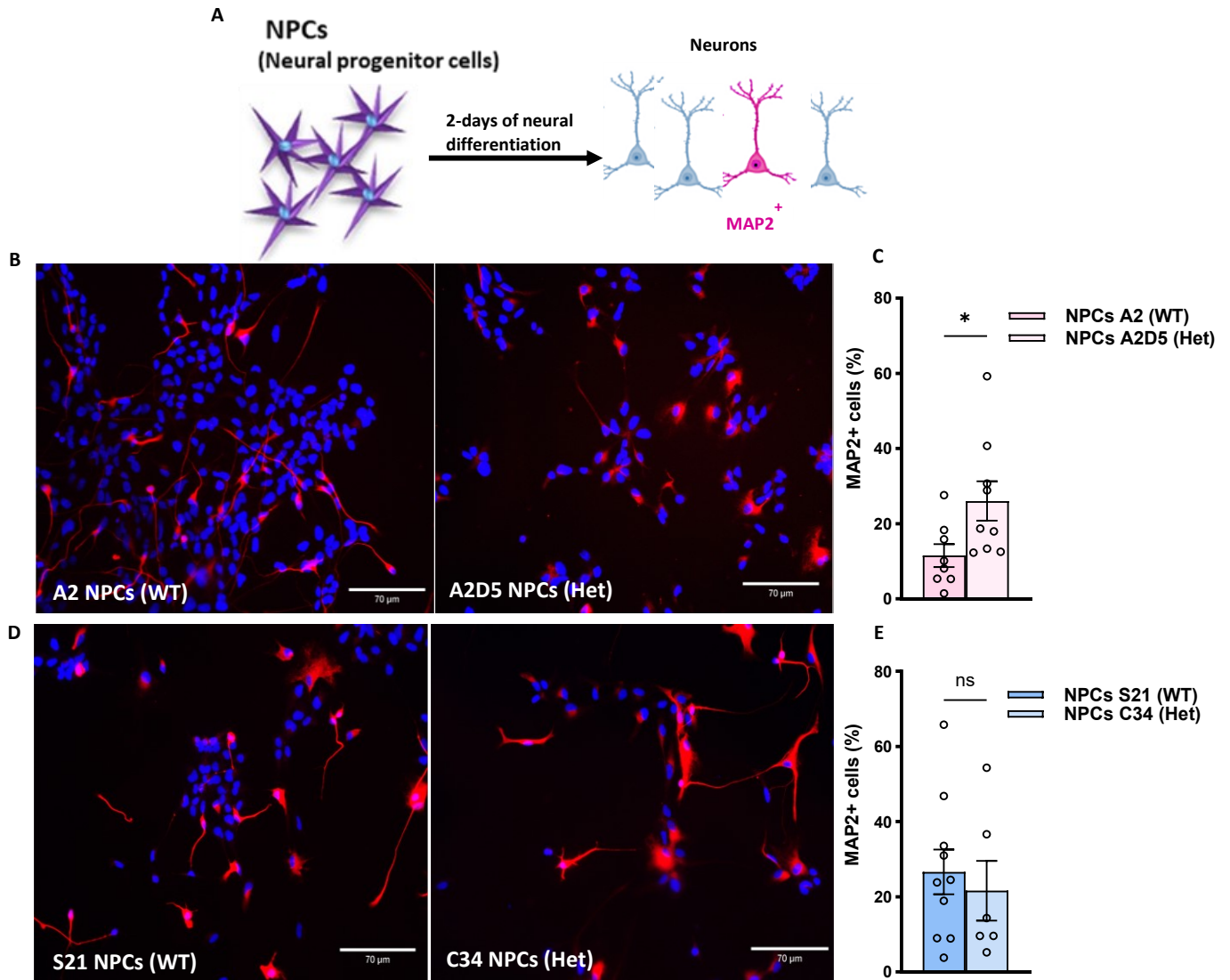


**Fig.36 Neural differentiation assay to analyze population of MAP2+ cells.** A: a graph shows that NPCs induced to differentiate into neurons for 2 days expressing MAP2. B & D: Immunostaining of nucleus with DAPI and MAP2 in female (B) and male (D) NPCs; scale bar: 70  $\mu$ M. C&E: quantification of MAP2+ neurons in female A2D5 (n= 9) compared to A2 (n= 8) NPCs (C) and in male C34 (n= 6) compared to S21 (n= 10) NPCs (E) after two days of neural differentiation. Map2+ neurons were quantified in terms of % of % positive area/total DAPI+ area. 4 biological replicates were used, 3 coverslips per cell line per each replicate were quantified; n= a coverslip. ns; non-significant, WT; wildtype, Het; heterozygous. Significances were calculated using unpaired t-tests; \*= P < 0.01. Values are mean  $\pm$  SEM.

#### 4.4.1.4 Investigation of proliferation, DNA damage and apoptosis markers in NPCs

POGZ has been identified as a key player in DNA double-strand breaks (DSBs) repair, functioning through an HP1-dependent mechanism [136]. Moreover, POGZ is needed for formation of the kinetochore and spindle assembly checkpoints (SAC) during mitosis (M) [113] and hence *POGZ* mutations may disrupt cell proliferation and induce apoptosis [116, 134, 135]. To assess these potential effects, flow cytometry was employed to analyze key cellular markers including PHH3 (a mitotic marker), Ki67 (a proliferation marker),  $\gamma$  H2AX (a marker for DNA DSBs) and Cas3 (a marker for apoptosis) in both the mutated and

wildtype NPCs. Surprisingly, the data revealed no significant differences in the expression of these markers between A2D5 mutant NPCs and their wildtype A2 control ( $p$ -values=0.132,0.522,0.993 and 0.146 for ki67, PHH3,  $\gamma$  H2AX and Cas3 respectively), as well as between the C34 mutant NPCs and wildtype S21 controls ( $p$ -values=0.259,0.715,0.814 and 0.649 for ki67, PHH3,  $\gamma$  H2AX and Cas3 respectively). These results suggest that *POGZ* mutations may not significantly impact mitotic progression or apoptotic pathways in these specific NPC lines, or that compensatory mechanisms may mitigate the potential impact of these mutations (Fig.37).

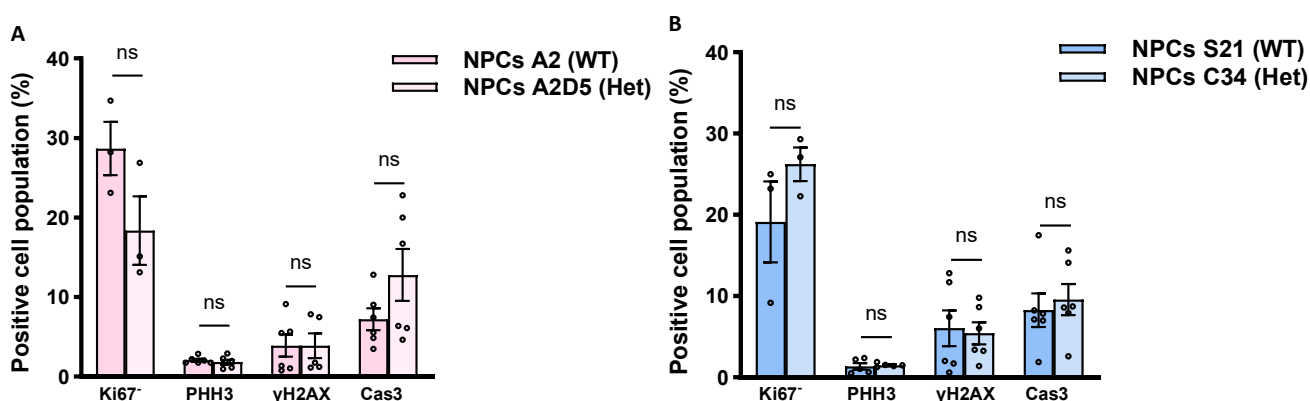


**Fig.37. Assay of proliferation and apoptosis in female and male NPCs by flowcytometry.** Immunostaining of proliferation markers; Ki67; PHH3, DNA DSBs marker;  $\gamma$  H2AX and apoptosis marker; Cas3, and quantification of positive population of cells were measured via flow cytometry in female A2D5 (Het) compared to A2 (WT) NPCs and in male C34 mutant NPCs compared to S21. For all samples;  $n=6$  except for Ki67;  $n=3$  and only in male NPCs, for PHH3;  $n=5$ . WT, wildtype; Het, heterozygous. ns; nonsignificant. Significances were calculated using unpaired t-tests. Values are mean  $\pm$  SEM.

#### 4.4.2 Effect of *POGZ*<sup>+/-</sup> on proliferation & differentiation in 3D culture

To investigate the effect of heterozygous *POGZ* mutations on the proliferation, neurogenesis and neuronal migration within a more physiologically relevant spatial cellular context, 3D models, including neurospheres and cerebral organoids were generated from the *POGZ*<sup>+/-</sup> mutant cell lines and the corresponding controls. This approach allows for a more comprehensive assessment of how these mutations affect neural development compared to traditional 2D cultures, reflecting the complex interactions and microenvironment present in vivo.

##### 4.4.2.1 Neurospheres

Neurospheres were generated from *POGZ*<sup>+/-</sup> mutant NPCs and the corresponding controls to investigate whether the observed increase in the neuronal differentiation in *POGZ*<sup>+/-</sup> mutant female A2D5 NPCs might result from enhanced NPCs proliferation, providing a larger pool of cells for differentiation which was not observed in any of the 2D

proliferation experiments, or from an accelerated process of neuronal differentiation itself.

First, the morphology and structure of neurospheres were checked using inverted microscope, then the immunofluorescence staining was performed on floating neurospheres to assess their structure and confirm proper cells composition of neurospheres (Fig.38). The staining revealed that the neurospheres exhibited a grape cluster-like morphology when viewed through a Revolve fluorescent microscope (Fig.38). NESTIN-positive cells were localized both at the periphery and within the sphere (Fig.38), indicating active neurogenic potential. Additionally, SOX2-positive cells were also present at similar locations within the sphere (Fig.38). The merged image demonstrated the presence of NESTIN and SOX2 double-positive cells (Fig.38). suggesting the NPCs formed neurospheres that still retain the potential to differentiate into neurons and glial cells while still retaining their progenitor characteristics. After characterizing the structure of the neurospheres, proliferation and migration assays were conducted to better understand *POGZ*<sup>+/-</sup> effect on cell proliferation and differentiation.

#### 4.4.2.1.1 Neurospheres proliferation assay

Neurospheres were cultured for 5 days into a 96-well V-bottom plate in NMM media (12000 cells in 150  $\mu$ l per well) and incubated at 37°C with 5% CO<sub>2</sub> in a humidified environment, with medium change every other day. On the fifth day, neurospheres were visualized and imaged using an inverted microscope, in order to measure their diameters, which reflect the proliferation capacity of the NPCs (Fig.39 A&C). Notably, the neurospheres generated from *POGZ*<sup>+/-</sup> A2D5 female and male C34 NPCs, were significantly smaller (p-value <0.0001 for both) compared to those from corresponding control lines, A2 and S21 respectively (Fig.39B&D). These results align with the low expression of the proliferation marker *CCND2* observed in male C34 NPCs (Fig.34B), indicating that *POGZ*<sup>+/-</sup> mutation impairs the self-renewal activity in neurospheres derived from *POGZ*<sup>+/-</sup> NPCs. However, it is important to note that these results contrast with the findings from the 2D proliferation assays conducted on the mutant NPCs.

#### 4.4.2.1.2 Neurospheres migration assay

Neurospheres were cultured under same conditions as for the previous proliferation assay but only for 3 days. On the third day, neurospheres were transplanted using cut 1mL tip and plated into neuronal differentiation medium (Neurobasal+) on into poly-

Ornithine/Laminin-coated 6-well plates (5-6 neurospheres per well) and kept for two days at 37°C with 8% CO<sub>2</sub> in a humidified environment. These adherent culture conditions should induce spontaneous radial migration of NPCs outward from the neurospheres (Fig.40A). On the second day of neuronal differentiation, neurospheres were imaged using an inverted microscope, and NPCs migration was evaluated by measuring the average distance from the edge of the neurosphere to the nucleus of the most distant cells in all directions using FIJI software (Fig.40B&D).

This *in-vitro* migration assay showed that the radial migration of young neurons was significantly enhanced in the *POGZ*<sup>+/-</sup> NPC-generated neurospheres, A2D5 and C34, (p-value <0.0001 for both) compared to the corresponding controls A2 and S21 respectively (Fig.40C&E). These findings, consistent with the increased neuronal differentiation seen in A2D5 and in C34 NPCs —reflected in the higher number of MAP2+ neurons in A2D5 NPCs and a trend toward increased *MAP2* expression in A2D5, increased *DCX* expression in C34 mutant NPCs (Fig.34 A-B)—suggest that neuronal migration is also accelerated in *POGZ*<sup>+/-</sup> NPC-generated neurospheres.

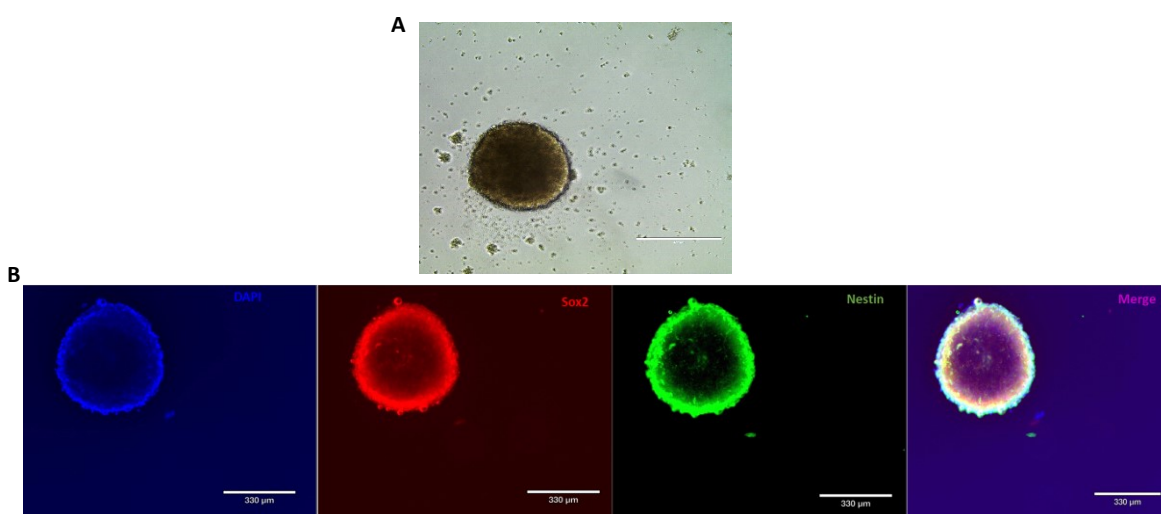


**Fig.38. Morphology and immunofluorescence staining of A2D5 neurosphere after 5 days in culture.** A. White light picture of the neurosphere shows Floating grape cluster-like neurosphere; Scale bar: 400  $\mu$ M and B. after immunofluorescence staining. SOX2 -positive cells (red) are localized at the edge of and inside the sphere. NESTIN-positive cells (green) are also present at the edge of and inside the sphere. The merged image shows NESTIN and SOX2 double-positive cells (yellow). The nuclei are counterstained with DAPI (blue); Scalebar: 330 $\mu$ m.

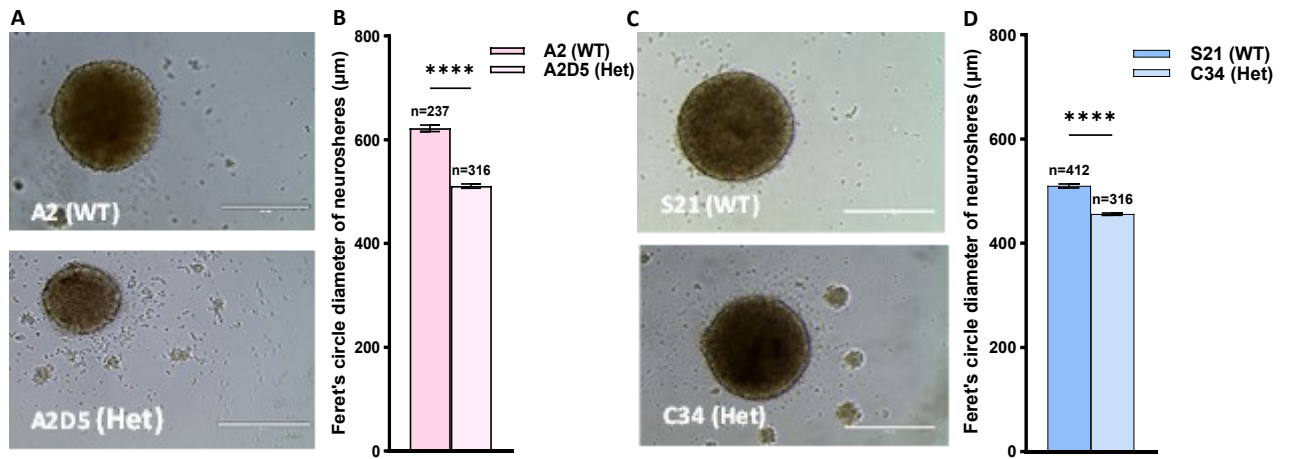


**Fig.39. Proliferation assay for 5- days old neurospheres of female (A) and male (C) NPCs.** B&D: Average diameter of A2 and S21 neurospheres was significantly longer compared to A2D5 and C34 neurospheres respectively. WT, wildtype; Het, heterozygous. Significances were calculated using unpaired t-tests; \*\*\*\*= $P < 0.0001$ . Values are mean  $\pm$  SEM. Scalebar: 400  $\mu$ m.

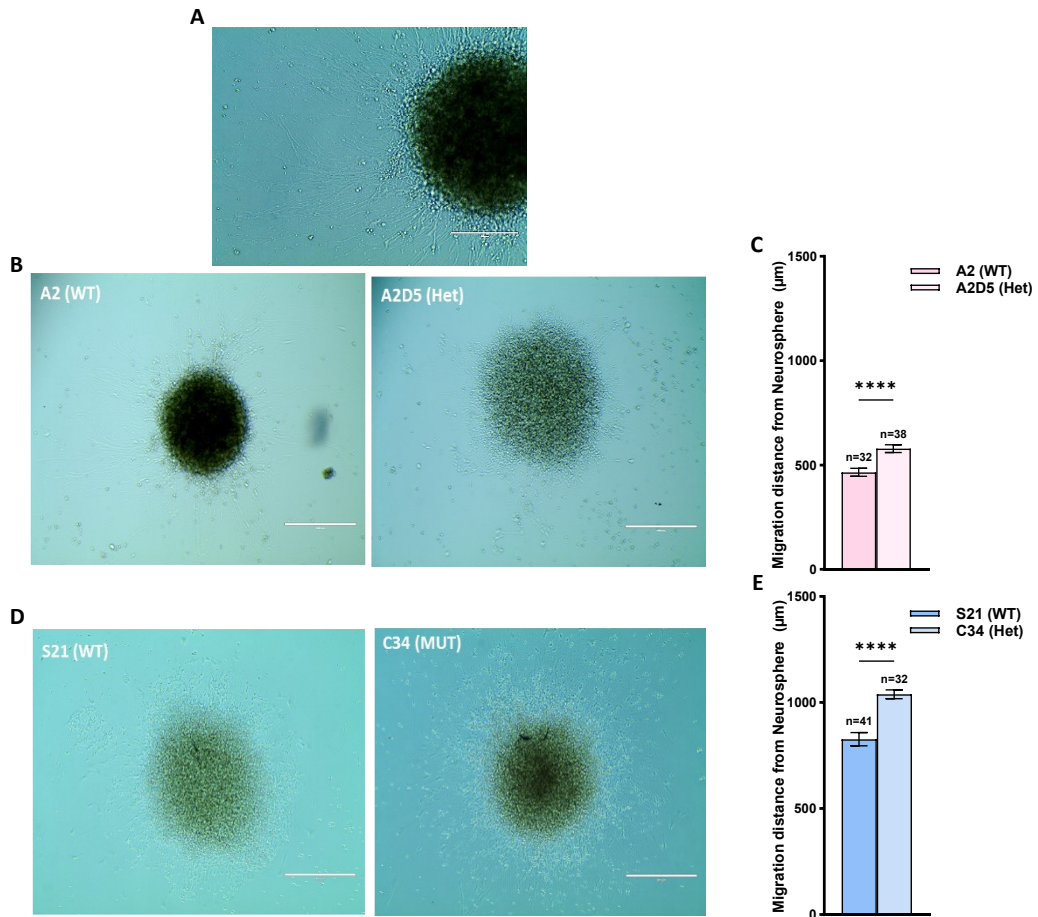


**Fig.40. Migration assay for 3- days old neurospheres after 2 days of neural induction (A).** B&D: Radial migration of the A2 and A2D5 (B), S21 and C34 (D) neurons migrating outward after 2 days of plating 3-days old Neurospheres into neuronal differentiation medium. C&E: Quantification of the migration distance of the migrating neurons in A2 and A2D5(C), S21 and C34 (E) neurospheres. WT, wildtype; Het, heterozygous. Significances were calculated using unpaired t-tests; \*\*\*\*= $P < 0.0001$ . Values are mean  $\pm$  SEM. Scalebar: 200  $\mu$ m- 400  $\mu$ m.

#### 4.4.2.2 Brain organoids

Brain organoids provide a more comprehensive model for studying complex neurodevelopmental processes, including neuronal migration, synaptogenesis and cortical layer formation [245]. These systems enable the examination of later developmental stages and are valuable for investigating NDDs. They have been used to model different NDDs such as a microcephaly associated with ID [246] and Seckel syndrome [246] highlighting organoids' utility for modeling patient-specific phenotypes.

In this project, brain organoids were generated for 30 days, according to an established in-house method provided from collaborators in Erlangen (Prof. Dr. Marisa Karow group), based on the original protocol published by Lancaster [168], providing a more physiological environment than the 2D culture. During culturing organoids, ventricle zone-like structures (VZLS) populated with NPCs and mature neurons were formed (Fig.41A), enabling the exploration of how *POGZ* mutations alter these structures and impact neuronal organization and maturation. By using markers such as MAP2 to track neural maturation (Fig.41C), these models can help investigating the maturation efficiency of neurons and how *POGZ* mutations influence neural development over time.

The analysis of the organoids was done in terms of how many ventricles formed (Fig.41A). and how big the area of those ventricles relative to the whole organoid area (Fig.41B). where those can be correlated to proliferation and differentiation of NPCs within the organoids. This can show how *POGZ* regulates the neuronal development and the cellular composition and cytoarchitectures of brain organoids in vitro.

Brain organoids from the female A2 (WT) and A2D5 (*POGZ*<sup>+/-</sup>) iPSCs and also from the male S21 (WT) and C34 (*POGZ*<sup>+/-</sup>) patient iPSCs were generated (Fig.41D). While several batches of organoids were produced, only one batch of female organoids was analyzed in this study. To obtain more conclusive results, it is essential to analyze the remaining batches.

##### 4.4.2.2.1 Organoids of the female cell lines (A2 and A2D5 lines)

A single batch of female brain organoids, A2 and A2D5, was analyzed after 30 days in culture. For this analysis, the organoids were fixed, cryosectioned, and stained with DAPI (Fig.41A). The number of ventricles formed and the relative area of these ventricles compared to the total organoid area were measured (Fig.41B). A2D5 organoids exhibited a significantly smaller ventricular area compared to control organoids A2 (Fig.42B). while the number of ventricles remained unchanged (Fig.42A). These findings that the *POGZ*

mutation in A2D5 organoids may affect the structural development of the VZLS. This could suggest a role for POGZ in maintaining the cellular composition or proliferation within the VZLS. To validate these results, further studies with additional batches and extended time points are recommended, which could help clarify the specific mechanisms through which POGZ affects neural development.

To investigate the cellular composition of the VZLS, the organoid sections were stained for the NPC marker SOX2 and the neuronal marker MAP2 (Fig.41C). Analysis of the SOX2+ area (ventricular area) relative to the total neural area (SOX2+ area + MAP2+ area) revealed that A2D5 organoids had a nearly significant reduction in the SOX2+ area ( $p=0.058$ ) compared to organoids derived from A2 WT iPSCs (Fig.42C). This suggests a smaller SOX2+ cell population that might be due to impaired proliferation capacity as it was observed in neurospheres in terms of their diameters. Of noticed, that these results differ from the findings obtained from the 2D proliferation assays performed on the mutant NPCs. Conversely, measuring the MAP2+ area relative to the total neural area indicated that A2D5 organoids had a nearly significant increase in the MAP2+ area ( $p=0.058$ ) compared to A2 WT organoids (Fig.42D), suggesting an increased MAP2+ cell population that could indicate more differentiation. This finding along with the smaller SOX2+ cell population suggested that this increased MAP2+ cell population is due to accelerated process of NPCs differentiation and not due to NPCs proliferation (smaller NPCs pool).

In addition, other organoids from the same batch were treated with neural tissue dissociation kit at day 30 into single-cell suspensions. The dissociated cells were plated and cultured in neural differentiation media. After 24 hr, the dissociated cells were fixed and immunostained for MAP2 (Fig.41E). The purpose of using this kit was to break down the complex 3D structure into single-cell suspensions, allowing for a detailed analysis of individual cell populations within the organoid. Staining for MAP2 in these dissociated cells enabled the identification and quantification of mature neurons, providing insights into the extent of neuronal differentiation and maturation within the organoid model. This approach helps assess the impact of *POGZ*<sup>+/-</sup> mutation on neuronal development in organoids.

The dissociated cells of A2D5 (*POGZ*<sup>+/-</sup>) organoids exhibited a significantly elevated number of MAP2+ neurons relative to those obtained from A2 (WT) organoids (Fig.42E).

This observation corroborates findings from the 2D neuronal differentiation assays, which revealed that female A2D5 mutant NPCs presented a significantly greater number of MAP2+ cells in comparison to A2 controls during the early stages of neuronal differentiation. These results imply an accelerated or enhanced differentiation process in the A2D5 mutant cells.

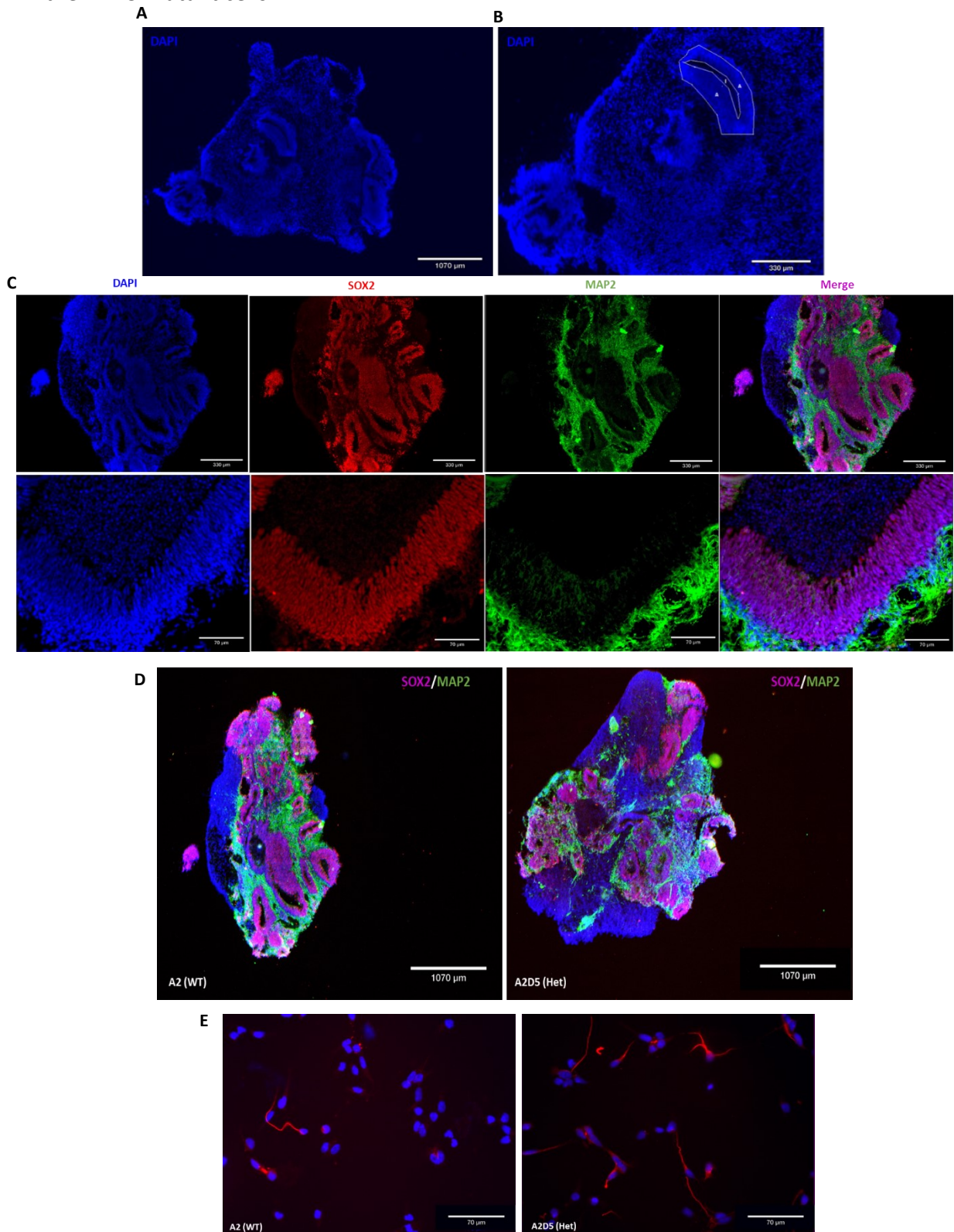


**Fig.41. Overview of female line A2 (WT) and A2D5 (*POGZ*<sup>-/-</sup>) cerebral organoids after 30 days in culture.** A. Representative cryostat cross sections of cerebral organoids generated from A2(WT) and stained with DAPI showing ventricle zone like structures (VZLS); Scale bar: 1070  $\mu$ m. B. Analysis of area of the ventricles= Difference of total area of ventricle (A) and internal area of ventricle (I); Scale bar: 330  $\mu$ m. C. Immunofluorescence staining of 30-day old cerebral organoid; SOX2 -positive cells (red) are localized at the inside layer of VZLS. MAP2-positive cells (green) are present at the edge/outside of the VZLS; Scalebar: 70-330 $\mu$ m. D. Immunofluorescence staining of female line A2 (WT) and A2D5 (*POGZ*<sup>-/-</sup>) 30-day-old cerebral organoids; Scale bar: 1070  $\mu$ m. E. Immunostaining of nucleus with DAPI and MAP2 of dissociated cells, of female line A2 (WT) and A2D5 (*POGZ*<sup>-/-</sup>) 30-day-old cerebral organoids, 24hr after plated and cultured in neural differentiation media, scale bar: 70  $\mu$ m. WT, wildtype; Het, heterozygous.

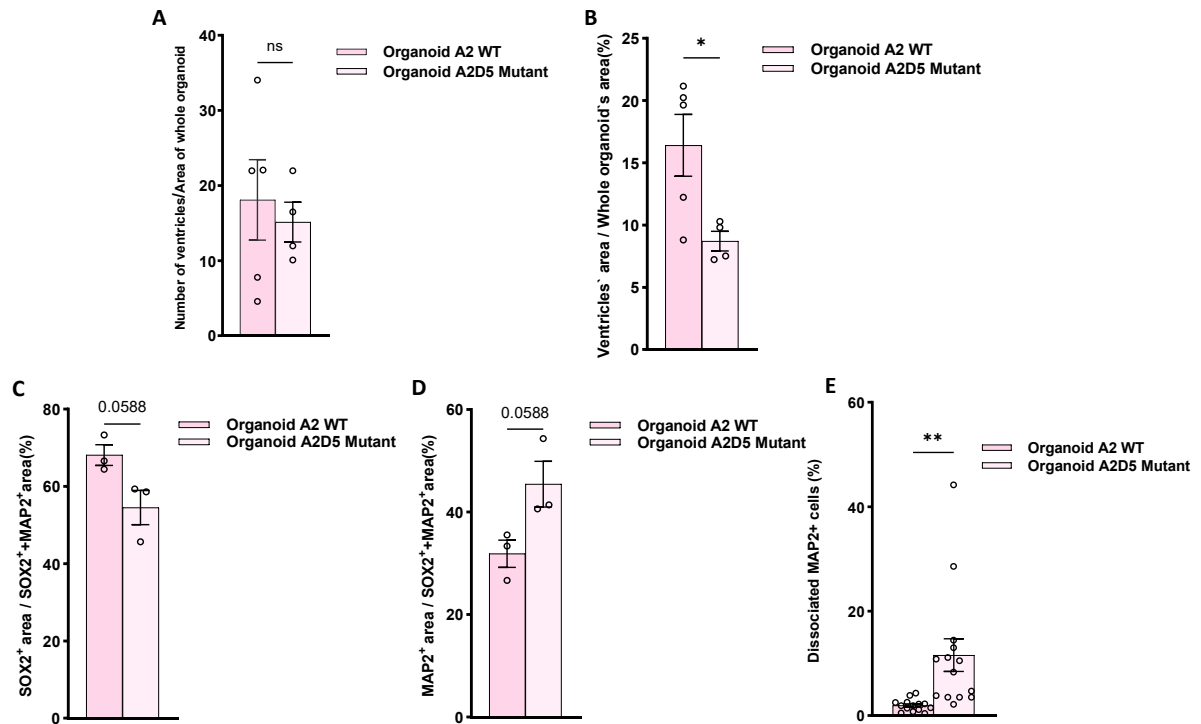


**Fig.42. Overview of the analysis of female line A2 (WT) and A2D5 (*POGZ*<sup>-/-</sup>) cerebral organoids after 30 days in culture.** A. Quantification of total number of the ventricles formed relative to the total area of the organoid; n=5 for A2(WT) and n= 4 for A2D5 (Mutant). B. Quantification of total area of the ventricles formed relative to the total area of the organoid; n=5 for A2(WT) and n = 4 for A2D5 (Mutant). C. Quantification of total the SOX2+ area (ventricular area) relative to the total neural area (SOX2+ area + MAP2+ area); n=3. D. Quantification of total the MAP2+ area relative to the total neural area (SOX2+ area + MAP2+ area); n=3. E. Quantification of MAP2+ neurons in the dissociated cells of organoids A2D5(Mutant); n= 9, compared to organoids A2 (WT); n= 8, 24 hr after plating and culturing in neural differentiation medium. Map2+ neurons were quantified in terms of % of % positive area/total DAPI+ area. 2-3 organoids were pooled and used, 3 coverslips per cell line-organoids were quantified; n= 14 where n= a photo of coverslip. ns; non-significant, WT; wildtype. Significances were calculated using unpaired t-tests; \*= P < 0.01, \*\*= P < 0.001. Values are mean  $\pm$  SEM.

#### **4.5 Transcriptomic profiling of *POGZ* wildtype and mutant NPCs**

To investigate gene expression profile changes associated with different *POGZ* mutations, mRNA sequencing was performed on total RNA extracted from female A2, A2D5 and male S21, C34 NPCs. Three biological replicates of each cell line were sequenced after checking the concentration and quality of total RNA.

##### **4.5.1 Cell pellets, RNA quality control and RNA sequencing**

For each cell line, at least three cell pellets were collected from two different NPC differentiation batches. Total RNA was extracted and its concentration and quality were evaluated using Bioanalyzer. Only samples with RNA integrity number (RIN)  $\geq 9$  were used for the later characterization and RNA sequencing. The samples were further characterized by quantification of RNA expression of iPSCs and NPCs markers using RT-qPCR prior to sequencing to ensure NPC differentiation status. The pluripotency genes (*KLF4*, *NANOG*, *OCT4*) were downregulated while NPC marker genes (*NESTIN*, *PAX6*, *SOX2*) were upregulated compared to the respective iPSCs. Three biological replicates were then used for RNA sequencing for each cell line including two from the same NPC differentiation batch and a third one from another batch. mRNA sequencing was conducted by StarSEQ GmbH (Mainz) on a NextSeq 2000 device using NEBNext Ultra II Directional RNA library preparation kit producing a mean of 50 million 150-bp paired-end reads per sample. The obtained data was processed and analyzed with the help of Dr. Hristo Todorov.

##### **4.5.2 RNA-seq analysis**

###### **4.5.2.1 Sample clustering**

Quantification of gene expression levels was done for each sample at the gene level and not at the transcript level. This means reads were counted using the consensus gene model so the expression levels represent the gene overall and not individual isoforms. Principle component analysis showed clustering of the samples according to their sex and the genotype (Fig.43 A-C). Therefore, the female NPC replicates clustered together depending on the genotype: A2 female wildtype (WT) (x1, x2 and x3) and A2D5 female mutant (Mut) (x4 and x5) except for one female mutant sample (x6) (Fig.43A). This replicate (x6) showed a highly different transcriptome compared to the remaining mutant replicates and was excluded from any further analysis due to being an outlier (Fig.43B). This replicate (x6) deviation can be explained by being generated from another NPC differentiation batch suggesting batch to batch variability depending on iPSCs quality used in the differentiation and culturing environment. Another argument could be that the

transcriptomic profile of this sample (x6) is more similar to the WT samples. However, it is important to note that this analysis is based on the top 500 most variable genes. For the male NPC replicates, the samples also clustered according to the genotype: S21 male wildtype (x10, x11 and x12) and C34 male mutant (x7, x8 and x9) (Fig.43A-B).

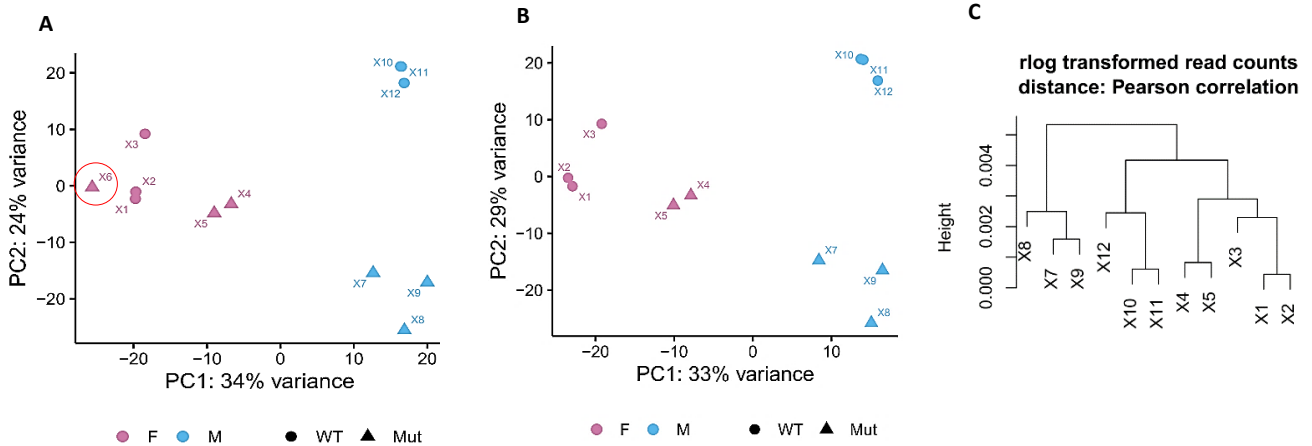


**Fig.43. Principal component analysis (PCA) of transcriptome from WT and mutant NPCs (A&B) and dendrogram (C)** showing Pearson correlation between individual samples. The samples form clusters depending on their sex and their genotype that fit their known cellular identity. Female mutant sample x6 (highlighted with red circle) was excluded from the following analysis due to being an outlier (A).

#### 4.5.2.2 Differentially expressed genes (DEGs):

Differential gene expression analysis revealed 2915 DEGs between mutant female A2D5 NPCs and control A2 wildtype NPCs (Fig.44A). Meanwhile, 3180 DEGs were identified between mutant male patient C34 NPCs and control S21 wildtype NPCs (Fig.44A). The slightly higher number of DEGs between male NPCs could potentially be influenced by the differences in genetic background, in addition to the genotype status. Furthermore, it is important to note that the effect of sex should also be considered, besides dealing with different POGZ mutations that makes it difficult to fully separate these factors. Interestingly, 870 of these DEGs were common in both female and male cells (Fig.44A). To analyze if these DEGs intersect known autism risk genes, the DEGs between female A2 and A2D5 and male S21 and C34 NPCs were compared with genes listed in the Simons Foundation Autism Research Initiative (SFARI) database which includes risk genes commonly mutated in autism spectrum disorder. 189 DEGs in mutant A2D5 NPCs and 168 DEGs in mutant C34 NPCs, respectively overlapped with SFARI genes (Fig.44B). 57 genes were present in all three data sets (Fig.44B). These 57 genes include *HNRNPU* (Heterogeneous Nuclear Ribonucleoprotein U), *SCN2A* (Sodium channel protein type 2 subunit alpha) and *NLGN3* with gene score of 1 meaning high confidence level in the gene's association with ASD and *GRID1* (Glutamate Ionotropic Receptor Delta Type Subunit 1)

with gene score 2 and *HCN1* (Hyperpolarization-Activated Cyclic Nucleotide-Gated Channel 1) which has 5 gene score meaning that *HCN1* is linked to syndromic forms of autism, where ASD is one of several symptoms associated with this syndrome.

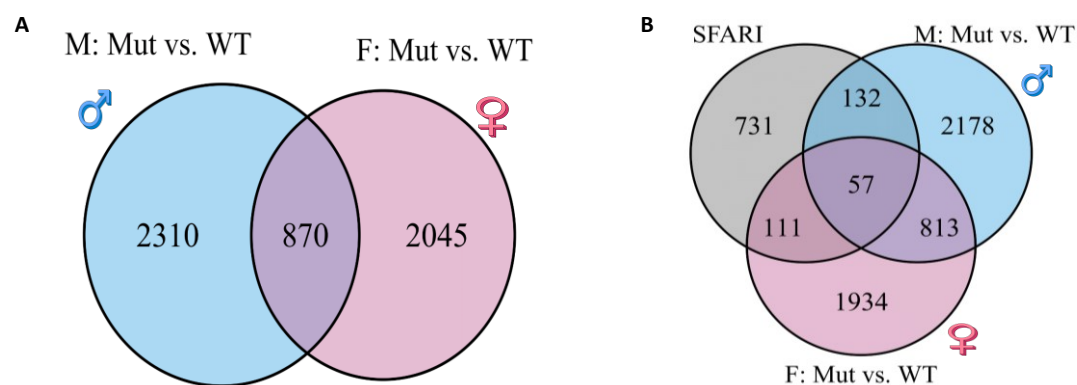


**Fig.44. Overlapping differentially expressed genes (DEGs) between mutant and wildtype female and male NPCs (A) and with SFARI genes (B).** M: male, F: female, Mut: mutant, WT: wildtype, vs.: versus and SFARI: Simons Foundation Autism Research Initiative.

#### 4.5.2.3 Differentially expressed genes (DEGs) in female NPCs:

Out of the 2915 DEGs between mutant female A2D5 NPCs and control A2 wildtype NPCs, 1593 were downregulated and 1322 were upregulated in mutant A2D5 NPCs. Volcano plot shows the top 10 up- and downregulated DEGs for A2D5 mutant and A2 wildtype NPCs (Fig.45). Many of the top 10 up- and downregulated DEGs in A2D5 mutant NPCs are associated with NDDs and/or autism such as the upregulated genes *HCN1*[247], *AGAP2* (Arf-GAP with GTPase, ANK repeat, and PH domain-containing protein 2) [248], *SILTRK3*[249, 250], and the downregulated genes as *TRIM65* (Tripartite Motif Containing 65) [251, 252]. To gain insight into the functional properties/implications of DEGs, the gene ontology (GO) enrichments were done for biological process (BP), cellular components (CC), and molecular functions (MF). Downregulated DEGs were significantly enriched for BP terms including chromosome segregation, mitotic chromatid segregation and nuclear division, among others (Fig.46A). The upregulated DEGs were significantly enriched for BP terms including synaptic signaling and transmission, membrane depolarization and cell projection organization, among others (Fig.46B). Moreover, to emphasize on detailed molecular reactions and biological pathways, in which DEGs are involved, an enrichment analysis was performed with the Reactome database (Fig.46C-D). Interestingly, some of the downregulated DEGs were significantly enriched for nonsense mediated decay (NMD) (Fig.46C). Down-regulation of the NMD pathway could potentially explain the normal *POGZ* mRNA level in mutant A2D5 NPCs assuming this pathway is directly responsible for degrading the mutant transcript and hence be detected in RT-qPCR and pyrosequencing

experiments. Again, the upregulated DEGs were involved in diverse synapses related processes (Fig.46D).

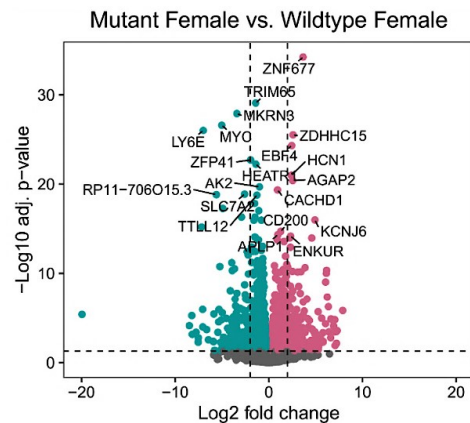


**Fig.45. Volcano plots of the up- and downregulated DEGs for A2D5 mutant female and A2 wildtype female NPCs control.** Positive log2 fold changes indicate genes that are up-regulated and negative log2 fold changes correspond to down-regulated genes in mutant NPCs. The top 10 up- and down-regulated genes are labeled with their gene symbols.

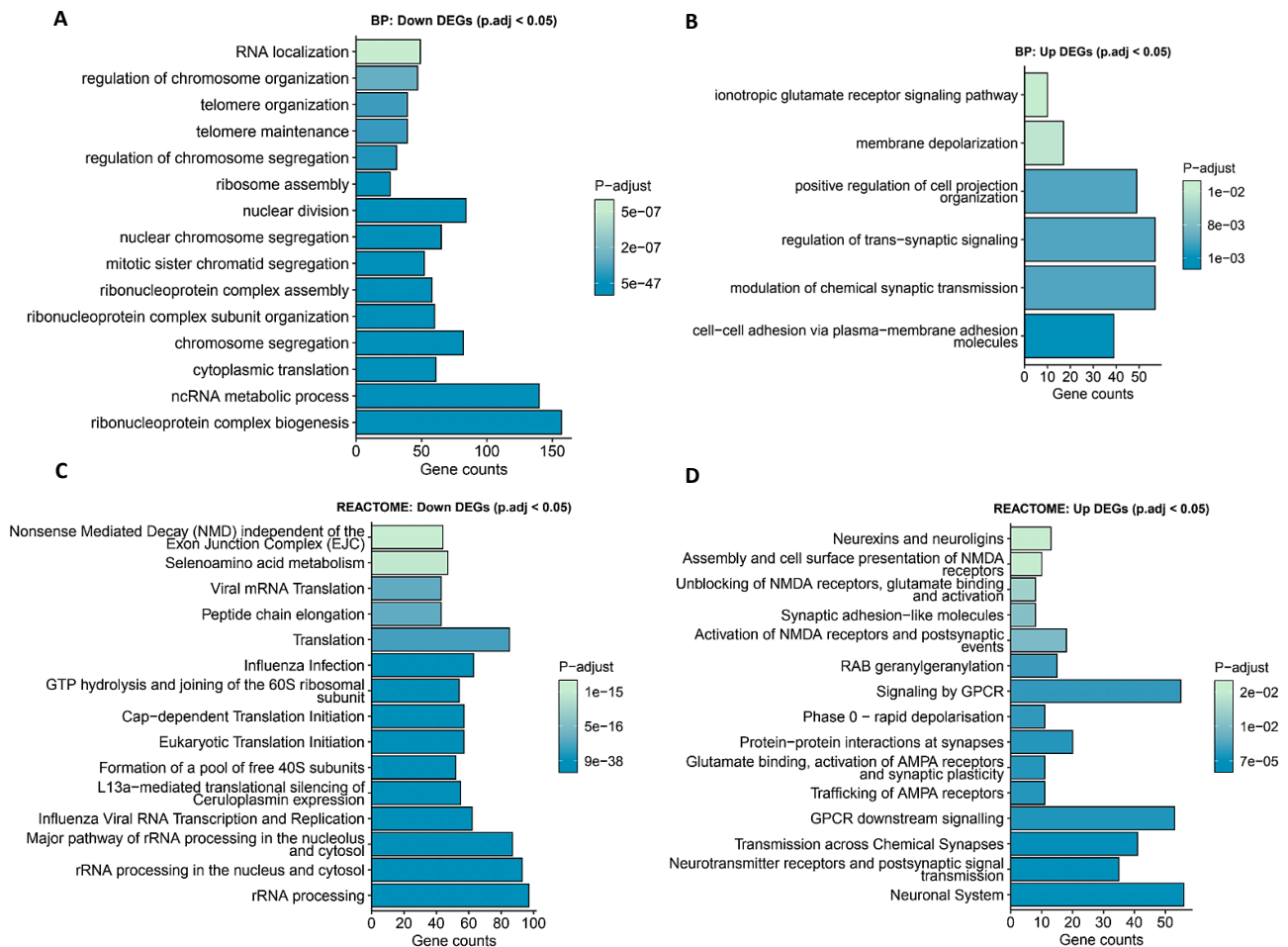


**Fig.46. Bar plots with the top 15 significantly enriched Gene Ontology Biological Process (A&B) and Reactome terms (C&D) for down- and up-regulated DEGs for A2D5 mutant female versus A2 wildtype female NPCs controls.** In case fewer than 15 terms were significantly enriched, then all significant terms (adjusted  $p < 0.05$ ) are shown.

#### 4.5.2.4 Differentially expressed genes (DEGs) in male NPCs:

Out of the 3180 DEGs between mutant male C34 NPCs and control S21 wildtype NPCs, 1591 were downregulated and 1589 were upregulated in mutant C34 NPCs. Volcano plot shows the top 10 up- and downregulated DEGs for C34 mutant and S21 wildtype NPCs control (Fig.47). *CHCHD2* (Coiled-coil-helix-coiled-coil-helix domain containing 2) gene is one of those upregulated genes, which is a mitochondrial protein involved in cell migration and differentiation and has been recently linked with neurometabolic failure [253, 254]. Similar to female NPCs, the gene ontology analyses were done for biological process (BP), cellular components (CC), and molecular functions (MF) (Fig.48). These analyses revealed that the downregulated DEGs were significantly enriched for GO biological process (BP) terms, similar to female NPCs, including chromosome segregation, mitotic chromatid segregation in addition to DNA repair, DNA replication, alternative splicing and cell cycle checkpoints, among others (Fig.48A). The upregulated DEGs were significantly enriched for GO biological process (BP) terms including synaptic signaling and organization, synapse assembly and regulation, among others (Fig.48B). Overrepresentation analyses using the Reactome database revealed that the downregulated DEGs were significantly enriched for many homology-directed DNA repair (HDR) related pathways and cell cycle (Fig.48C). In addition, unlike female A2D5 mutant NPCs, nonsense mediated decay (NMD) was not among pathways enriched for downregulated DEGs (Fig.48C). The upregulated DEGs were involved in interactions at synapses, GPCR signaling and ion channel transport, among others (Fig.48D).

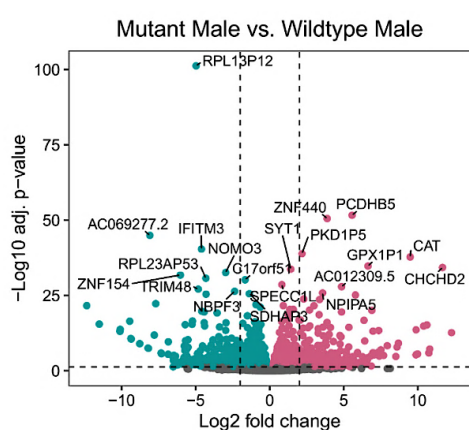


**Fig.47. Volcano plots of the up- and downregulated DEGs for C34 mutant male and S21 wildtype male NPCs control.** Positive log2 fold changes indicate genes that are up-regulated and negative log2 fold changes correspond to down-regulated genes in mutant NPCs. The top 10 up- and down-regulated genes are labeled with their gene symbols.

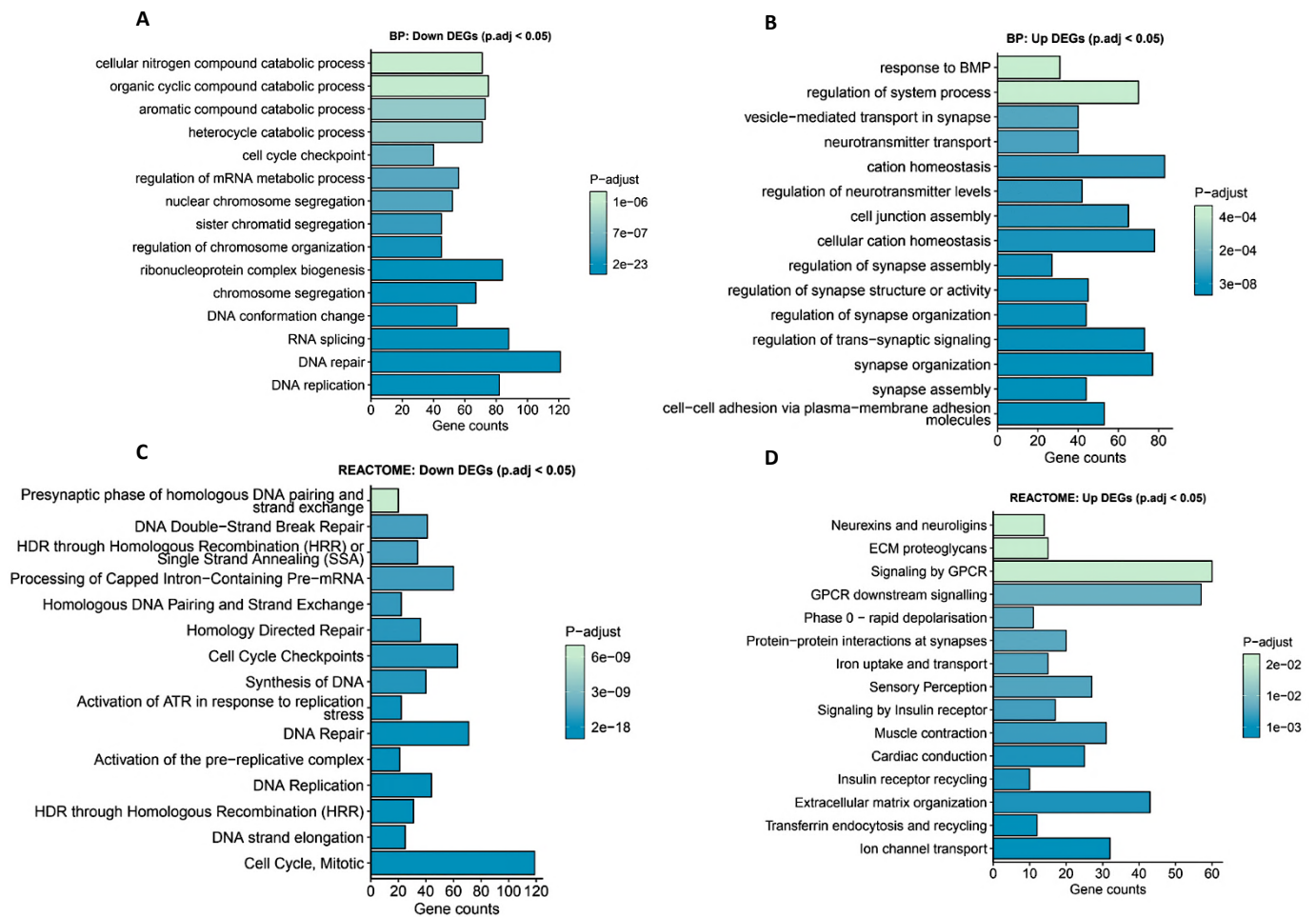


**Fig.48.** Bar plots with the top 15 significantly enriched Gene Ontology Biological Process (A&B) and Reactome (C&D) terms for down- and up-regulated DEGs for C34 mutant male versus S21 wildtype male NPCs controls. In case fewer than 15 terms were significantly enriched, then all significant terms (adjusted  $p < 0.05$ ) are shown.

#### 4.5.2.5 Differentially expressed genes (DEGs) between female and male NPCs

The transcriptome profiles of the wildtype A2 female and S21 male NPCs were compared while those of the mutant A2D5 female and C34 male NPCs were compared. 4323 DEGs were identified between wildtype female A2 and male S21 NPCs in comparison to only 1548 DEGs between mutant female A2D5 and male C34 NPCs (Fig.49). This raises the possibility that the transcriptomes of cell lines carrying *POGZ* mutations may be more similar to each other than to the transcriptomes of wildtype cell lines, which might indicate that *POGZ* mutations have some influence on a specific transcriptomic profile. 718 DEGs were found to be common between wildtype and mutant NPCs. This suggests that the expression of these genes is not influenced by *POGZ* mutations. Instead, the differences in gene expression observed in wildtype or in mutant NPCs may be attributed to variations in genetic backgrounds or sex differences.

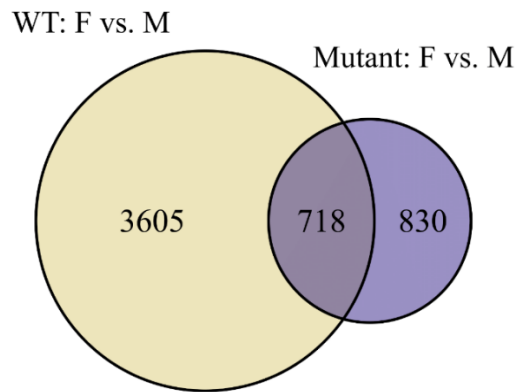


**Fig.49. Overlapping differentially expressed genes (DEGs) between mutant and wildtype female and male NPCs.** M: male, F: female, Mut: mutant, WT: wildtype and vs.: versus.

#### 4.5.2.6 Validation of RNA-Seq Data Using qPCR:

To confirm the differential expression identified through RNA-Seq analysis, a subset of genes was validated using qPCR (Fig.50). DEGs selected for validation included *NLGN3* and *PINK1*, in both female and male NPCs and *MKI67*, *CHD8* and *SLC25A25* only in female NPCs and *CCND2*, *HNRNPR* and *SLC5A6* only in male NPCs, which showed significant upregulation or downregulation in the RNA-Seq data. These genes were chosen based on their biological relevance to the study and their expression patterns observed in the RNA-Seq results.

qPCR analysis revealed that the expression trends of the selected genes closely matched those observed in the RNA-Seq data. For example, *NLGN3*, which exhibited a 1.16-fold and a 0.96-fold upregulation in mutant female and mutant male NPCs respectively in RNA-Seq, showed an increase in expression (2.4-fold, p-value=0.003) and (1.9-fold, p-value=0.044) respectively as measured by qPCR (Fig.50A-B). For *PINK1*, a 0.46-fold and a 0.55-fold upregulation in female and male NPCs respectively in RNA-Seq was observed, and showed an increase in expression (1.6-fold, p-value=0.005) and (1.6-fold, p-value=0.089) respectively as measured by qPCR (Fig.50A-B). Similarly in mutant female NPCs only, *SLC25A25* identified as upregulated with RNA-seq fold change of 0.49 with consistent upregulation in qPCR with fold change of 1.75 (p-value <0.0001) (Fig.50A). Also in female NPCs, RNA-Seq identified downregulated DEGs *MKI67* and *CHD8*, with fold changes of -0.93 and -0.26, respectively, showed consistent trend of downregulation in qPCR with fold changes of -0.70 (p-value=0.11) but no change in *CHD8* expression (Fig.50A). In mutant male NPCs, *CCND2*, *HNRNPR* and *SLC5A6* identified as downregulated with RNA-seq fold change of -2.04, -0.24 and -0.92 respectively with consistent down regulation in qPCR with fold change of -0.19 (p-value=0.009), -0.74(p-value=0.086), -0.50 (p-value=0.026)

(Fig.50B). These findings validate the RNA-Seq data and support the robustness of the differential expression analysis, confirming that the identified DEGs are truly differentially expressed under the experimental conditions.

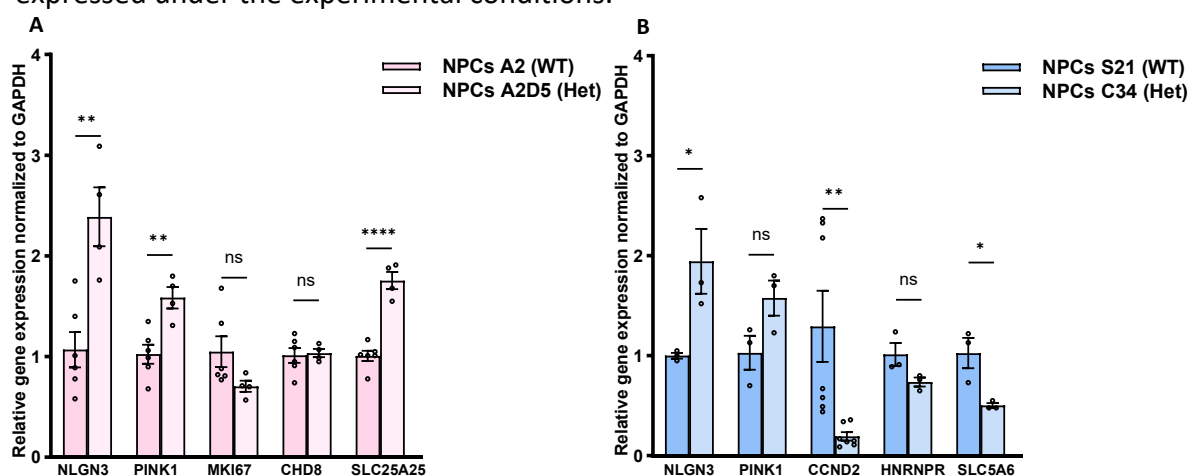


**Fig.50 RT-qPCR of the DEGs of female (A) and male (B) NPCs found in RNA-seq data.** Mutant female A2D5(A) and mutant male C34 (B) NPCs showed an increased mRNA expression of *NLGN3* and *PINK1* relative to their corresponding wildtypes A2 and S21 NPCs. A2D5 NPCs (A) showed increased *SLC25A25*, an almost unchanged *CHD8* and a trend of decreased *MKI67* mRNA expression. C34 NPCs (B) showed an increased *SLC5A6* and a decreased *CCND2* and a trend of decreased *HNRNPR* mRNA expression. *GAPDH* was used for normalization. n=6 (A2); n=4 (A2D5); n=3 (S21 except for *CCND2* n=7); n=3(C34 except for *CCND2* n=7). Values are mean ± SEM.

#### 4.5.2.7 Inferring the differentiation status of WT and mutant NPCs

In the previous analyses of marker expression and differentiation, it was observed that trend of higher expression of neuronal markers, *DCX*, was exhibited by mutant female A2D5 NPCs and *MAP2*, by mutant WHSUS C34 male NPCs. This was along with a significantly greater number of MAP2+ cells at early stages of neuronal differentiation in female A2D5 NPCs. In contrast, with the mutant WHSUS C34 male NPCs, the increase in MAP2+ cells was not statistically significant. These findings lead to the hypothesis that the mutant NPCs may show an upregulation of differentiation-related genes, which requires further investigation. To test this hypothesis, whether the mutant NPCs are potentially more differentiated than wildtype NPCs, a list of 19 NPC-distinguishing and 25 neuron-predicting genes obtained from a study by Burke *et al.* 2020 [242] was utilized. Two of the neuron-predicting genes from this set were not expressed in the POGZ data set; this can be explained by that the cells still being in the neural progenitor cell (NPC) stage and not yet having fully differentiated into neurons. However, this explanation remains speculative and further investigation is needed to confirm whether the absence of expression is indeed due to the cells' undifferentiated state. Therefore, these genes were not included in the subsequent analyses. Notably, looking at the expression patterns of the NPC- and neuron-predicting genes from the Burke *et al.* (2020) study[242] revealed

that *POGZ* mutant cells and wildtype samples, respectively clustered together (Fig.51A). However, it is important to note that, when analyzing the overall transcriptomic patterns, samples of the same sex displayed greater similarity to each other, irrespective to their genotype (Fig.51A). Furthermore, the expression of neuron-predicting genes was on average lower in wildtype cells, with this effect being more prominent in the female A2 wildtype (WT\_F) NPCs (Fig.51A). In a PCA using these neuron and NPC predicting genes, the mutant female (Mut\_F) and male (Mut\_M) cells were clearly separated from the WT cells along the first principal component (PC1) (Fig.51B) indicating that indeed the genotype effect was the main factor responsible for differences in expression levels of the NPC- and neuron-predicting genes.

To investigate which marker genes, explain the pattern in the PCA, the loadings of on PC1 were calculated. In this context, loadings represent correlations of expression values for the marker genes with the first multivariate dimension in the PCA (Fig.51C). Genes with high loading values (absolute value greater than 0.4) are the main variables responsible for explaining the observed pattern (Fig.51C). The separation along PC1 was explained by 15 out of 23 neuron predicting genes and 12 out of 19 NPC genes. All but one neuron predicting genes were positively correlated with PC1, indicating that higher expression of these genes in mutant cells (Fig.51C). The opposite was true for NPC predicting genes. This pattern might indicate that mutant cells were in a more differentiated state than wildtype cells (Fig.51C).

#### **4.6 POGZ binding genes analysis via CUT&Tag sequencing:**

*POGZ* has at least 8 C2H2 zinc fingers, suggesting it can bind DNA and function as transcriptional regulator. Therefore, to study role of *POGZ* in transcription regulation in NPCs, CUT&Tag analysis was done to identify the DNA sites where *POGZ* can bind directly or indirectly.

For an unbiased screen of *POGZ* occupancy genome-wide in NPCs, CUT&Tag (C&T) was performed in female A2, A2D5 and A2A1 and male S21, C34 NPCs using anti-*POGZ* antibody (Abcam (ab167408)). Three replicates were analyzed in each experimental group Compound heterozygous female A2A1 NPCs and IgG were used as negative controls. Peak calling using Seacr with IgG control showed 16890, 3677 consensus *POGZ* peaks respectively in A2 (F WT) and A2D5 (F HET) female NPCs (Fig.52A) and 5252, 4491 consensus *POGZ* peaks respectively in S21 (M WT) and C34 (M HET) male NPCs (Fig.52A).

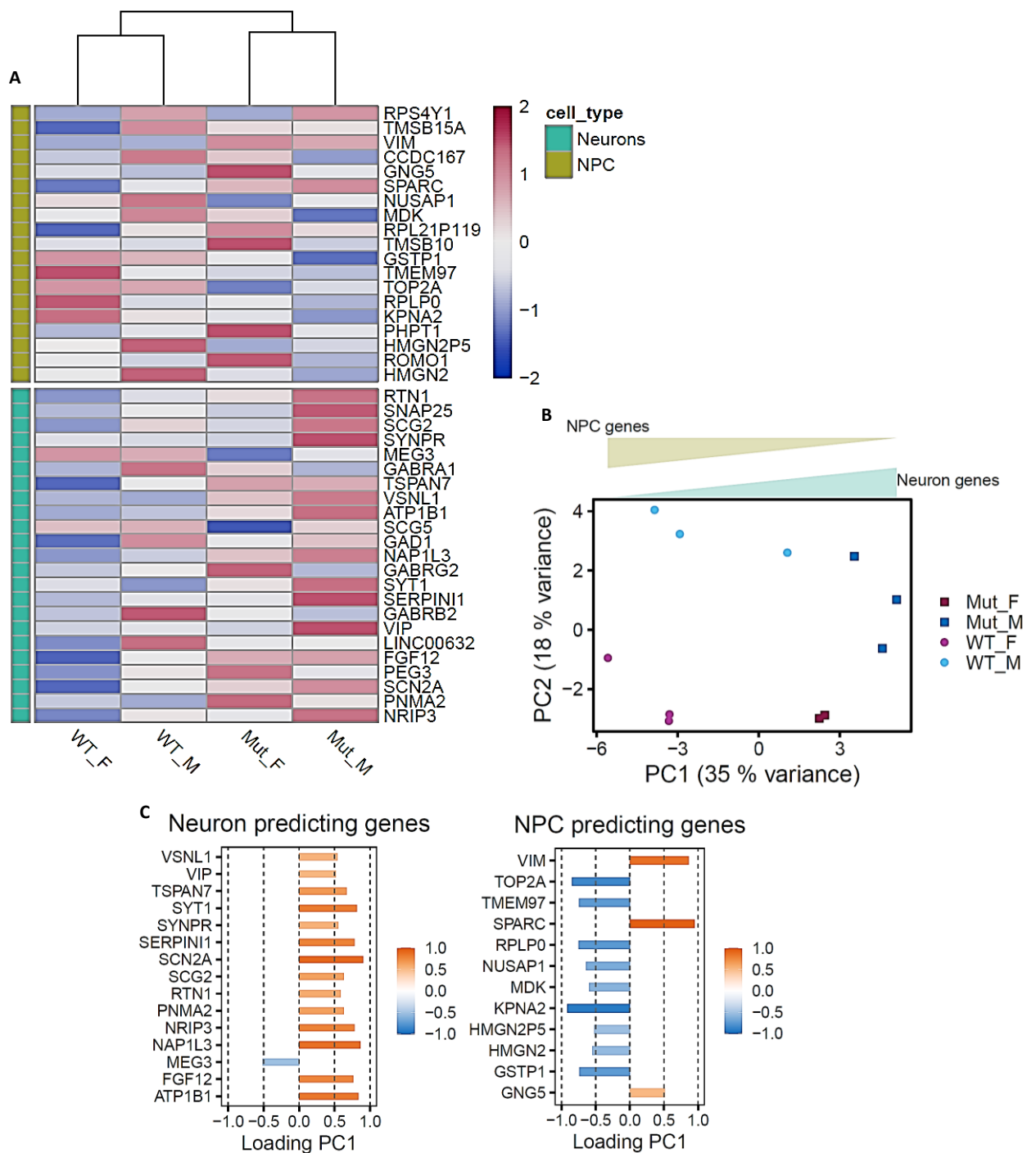


**Fig.51** Heatmap showing z-score-transformed average expression of NPC and neuron predicting genes in each experimental group (A). Principle component analysis (PCA) using NPC and neuron predicting genes (B) and the loadings of genes on PC1 (C). Loadings correspond to correlations of the original expression values for the marker genes with the first multivariate dimension in the PCA (PC1). Only genes with absolute loading values greater than 0.4 are depicted.

The majority of genes intersecting consensus peaks in the HET samples were also detected in the WT samples (Fig.52B). The number of consensus peaks in the M WT group is much lower due to two of the replicates having low number of peaks detected whereas one replicate had a comparable number of peaks to the female samples. As consensus peak were determined as being present in at least 2 replicates, many of the potential peaks

from the third WT male NPC sample could not be considered. POGZ C&T peaks showed a greatly reduced signal in compound heterozygous female A2A1 (F KO) NPCs and IgG experiments, demonstrating the validity of the C&T experiment (Fig. 53).

The majority of POGZ consensus peaks intersected promoter regions within 1kb of the transcription start sites of genes ( $\approx 38\%$ ) (Fig.54), supporting the notion that POGZ acts as transcriptional factor. However, a large fraction of consensus peaks was also detected in distal intergenic regions (Fig.54).

To investigate the replicability of consensus peaks in the POGZ WT cells and compare results to existing reports, peaks were annotated to genes using CHIPseeker and then intersected with POGZ-occupied genes from the study by Papadimitriou *et al.* [111], that investigated POGZ binding in 17 gw/18 gw human fetal cortex samples. The Venn diagram shows the number of genes overlapping between the two data sets (Fig.55A). The same analysis was performed for HET consensus peaks (Fig.55B). 2983 and 1385 of the peaks in F WT and M WT respectively overlapped with POGZ bound genes from human fetal cortex samples (17 gw and 18 gw ) in Papadimitriou *et al.* [111](Fig.55B), indicating a substantial overlap of the C&T results with existing reports on POGZ binding.

GO (BP) analysis of POGZ targets in female WT NPCs revealed the enrichment of biological processes important for the development of the central nervous system including axonogenesis, cell-cell signaling by Wnt, Wnt signaling, regulation of neuron projection development and forebrain development among others (Fig. 56). In male WT NPCs, similar terms were enriched including axonogenesis, cell-cell signaling by Wnt, Wnt signaling, neuron projection guidance, regulation of neuron projection development and forebrain development among the top enriched terms (Fig.57). These GO results are in line with the observation that POGZ mutations are frequently linked with neurodevelopmental or brain related disorders.

Furthermore, to investigate whether POGZ occupies gene loci implicated in ASD, POGZ-bound genes were intersected with the SFARI database. POGZ-bound genes were significantly enriched for autism risk genes reported in the SFARI database in both female (Fig.58A) and male (Fig.58B) WT NPCs. For example, *RERE*, *CHRM3* and *PCDH15* were among the autism risk genes that were found to be POGZ binding targets. *RERE* (Arginine-Glutamic Acid Dipeptide Repeats) encodes a nuclear receptor coregulator involved in chromatin remodeling and transcriptional regulation.

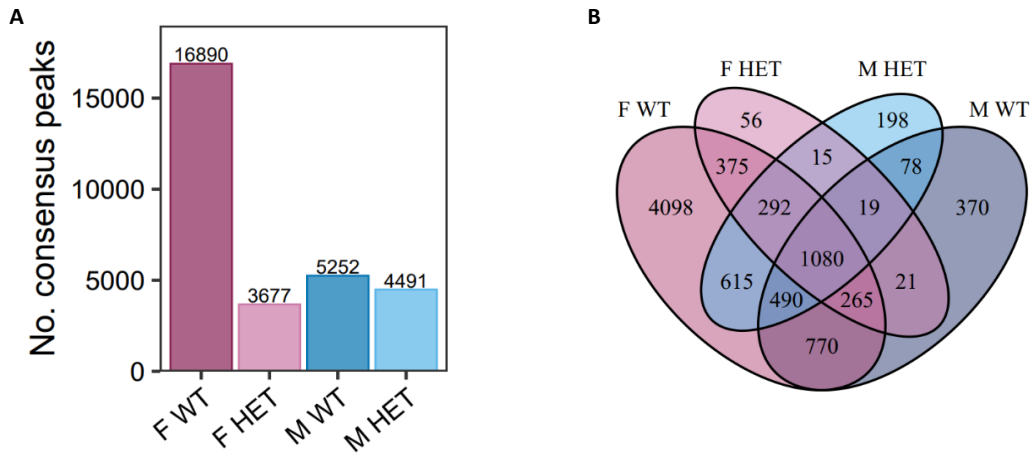


**Fig.52. Consensus peaks in female wildtype (F-WT) & heterozygous (F-HET) and male wildtype (M-WT) & heterozygous (M-HET) NPCs (A). Venn diagram of intersecting consensus peaks in the HET samples that were also detected in the WT samples (B)**

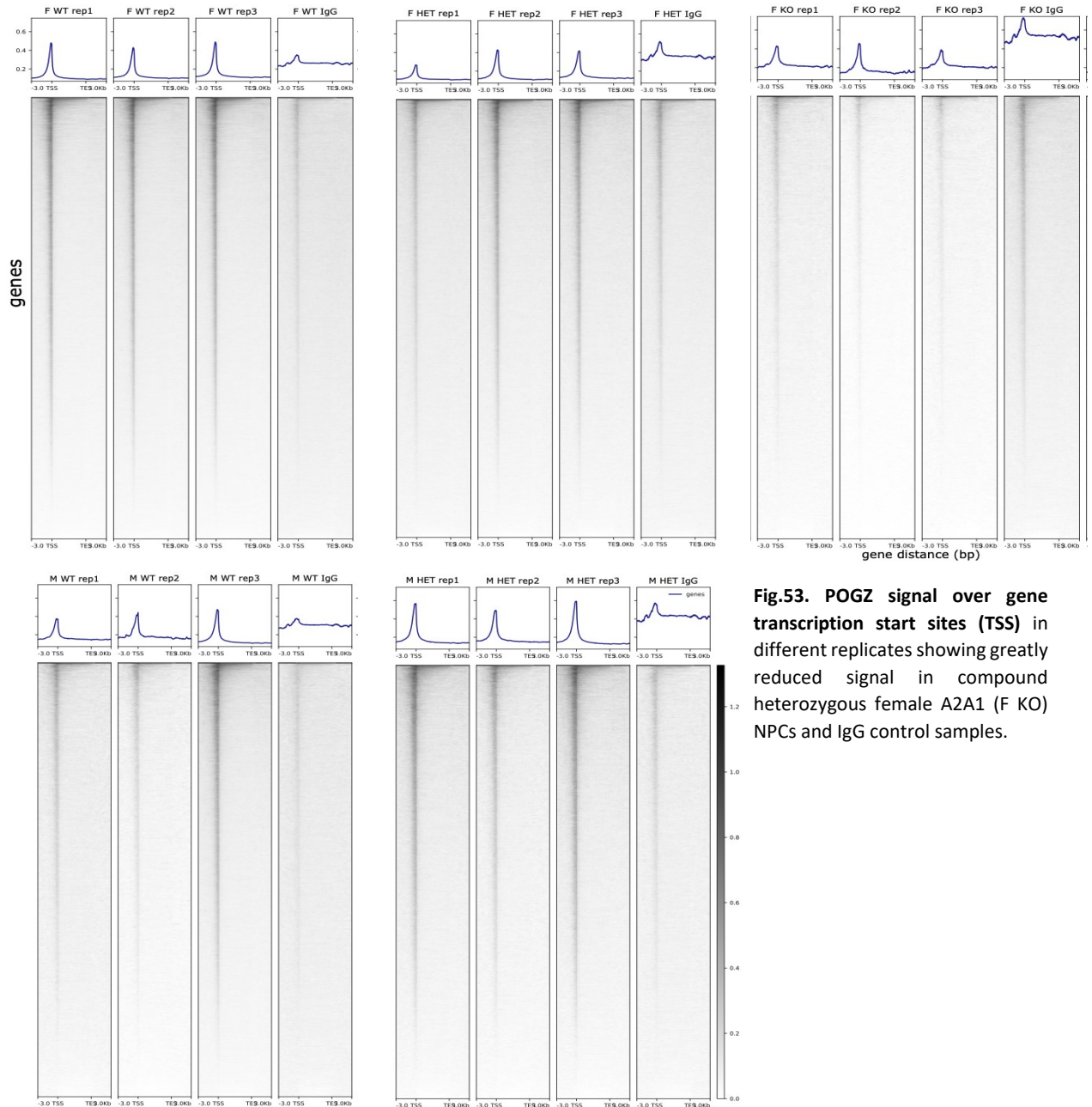


**Fig.53. POGZ signal over gene transcription start sites (TSS) in different replicates showing greatly reduced signal in compound heterozygous female A2A1 (F KO) NPCs and IgG control samples.**

*RERE* has been implicated in several neurodevelopmental disorders (NDDs) [255, 256]. *CHRM3* (Cholinergic Receptor Muscarinic 3) encodes the M3 muscarinic acetylcholine receptor, which belongs to the G protein-coupled receptor family. This receptor is involved in various physiological functions, such as smooth muscle contraction, glandular secretion, and the modulation of neurotransmitter release[257]. For *PCDH15*, is a gene encoding a member of the cadherin superfamily, which plays a key role in cell-cell adhesion, particularly in neural differentiation and synapse formation [258]. It influences the proliferation of oligodendrocyte progenitor cells and hence white matter development and myelination[259]. Mutations in *PCDH15* have been primarily linked to Usher syndrome type 1F, a condition characterized by hearing loss and vision impairment[260]. However, emerging research suggests that *PCDH15* may also be involved in NDDs like ASD [261].

To investigate how *POGZ* mutations influence the binding activity of the protein, differential occupancy analysis was performed in female NPCs (Fig.59A). WT and HET samples clustered together indicating an adequate within group correlation of replicates (Fig.59B). When comparing HET versus WT female NPCs, 6668 peaks were associated with a significant loss of binding (Fig.60A). Peaks intersecting *DNAH9*, *FLG-AS1* and *SLC38A4* exhibited the highest negative fold change (Fig.60A). In contrast, 529 peaks were associated with gain of binding. *ICE2P2*, *RN7SL424P* and *LINC02501* intersected peaks with the highest positive fold change. As expected, the *POGZ* mutations therefore led to significantly reduced binding in HET female NPCs (Fig.60B).

In the male NPCs, differential occupancy analysis showed that WT and HET NPCs did not cluster according to the experimental condition (Fig.61A-B). Poor within group correlation of replicates indicate that technical or experimental biases might have impacted results in the male NPCs (Fig.61B). The comparison of HET versus WT male NPCs showed 9 peaks with a significant loss of binding including peaks intersecting *LINC00578*, *CEMIP* and *APOLD1* (Fig.62A-B). In contrast, 35 peaks showed gain of binding including peaks intersecting *NXPH1*, *FAM171A1* and *FAM86B3P* (Fig.62A-B).

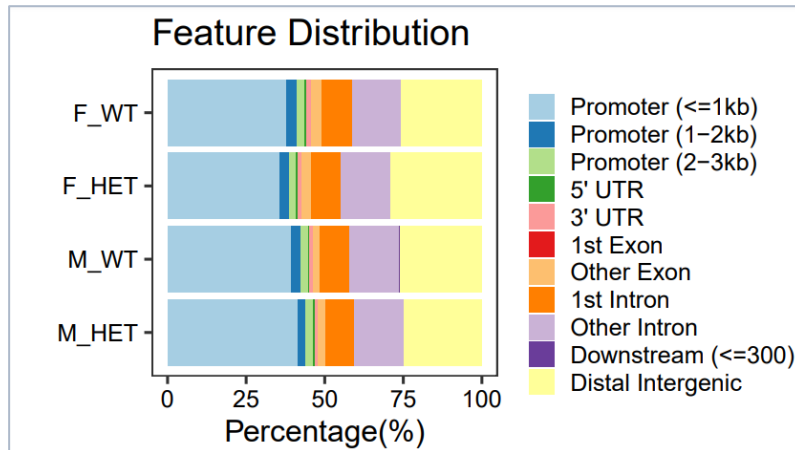


**Figure 54 Consensus POGZ peak distribution.** The majority of consensus peaks intersect promoter regions or distal intergenic regions in all conditions.

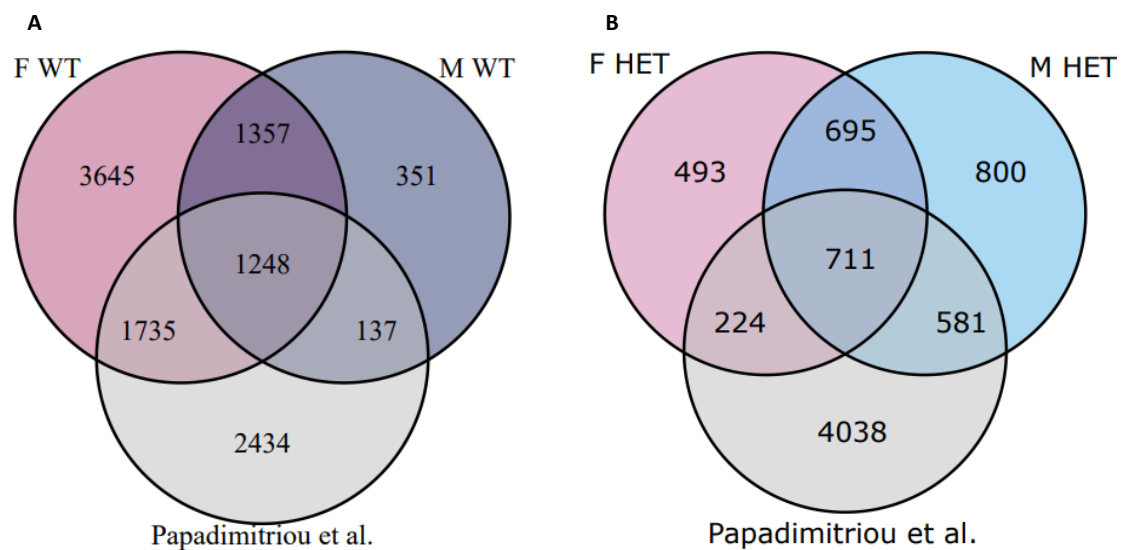


**Fig.55. Venn diagram of overlapping genes** intersecting wildtype WT (A) and heterozygous HET (B) consensus peaks with previously reported POGZ bound genes from the study by Papadimitriou et al.

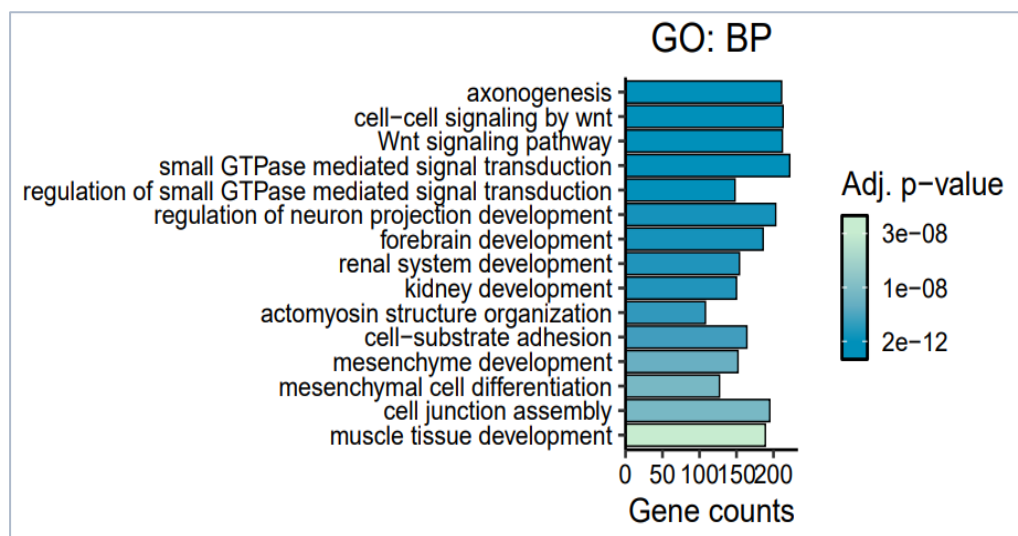


**Fig.56. Gene ontology analysis of POGZ bound genes in wildtype female (WT) NPCs** showing enrichment of biological process terms including axonogenesis, regulation of neuron projection development and Wnt signaling. The top 15 enriched terms (adjusted  $p < 0.05$ ) are depicted.

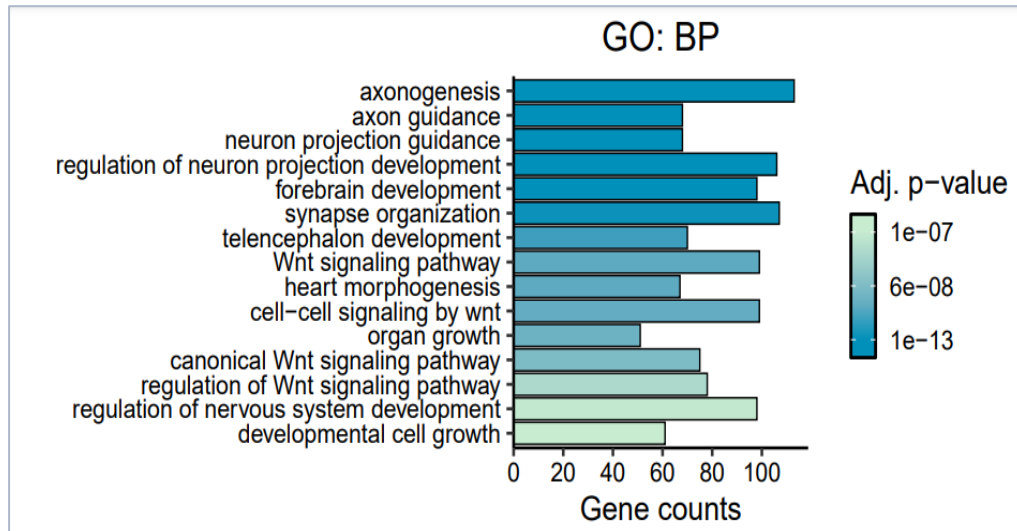


**Fig.57. Gene ontology analysis of POGZ bound genes in wildtype male (WT) NPCs** showing significantly enriched biological process terms including axonogenesis, regulation of neuron projection development and Wnt signaling. The top 15 enriched terms (adjusted  $p < 0.05$ ) are depicted.

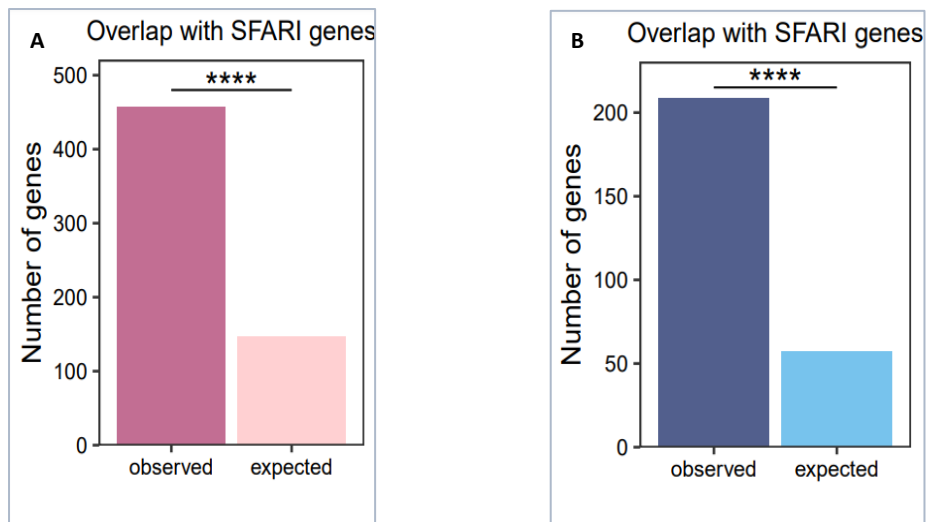


**Fig.58. Overlap of POGZ bound genes with autism risk genes reported in the SFARI database.** The bar plots below show the observed versus expected overlap for female (A) and male (B) wildtype cells. \*\*\*\* $p < 0.0001$ .

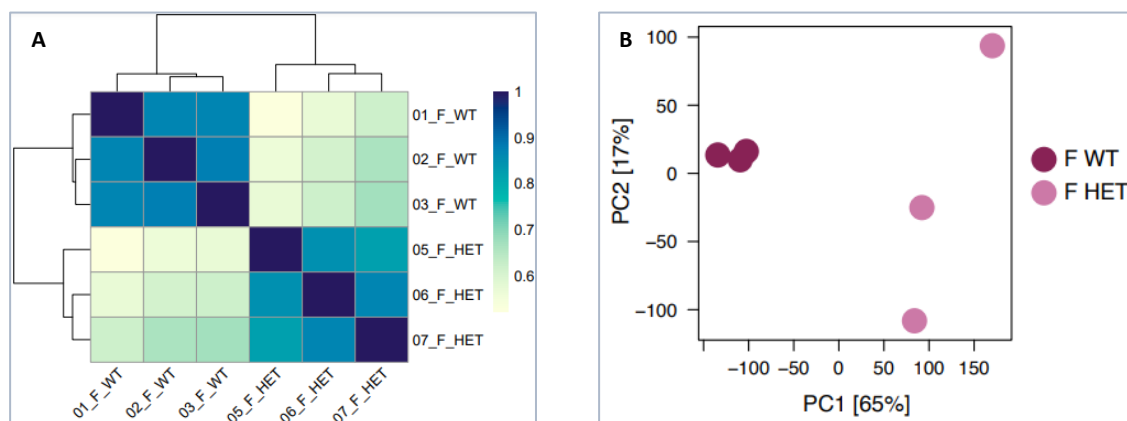


**Fig.59. Differential occupancy analysis of WT and HET female samples using the DiffBind R package (A)** showed the impact of POGZ mutations on binding activity of the protein. **Principal component analysis (PCA) (B)** showed WT and HET female samples clustered together indicating an adequate within group correlation of replicates.

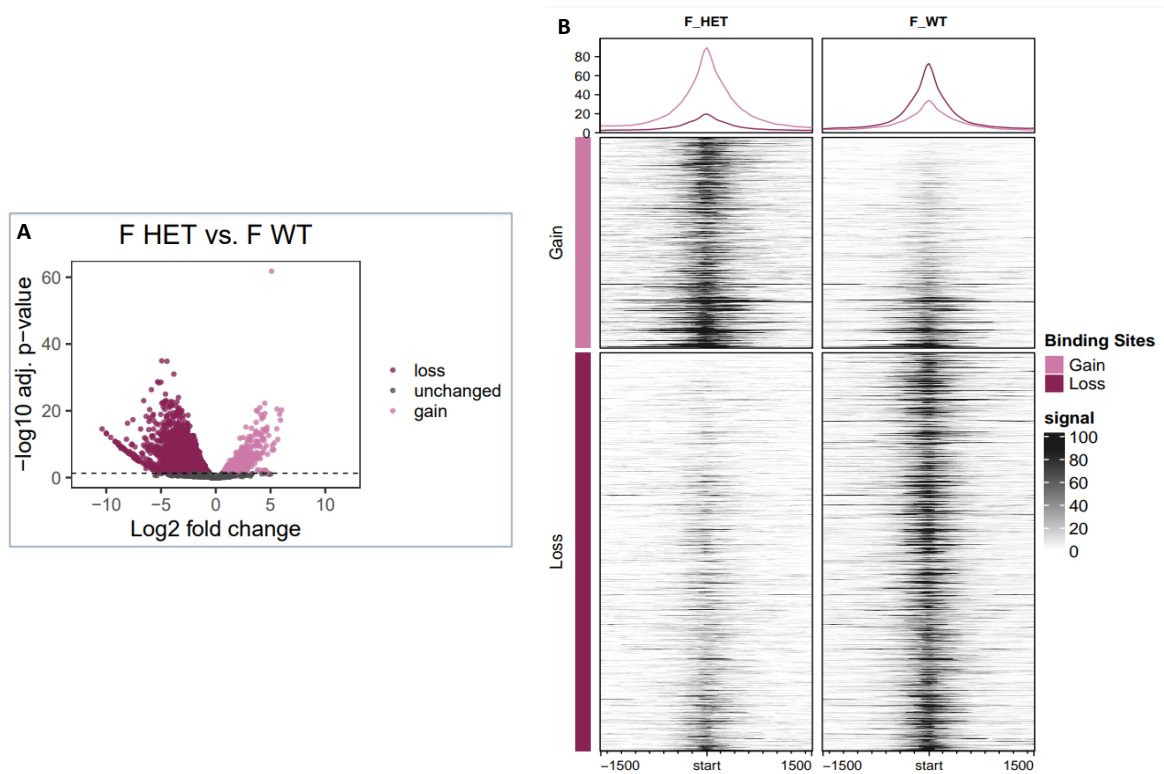


**Fig.60. Volcano plot (A) shows differentially bound peaks.** Negative log<sub>2</sub> fold changes indicate peaks with significantly reduced binding in HET vs WT female samples. 6668 peaks were associated with a significant loss of binding and 529 peaks with gain of binding. **The heatmap and profile plot (B) show all loci with gain of binding and the top 1000 loci with loss of binding.**

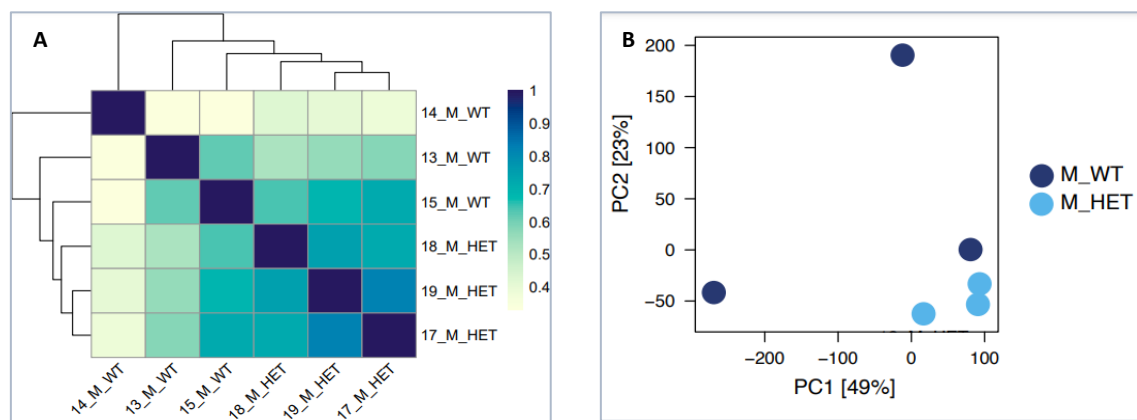


**Fig.61. Differential occupancy analysis of WT and HET male samples using the DiffBind R package (A) showed the impact of POGZ mutations on binding activity of the protein. Principal component analysis (PCA) (B) showed WT and HET male samples did not cluster together indicating poor within group correlation of replicates.**

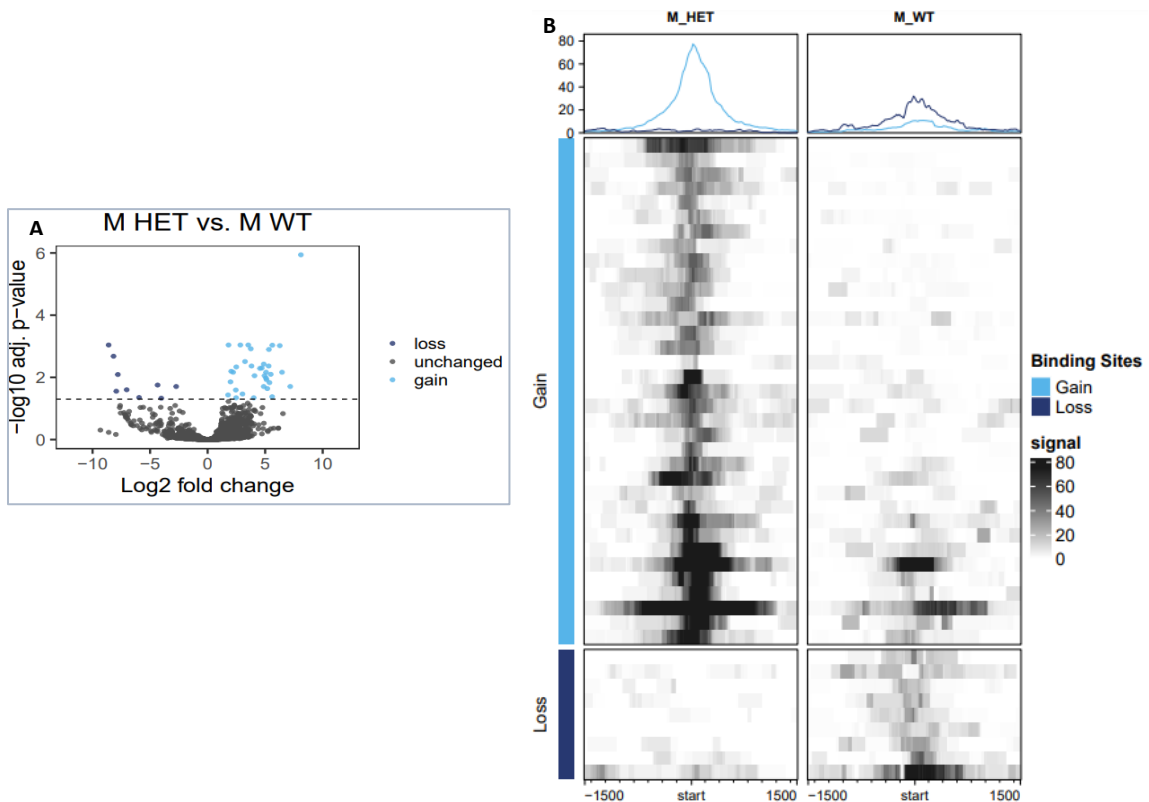


**Fig.62. Volcano plot (A) shows differentially bound peaks.** Negative log<sub>2</sub> fold changes indicate peaks with significantly reduced binding in HET vs WT male samples. 9 peaks were associated with a significant loss of binding and 35 peaks with gain of binding. **The heatmap and profile plot (B) show all loci with gain or loss of binding.**

#### 4.7 Relationship between POGZ-regulated gene expression, POGZ binding

To gain further insights into how POGZ binding regulates gene expression, an integrative analysis of RNA-seq and C&T data was performed. In both female and male NPCs, POGZ showed binding to both up- and down-regulated genes. In female NPCs, approximately 985 POGZ-bound genes (~ 12% of total targets) were deregulated in HET female NPCs (Fig.63A). Of these, 454 genes were upregulated and 531 were down-regulated, accounting for ~ 34% of all differentially up- and down-regulated genes (Fig.63A-C). The up-regulated genes included *HCN1*, *GRID1* (common DEGs in both female and male NPCs that intersect with SFRAI genes), and *NRG3* that are mainly involved in synaptic transmission and were detected as common DEGs in both female and male NPCs that intersect with SFRAI genes. Down-regulated POGZ targets included chromosome segregation associated genes such as *HNRNPU* (a common DEG in both female and male NPCs that intersect with SFRAI genes) and *RCC1* (Regulator of Chromosome Condensation 1). In male NPCs, approximately 413 POGZ-bound genes (~ 13% of total targets) were deregulated in HET male NPCs (Fig.64A). Of these 235 genes were upregulated and 178

were down-regulated, accounting for ~ 13% of all differentially up- and down-regulated genes (Fig.64A-C). The up-regulated genes included *HCN1*, *GRID1*, and *NRG3* and the down-regulated ones included *HNRNPU* and *RCC1* as observed in female NPCs. The overlap of POGZ-bound genes with differentially expressed genes in HET vs WT female and male NPCs was significantly higher than expected by chance, indicating that POGZ-bound genes are enriched for differentially regulated genes. Moreover, these observations suggested that POGZ functions as both a transcriptional activator and repressor.

To gain insight into the role of differential occupancy on transcription, differentially bound genes were intersected with differentially expressed genes in HET vs WT female cells. The UpSet plot shows the number of genes in each intersection (Fig.65). The most interesting intersections include 125 genes that were upregulated and lost POGZ binding in female HET NPCs such as *ANKS1B*, *CACNA1C* and *CHRM3* (Fig.65). All these are autism risk genes in the SFARI database. In contrast, 175 genes were downregulated and lost POGZ binding in female HET NPCs such as *ADA*, *AGO2* and *ASPM* (Fig.65). These genes are also listed as autism risk genes in the SFARI database.

Wnt signaling, which is one of the key developmental pathways, was significantly enriched for POGZ binding targets in both female and male cells (Fig.66). Therefore, the differential expression pattern of POGZ bound genes associated with Wnt signaling was investigated. In female NPCs, POGZ bound genes such as *SFRP4*, *NDP* and *GPC4* were up-regulated while *KLF15*, *LGR4* and *CHD8* were down-regulated (Fig.66A). In male NPCs, POGZ bound genes such as *EGF*, *SOX9* and *TMEM64* were up regulated while *FGF10*, *LRP6* and *DKK2* were downregulated (Fig.66B).

In the comparison of HET versus WT female NPCs, Wnt genes that were not only differentially expressed but also associated with loss of POGZ binding included *LGR4*, *SFRP1*, *ASPM*, *GRB10*, *RUVBL1*, *RPS12*, *BCL9*, *KLHL12*, *LRP6*, *TRPM4*, *CELSR1*, *FZD5*, *MCC*, *RBMS3*, *GPC4* and *NDP*. On the other hand, the genes that were associated with gain of binding included *FGFR2* and *MCC*.

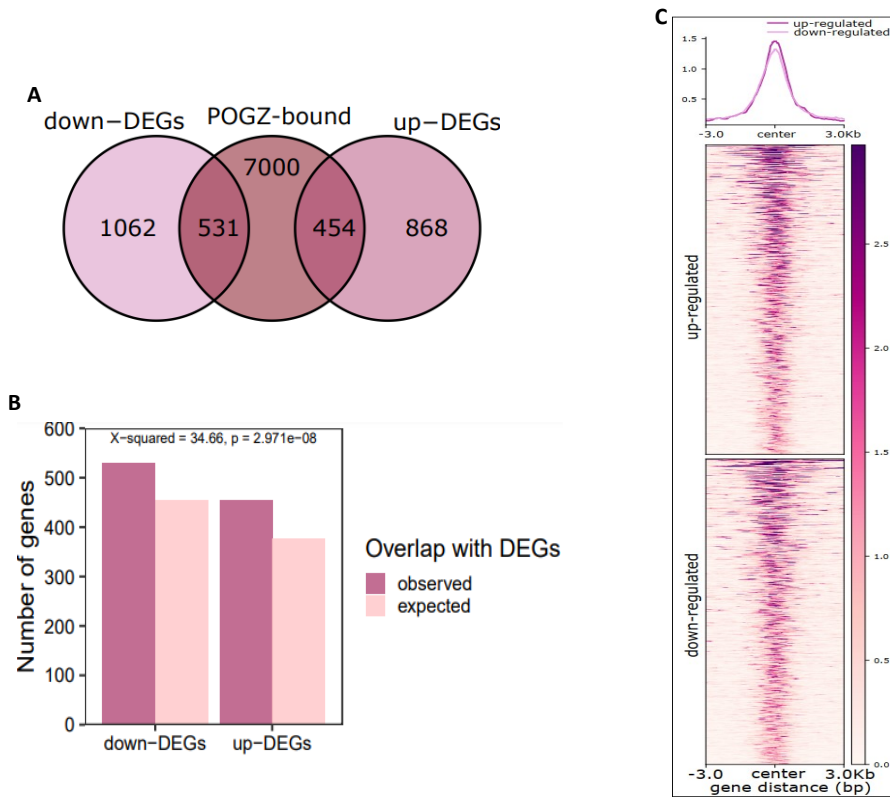


**Fig.63. Venn diagram (A) and bar plots (B) show the distribution for the expected and observed overlap of POGZ-bound and differentially regulated genes in HET vs WT female NPCs. Heatmaps and profile plots (C) show signal over peaks intersecting DEGs in HET vs WT female NPCs indicating that POGZ binds to both up- and down-regulated genes.**

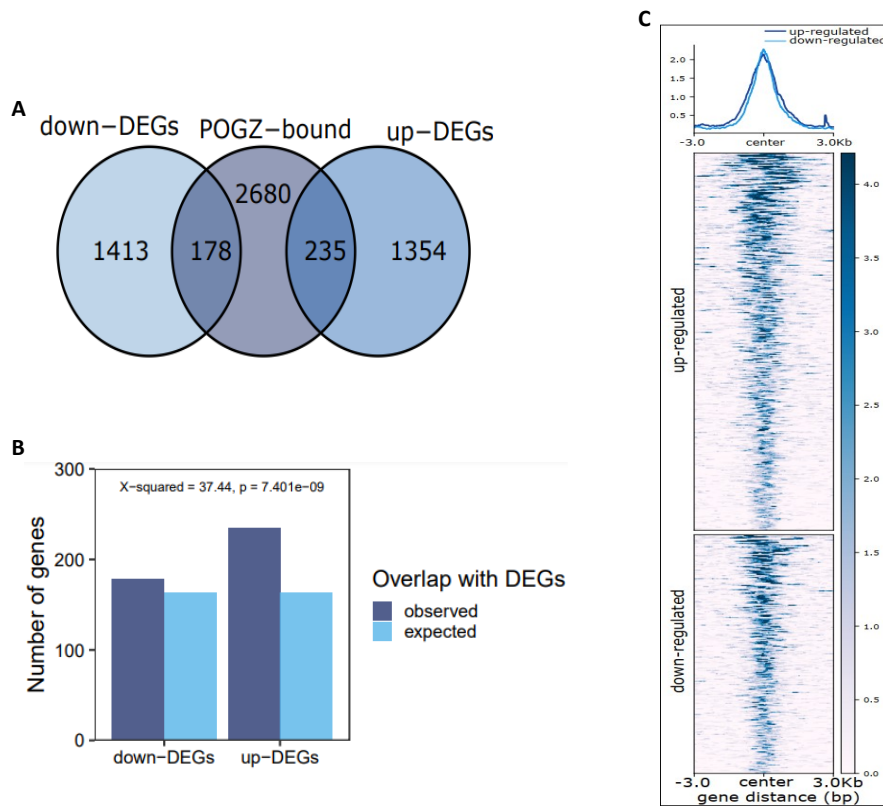


**Fig.64. Venn diagram (A) and bar plots (B) show the distribution for the expected and observed overlap of POGZ-bound and differentially regulated genes in HET vs WT male NPCs. Heatmaps and profile plots (C) show signal over peaks intersecting DEGs in HET vs WT male NPCs indicating that POGZ binds to both up- and down-regulated genes.**

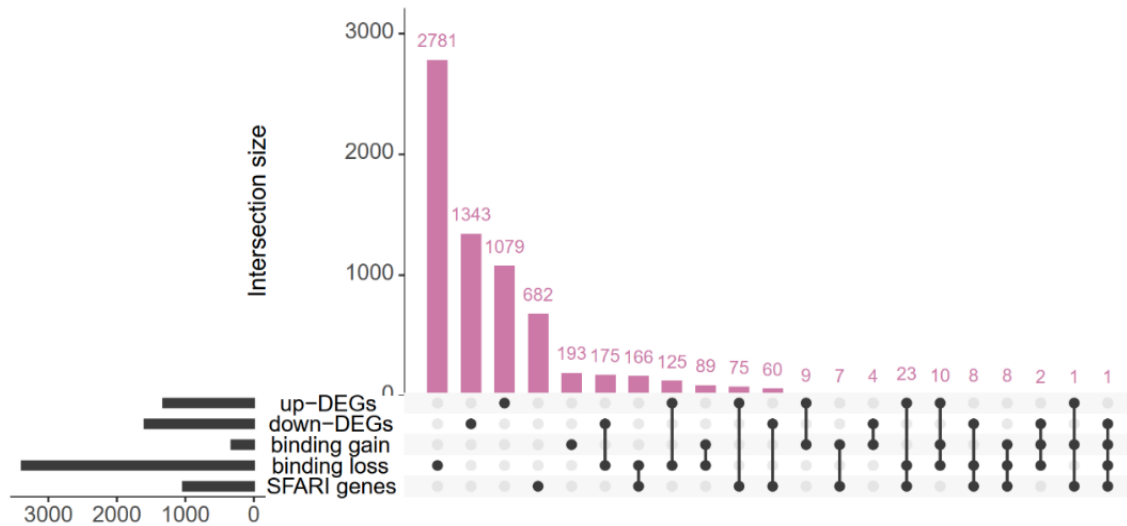


**Fig.65. UpSet plot** shows the number of genes in the intersection of differentially bound genes with differentially expressed genes (DEGs) in HET vs WT female NPCs and autism risk genes included in the SFARI data base.

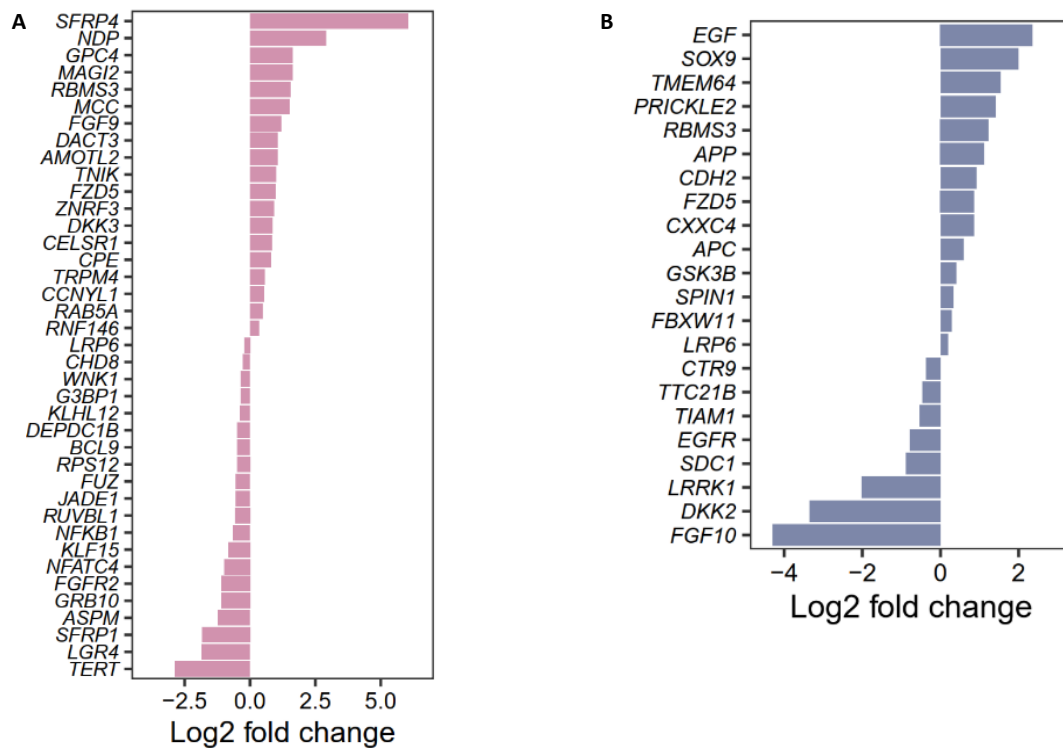


**Fig.66. Bar plots** show the POGZ bound and differentially expressed genes associated with the WNT pathway in both female (A) and male (B) NPCs. Positive log<sub>2</sub> fold changes indicate up-regulation in HET vs WT cells.

## 5 Discussion

Disruptive mutations in the *POGZ* gene have emerged as one of the recent recurrent identified in neurodevelopmental disorders (NDDs), including autism spectrum disorder (ASD) and intellectual disability (ID). Despite their significance, understanding the pathophysiological mechanisms of these mutations during brain development remains challenging. Human induced pluripotent stem cells (iPSCs), with their ability to differentiate into neurons, offer a promising human-based model for investigating the molecular and cellular mechanisms underlying NDDs. In this study, patient derived and CRISPR/Cas9-mediated *POGZ* knockout iPSCs differentiated into neurons in both 2D and 3D models were utilized to explore the cellular and molecular mechanisms of *POGZ* mutations. This project was structured around two key objectives. The first was to generate and validate CRISPR/Cas9-mediated full/heterozygous *POGZ* knockout and patient iPSC-derived neural cells. The second objective focused on the functional analysis of these *POGZ* wild-type and mutant iPSCs and their derived neural progenitor cells (NPCs). Most of *de novo* loss-of-function (LoF) *POGZ* mutations identified in NDD patients are nonsense or frameshift mutations [18, 115], which are believed to result in a potential loss of *POGZ* protein function [18, 115]. Despite that, this hypothesis has not been experimentally tested for the majority of *POGZ* disease variants in human-based models. The lack of widely available iPSCs or rodent models for LoF variants adds to the uncertainty. A recent study reported the generation of human iPSC models from a patient and a healthy individual, but the observed missense variant only showed a subtle differentiation and migration phenotype [115]. To address this gap, we developed CRISPRed iPSC models of *POGZ* frameshift mutations, resulting in complete or partial loss of the *POGZ* protein, including both heterozygous and homozygous mutants with their corresponding isogenic controls. By leveraging CRISPR/Cas9 genome editing, *POGZ* LoF lines were generated in the same genetic background, circumventing the challenge of sourcing multiple patient tissues for iPSC reprogramming and enabling direct comparison with isogenic controls. Through highly efficient *in vitro* neural differentiation approaches, robust models have been established to study the impact of *POGZ* loss on human cortical development.

## 5.1 Generation and validation of CRISPR/Cas9-mediated full/heterozygous *POGZ* knockout and patient iPSC-derived NPCs

First step of this project was to develop a workflow (Fig.67) starting with human skin punch biopsies for isolating fibroblasts, which were then reprogrammed into iPSCs and subsequently differentiated into neuronal progenitor cells (NPCs). Each step of the process was validated by characterizing the corresponding cell type and comparing it with the preceding cell type.

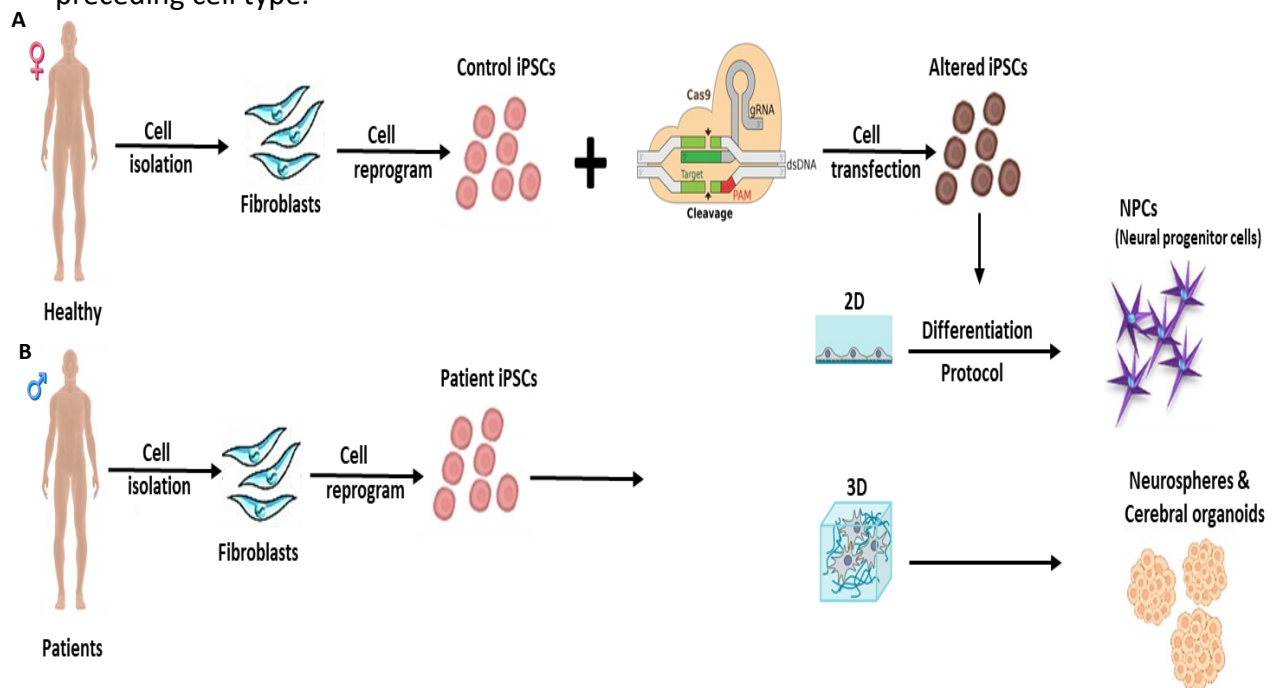


**Fig.67. Diagram of work plan to understand the molecular basis of *POGZ* mutations in 2D and 3D culture models** using neural progenitor cells (NPCs) derived from induced pluripotent stem cells (iPSCs). CRISPR/Cas9-mediated (A) and Patient-specific (B) iPSCs are generated from human somatic cells. After characterization, expansion, and stabilization of iPSCs, CRISPR/Cas9-mediated and ASD patient-derived cells are differentiated in neuronal culture or neurospheres and cerebral organoids.

### 5.1.1 Reprogramming of skin fibroblasts

The first protocol to reprogram human somatic cells into iPSCs as published by Takahashi et al. in 2007[262]. This protocol utilized skin fibroblasts transduced with retroviruses carrying four reprogramming factors, now known as the Yamanaka factors[262]. Fibroblasts are readily accessible and can be cultured with minimal effort under standard conditions. While many other cell types have been shown to be reprogrammable, fibroblasts remain the most commonly used source for this process.

Skin fibroblasts are crucial in synthesizing the extracellular matrix and collagen. A key protein in collagen synthesis is SERPINH1, a serine proteinase inhibitor of the serpin superfamily, also known as HSP47 making it a suitable fibroblast marker. Located in the endoplasmic reticulum, SERPINH1 acts as a molecular chaperone, interacting with collagen to facilitate its maturation [263, 264].

Transduction of the reprogramming factors initiates a process that alters the cells' methylome, transcriptome, and proteome. During this process, genes responsible for self-renewal and maintaining pluripotency are upregulated, while those characteristics of the somatic donor cells are silenced. The morphology of the reprogrammed cells changes, and they become capable of maintaining the pluripotent state independently.

In this study, fibroblasts from different donors were reprogrammed. All fibroblasts exhibited expression of *SERPINH1* and had the typical morphology described as "plump spindle-shaped or stellate-shaped cells (active fibroblasts) with a centrally placed oval or round nucleus" [265]. Regardless of the reprogramming method used, the cells' morphology transitioned to the characteristic ESC- and iPSC-like morphology. The reprogrammed cells became round, displayed prominent nucleoli, and had a high nucleus-to-cytoplasm ratio. They began to form the typical compact colonies observed in ESCs, featuring well-defined smooth edges and a flat overall appearance [266].

It is well known that copy number variations and chromosomal rearrangements are common abnormalities during reprogramming [267, 268]. Therefore, the karyotype of the cells was checked after the reprogramming and after the CRISPR/Cas9 genome editing revealing a normal karyotype of 46, XX or 46, XY, cells respectively. Consistent with previous publications [269], RT-qPCR analysis revealed elevated expression levels of pluripotency markers, except for *KLF4*, which was downregulated compared to the original fibroblasts. *KLF4*, a transcription factor involved in skin barrier formation, is relatively highly expressed in skin fibroblasts [270, 271]. Immunofluorescent staining for stem cell markers further confirmed the successful reprogramming of skin fibroblasts into iPSCs [272]. Additionally, routine mycoplasma testing was performed, and all fibroblasts tested negative for HIV, HBV, and HCV in the "Zentrallabor der Universitätsmedizin Mainz".

One limitation was that further experiments needed to confirm and assess the pluripotency of the iPSCs. A common method to demonstrate the pluripotent state of generated iPSCs is differentiation into all three germ layers. This can be achieved either through a teratoma assay, where iPSCs are injected into immunosuppressed mice, or via an in vitro differentiation assay where iPSCs spontaneously differentiate [262, 272, 273].

A protocol was established to directly differentiate iPSCs into all three germ layers: endoderm, mesoderm, and neuroectoderm, confirming that the reprogramming method used in our lab produces iPSCs with the capability to differentiate into cells from all three germ layers. While this protocol successfully validated the pluripotency of iPSCs generated through such reprogramming protocol, the specific iPSC lines used in this study were not subjected to this three-germ layer differentiation test.

### **5.1.2 CRISPR/Cas9 mediated genome editing in iPSCs:**

The advent of CRISPR-Cas9 technology has revolutionized the field of genome editing, offering unprecedented precision and efficiency in modifying the genetic code. Originally derived from the adaptive immune system of bacteria [226], CRISPR-Cas9 uses a guide RNA (gRNA) to direct the Cas9 endonuclease to a specific DNA sequence, where it introduces double-strand breaks. Cells have two repair pathways available: non-homologous end-joining (NHEJ) or homology-directed repair (HDR) pathways[225, 229]. This targeted approach allows for precise genetic modifications, including gene knockouts, insertions, and corrections[229].

In this project, CRISPR-Cas9 genome editing was applied to iPSCs to introduce or correct specific *POGZ* mutations. To introduce *POGZ* mutation, gRNAs were designed to introduce the deletions in the first coding exon of *POGZ*. This exon presents in all isoforms to ensure complete allele deletion via non-homologous end-joining (NHEJ). This approach allowed the generation of isogenic female cell lines, where a heterozygous (A2D5) or compound heterozygous (A2A1) *POGZ* mutation differs between the edited and unedited cells. Such models allow studying the pathophysiology of the disease (WHSUS) in a controlled environment, as they recapitulate the genetic context.

Conversely, CRISPR-Cas9 can be used to correct genetic mutations in iPSCs derived from patients via homology-directed repair (HDR). Repairing the defective gene is not only important to restore normal function to the cells but also to generate isogenic wildtype control cell lines. Once corrected, these iPSCs can be differentiated into various cell types for further study, offering insights into the cellular consequences of gene correction [274, 275].

In this project, WUSUS patient derived iPSCs (C34) carrying a heterozygous 1 bp insertion (c.2470dup) were supposed to be corrected to generate an isogenic wildtype control. Unfortunately, the correction of the patient iPSCs (C34) was unsuccessful after several

attempts. The main limitation for such correction is associated with homology-directed repair (HDR) efficiency. First, HDR efficiency is inherently lower than non-homologous end joining (NHEJ), the predominant DNA repair pathway in mammalian cells[276]. This inefficiency is particularly pronounced in iPSCs [277]. While NHEJ quickly ligates broken DNA ends, often leading to insertions or deletions (indels) rather than precise corrections, HDR relies on a repair template to guide accurate repair. The competition between these two repair pathways often results in a lower frequency of HDR events [278].

Moreover, the design of HDR repair templates is critical for achieving high-efficiency genome editing. The length and sequence of the homologous arms flanking the mutation site can significantly impact HDR efficiency. In this project, the homology arms to correct the WHSUS patient mutation were 50 nt and 80 nt flanking the mutation site. Such short homologous arms may not provide sufficient homology, longer arms may be more effective but also increase the risk of unwanted genomic rearrangements [279, 280].

In this project, electroporation was used as a method for the transfection and delivery of HDR templates into iPSCs. Although the electroporation can introduce repair templates efficiently high cell death afterwards decreases the chance of finding the clone with the right insertion. Other methods might be applied like viral vectors that can deliver large quantities of DNA but carry risks of insertional mutagenesis. Lipid nanoparticles can be also used, and they are less invasive but require optimization for effective delivery into iPSCs [280, 281].

Another way to increase the HDR efficiency in the patient iPSCs is by synchronizing iPSCs to enhance HDR during the S and G2 phases as it is known that HDR is closely linked to the cell cycle, specifically during these phases when cells are actively replicating DNA[282]. Using cell cycle-modulating agents can also be a strategy to improve HDR efficiency[282, 283] . For hPSCs, the Fluorescence Ubiquitination Cell Cycle Indicator (FUCCI) system was used for live imaging and sorting of hPSCs based on cell cycle phases. It has limitations such as difficulty in sorting large cell numbers, inability to distinguish between S and G2/M phases, and early G1 and quiescent cells[284, 285]. Alternatively, small molecules were traditionally used for cell cycle synchronization in somatic cells include G1 inhibitors like lovastatin[286] and mimosine [287], G1/S inhibitors like thymidine and aphidicolin, and G2/M inhibitors like colcemid and nocodazole[285]. While some of these methods have

been applied to hPSCs, they often cause issues like cell death, genomic instability, and effects on pluripotency, which need further investigation[285].

To boost HDR efficiency, compounds such as SCR7 and RS-1 have shown promise in increasing HDR rates by inhibiting NHEJ or promoting repair pathway choice. These agents are used in conjunction with CRISPR-Cas9 to improve the likelihood of precise genetic corrections [288, 289]. Although the effects of such compounds on iPSCs have been studied before [290] they should be carefully validated in our lab.

Ultimately, despite the promising potential of CRISPR-Cas9 in iPSC research, several challenges remain to be resolved. One major concern is off-target effects, where the Cas9 enzyme may introduce cuts at unintended genomic sites, potentially leading to genomic instability and unintended genetic alterations [291]. While advancements in gRNA design and the generation of high-fidelity Cas9 variants have helped to minimize these off-target effects, continuous improvements are essential to enhance the safety and precision of CRISPR-based genome editing [292].

### **5.1.3 Differentiation of induced pluripotent stem cells (iPSCs) into neural progenitor cells (NPCs)**

In this PhD project, a specific differentiation protocol was conducted by requiring only a media change to induce differentiation, which simplifies a previous differentiation process by eliminating the need for intermediate steps such as embryoid body formation, co-culture with feeder cells. This simplified protocol depends on the inhibition of the BMP and TGF $\beta$  signaling pathways, hence termed "dual SMAD inhibition"[293], inducing a neural conversion in the treated iPSCs (and ESCs), guiding them toward a neural progenitor cell (NPC) fate [294].

This method has been shown to be less prone to failure due to its reduced complexity, fewer procedural steps, and the elimination of manual selection, which can introduce variability in differentiation outcomes. The NPCs produced using this approach exhibited a significant increase in *PAX6* expression, along with a moderate increase in *SOX2* and *NESTIN* expression at the RNA level, confirming successful induction of neural progenitors. Pluripotency markers, typically high in iPSCs, were markedly downregulated, further validating the transition from a pluripotent state to a neural progenitor state.

The expression of *SOX2*, a marker shared by both iPSCs and NPCs due to their mutual ability to self-renew, showed a modest change, which was anticipated given its dual role

in maintaining both pluripotency and neural progenitor identity. Successful differentiation of iPSCs into NPCs was further confirmed through immunofluorescent staining, providing visual confirmation of neural progenitor marker expression and the downregulation of iPSC markers. This robust and reliable differentiation protocol has been critical in advancing the understanding of neural development and holds significant promise for studying neurodevelopmental disorders in vitro.

#### **5.1.4 Difference between studying in 2D and 3D cell culture models**

Neurodevelopmental disorders (NDDs), including ASD, ID, and others, are complex conditions resulting from a combination of genetic and environmental factors. Traditional animal models have provided significant insights into the pathophysiology of NDDs, but they often fall short in recapitulating the full spectrum of human brain development and the intricate mechanisms underlying these disorders. The advent of human induced pluripotent stem cells (iPSCs) has revolutionized the study of NDDs by enabling the generation of patient-specific neurons, thereby providing a human-based platform for investigating the molecular and cellular mechanisms underlying these conditions. Within this framework, both 2D and 3D in vitro models, such as neurospheres and brain organoids, have emerged as invaluable tools for studying NDDs.

A study done by Chandrasekaran *et al.*, was questioning if hiPSCs that are often differentiated into neural progenitor cells (NPCs) using 3D culture methods, are considered superior to monolayer (2D) neural induction. This study aimed to compare the efficiency of 2D versus 3D induction methods in generating NPCs, and subsequently neurons and astrocytes. Neural differentiation was assessed qualitatively by immunocytochemistry and quantitatively by flow cytometry, focusing on NPC markers (SOX1, PAX6, NESTIN), neuronal markers (MAP2, TUBB3), cortical layer markers (TBR1, CUX1), and glial markers (SOX9, GFAP, AQP4). Electron microscopy revealed that both methods produced morphologically similar neural rosettes. However, 3D neural induction resulted in a higher number of PAX6/NESTIN double-positive cells, and the derived neurons exhibited longer neurites. Conversely, 2D neural induction led to a greater number of SOX1-positive cells. While 2D monolayer induction produced slightly less mature neurons at an early differentiation stage, patch-clamp analysis showed no significant differences in electrophysiological properties between the two methods. Overall, 3D neural induction increased the yield of PAX6+/NESTIN+ cells and generated

neurons with longer neurites, which may be advantageous for producing forebrain cortical neurons, underscoring the potential of 3D neural induction regardless of the genetic background of the hiPSCs[295].

#### **5.1.4.1 Advantages and Limitations of 2D Models**

2D culture systems, where iPSCs are differentiated into neural progenitor cells (NPCs) and further into neurons, have been widely used to study the molecular and cellular phenotypes associated with NDDs. The simplicity of 2D cultures allows for high-throughput screening and precise control over the cellular environment, making it easier to dissect specific molecular pathways and conduct pharmacological testing[296]. For example, in a study using iPSC-derived neurons from patients with Rett syndrome, a monogenic form of ASD, it was shown that the neurons exhibited defects in synaptic function and dendritic morphology, which could be rescued by IGF-1 treatment [297]. This kind of targeted investigation is facilitated by the controlled environment of 2D cultures. However, while 2D models provide a reductionist approach that is highly valuable for mechanistic studies, they lack the spatial organization and complex cell-cell interactions that are characteristic of the developing brain [296]. This limitation hinders the ability to fully recapitulate the microenvironment of the human cortex, which is critical for understanding how neurons develop, migrate, and establish synaptic connections *in vivo*. Consequently, while 2D models are powerful for initial studies, they are often insufficient for capturing the full complexity of NDDs [298].

#### **5.1.4.2 The emergence of 3D Models: Neurospheres and Brain Organoids**

3D culture systems, including neurospheres and brain organoids, have been developed to overcome the limitations of 2D cultures by more closely mimicking the architecture and cellular diversity of the developing brain. Neurospheres are spherical clusters of NPCs that can differentiate into various neural cell types, including neurons, astrocytes, and oligodendrocytes, within a 3D context. Brain organoids, on the other hand, are more complex 3D structures that can recapitulate many aspects of early brain development, including the formation of distinct brain regions and cortical layers [298, 299].

Neurospheres have been particularly useful in modeling early neurodevelopmental processes and have been employed to study NDDs such as ASD [300-303]. For instance, Oliveira et al. (2015) used *SCN2A* knock out and *RELN* mutant autistic patient-derived iPSCs to generate neurospheres and compare the effect of both mutations on differentiation

and migration. The study showed that *SCN2A* doesn't have a main role during neuronal migration and led to hypothesize that *RELN* is related to neuronal migration and growth[304].

Brain organoids take this approach a step further by providing a more comprehensive model of brain development. Organoids can be cultured for extended periods, allowing for the study of later stages of neurodevelopment, including neuronal migration, synaptogenesis, and the formation of cortical layers. This makes organoids a powerful tool for studying NDDs that involve complex developmental processes [245]. For example, brain organoids derived from patients with microcephaly, a condition often associated with ID, have revealed deficits in NPC proliferation and abnormal neuronal differentiation, providing insights into the cellular mechanisms underlying this disorder [246]. Moreover, organoids have been used to model the effects of genetic mutations associated with NDDs. Lancaster et al. (2013) developed brain organoids from iPSCs of patients with microcephaly caused by mutations in the *CDK5RAP2* gene, demonstrating that these organoids exhibited reduced cortical size and impaired NPC function, thereby mimicking the patient's phenotype [246]. This study underscores the potential of brain organoids to model patient-specific disease phenotypes and to serve as a platform for studying the impact of genetic mutations on brain development.

#### **5.1.4.3 Challenges and Future Directions**

Despite their promise, 3D models also come with challenges. One of the primary limitations of brain organoids is the lack of vasculature, which limits their growth and leads to necrosis in the inner regions of the organoid, thereby constraining the study of later stages of neurodevelopment. Additionally, the variability in organoid formation and differentiation poses a challenge for reproducibility and standardization, which are critical for large-scale studies and therapeutic screening [169].

Furthermore, while 3D models provide a more realistic environment compared to 2D cultures, they still lack the full complexity of an *in vivo* brain. For instance, organoids typically do not contain all the cell types present in the brain, such as microglia, and they do not fully replicate the intricate cell-cell and cell-matrix interactions that occur *in vivo* [170]. Moreover, the use of brain organoids for long-term studies is limited by their relatively immature state, which corresponds to early fetal development rather than later stages of brain maturation [169, 170].

To address these challenges, ongoing efforts focus on enhancing the complexity and maturity of 3D models. For example, integrating microfluidic systems to supply nutrients and remove waste could potentially overcome the issue of necrosis in organoids, allowing them to grow larger and more complex [305-307]. Additionally, co-culture systems that incorporate microglia and other non-neuronal cells are being developed to more accurately model the brain's cellular environment [308, 309]. Furthermore, advancing protocols for organoid maturation could enable the study of later developmental stages, providing deeper insights into the pathophysiology of NDDs [310].

## **5.2 Functional analyses of *POGZ* wildtype/mutant iPSCs and iPSC-derived NPCs**

The second aim was to characterize the effect of different *POGZ* mutations on *POGZ* protein and its function. Two different N-terminal mutations induced in female wildtype iPSCs by genome editing resulted in *POGZ* heterozygous and compound heterozygous iPSCs. A C-terminal mutation in male patient iPSCs was also investigated. WHSUS is caused by heterozygous mutations in the *POGZ* gene. A loss-of-function mechanism with an autosomal dominant inheritance underlying WHSUS is presumed. Supported by patients, it has been noticed that the symptoms of WHSUS are variable depending on the type of the *POGZ* genetic variants; missense, nonsense and frameshift variants and deletions [103]. To induce mutations in *POGZ*, CRISPR/Cas9 genome editing was used to introduce frameshift mutations into coding exon 1 thus generating the two female heterozygous and compound heterozygous iPSC lines. In the male patient iPSC line, the heterozygous mutation close to the C-terminus also leads to a frameshift and a premature stop codon.

### **5.2.1 Effect of missense *POGZ* mutations on its expression and cellular distribution in iPSCs and NPCs**

Both *POGZ* heterozygous and compound heterozygous nonsense frameshift mutations in the female iPSCs and NPCs were expected to cause an early stop codon (PTC) that might lead to non-sense mediated mRNA decay (NMD) according to the prediction of NMDescPredictor (*POGZ* NM\_015100.4) (Fig.68A) [103]. Unexpectedly, the RT-qPCR and pyrosequencing results indicated that the mutant allele was still expressed at similar levels as the wildtype allele in iPSCs and NPCs. Typically, NMD is triggered when a PTC is located more than 50-55 nucleotides upstream of the last exon-exon junction. If the PTC is closer, the exon junction complex (EJC) may not be deposited at a sufficient distance downstream from the stop codon to trigger NMD [311-313]. This phenomenon is known as the "last exon rule" which can explain only ~50% of the systematic variation in NMD efficiency

across PTCs [313, 314]. In the female heterozygous A2D5 and compound heterozygous A2A1 cell lines, the PTCs do not follow the canonical NMD rule, "last exon rule". However, "the start-proximal rule", which is a "noncanonical" rule, can explain evading NMD in mutant female cells [311-313]. In the heterozygous A2D5 cells, PTC is 36 nucleotides upstream of the splice region. On the other hand, in the compound heterozygous A2A1 cells, the two PTCs are 35 and 57 nucleotides upstream of splice region. Such number of nucleotides to the PTC would interfere with EJC positioning resulting in escaping the NMD "the start-proximal rule" [311-313]. This rule indicates the NMD efficiency is reduced in the 5'-most ~150 nucleotides of a transcript's coding region, with efficiency gradually increasing from 5' to 3' within this segment with the possibility of reinitiation of translation at a downstream start codon [313].

Another explanation could be the downregulation in one of the core components of the NMD pathway, UPF2, that has been noticed in the mutant female cells in the RNA seq data. This can result in the escape of the transcripts from degradation even if they contain PTCs [315, 316]. On the other hand, the RNA seq data also shows the downregulation of some of the protective RNA-binding proteins (RBPs) in mutant female cells such as PABPC1 and PABPC4 that bind to poly (A) tail in the 3' UTR and stabilize the mRNA to evade NMD [317, 318].

For the *POGZ* heterozygous patient male iPSCs and NPCs, the frameshift mutation is located in exon 17. However, the premature stop codon (PTCs) locates in the last coding exon (exon 19) suggesting escape from NMD according to the last exon rule and the prediction of Nagy, D., et al (Fig.68B) [103]. The RT-qPCR and pyrosequencing experiments show as expected that the mutant allele is still transcribed making the *POGZ* mRNA level in the mutant male iPSCs and NPCs insignificantly different from the wildtype level in the male iPSCs and NPCs. The absence of downstream EJCs might explain how the patient transcript evades the NMD as the PTC is in the last coding exon with 1601 nucleotides upstream of the 3' UTR [311, 313]. In addition, such PTC location is close to the poly(A) tail making it less likely to be identified by the NMD machinery. This proximity of the PTC to the poly(A) tail influences the binding of NMD factors like UPF1 impairing NMD induction [315, 318]. Understanding these mechanisms helps in predicting if truncated proteins can be translated and, potentially leading to functional or partially functional protein products.

On protein level, both N- (abcam#171934) and C- (Bethyl#A302-510A) terminal antibodies detected approximately 50% of the normal POGZ protein levels in *POGZ* heterozygous A2D5 female iPSCs and NPCs. Although the mutant transcript escaped the NMD, the resulting truncated protein, predicted to be 3.35 KDa in size (corresponding to only 28 amino acids), was too small to be detected by the western blot [319]. To explore the potential presence of an alternative downstream start codons in exons 2 and 3 of the mutant allele in A2D5 cells, the NCBI ORF Finder tool was used. This tool identified 5 potential alternative open reading frames (ORFs) in the mutant allele in A2D5 cells considering "ATG" and alternative initiation codons as start codon (Fig.69). In the *POGZ* compound heterozygous A2A1 female iPSCs and NPCs, it was expected to have no full-length undetectable protein for the similar reasons. The resulting truncated protein would consist of 10 and 27 amino acids, with predicated molecular weights of 1.19 KDa and 3.14 KDa, respectively, from the two mutant transcripts of each allele. Western blot using the C-terminal antibody (Bethyl#A302-510A) revealed a faint band in the mutant A2A1 NPC lysates, but not in wildtype A2 NPC lysates, suggesting the presence of a smaller protein than the wildtype POGZ band (Fig.28C). This finding indicates that an alternative downstream start codon may be present, resulting in the production of an N-terminally truncated POGZ protein. The NCBI ORF Finder tool predicted 5 alternative ORFs from one of the mutant alleles (Fig.70A), and 4 alternative ORFs from the other allele (Fig.70B). Those results suggest that the N-terminal truncated POGZ protein in the compound heterozygous female cells could arise from the use of these alternative start codons.



**Fig.68. Using NMDEscpredictor tool to predict the effect of POGZ mutations depending on Nagy, D., et al.**

A: In A2D5 female line carrying N-terminus heterozygous mutation, mRNA was expected to subject to degradation by NMD. B: In C34 male line carrying HPZ-domain heterozygous mutation, mRNA was expected to escape to degradation by NMD.

Mark subset... Marked: 0 Download marked set as Protein FASTA

Label	Strand	Frame	Start	Stop	Length (nt   aa)
ORF1	+	1	22	>282	261   86
ORF5	-	3	<281	96	186   61
ORF4	-	2	231	103	129   42
ORF3	+	2	167	268	102   33
ORF2	+	2	<2	88	87   28

**Fig.69. Prediction of alternative downstream start codons using NCBI ORFinder tool in A2A5 female line carrying heterozygous POGZ mutation. ORFs found on the allele with one nucleotide deletion.**

**A**

Mark subset... Marked: 1 Download marked set as Protein FASTA

Label	Strand	Frame	Start	Stop	Length (nt   aa)
ORF1	+	1	52	>282	231   76
ORF5	-	3	<281	96	186   61
ORF4	-	2	231	103	129   42
ORF3	+	2	167	268	102   33
ORF2	+	2	<2	88	87   28

**B**

Mark subset... Marked: 0 Download marked set as Protein FASTA

Label	Strand	Frame	Start	Stop	Length (nt   aa)
ORF2	+	3	45	>275	231   76
ORF4	-	3	<274	89	186   61
ORF3	-	2	224	96	129   42
ORF1	+	1	160	261	102   33

**Fig.70. Prediction of alternative downstream start codons using NCBI ORFinder tool in A2A1 female line carrying compound heterozygous *POGZ* mutation.** A: ORFs found on the allele with one nucleotide deletion. B: ORFs found on the allele with seven nucleotides deletion.

For WHSUS patient cells, as anticipated, reduced *POGZ* protein was detected in both iPSCs and NPCs in the western blot. A truncated protein was detected in NPC lysates using an additional N-terminal antibody (Bethyl#A302-509A) which aligns with the fact that the PTC in these patient cells locates in the last coding exon, resulting in the termination of the protein at amino acid 864.

*POGZ* mutations that result in the deletion or truncation of the CENP-DB domain impair the nuclear localization of *POGZ* [244]. In this study, the localization of *POGZ* protein remained unchanged in both female and male mutant cells, as none of the mutations studied affected the CENP-DB domain. This suggests that the effect of *POGZ* mutations on its cellular localization is mutation dependent, varying according to the type and the position of the mutation. Therefore, heterozygous frameshift *POGZ* mutations, either in the N-terminus or in the HP1-binding zinc finger-like (HPZ) domain, escape NMD and decrease protein expression without affecting its nuclear localization.

## 5.2.2 *POGZ* variants effects in 2D culture models:

### 5.2.2.1 Effect on proliferation

By investigating proliferation in 2D culture, findings suggest that *POGZ* mutations did not significantly alter NPC proliferation under the experimental conditions in this study, as indicated by flow cytometry analysis of Ki67 and PHH3 markers, which revealed no differences in proliferation between male and female heterozygous mutant NPCs and wildtype controls. Given *POGZ*'s established role in essential mitotic processes, as well as its impact on NPC proliferation [113, 135], the absence of a proliferation difference here could reflect specific mutation effects, distinct domain involvement, or passage number rather than a technical issue with the assays. In this study, the passages range (13-19 for female NPCs and 8-17 for male NPCs) may have influenced these dynamics, aligning with prior findings that *POGZ*'s influence on proliferation varies with mutation type, affected domain, and cellular passage number. Comparative analysis with other studies supports

this interpretation. Previous studies showed that the effect of *Pogz* depletion on proliferation is significant in late cell passages (>15) resulting in reduced number of (PHH3)-positive cells [116]. Also 21-day old neural rosettes had significantly reduced level of both PHH3 and MKI67 in *POGZ*<sup>-/-</sup> lines, with a moderate reduction in PHH3+ cells observed in the *POGZ*<sup>+/-</sup> line after performing immunostaining [135].

In a study by Suliman-Lavie, R., *et al.*, *Pogz*'s role in embryonic neurogenesis was investigated by examining PAX6 and TBR2, markers for apical and intermediate neural progenitors, respectively, in the developing cerebral cortex (E15.5) of *Pogz*-conditional knockout mice. These brain-specific knockout mice were generated using the Cre-lox system, with loxP sites flanking exons 13–19 [134]. These exons encoded the DDE transposase domain, the CENP DNA binding domain, and part of the zinc finger domain that binds HP1 proteins (HPZ) [134]. This study found a modest increase in the TBR2+ layer length in *Pogz*-deficient mice due to accelerated cell-cycle exit, leading to a reduction in symmetrical divisions of NPCs and a corresponding increase in differentiated cells produced by asymmetric division. Daughter cells resulting from asymmetric division were able to differentiate into neurons or migrate to the subventricular zone to become intermediate progenitor cells (TBR2+), with no significant change in the PAX6+ layer or overall cortical thickness [134]. In adult mice, the proliferation (Ki67+ cells) did not differ during neurogenesis in *Pogz*-deficient mice [134].

Additionally, increased BrdU incorporation was detected in patient-derived NSCs carrying a *de novo* missense Q1042R mutation in the CENP-DB domain. This increased BrdU incorporation revealed more cells are in the active DNA synthesis phase of the cell cycle (S-phase) in the patient-derived NSCs compared to control NSCs and hence more proliferation [115].

These studies showed findings that vary with what has been found in this study but support that the effect of *POGZ* mutation on proliferation differ not only depending on the mutation type and which domain is affected but also how old the cells are in terms of passage number. In this project, both mutations in the N-terminus of *POGZ* like in female mutant A2D5 NPCs, and in the HPZ domain like male mutant C34 NPCs show no significant change in Ki67+ and PHH3+ cells which is similar to the findings in adult *Pogz*-deficient mice neurogenesis [134]. Another reason for the discrepancy between the published studies and the results of this work could be that such proliferation assays in 2D culture

come with limitations and potential sources of error. The Ki67 assay detects the Ki67 protein, a marker present throughout the cell cycle, thus providing an indication of cell proliferation but not differentiating between specific phases of the cell cycle [320] ( Fig 71-72).

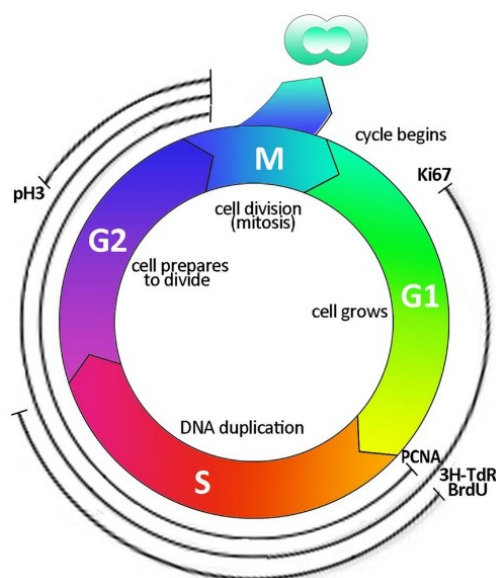


**Fig.71. Cell cycle labelling.** Schematic representation of the cell cycle and indication of the principal markers that are traditionally used to label the different phases. 3-TdR, tritiated thymidine; BrdU, 5-bromo-2'-deoxyuridine; PCNA, proliferating cell nuclear antigen; pH3, phosphohistone H3; G1, gap 1 phase; S, synthesis; G2, gap 2 phase; M, mitosis [321].

This lack of phase-specific information can lead to variability in the proliferation rates reported, influenced by factors such as cell type and experimental conditions [320, 322]. On the other hand, the PHH3 assay targets histone H3 phosphorylated at serine 10, which specifically marks cells in mitosis. This short window of PHH3 expression in mitosis may lead to an underestimation of proliferation if the mitotic index is low or if cells progress rapidly through mitosis [323]. However, this issue was ruled out as a factor in this study, given the consistent results observed with the Ki67 assay with no difference between mutant and wildtype NPCs. To provide a more comprehensive view of cell proliferation and cell cycle dynamics, complementary assays could be included. For instance, combining Ki67 and PHH3 with BrdU/EdU incorporation assays can offer additional insights into DNA synthesis and cell cycle phase progression [324]. Additionally, integrating imaging techniques such as live-cell microscopy can help monitor cell proliferation in real-time and reduce issues related to transient mitotic phases [325, 326]. By addressing these technical

challenges, more precise and consistent measurements of NPC proliferation can be achieved.

CCND2 is a well-known cell cycle marker and a critical regulator of cell growth and proliferation. It plays a key role in controlling the G1-S transition, where the cell progresses from the G1 phase (cell growth) to the S phase (DNA replication) in preparation for cell division (Fig.72) [327]. In addition, frameshift and stop-gain variants in the proximal portion of *CCND2* would lead to G1 Phase Arrest and are associated with human microcephaly, symmetric short stature, and mild developmental delay [328-330].

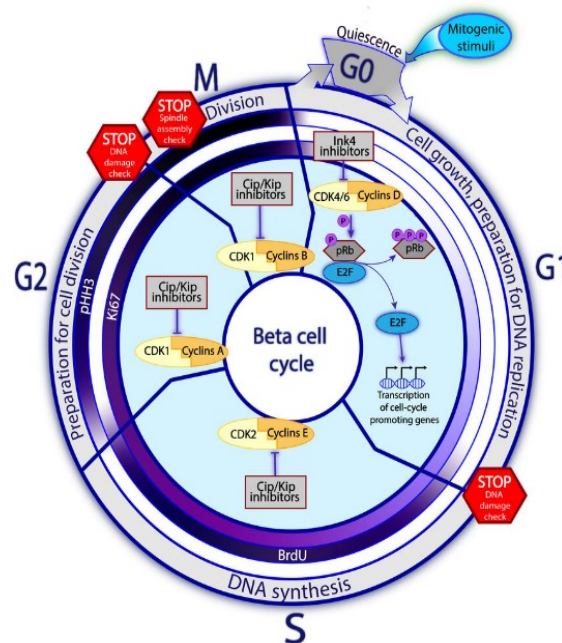


**Fig.72. Principles of cell cycle in beta cells.** Upon mitogenic stimulation, Cyclins D and CDK4/6 complexes form, leading to pRb inactivation and cell cycle entry. This process releases E2F transcription factors, which enhance the expression of cell cycle-promoting genes. Different Cyclins-CDK complexes dominate at various cell cycle phases: Cyclins D-CDK4/6 in G1, Cyclins E-CDK2 in S phase, Cyclins A-CDK1 in G2, and Cyclins B-CDK1 in M phase. These activities are regulated by cell cycle inhibitors, including the Ink4 and Cip/Kip families. Cells must pass checkpoints that assess DNA integrity and cell conditions, with failure resulting in arrest or apoptosis. The inner circles in Figure 1 represent common proliferation markers: Ki67, BrdU, and pHH3, with color intensity indicating their abundance in each phase[331].

RT-qPCR analysis revealed no change in *CCND2* expression in female NPCs carrying a *POGZ* heterozygous nonsense frameshift mutation near the N-terminus. In contrast, male NPCs with a *POGZ* mutation in the HPZ domain (resulting in a threonine to asparagine substitution at position 824 and truncation at amino acid 864) showed reduced *CCND2* expression.

To examine the number of cells entering the G1- and S- phase in mutant NPCs, click iT-Edu assay was used. Similar to BrdU assays, this assay evaluates the incorporation of a thymidine analog of into DNA during the active DNA synthesis phase of the cell cycle (S-phase) (Fig.72). The results showed no significant difference in the number of cells in the

S-phase or G2-phase for either heterozygous *POGZ* frameshift mutant NPC line (mutations located in the N-terminus in female NPCs and the HPZ domain in male NPCs) when compared to their respective wildtypes. Moreover, the number of cells in the G1 phase did not differ significantly in both mutant NPCs, a slight increase was observed in male mutant NPCs.

In mutant male NPCs with reduced *CCND2* expression, no G1-phase arrest was observed; instead, there was only a slight, non-significant increase in cells in G1. Interestingly, RNA-seq data revealed an upregulation of *CDKN1A* (p21) in these HPZ domain heterozygous mutant male NPCs. *CDKN1A* (p21) is a cyclin-dependent kinase inhibitor (CDKI) that modulates CDK4/6 activity, which typically partners with cyclins like *CCND2* to drive cell cycle progression from G1 to S phase [332, 333]. The combination of reduced *CCND2* and increased *p21* levels would typically be expected to promote G1 arrest by inhibiting CDK4/6 activity. These findings could relate to prior observations by Nozawa *et al.*, where the HPZ domain, particularly the region spanning amino acids 791–850, was identified as a key interactor with HP1 $\alpha$ , influencing mitotic progression and cell proliferation [113]. Thus, while reduced *CCND2* and elevated *p21* might suggest a G1-phase arrest, the functional role of the HPZ domain may counterbalance these effects, allowing cell cycle progression to continue in the mutant NPCs.

#### **5.2.2.2 Effect on cell survival:**

To analyze the impact of *POGZ* on apoptosis and DNA damage, previous analysis of *Pogz*<sup>-/-</sup> mESCs found that *POGZ* depletion led to an increase in apoptotic cell death, indicated by annexin-V staining, suggesting that *POGZ* is critical for normal mitotic progression and cell viability [116]. Additionally, *POGZ* was shown to support homology-directed DNA repair through an HP1-dependent mechanism, with *POGZ* deficiency impairing the repair of double-strand breaks (DSBs) [136].

In this study, apoptosis (via Cas3 marker) and DNA damage (via  $\gamma$ -H2AX marker) were assessed in NPCs with heterozygous N-terminal and HPZ-domain *POGZ* mutations in female and male lines, respectively. Results indicated no significant increase in apoptosis or DNA damage in these mutant NPCs compared to wildtype. However, both mutant lines showed a trend toward a higher proportion of Cas3-positive cells than wildtype, possibly reflecting subtle compensatory mechanisms that mitigate the potential impact of these mutations on cell survival and DNA repair pathways.

### 5.2.2.3 Effect on neural differentiation:

In previous studies, POGZ deficiency has been associated with impaired neural differentiation, often linked to disrupted cell proliferation in both mouse models and human cell [116, 134, 135].

Analysis of 26-day-old neural rosettes derived from both *POGZ*<sup>-/-</sup> and *POGZ*<sup>+/-</sup> hESCs showed reduced numbers of TBR2+ intermediate progenitors (IP) cells and TBR1+ cortical neurons compared to the isogenic control lines. These observations indicated that POGZ deficiency impairs NSC lineage differentiation at later stages of neural rosette development. Additionally, when NSC from 21-day-old neural rosettes were dissociated and differentiated into neurons, *POGZ*<sup>-/-</sup> and *POGZ*<sup>+/-</sup> lines showed a significantly lower mean intensity of TUBB3 immunoreactivity per cell, a marker for mature neurons. Together, these findings suggest that POGZ is crucial for NSCs to properly exit the proliferative cycle and differentiate into post-mitotic neurons [135].

*POGZ* shRNA knockdown using in utero electroporated mouse models increased the number of PAX6+ apical progenitors (NSCs) and reduced the TBR2+ intermediate neural progenitor (IP) cell pool and SATB2+ upper layer differentiated neurons in E16.5 mouse cortices electroporated at E14.5 [115]. In contrast, homozygous null mice with conditional deletion of *Pogz* in NSCs at E15.5 developed a modest increase of TBR2+ IPs layer, while there was no significant difference in the PAX6+ NSCs layer [134]. In adult neurogenesis, *Pogz*-deficient mice had fewer immature neurons (DCX+) in the dentate gyrus [134].

This observed discrepancy in TBR2+ populations between these two different studies likely arises from differences in gene inactivation timing and method as neurogenesis is highly sensitive to both the timing of gene expression changes [334] and the gene dosage. The shRNA knockdown model, induced via in utero electroporation at E14.5, partially reduced POGZ expression, which may allow for compensatory mechanisms, unlike the complete deletion at E15.5 in the conditional knockout model. This variation could lead to distinct effects on progenitor populations, with the knockdown increasing PAX6+ NSCs and decreasing TBR2+ IPs, while the full knockout modestly increased TBR2+ IPs without affecting PAX6+ cells. Additionally, developmental timing and specific brain regions further influence these outcomes. For instance, in adult neurogenesis, *Pogz*-deficient mice showed fewer immature neurons (DCX+) in the dentate gyrus.

Gene dosage dependent effects have been also noticed with *Shank2* gene which is implicated in various NDDs, including ASD, intellectual disability, ADHD, and schizophrenia supporting the sensitivity of neurogenesis for such variations [335, 336]

All these findings suggest that phenotypic variability across models can stem from differences in gene dosage, developmental stage, and neurogenic context, underscoring the importance of model selection and timing in POGZ studies.

Additionally, NSCs derived from an ASD patient with a *de novo* missense Q1042R mutation in *POGZ* and control NSCs were seeded into neuronal differentiation medium on day 0 of differentiation. The number of MAP2+ neurons was analyzed on day 2, during the early stage of neuronal differentiation. The proportion of MAP2+ neurons was significantly lower in the patient-derived NSCs compared to the control NSCs, indicating that neuronal differentiation is impaired in the patient-derived NSCs [115].

In this project, female and male mutant NPCs (A2D5 and C34) carrying a heterozygous N-terminus and HPZ-domain mutation respectively, showed a differentiation trajectory distinct from previous findings. Specifically, these female mutant NPCs exhibited a trend toward a more differentiated state, as indicated by increased expression of DCX, even without neural induction. In NPCs from WHSUS male patient with a heterozygous mutation in the HPZ domain, there was a similar trend, with higher MAP2 expression observed in the absence of neural induction. MAP2 and DCX are well-established markers used to distinguish neuronal cells from non-neuronal cells in both brain tissue sections and in vitro cultures. MAP2, a cytoskeletal protein, is primarily localized to neuronal dendrites [337, 338], while DCX is strongly expressed in developing neurons, particularly in neuroblasts and postmitotic newborn neurons, with its expression decreasing as neuronal development progresses [339-341].

The findings were further supported by data showing that female mutant NPCs had a significantly higher proportion of MAP2+ neurons after two days of neural induction, a phenotype absent in WHSUS patient NPCs. These results suggest that WHSUS patient-derived NPCs may retain a milder phenotype. Additionally, this distinction could be attributed to differences in genetic background when compared to the control group.

These results indicate that neuronal differentiation is enhanced in female NPCs carrying heterozygous frameshift *POGZ* mutations in the N-terminus, with a lesser but noticeable extent in male NPCs carrying heterozygous frameshift *POGZ* mutations in the HPZ domain.

This enhanced neuronal differentiation occurs without evidence of increased proliferation or defects in cell cycle progression. In the case of WHSUS patient NPCs with a heterozygous HPZ-domain mutation, this differentiation trend could be attributed to the truncated, partially functional protein. However, this interpretation remains to be fully validated, as further experimental investigation is required to determine the extent of functionality of the truncated protein. In contrast, studies such as Nagy *et al.* have demonstrated that frameshift and nonsense variants occurring after amino acid residue 810—similar to the WHSUS patient—tend to evade NMD but are nonetheless associated with severe phenotypes in POGZ-related NDDs [103].

In female NPCs with N-terminal POGZ mutations, the resulting protein is a significantly truncated comprising only 28 amino acids. Although this mutant mRNA also evades NMD, the resulting protein lacks nearly all functional domains, leading to haploinsufficiency. This truncated protein is likely subjected to degradation by the ubiquitin-proteasome system due to misfolding [342, 343]. Clinically; pathogenic variants located at the very N-terminus, such as p.Asp3fs and p.Met1Val, correlate with more severe phenotypes ([ClinVar/POGZ](#)). Together, these findings suggest that while mutations in the HPZ domain may retain partial protein function, extensive truncations resulting from N-terminal mutations eliminate functionality, further supporting the enhanced differentiation observed in these mutant NPCs. Further experiments are necessary to confirm whether the truncated protein in the HPZ domain is indeed partially functional, as this has important implications for understanding genotype-phenotype relationships in POGZ-related disorders.

### **5.2.3 POGZ variants effects in 3D culture models**

#### **5.2.3.1 Effect on proliferation**

The effects of heterozygous *POGZ* mutations on the proliferation were investigated in neurospheres, which provide a more physiologically representative cellular environment compared to traditional 2D cultures, potentially influencing the observed results. The diameter of the neurospheres formed by *POGZ*<sup>+/-</sup> NPCs carrying mutations in N-terminus and HPZ domain, was significantly smaller than that of the corresponding control neurospheres. This suggests that POGZ deficiency impairs the self-renewal capacity of *POGZ*<sup>+/-</sup> NPCs in neurospheres. These findings are consistent with those of Sun, X. *et al.*, where neurospheres derived from *Pogz*<sup>-/-</sup> mESCs were smaller than those from wild-type mESCs after a 7-day differentiation period [116]. Similarly, another study showed that

*Pogz*<sup>-/-</sup> mESCs-derived neurospheres were smaller and more irregular compared to controls and exhibited downregulated expression of neural progenitor markers such as PAX6 and Sox1 [117]. In human cell cultures, Deng *et al.* reported a significant reduction in proliferation in neural rosettes derived from both *POGZ*<sup>-/-</sup> and *POGZ*<sup>+/-</sup> lines after 21 days [135]. Moreover, the type of *POGZ* mutation affects the neurosphere phenotype. For example, in patient-derived NSCs carrying a *de novo* missense mutation (Q1042R) in the CENP-DB domain, neurospheres were larger compared to controls, indicating an increase in self-renewal activity [115].

To be noticed, no such proliferation impairment was observed in 2D culture assays such as Ki67<sup>+</sup> and PHH<sup>+</sup> staining or the Click-iT Edu assay. In addition, there was no significant difference in cell survival, as measured by Cas3<sup>+</sup> and  $\gamma$ -H2AX<sup>+</sup> populations, between mutant and control NPCs. This suggests that the different growth conditions between 2D and 3D cultures might be contributing to the differences in how these cells proliferate or self-renew. However, variations in factors like cell density, aggregation or changes in extracellular matrix production could play a role in the observed neurospheres proliferation [344-348].

#### **5.2.3.2 Effect on differentiation (migration):**

As noted in the introduction, migration is a crucial process during neurogenesis for neuron maturation and differentiation [349]. During fetal cortex development, various migratory processes are involved that are primarily driven by radial glia cells (RG) and neurons [350, 351]. Human RGs play two crucial roles in cortex development: 1) their self-renewing capacity increases the cortical cell pool, leading to cortical expansion, enhanced neurogenesis, and the folded cerebral cortex characteristic of gyrencephalic species like humans, and 2) they form scaffolds for migrating neurons [350, 351]. Disruptions in RG function during brain development can result in neurodevelopmental disorders such as heterotopia and lissencephaly [352, 353]. Given these characteristics, neurospheres provide an effective model for studying neural cell migration, as cells naturally in these 3D cultures spontaneously migrate out of the spheres when placed on an appropriate matrix [346, 348].

In this project, to compare the effect of *POGZ* mutations on NPCs differentiation in 2D culture with 3D culture, neural migration of NPCs was investigated by culturing the 3-day-old neurospheres under adherent conditions for two days in neural induction media. The

radial migration of newborn neurons from neurospheres was significantly enhanced in both NPCs carrying heterozygous frameshift *POGZ* mutations in the N-terminus and in the HPZ domain. These Observations interfere with findings from Deng *et al*, where they counted number of migrating newborn neurons not the radial migration distance from neural rosettes to evaluate neuron migration [135]. In this study, there were fewer neurons observed outside the *POGZ*<sup>-/-</sup> neural rosettes shortly after rosette formation. In contrast to the *POGZ*<sup>-/-</sup> rosettes, many neurons originating from isogenic control and *POGZ*<sup>+/-</sup> lines extended away from the rosettes [135]. In terms of rosette size, it has been noticed that the rosette size was similar between control and *POGZ*<sup>-/-</sup> lines; however, *POGZ*<sup>+/-</sup> rosettes were slightly bigger than control rosettes [135]. It has been reported that larger rosettes exhibit enhanced radial migration [354]. Such variations between the findings of Deng *et al*, study and the neurospheres findings in can be explained by using a different 3D model, these rosettes were cultured for 26 days then inducing neural differentiation for 7 days afterwards.

In a previous study, it was found that the radial migration of young neurons was significantly attenuated in neurospheres of the patient-derived NSCs carrying a *de novo* missense Q1042R *POGZ* mutation [115]. Together, these findings underscore that both *POGZ* gene dosage and specific mutation types significantly influence NPC migration patterns.

In this PhD study, the enhanced migration observed in NPCs with frameshift mutations in the N-terminus and in HPZ domain suggests these NPCs may represent a later differentiation stage compared to the corresponding controls. This migration pattern likely reflects the differential impact of *POGZ* mutations on neuronal maturation, further underscoring the importance of mutation type in determining the resulting phenotype.

#### **5.2.3.3 Effect on brain organoids:**

The 3D differentiation of iPSCs into cerebral organoids was first described in 2013 by Lancaster *et al* [246]. Using embryoid bodies and specialized culture media, iPSCs can form small brain-like structures approximately 4 mm in diameter. These brain organoids typically consist of neuronal stem cells and neurons with various fates but can also contain retinal tissue or cells of the choroid plexus [168]. The differentiation of cerebral organoids tends to favor either a ventral or dorsal fate, depending on the iPSC line and its genetic background. This patterning can be directed toward the desired identity using certain

drugs that interfere with SHH signaling and other pathways responsible for defining the dorsal-ventral axis [355].

In this study, cerebral organoids were generated and differentiated for 30 from the female iPSCs A2 (wildtype) and A2D5 (mutant) and the male iPSCs S21 (wildtype) and C34 (mutant). However, only the organoids generated from the female iPSCs were analyzed in this study. The wildtype A2 organoids developed with typical morphology showing ventricle-like structures surrounded by neurons, which closely resembles the expected organization of early neuroepithelial tissue. In contrast, organoids from the A2D5 mutant iPSCs exhibited a significantly reduced area of ventricle-like structures, although the number of ventricles did not differ between the wildtype and mutant groups. Additionally, the SOX2-positive areas, marking NPC populations, were almost significantly smaller in the mutant A2D5 compared to A2 organoids, while the areas positive for MAP2, a marker of mature neurons, were nearly significantly larger in the mutant A2D5 compared to A2 organoids. These findings correlate with the results from 2D NPC cultures, where heterozygous frameshift mutations in the N-terminus of POGZ were associated with a tendency toward enhanced neuronal differentiation. These A2D5 mutant female NPCs exhibited a differentiation bias, as demonstrated by an increased expression of DCX marker without neural induction. This accelerated differentiation could account for the reduced SOX2-positive progenitor regions and increased MAP2-positive mature neuron areas observed in the mutant organoids, suggesting that differentiation may occur prematurely in these mutant organoids, reducing NPC pool size while expanding neuronal populations.

Moreover, dissociating the A2D5 mutant organoids into single-cell suspensions revealed a significantly higher proportion of MAP2<sup>+</sup> neurons in comparison to the wildtype—a finding that aligns with 2D differentiation experiments, where A2D5 mutant NPCs also showed an increased proportion of MAP2<sup>+</sup> neurons following a short induction period (2days). Together, these results from both 2D and 3D organoid models further support the hypothesis that heterozygous N-terminal *POGZ* frameshift mutations promote an accelerated differentiation trajectory in NPCs, potentially at the expense of sustained progenitor proliferation. This suggests a broader role for POGZ in balancing the timing of

neural differentiation and maintaining progenitor pools within developing neural structures.

#### **5.2.4 *POGZ* mutations change the transcriptome in the NPCs**

*POGZ* is reported to act as a transcription factor (TF) and chromatin regulator [19-21]. Therefore, RNA-seq experiments were performed to identify which genes were differentially expressed (DEGs) in *POGZ* mutant versus control NPCs and in which pathways they were involved.

A previous study analyzing DEGs in neural stem cells (NSCs) from an ASD patient with a Q1042R mutation in *POGZ* and from E16.5 *POGZ*<sup>WT/Q1038R</sup> mice showed an enrichment in neuronal developmental processes. Specifically, 78 out of human and mouse DEGs annotated to neurogenesis, showed commonly differential expression between human and mouse. Among the upregulated DEGs, the Notch ligand *JAG2* was approximately two-fold up-regulated in patient-derived NSCs and *POGZ*<sup>WT/Q1038R</sup> mice compared to controls, highlighting its potential role in the pathogenesis of *POGZ* related disorders [115].

To understand *POGZ*'s role in regulating embryonic stem cells (ESCs), Sun *et al.*, conducted RNA sequencing (RNA-seq) analysis on control and *Pogz*<sup>-/-</sup> mouse ESCs at passage 10. Up-regulated genes included endodermal markers (*Gata4/6*, *Sox17*, *Foxa2*) and genes involved in neural differentiation and axonogenesis (*App*, *En2*, *Neurog3*). Additionally, genes related to cellular senescence, apoptosis (*Cdkn2a*, *Cdkn1a*), and meiosis (*Smc1b*, *Dmc1*) were deregulated. Gene ontology (GO) analysis highlighted terms like neurogenesis and nervous system development for up-regulated DEGs, and meiotic chromosome segregation and cell cycle for down-regulated DEGs. Further RNA-seq analysis was done on day 6 control and mutant ESC-derived embryoid bodies (EBs). Down-regulated genes included pluripotency markers (*Pou5f1*, *Nanog*) and neural genes (*Pax6*, *Sox1*), while cardiac progenitor markers (*Gata4*, *Nkx2.5*) were up-regulated. GO and KEGG analyses of down-regulated DEGs showed enrichment in forebrain development, axonogenesis, and pathways regulating stem cell pluripotency. The down-regulation of neural lineage genes is particularly significant given the known link between *POGZ* mutations and neurodevelopmental disorders [116].

In another study by Sun *et al.*, RNA-seq was conducted on control and early passage *Pogz* knockout (*Pogz*<sup>-/-</sup>) mouse ESCs. The results showed minimal changes in the expression of

pluripotency and three germ layer marker genes, indicating that acute depletion of POGZ did not cause premature differentiation. Notably, genes specific to the 2-cell (2C) stage which is “two-cell embryonic-like” cells (2CLCs), such as the *Zscan4* cluster, *Fth17ls*, and *Tcstv3*, were significantly activated in *Pogz*<sup>-/-</sup> mouse ESCs [117].

Moreover, RNA-seq analysis was performed on six RNA samples from *Pogz* *cKO*<sup>-/-</sup>, *Pogz* *cKO*<sup>+/-</sup>, and control mice [356]. Accounting for sex and treating *Pogz* genotypes as quantitative measures, 636 DEGs were identified in the hippocampus and 1,916 in the cerebellum. Most DEGs showed an additive effect, with the expression in *cKO*<sup>+/-</sup> between *cKO*<sup>-/-</sup> and control levels[356].

Consistent with POGZ's role in gene repression, the majority of DEGs were upregulated (hippocampus: 67-93%, cerebellum: 77-83%). Significant overlap and correlation in DEGs were observed between the hippocampus and cerebellum (41.1% overlap,  $r^2 = 0.30$ ). Notably, *Dach2* which is a transcription factor, was highly upregulated in both regions[356].

Gene ontology (GO) analysis revealed that upregulated genes in the cerebellum were linked to nervous system development and metabolic processes, while downregulated genes were associated with DNA repair and RNA processing. In the hippocampus, upregulated genes were related to metabolic processes, and downregulated genes were related to synapses. A significant enrichment of ASD candidate genes was found among the downregulated genes in the hippocampus. Upregulated genes in the cerebellum were associated with mammalian phenotypes such as decreased body size and abnormal nervous system electrophysiology, while hippocampal DEGs did not show significant phenotype enrichment [356].

Papadimitriou *et.al.*, performed RNA-seq on wildtype and *Pogz*<sup>-/-</sup> mice at E13.5 in the cortex and basal ganglia. These regions were chosen due to high POGZ expression and their roles in generating neurons linked to ASD. In the *Pogz*<sup>-/-</sup> cortex, 177 genes were downregulated and 154 were upregulated, while in the basal ganglia, 230 genes were downregulated and 267 upregulated. The most significantly downregulated gene in both regions was *Pcdh11x*.

There was a correlation in differential expression between the two regions, with 22 commonly downregulated and 11 commonly upregulated genes. GO analysis of downregulated genes in the *Pogz*<sup>-/-</sup> cortex revealed enrichment for axonogenesis and

positive regulation of synapse assembly. Notably, multiple *Slitrk* family genes, involved in axon extension and synapse development, were downregulated in both regions. Additionally, genes encoding components of the GABAA receptor and GABA transporters were differentially expressed, with the latter being upregulated in the *Pogz*<sup>-/-</sup> cortex. These findings suggest that POGZ regulates genes critical for synapse formation and function, many of which are implicated in neurodevelopmental disorders [111].

In this project, to elucidate transcriptome profiling changes of neural function related pathways by different *POGZ* mutations, sequencing was performed using rRNA depleted total RNA extracted from female A2, A2D5 and male S21, C34 NPCs. Three biological replicates of each were sequenced after checking the concentration and quality of total RNA.

In this project, RNA-seq data showed *POGZ* mutations change transcriptome profiling of neural function related pathways in NPCs. In female NPCs, 1593 of the DEGs were downregulated and 1322 were upregulated in mutant A2D5 NPCs. Many of the top 10 up- and downregulated DEGs in A2D5 mutant NPCs are associated with NDDs and/or autism. For example, the up-regulated *HCN1* gene, encodes a protein of the HCN channel family. These channels are important for the electrical activity of neurons as they regulate the flow of ions across the cell membrane, therefore, it is essential for regulating neuronal excitability, rhythmic firing and synaptic function [357]. Studies have shown that mutations in *HCN1* are linked to early infantile epileptic encephalopathy [247], highlighting the gene's role in both epilepsy and broader neurodevelopmental abnormalities [357, 358].

Another top up-regulated gene in mutant female NPCs was *AGAP2* which is involved in intracellular trafficking, cellular signalling pathways and cytoskeletal organization [359]. Such processes are crucial for proper neuronal development and function [360]. Mutations or dysregulation in *AGAP2* can lead to altered neuronal connectivity and synaptic plasticity and have been implicated in various NDDs and ASD [248].

*SILTRK 3* was upregulated in the mutant female NPCs. *SILTRK* family genes encode leucine-rich repeat extracellular proteins that promote axon extension, excitatory synapse development, and neuronal survival [249, 250]

On the other hand, one of the top down-regulated genes was *TRIM65* (Tripartite Motif Containing 65) which encodes a protein involved in various cellular processes, including

ubiquitination and regulation of RNA metabolism. Such functions are essential for maintaining cellular homeostasis and proper neural function and hence dysregulation in TRIM65 might potentially lead to neurodevelopmental abnormalities [251, 252].

GABAergic neurotransmission was impaired in the mutant female NPCs as genes that encode different subunits of the GABAergic receptors and transporters were dysregulated. While *GABRG3* (GABA\_type A receptor  $\gamma$ 3 subunit) was up-regulated, *GABRA3* (GABA\_type A receptor  $\alpha$ 3 subunit) was down-regulated. Variations in *GABRG3* and *GABRA3* have been linked to ASD, intellectual disabilities and epilepsy [361, 362]. On another hand, the gene encoding the GABA transporter *SLC6A11* was downregulated. This gene has been associated with intellectual disability, epilepsy and stereotypic behavior in previous studies [363].

Gene ontology (GO) analyses revealed that DEGs are enriched for many terms including chromosome segregation, mitotic chromatid segregation and DNA repair, which are known processes involving POGZ-regulation. Nozawa *et al* demonstrated that POGZ is crucial for formation of the kinetochore and spindle assembly checkpoints (SAC) during mitosis by mediating the dissociation of HP1 $\alpha$  and the activation of Aurora B kinase[113]. Additionally, Heath *et al.* found that POGZ plays a role in DSBs repair by facilitating the recruitment of HP1 to DSBs in human cells [136].

The GO enrichment analyses confirmed findings in previous experiments that the mutant female NPCs carrying heterozygous frameshift *POGZ* mutation in the N-terminus are primed to a more differentiation status. The upregulated DEGs were significantly enriched for biological process terms including synaptic signaling and transmission, membrane depolarization and cell projection organization, among others.

The Reactome functional analysis showed that some of the down-regulated DEGs were significantly enriched for nonsense mediated decay (NMD) such as *RPL22*, *RPS8*, *SMG5*, *UPF2*, *PABPC1* and *RPS24*, among others. This might explain the normal *POGZ* mRNA level in mutant female NPCs, as the downregulation of NMD machinery would prevent the breakdown of the mutant transcript. As a result, the mutant mRNA is not degraded and can be detected in RT-qPCR and pyrosequencing experiments.

In male NPCs, 1591 of the DEGs were down-regulated and 1589 were up-regulated in the patient (C34) NPCs. Many of the top 10 up- and down-regulated DEGs in C34 mutant NPCs are associated with NDDs and/or autism.

Another SILTRK family gene member, *SILTRK 1*, was upregulated in the mutant male NPCs compared to the male wild-type NPCs. *SILTRK 1* is implicated in the excitatory synapses development and has been connected to Tourette's disorder [249, 250, 364, 365].

*LPHN3* was also upregulated and it encodes a GPCR that promotes excitatory synapse formation by trans-synaptic binding of FLRT family and Teneurin proteins [366].

GABAergic neurotransmission was also dysregulated in the mutant male NPCs but different genes of the subunits of the GABAergic receptors and transporters were differentially expressed in comparison to female NPCs. While *GABRR1* (GABA\_type C receptor  $\rho 1$  subunit) was upregulated, *GABRA3* (GABA\_type A receptor  $\alpha 3$  subunit), *GABRA2* (GABA\_type A receptor  $\alpha 2$  subunit), and *GABRB2* (GABA\_type A receptor  $\beta 2$  subunit), were downregulated. Alterations in such genes have been linked to ASD, neurodevelopmental delay and epilepsy [361, 362, 367].

The GABA transporter *SLC6A1* which is a high confidence ASD risk gene associated with myoclonic atonic epilepsy/absence seizures with developmental delay [368, 369], was also up-regulated. Furthermore, Jagged canonical Notch ligand 1 (*JAG1*) was upregulated and the Jagged canonical Notch ligand 2 (*JAG2*) was downregulated in the male mutant NPCs. This finding is in contrast to previous results in NSCs with a Q1042R mutation in *POGZ* where *JAG2* was upregulated [115]. *JAG1* and *JAG2* maintain the NSCs population by negatively regulating neuronal differentiation (Fig.73) [370]. These findings suggest that the mutation in the HPZ domain of *POGZ* may impair neuronal development by dysregulation of Notch signaling (Fig.73).

Gene ontology (GO) analyses revealed that DEGs are enriched for similar terms as in female NPCs including chromosome segregation, mitotic chromatid segregation and DNA repair, which are known processes involving *POGZ* as reported in Nozawa *et al.* and Heath *et al.* studies [113] [136].

GO enrichment analysis results were similar to what was observed in mutant female NPCs suggesting that the mutant male NPCs carrying heterozygous frameshift *POGZ* mutation in the HPZ- domain might be primed to a more differentiation status. The upregulated DEGs were significantly enriched for BP terms including synaptic signaling and organization, synapse assembly and regulation, among others.

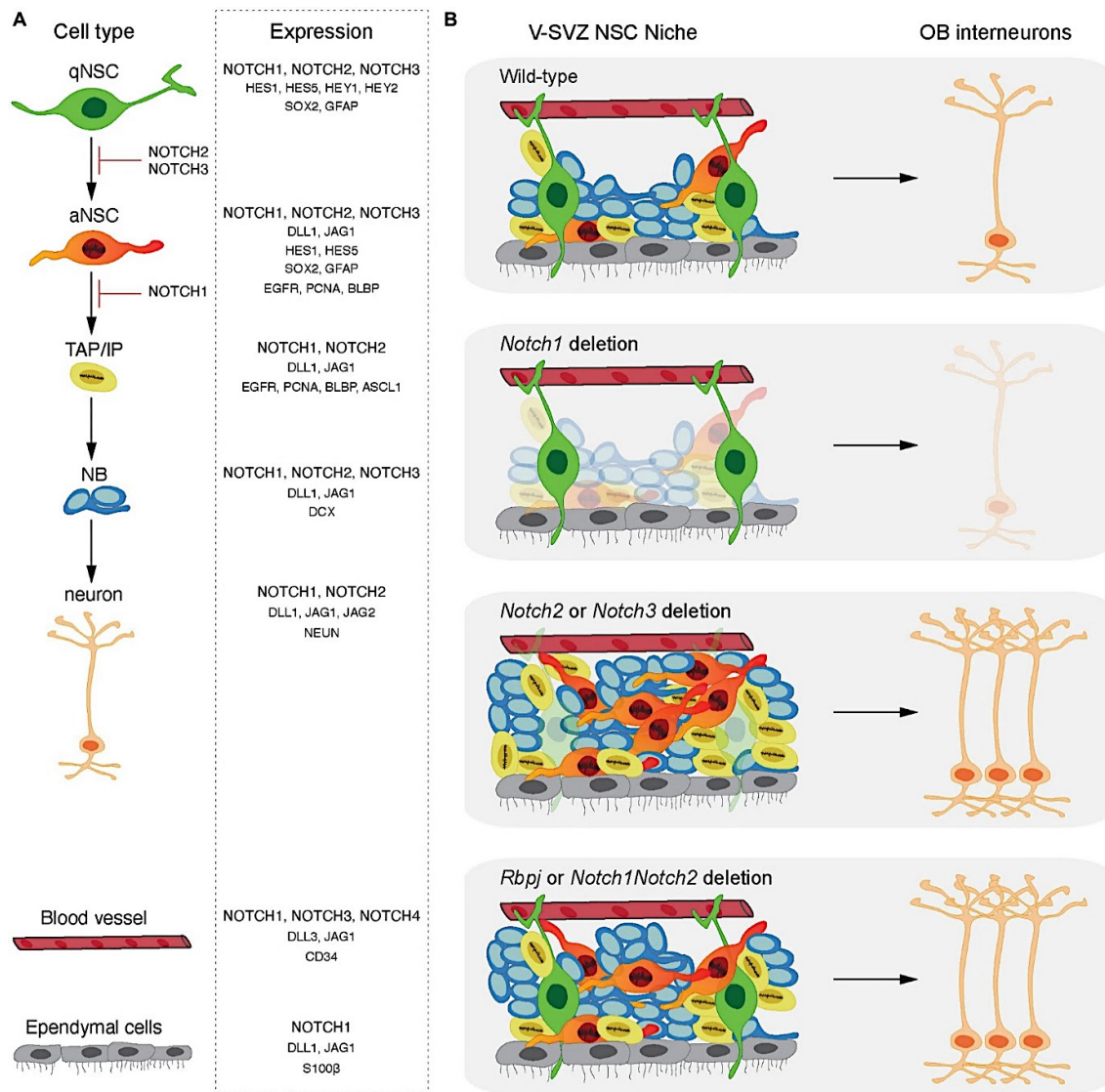


**Fig.73. Notch signaling in adult neurogenesis.** (A) Expression patterns of Notch ligands, receptors, and downstream effectors in the neuronal lineage and cells within the adult NSC niche. Notch receptor paralogues and *Rbpj* are expressed in all cell types of the mouse adult-born neuronal lineage, from NSCs to neurons. However, downstream effectors of the Notch signaling cascade, such as *Hes* and *Hey* factors, are only present in NSCs in both quiescent and activated states. *Dll* and *Jagged* ligands are expressed throughout the lineage, except in quiescent NSCs. (B) Functions of Notch receptors and their common downstream effector, *Rbpj*, in the V-SVZ. *Notch1* is crucial for maintaining activated NSCs, whereas *Notch2* and *Notch3* maintain NSC quiescence in the adult V-SVZ. Deletion of *Rbpj*, alongside *Notch1* and *Notch2*, results in similar phenotypes, indicating that *Rbpj*-mediated Notch signaling is essential for NSC maintenance downstream of both *Notch1* and *Notch2* receptors [370].

This suggests the normal *POGZ* mRNA levels are due to NMD evasion rather than impaired NMD machinery, supporting Nagy et al., study [103]. Furthermore, the transcriptomes of mutant NPCs with N-terminal and HPZ domain *POGZ* mutations displayed a "POGZ-specific transcriptome," indicating a distinct transcriptomic signature shaped by *POGZ* deficiency. The mutant female and male NPCs seemed to be in a later differentiation developmental time point "accelerated differentiation" based on their transcriptomic signatures derived from neuron- and NPC-predicting genes. This suggests heterozygous

frameshift *POGZ* mutations in the N-terminus and the HPZ domain change the transcriptome of the NPCs towards upregulation of neuronal and synaptic development genes. Similar observations of “accelerated differentiation” have been found in patient-derived NPCs carrying mutation *BRAF*<sup>Q257R</sup>, the most common cause of cardiofaciocutaneous syndrome (CFC)[371]. CFC syndrome is one of the Mendelian genetic syndromes termed RASopathies and primarily caused by gain-of-function mutations in the *BRAF* gene which is a key Ras signal mediator in Ras/MAPK pathway [371]. Individuals with CFC syndrome commonly exhibit developmental delay, intellectual disability (over 80%), a high risk for ASD (54–64%), seizures (45%), and a higher prevalence of structural brain abnormalities [371]. Yeh *et al*, found that after one week of differentiation *BRAF*<sup>Q257R</sup> NPCs displayed morphology associated with more mature neurons. Moreover, they were significantly enriched for both MAP2<sup>+</sup> and NEUN<sup>+</sup> cells, indicating premature neuronal maturation [371]. Overall, these findings highlight how early maturation of NPCs influences human-specific neurodevelopmental events. This suggests heterozygous frameshift *POGZ* mutations in the N-terminus and in the HPZ domain change the transcriptome of the NPCs towards upregulation of neuronal and synaptic development genes.

### **5.2.5 POGZ regulation via DNA-binding (Cut&Tag):**

*POGZ* has at least 8 C2H2 zinc fingers, suggesting it can bind to DNA and function as transcriptional regulator. CUT&Tag analysis was therefore performed to identify the DNA sites where *POGZ* can bind directly or indirectly. This analysis provided insights into the relationship between *POGZ*-regulated gene expression, *POGZ* binding and chromatin regulation and the potential link to neurodevelopmental disorders.

As it has been introduced, studies have demonstrated that *POGZ* has been shown to bind regulatory regions across the genome, playing a crucial role in transcriptional regulation and neurodevelopment. In cortical NSCs from E16.5 WT mice, Matsumura *et al*. demonstrated *POGZ* binding to the *Jag2* promoter via ChIP assays [115].

Sun *et al*. utilized CUT&Tag in *Pogz*<sup>-/-</sup> ESCs, identifying over 16,000 *POGZ*-enriched peaks, primarily at transcription start sites (TSS) and enhancers. Approximately 10,000 genes were identified as *POGZ* targets, many associated with pathways related to neurodegeneration, including Parkinson’s and Huntington’s diseases. Additionally, *POGZ* bound specific endogenous retroviruses (ERVs) like IAPEY and RLTR9E, and regulated *Dux*,

a positive regulator of the 2C-like state, whose expression was significantly derepressed in *Pogz*<sup>-/-</sup> ESCs [116, 117].

Papadimitriou *et al.*, conducted CUT&RUN in E13.5 WT mouse telencephalons, revealing over 2,000 POGZ binding sites. These peaks were enriched at TSS and brain-specific enhancers, with 4.7% overlapping enhancers active in the embryonic brain. HOMER motif analysis showed enrichment for homeobox and zinc finger motifs at POGZ binding sites. Genes near these loci were involved in processes like euchromatin maintenance and axon growth, supporting POGZ's role in regulating neural development. Collectively, these findings highlight POGZ's function as a transcriptional regulator with a specific impact on brain development and chromatin dynamics[111].

In this project, investigating POGZ occupancy genome wide with CUT&Tag in the female NPCs A2, A2D5 and A2A1 and male NPCs S21 and C34 showed that POGZ binds mainly to promotor regions (<=1kb) indicating it functions mainly as transcriptional regulator as it was mentioned earlier in different studies [111, 116]. Overlapping the consensus peaks found with published CUT & Tag data from Papadimitriou *et al.*, confirmed the reproducibility of findings and similarity of POGZ bound genes in NPCs and in 17gw/18 gw human fetal cortex samples in Papadimitriou et al [111]. POGZ bound genes are involved in pathways of axonogenesis, cell-cell signaling by Wnt, Wnt signaling, regulation of neuron projection development and forebrain development among others in both male and female NPCs. Such pathways are in line with that POGZ is involved in neurodevelopment and brain disorders.

Gene set enrichment analysis for these POGZ bound genes and genes in SFARI database confirmed that POGZ occupies gene loci implicated in ASD. *RERE* was one of the POGZ bound genes in both female and male NPCs. This gene showed a significant loss of binding in the mutant female NPCs while it was differentially upregulated in the mutant male NPCs only. *RERE* as mentioned encodes a nuclear receptor coregulator involved in chromatin remodeling and transcriptional regulation. Mutations in *RERE* have been associated with a spectrum of developmental delays, intellectual disabilities, and structural brain anomalies. Research has shown that *RERE* is critical for normal brain development, particularly in regions such as the cerebral cortex and the cerebellum. Haploinsufficiency or pathogenic variants in *RERE* can disrupt normal expression of key developmental genes, leading to a range of neurodevelopmental abnormalities. For instance, a study by Fregeau

*et al.* (2016) demonstrated that mutations in *RERE* cause a distinct syndrome characterized by intellectual disability, cerebellar atrophy, and other congenital anomalies[255, 256]. Additionally, *RERE* is one of the genes whose disruption contributes to a syndromic form of developmental delay and brain malformations, further underscoring its role in neurodevelopmental processes[256, 372]. *CHRM3* is another POGZ bound gene which was upregulated in both mutant female and male NPCs, although it showed a significant loss of binding in the mutant female NPCs only. *CHRM3*, one of the genes present in the SFARI database, encodes the M3 muscarinic acetylcholine receptor. This receptor is part of the G protein-coupled receptor family and is involved in smooth muscle contraction, glandular secretion, and modulation of neurotransmitter release. *CHRM3* has been proposed as a candidate gene responsible for autistic patient's specific phenotype with 1q43 deletion as well as the overlapping phenotypic features of other patients with 1q43 or 1q43-q44 deletions[257].

Moreover, *PCDH15* is POGZ bound gene that present in the SFARI database and showed a significant loss of binding in the mutant female NPCs. It encodes a member of the cadherin superfamily, which is crucial for cell adhesion, especially in the brain. This family of proteins plays an essential role in synapse formation and maintenance, helping neurons communicate effectively. Synaptic dysfunction is a common feature in many neurodevelopmental disorders, particularly in autism, where atypical connectivity between neurons has been observed in several brain regions [261].

Deficiency of POGZ in heterozygous mutant female NPCs (A2D5) resulted in a significant loss of POGZ binding to more additional genes. *FLG-AS1* was one of the loci associated with loss of POGZ binding in the HET female NPCs. The interaction between long non coding RNA *FLG-AS1* with *hsa-miR-34a-5p* and *FOSL1* is one of the potential interaction loops in the olfactory epithelium (OE) in schizophrenia pathogenesis where the OE contains olfactory receptor neurons, which show similar expression patterns to developing brain cells [373].

A substantially reduced number of affected genes were detected in HET male (C34) NPCs. The most likely explanation for these results is poor correlation between the replicates due to potential experimental or technical limitations such as uneven library sizes in the CUT&Tag sequencing. POGZ lost its binding to *LINC00578*, *CEMIP* and *APOLD1* genes, among others in male HET NPCs. *APOLD1* encodes a protein involved in the regulation of

endothelial cell signaling and vascular function particularly in the endothelial cells of the blood-brain barrier [374-377]. Its expression is thought to play a role in maintaining the integrity of the blood-brain barrier [376, 377]. Disruptions in the blood-brain barrier have been implicated in several neurodevelopmental and neuropsychiatric disorders, including ASD, schizophrenia, and epilepsy [378-380]. In addition, changes in *APOLD1* expression might influence the inflammatory response within the brain [375, 381], that possibly contribute to disorders such as ASD, ADHD, or intellectual disabilities due to neuroinflammation [380-383]. Meanwhile, genes such as *NXPH1*, *FAM171A1* and *FAM86B3P* were associated with a gain of POGZ binding in male HET NPCs. *NXPH1* (Neurexophilin 1) encodes a secreted glycoprotein that is part of the neurexophilin family. This protein interacts with neurexins which are synaptic cell adhesion molecules involved in the synaptic organization and neurotransmitter release[384]. *NXPH1* interacts with neurexin  $\alpha$ , a protein that promotes adhesion between dendrites and axons and reportedly carries variants in autism patients[384, 385]. Proper synaptic function is crucial for communication between neurons and is essential for cognitive processes therefore, dysregulation of synaptic proteins, including neurexins and their ligands like *NXPH1*, has been implicated in various neurodevelopmental disorders, including autism spectrum disorders (ASD), intellectual disabilities, and schizophrenia[386, 387].

The integration of POGZ CUT&Tag and RNA-seq data revealed that POGZ regulates gene expression in both male and female WT and HET NPCs. In female NPCs, 985 POGZ-bound genes were deregulated in HET cells, with 454 upregulated and 531 downregulated. In males, 413 genes were deregulated, with 235 upregulated and 178 downregulated. This significant overlap of POGZ-bound genes with DEGs suggests POGZ functions as both a transcriptional activator and repressor.

Several POGZ-bound DEGs are implicated in neurodevelopmental processes and disorders. For instance, *HCN1*, *GRID1*, and *NRG3* (Neuregulin 3), which were upregulated in both male and female HET NPCs, are associated with synaptic transmission. *HCN1* is involved in the regulation of neuronal excitability and has been linked to epilepsy and other neurological disorders[388, 389]. *GRID1* plays a role in synaptic plasticity, and its dysfunction has been associated with schizophrenia and ASD [390-392]. *NRG3* is crucial for neuronal differentiation and migration, with variations in this gene being linked to schizophrenia and autism [393-397].

Conversely, downregulated genes such as *HNRNPU* and *RCC1*, are involved in essential cellular processes. *HNRNPU* is critical for RNA processing and chromatin organization, and mutations in this gene have been associated with intellectual disability and developmental delays [398-404]. *RCC1* is involved in the regulation of chromosome condensation during cell division, and its proper function is vital for maintaining genomic stability [405, 406]. The intersection of differentially bound and expressed genes in female NPCs provided further insights into the transcriptional impact of POGZ binding. 125 upregulated genes in female HET NPCs lost POGZ binding, including *ANKS1B*, *CACNA1C*, and *CHRM3*. All these targets are classified as autism risk genes in the SFARI database. *ANKS1B* (Ankyrin Repeat and Sterile Alpha Motif Domain Containing 1B) is involved in synaptic development and plasticity, and mutations in this gene have been linked to ASD and intellectual disability [407, 408]. *CACNA1C* (Calcium Voltage-Gated Channel Subunit Alpha1 C) is essential for calcium signaling in neurons, and mutations in this gene are associated with Timothy syndrome, a condition that includes ASD and cardiac arrhythmias [409-411]. *CHRM3* plays a role in neurotransmitter signaling and has been implicated in neurodevelopmental disorders, including ASD [412, 413].

In addition to these findings, 175 downregulated genes in female HET NPCs also lost POGZ binding, including *ADA* (Adenosine Deaminase), *AGO2* (Argonaute RISC Catalytic Component 2), and *ASPM* (Abnormal Spindle Microtubule Assembly). *ADA* is involved in purine metabolism, and its deficiency can lead to severe combined immunodeficiency, which may also impact neurodevelopment [414-417]. *AGO2* is a critical component of the RNA-induced silencing complex (RISC) and is involved in gene silencing processes. Dysregulation of *AGO2* has been associated with various neurodevelopmental disorders. *ASPM* is essential for neurogenesis and brain size regulation. Mutations in this gene have been linked to microcephaly, a condition characterized by a reduced head circumference and associated cognitive impairments [418-421].

Interestingly, the Wnt signaling pathway was significantly enriched among POGZ-bound genes in both male and female NPCs. In female NPCs, POGZ targets such as *SFRP4* (Secreted Frizzled-Related Protein 4), *NDP* (Norrin), and *GPC4* (Glypican 4) were upregulated. *SFRP4* is an antagonist of Wnt signaling and plays a role in regulating cellular proliferation and differentiation; its dysregulation is implicated in cancer and neurodevelopmental disorders [422, 423]. *NDP* is involved in retinal development and

vascularization, with mutations leading to Norrie disease, a condition that includes blindness and cognitive impairments [424, 425]. *GPC4* is associated with synapse formation and cognitive function, and its alterations have been linked to neurodevelopmental disorders, including ASD [426, 427]. On the other hand, downregulated genes in female NPCs, such as *KLF15* (Kruppel Like Factor 15)[428, 429], *LGR4* (Leucine Rich Repeat Containing G Protein-Coupled Receptor 4)[430, 431], and *CHD8* (Chromodomain Helicase DNA Binding Protein 8)[432], are also critical for neurodevelopment. *CHD8*, in particular, is a well-established autism risk gene that plays a role in chromatin remodeling and neuronal development [433, 434].

In male NPCs, the analysis revealed upregulated POGZ-bound genes such as *EGF* (Epidermal Growth Factor), *SOX9* (SRY-Box Transcription Factor 9), and *TMEM64* (Transmembrane Protein 64). Down-regulated genes included *FGF10* (Fibroblast Growth Factor 10), *LRP6* (Low Density Lipoprotein Receptor-Related Protein 6), and *DKK2* (Dickkopf WNT Signaling Pathway Inhibitor 2). *SOX9* is critical for neural crest development and has been linked to neurodevelopmental disorders, including campomelic dysplasia and Pierre Robin sequence [435, 436]. *FGF10* plays a role in brain development, and its dysregulation has been associated with congenital malformations and neurodevelopmental anomalies [437-439].

In conclusion, this comprehensive analysis highlights the critical role of POGZ in transcriptional regulation within NPCs, particularly in genes associated with synaptic function, chromosome segregation, and Wnt signaling. The observed sex-specific differences in POGZ-mediated gene regulation underscore the complexity of its role in neurodevelopment. Additionally, the overrepresentation of autism risk genes among POGZ-regulated targets provides a potential link between POGZ dysregulation and the etiology of neurodevelopmental disorders, including autism spectrum disorder. Understanding these mechanisms is crucial for developing targeted therapeutic strategies for conditions associated with POGZ dysfunction.

## References

1. Matson, J.L., et al., *Examination of adaptive behavior differences in adults with autism spectrum disorders and intellectual disability*. Research in Developmental Disabilities, 2009. **30**(6): p. 1317-1325.
2. van Bokhoven, H., *Genetic and Epigenetic Networks in Intellectual Disabilities*. Annual Review of Genetics, 2011. **45**(1): p. 81-104.
3. Mefford, H.C., M.L. Batshaw, and E.P. Hoffman, *Genomics, Intellectual Disability, and Autism*. New England Journal of Medicine, 2012. **366**(8): p. 733-743.
4. Sanders, Stephan J., et al., *Insights into Autism Spectrum Disorder Genomic Architecture and Biology from 71 Risk Loci*. Neuron, 2015. **87**(6): p. 1215-1233.
5. Srivastava, A.K. and C.E. Schwartz, *Intellectual disability and autism spectrum disorders: Causal genes and molecular mechanisms*. Neuroscience & Biobehavioral Reviews, 2014. **46**: p. 161-174.
6. Matsumura, K., et al., *Pathogenic POGZ mutation causes impaired cortical development and reversible autism-like phenotypes*. Nature Communications, 2020. **11**(1): p. 859.
7. O'Roak, B.J., et al., *Exome sequencing in sporadic autism spectrum disorders identifies severe de novo mutations*. Nat Genet, 2011. **43**(6): p. 585-9.
8. De Rubeis, S., et al., *Synaptic, transcriptional and chromatin genes disrupted in autism*. Nature, 2014. **515**(7526): p. 209-15.
9. Iossifov, I., et al., *The contribution of de novo coding mutations to autism spectrum disorder*. Nature, 2014. **515**(7526): p. 216-21.
10. Krumm, N., et al., *A de novo convergence of autism genetics and molecular neuroscience*. Trends Neurosci, 2014. **37**(2): p. 95-105.
11. Matsumura, K., et al., *De novo POGZ mutations in sporadic autism disrupt the DNA-binding activity of POGZ*. Journal of Molecular Psychiatry, 2016. **4**(1): p. 1.
12. Gilissen, C., et al., *Genome sequencing identifies major causes of severe intellectual disability*. Nature, 2014. **511**: p. 344.
13. Neale, B.M., et al., *Patterns and rates of exonic de novo mutations in autism spectrum disorders*. Nature, 2012. **485**: p. 242.
14. Fukai, R., et al., *A case of autism spectrum disorder arising from a de novo missense mutation in POGZ*. Journal Of Human Genetics, 2015. **60**: p. 277.
15. Buxbaum, Joseph D., et al., *The Autism Sequencing Consortium: Large-Scale, High-Throughput Sequencing in Autism Spectrum Disorders*. Neuron, 2012. **76**(6): p. 1052-1056.
16. Krumm, N., et al., *Excess of rare, inherited truncating mutations in autism*. Nature Genetics, 2015. **47**: p. 582.
17. Stessman, H.A.F., et al., *Disruption of POGZ Is Associated with Intellectual Disability and Autism Spectrum Disorders*. Am J Hum Genet, 2016. **98**(3): p. 541-552.
18. Ye, Y., et al., *De novo POGZ mutations are associated with neurodevelopmental disorders and microcephaly*. Cold Spring Harb Mol Case Stud, 2015. **1**(1): p. a000455.
19. Ostapcuk, V., et al., *Activity-dependent neuroprotective protein recruits HP1 and CHD4 to control lineage-specifying genes*. Nature, 2018. **557**(7707): p. 739-743.
20. Gudmundsdottir, B., et al., *POGZ Is Required for Silencing Mouse Embryonic  $\beta$ -like Hemoglobin and Human Fetal Hemoglobin Expression*. Cell Reports, 2018. **23**(11): p. 3236-3248.
21. Gunther, M., M. Laithier, and O. Brison, *A set of proteins interacting with transcription factor Sp1 identified in a two-hybrid screening*. Mol Cell Biochem, 2000. **210**(1-2): p. 131-42.
22. Romero-Ayuso, D., *Future Challenges in Research in Children with Neurodevelopmental Disorders*. Children-Basel, 2021. **8**(5).

23. Micai, M., et al., *Early behavioral markers for neurodevelopmental disorders in the first 3 years of life: An overview of systematic reviews*. Neuroscience and Biobehavioral Reviews, 2020. **116**: p. 183-201.
24. Hanly, C., et al., *Description of neurodevelopmental phenotypes associated with 10 genetic neurodevelopmental disorders: A scoping review*. Clinical Genetics, 2021. **99**(3): p. 335-346.
25. Bergner, C.L., et al., *Mouse Models for Studying Depression-Like States and Antidepressant Drugs*. Methods Mol Biol, 2016. **1438**: p. 255-69.
26. Ding, B., *Gene expression in maturing neurons: Regulatory mechanisms and related neurodevelopmental disorders*. Sheng li xue bao : [Acta physiologica Sinica], 2015. **67**: p. 113-33.
27. Hu, W.F., M.H. Chahrour, and C.A. Walsh, *The Diverse Genetic Landscape of Neurodevelopmental Disorders*. Annual Review of Genomics and Human Genetics, 2014. **15**(1): p. 195-213.
28. Shen, H.Y., et al., *Associations of Parental Depression With Child School Performance at Age 16 Years in Sweden*. Jama Psychiatry, 2016. **73**(3): p. 239-246.
29. Homberg, J.R., et al., *Improving treatment of neurodevelopmental disorders: recommendations based on preclinical studies*. Expert Opin Drug Discov, 2016. **11**(1): p. 11-25.
30. Ismail, F.Y. and B.K. Shapiro, *What are neurodevelopmental disorders?* Curr Opin Neurol, 2019. **32**(4): p. 611-616.
31. Au, P.Y.B., A. Eaton, and D.A. Dymont, *Genetic mechanisms of neurodevelopmental disorders*. Handb Clin Neurol, 2020. **173**: p. 307-326.
32. Savatt, J.M. and S.M. Myers, *Genetic Testing in Neurodevelopmental Disorders*. Front Pediatr, 2021. **9**: p. 526779.
33. Michaelson, J.J., et al., *Whole-genome sequencing in autism identifies hot spots for de novo germline mutation*. Cell, 2012. **151**(7): p. 1431-42.
34. O'Roak, B.J., et al., *Multiplex targeted sequencing identifies recurrently mutated genes in autism spectrum disorders*. Science, 2012. **338**(6114): p. 1619-22.
35. Talkowski, M.E., et al., *Sequencing Chromosomal Abnormalities Reveals Neurodevelopmental Loci that Confer Risk across Diagnostic Boundaries*. Cell, 2012. **149**(3).
36. Deciphering Developmental Disorders, S., *Prevalence and architecture of de novo mutations in developmental disorders*. Nature, 2017. **542**(7642): p. 433-438.
37. Brunet, T., et al., *De novo variants in neurodevelopmental disorders-experiences from a tertiary care center*. Clin Genet, 2021. **100**(1): p. 14-28.
38. Karam, S.M., et al., *Genetic causes of intellectual disability in a birth cohort: a population-based study*. Am J Med Genet A, 2015. **167**(6): p. 1204-14.
39. Reichenberg, A., et al., *Discontinuity in the genetic and environmental causes of the intellectual disability spectrum*. Proc Natl Acad Sci U S A, 2016. **113**(4): p. 1098-103.
40. Vissers, L.E., C. Gilissen, and J.A. Veltman, *Genetic studies in intellectual disability and related disorders*. Nat Rev Genet, 2016. **17**(1): p. 9-18.
41. Posserud, M.B., et al., *Male to female ratios in autism spectrum disorders by age, intellectual disability and attention-deficit/hyperactivity disorder*. Acta Psychiatr Scand, 2021. **144**(6): p. 635-646.
42. Faraone, S.V., et al., *The World Federation of ADHD International Consensus Statement: 208 Evidence-based conclusions about the disorder*. Neuroscience and Biobehavioral Reviews, 2021. **128**: p. 789-818.
43. Zablotsky, B., et al., *Prevalence and Trends of Developmental Disabilities among Children in the United States: 2009-2017*. Pediatrics, 2019. **144**(4).
44. Lord, C., et al., *The Lancet Commission on the future of care and clinical research in autism*. Lancet, 2022. **399**(10321): p. 271-334.

45. Bolte, S., et al., *Sex and gender in neurodevelopmental conditions*. Nat Rev Neurol, 2023. **19**(3): p. 136-159.
46. Dougherty, J.D., et al., *Can the "female protective effect" liability threshold model explain sex differences in autism spectrum disorder?* Neuron, 2022. **110**(20): p. 3243-3262.
47. Robinson, E.B., et al., *Examining and interpreting the female protective effect against autistic behavior*. Proc Natl Acad Sci U S A, 2013. **110**(13): p. 5258-62.
48. van Rijn, S., *A review of neurocognitive functioning and risk for psychopathology in sex chromosome trisomy (47,XXY, 47,XXX, 47,XYY)*. Current Opinion in Psychiatry, 2019. **32**(2): p. 79-84.
49. Grünblatt, E., et al., *The involvement of the canonical Wnt-signaling receptor and gene variants with ADHD and sexual dimorphism: Association study and meta-analysis*. American Journal of Medical Genetics Part B-Neuropsychiatric Genetics, 2019. **180**(6): p. 365-376.
50. Berkel, S., et al., *Sex Hormones Regulate SHANK Expression*. Front Mol Neurosci, 2018. **11**: p. 337.
51. Cardoso, A.R., et al., *Essential genetic findings in neurodevelopmental disorders*. Hum Genomics, 2019. **13**(1): p. 31.
52. Parenti, I., et al., *Neurodevelopmental Disorders: From Genetics to Functional Pathways*. Trends Neurosci, 2020. **43**(8): p. 608-621.
53. Neul, J.L., et al., *Specific mutations in Methyl-CpG-Binding Protein 2 confer different severity in Rett syndrome*. Neurology, 2008. **70**(16): p. 1313-1321.
54. Percy, A.K., *Rett syndrome: exploring the autism link*. Arch Neurol, 2011. **68**(8): p. 985-9.
55. Mount, R.H., et al., *Features of autism in Rett syndrome and severe mental retardation*. J Autism Dev Disord, 2003. **33**(4): p. 435-42.
56. Chahrour, M. and H.Y. Zoghbi, *The story of Rett syndrome: from clinic to neurobiology*. Neuron, 2007. **56**(3): p. 422-37.
57. Tudor, M., et al., *Transcriptional profiling of a mouse model for Rett syndrome reveals subtle transcriptional changes in the brain*. Proc Natl Acad Sci U S A, 2002. **99**(24): p. 15536-41.
58. Lewis, J.D., et al., *Purification, Sequence, and Cellular-Localization of a Novel Chromosomal Protein That Binds to Methylated DNA*. Cell, 1992. **69**(6): p. 905-914.
59. Amir, R.E., et al., *Rett syndrome is caused by mutations in X-linked , encoding methyl-CpG-binding protein 2*. Nature Genetics, 1999. **23**(2): p. 185-188.
60. Marchetto, M.C., et al., *A model for neural development and treatment of Rett syndrome using human induced pluripotent stem cells*. Cell, 2010. **143**(4): p. 527-39.
61. Homberg, J.R., et al., *Understanding autism and other neurodevelopmental disorders through experimental translational neurobehavioral models*. Neuroscience and Biobehavioral Reviews, 2016. **65**: p. 292-312.
62. Reiner, O., et al., *Isolation of a Miller-Dieker Lissencephaly Gene Containing G-Protein Beta-Subunit-Like Repeats*. Nature, 1993. **364**(6439): p. 717-721.
63. Guerrini, R. and W.B. Dobyns, *Malformations of cortical development: clinical features and genetic causes*. Lancet Neurology, 2014. **13**(7): p. 710-726.
64. des Portes, V., et al., *A novel CNS gene required for neuronal migration and involved in X-linked subcortical laminar heterotopia and lissencephaly syndrome*. Cell, 1998. **92**(1): p. 51-61.
65. Benvenuto, A., et al., *Syndromic autism: causes and pathogenetic pathways*. World J Pediatr, 2009. **5**(3): p. 169-76.
66. Caglayan, A.O., *Genetic causes of syndromic and non-syndromic autism*. Dev Med Child Neurol, 2010. **52**(2): p. 130-8.

67. Verkerk, A.J., et al., *Identification of a gene (FMR-1) containing a CGG repeat coincident with a breakpoint cluster region exhibiting length variation in fragile X syndrome*. Cell, 1991. **65**(5): p. 905-14.
68. Lubs, H.A., *A marker X chromosome*. Am J Hum Genet, 1969. **21**(3): p. 231-44.
69. Zoghbi, H.Y. and M.F. Bear, *Synaptic dysfunction in neurodevelopmental disorders associated with autism and intellectual disabilities*. Cold Spring Harb Perspect Biol, 2012. **4**(3).
70. Belmonte, M.K. and T. Bourgeron, *Fragile X syndrome and autism at the intersection of genetic and neural networks*. Nature Neuroscience, 2006. **9**(10): p. 1221-1225.
71. Irwin, S.A., R. Galvez, and W.T. Greenough, *Dendritic spine structural anomalies in fragile-X mental retardation syndrome*. Cerebral Cortex, 2000. **10**(10): p. 1038-1044.
72. O'Donnell, W.T. and S.T. Warren, *A decade of molecular studies of fragile X syndrome*. Annu Rev Neurosci, 2002. **25**: p. 315-38.
73. Nimchinsky, E.A., A.M. Oberlander, and K. Svoboda, *Abnormal development of dendritic spines in knock-out mice*. Journal of Neuroscience, 2001. **21**(14): p. 5139-5146.
74. Malzac, P., et al., *Mutation analysis of UBE3A in Angelman syndrome patients*. Am J Hum Genet, 1998. **62**(6): p. 1353-60.
75. Matsuura, T., et al., *De novo truncating mutations in E6-AP ubiquitin-protein ligase gene (UBE3A) in Angelman syndrome*. Nat Genet, 1997. **15**(1): p. 74-7.
76. Clayton-Smith, J., *Clinical research on Angelman syndrome in the United Kingdom: observations on 82 affected individuals*. Am J Med Genet, 1993. **46**(1): p. 12-5.
77. Hart, H., *'Puppet' children. A report on three cases (1965)*. Dev Med Child Neurol, 2008. **50**(8): p. 564.
78. Sato, M. and M.P. Stryker, *Genomic imprinting of experience-dependent cortical plasticity by the ubiquitin ligase gene Ube3a*. Proc Natl Acad Sci U S A, 2010. **107**(12): p. 5611-6.
79. Yashiro, K., et al., *Ube3a is required for experience-dependent maturation of the neocortex*. Nature Neuroscience, 2009. **12**(6): p. 777-U132.
80. Jiang, Y.H., et al., *Mutation of the Angelman ubiquitin ligase in mice causes increased cytoplasmic p53 and deficits of contextual learning and long-term potentiation*. Neuron, 1998. **21**(4): p. 799-811.
81. Comery, T.A., et al., *Abnormal dendritic spines in fragile X knockout mice: maturation and pruning deficits*. Proc Natl Acad Sci U S A, 1997. **94**(10): p. 5401-4.
82. Guy, J., et al., *Reversal of neurological defects in a mouse model of Rett syndrome*. Science, 2007. **315**(5815): p. 1143-7.
83. Asaka, Y., et al., *Hippocampal synaptic plasticity is impaired in the -null mouse model of Rett syndrome*. Neurobiology of Disease, 2006. **21**(1): p. 217-227.
84. Moretti, P., et al., *Learning and memory and synaptic plasticity are impaired in a mouse model of Rett syndrome*. Journal of Neuroscience, 2006. **26**(1): p. 319-327.
85. Hamdan, F.F., et al., *Mutations in SYNGAP1 in autosomal nonsyndromic mental retardation*. N Engl J Med, 2009. **360**(6): p. 599-605.
86. Kaufman, L., M. Ayub, and J.B. Vincent, *The genetic basis of non-syndromic intellectual disability: a review*. Journal of Neurodevelopmental Disorders, 2010. **2**(4): p. 182-209.
87. Sala, C., et al., *Regulation of dendritic spine morphology and synaptic function by Shank and Homer*. Neuron, 2001. **31**(1): p. 115-30.
88. Phelan, K. and H.E. McDermid, *The 22q13.3 Deletion Syndrome (Phelan-McDermid Syndrome)*. Mol Syndromol, 2012. **2**(3-5): p. 186-201.
89. Jamain, S., et al., *Reduced social interaction and ultrasonic communication in a mouse model of monogenic heritable autism*. Proc Natl Acad Sci U S A, 2008. **105**(5): p. 1710-5.
90. Peça, J., et al., *mutant mice display autistic-like behaviours and striatal dysfunction*. Nature, 2011. **472**(7344): p. 437-U534.

91. Chubykin, A.A., et al., *Activity-dependent validation of excitatory versus inhibitory synapses by neuroligin-1 versus neuroligin-2*. *Neuron*, 2007. **54**(6): p. 919-31.
92. Radyushkin, K., et al., *Neuroligin-3-deficient mice: model of a monogenic heritable form of autism with an olfactory deficit*. *Genes Brain Behav*, 2009. **8**(4): p. 416-25.
93. Gizer, I.R., C. Ficks, and I.D. Waldman, *Candidate gene studies of ADHD: a meta-analytic review*. *Hum Genet*, 2009. **126**(1): p. 51-90.
94. Li, D.W., et al., *Meta-analysis shows significant association between dopamine system genes and attention deficit hyperactivity disorder (ADHD)*. *Human Molecular Genetics*, 2006. **15**(14): p. 2276-2284.
95. Ebert, A.D., et al., *Induced pluripotent stem cells from a spinal muscular atrophy patient*. *Nature*, 2009. **457**(7227): p. 277-80.
96. Finkel, R.S., et al., *Nusinersen versus Sham Control in Infantile-Onset Spinal Muscular Atrophy*. *N Engl J Med*, 2017. **377**(18): p. 1723-1732.
97. De Rubeis, S., et al., *Synaptic, transcriptional and chromatin genes disrupted in autism*. *Nature*, 2014. **515**(7526): p. 209-15.
98. Gao, R. and P. Penzes, *Common mechanisms of excitatory and inhibitory imbalance in schizophrenia and autism spectrum disorders*. *Curr Mol Med*, 2015. **15**(2): p. 146-67.
99. Kleefstra, T., et al., *Disruption of an EHMT1-associated chromatin-modification module causes intellectual disability*. *Am J Hum Genet*, 2012. **91**(1): p. 73-82.
100. Assia Batzir, N., et al., *Phenotypic expansion of POGZ-related intellectual disability syndrome (White-Sutton syndrome)*. *Am J Med Genet A*, 2020. **182**(1): p. 38-52.
101. White, J., et al., *POGZ truncating alleles cause syndromic intellectual disability*. *Genome Med*, 2016. **8**(1): p. 3.
102. Merriweather, A., et al., *A novel, de novo intronic variant in POGZ causes White-Sutton syndrome*. *Am J Med Genet A*, 2022. **188**(7): p. 2198-2203.
103. Nagy, D., et al., *Genotype-Phenotype Comparison in POGZ-Related Neurodevelopmental Disorders by Using Clinical Scoring*. *Genes*, 2022. **13**(1): p. 154.
104. Pascolini, G., et al., *A novel patient with White-Sutton syndrome refines the mutational and clinical repertoire of the related phenotype and suggests further observations*. *American Journal of Medical Genetics Part A*, 2020. **182**(7): p. 1791-1795.
105. Dubourg, C., et al., *Identification of Nine New RAI1-Truncating Mutations in Smith-Magenis Syndrome Patients without 17p11.2 Deletions*. *Mol Syndromol*, 2014. **5**(2): p. 57-64.
106. Loviglio, M.N., et al., *Identification of a -associated disease network through integration of exome sequencing, transcriptomics, and 3D genomics*. *Genome Medicine*, 2016. **8**.
107. Assia Batzir, N., J. White, and V.R. Sutton, *White-Sutton Syndrome*, in *GeneReviews((R))*, M.P. Adam, et al., Editors. 1993: Seattle (WA).
108. Samanta, D., R. Ramakrishnaiah, and B. Schaefer, *The neurological aspects related to mutation: case report and review of CNS malformations and epilepsy*. *Acta Neurologica Belgica*, 2020. **120**(2): p. 447-450.
109. Stessman, H.A.F., et al., *Disruption of Is Associated with Intellectual Disability and Autism Spectrum Disorders*. *American Journal of Human Genetics*, 2016. **98**(3): p. 541-552.
110. Zerbino, D.R., et al., *Ensembl 2018*. *Nucleic Acids Res*, 2018. **46**(D1): p. D754-D761.
111. Markenscoff-Papadimitriou, E., et al., *Autism risk gene POGZ promotes chromatin accessibility and expression of clustered synaptic genes*. *Cell Rep*, 2021. **37**(10): p. 110089.

112. Ibaraki, K., et al., *Expression Analyses of POGZ, A Responsible Gene for Neurodevelopmental Disorders, during Mouse Brain Development*. *Developmental Neuroscience*, 2019. **41**(1-2): p. 139-148.
113. Nozawa, R.S., et al., *Human POGZ modulates dissociation of HP1alpha from mitotic chromosome arms through Aurora B activation*. *Nat Cell Biol*, 2010. **12**(7): p. 719-27.
114. Murch, O., et al., *Further delineation of the clinical spectrum of White-Sutton syndrome: 12 new individuals and a review of the literature*. *European Journal of Human Genetics*, 2022. **30**(1): p. 95-100.
115. Matsumura, K., et al., *Pathogenic POGZ mutation causes impaired cortical development and reversible autism-like phenotypes*. *Nat Commun*, 2020. **11**(1): p. 859.
116. Sun, X., L. Cheng, and Y. Sun, *Autism-associated protein POGZ controls ESCs and ESC neural induction by association with esBAF*. *Mol Autism*, 2022. **13**(1): p. 24.
117. Sun, X., et al., *POGZ suppresses 2C transcriptional program and retrotransposable elements*. *Cell Rep*, 2023. **42**(8): p. 112867.
118. Tesina, P., et al., *Multiple cellular proteins interact with LEDGF/p75 through a conserved unstructured consensus motif*. *Nature Communications*, 2015. **6**.
119. Vermeulen, M., et al., *Quantitative Interaction Proteomics and Genome-wide Profiling of Epigenetic Histone Marks and Their Readers*. *Cell*, 2010. **142**(6): p. 967-980.
120. Marcon, E., et al., *Human-chromatin-related protein interactions identify a demethylase complex required for chromosome segregation*. *Cell Rep*, 2014. **8**(1): p. 297-310.
121. Tomida, J., et al., *FAM35A associates with REV7 and modulates DNA damage responses of normal and BRCA1-defective cells*. *EMBO J*, 2018. **37**(12).
122. Findlay, S., et al., *SHLD2/FAM35A co-operates with REV7 to coordinate DNA double-strand break repair pathway choice*. *EMBO J*, 2018. **37**(18).
123. Huttlin, E.L., et al., *Dual proteome-scale networks reveal cell-specific remodeling of the human interactome*. *Cell*, 2021. **184**(11): p. 3022-+.
124. Go, C.D., et al., *A proximity-dependent biotinylation map of a human cell*. *Nature*, 2021. **595**(7865): p. 120-+.
125. Sundarraj, J., et al., *H3K36me3 and PSIP1/LEDGF associate with several DNA repair proteins, suggesting their role in efficient DNA repair at actively transcribing loci*. *Wellcome Open Res*, 2017. **2**: p. 83.
126. Xiaoyun, S., C. Linxi, and S. Yuhua, *Autism-associated protein POGZ maintains embryonic stem cells by association with esBAF and HP1γ*. *bioRxiv*, 2021: p. 2021.02.07.430173.
127. Isidor, B., et al., *De Novo Truncating Mutations in the Kinetochores-Microtubules Attachment Gene CHAMP1 Cause Syndromic Intellectual Disability*. *Hum Mutat*, 2016. **37**(4): p. 354-8.
128. Nagai, M., et al., *Deficiency of CHAMP1, a gene related to intellectual disability, causes impaired neuronal development and a mild behavioural phenotype*. *Brain Communications*, 2022. **4**(5).
129. Li, F., et al., *CHAMP1 binds to REV7/FANCV and promotes homologous recombination repair*. *Cell Rep*, 2022. **40**(9): p. 111297.
130. Järvelä, I., et al., *Exome sequencing reveals predominantly de novo variants in disorders with intellectual disability (ID) in the founder population of Finland*. *Human Genetics*, 2021. **140**(7): p. 1011-1029.
131. Sagi-Dain, L., et al., *The rare 13q33-q34 microdeletions: eight new patients and review of the literature*. *Human Genetics*, 2019. **138**(10): p. 1145-1153.
132. Pernicone, N., S. Grinshpon, and T. Listovsky, *CDH1 binds MAD2L2 in a Rev1-like pattern*. *Biochemical and Biophysical Research Communications*, 2020. **531**(4): p. 566-572.
133. Boersma, V., et al., *MAD2L2 controls DNA repair at telomeres and DNA breaks by inhibiting 5' end resection*. *Nature*, 2015. **521**(7553): p. 537-U291.

134. Suliman-Lavie, R., et al., *Author Correction: Pogz deficiency leads to transcription dysregulation and impaired cerebellar activity underlying autism-like behavior in mice*. Nat Commun, 2021. **12**(1): p. 3874.
135. Deng, L., et al., *Loss of POGZ alters neural differentiation of human embryonic stem cells*. Molecular and Cellular Neuroscience, 2022. **120**.
136. Heath, J., et al., *POGZ promotes homology-directed DNA repair in an HP1-dependent manner*. Embo Reports, 2022. **23**(1).
137. Marquezini, B.P., et al., *Exploring the molecular pathways linking sleep phenotypes and POGZ-associated neurodevelopmental disorder*. J Med Genet, 2024.
138. Holth, J.K., et al., *The sleep-wake cycle regulates brain interstitial fluid tau in mice and CSF tau in humans*. Science, 2019. **363**(6429): p. 880-883.
139. Grigg, I., et al., *Tauopathy in the young autistic brain: novel biomarker and therapeutic target*. Translational Psychiatry, 2020. **10**(1).
140. Zhu, B.K., et al., *Coactivator-Dependent Oscillation of Chromatin Accessibility Dictates Circadian Gene Amplitude via REV-ERB Loading*. Molecular Cell, 2015. **60**(5): p. 769-783.
141. Alfert, A., N. Moreno, and K. Kerl, *The BAF complex in development and disease*. Epigenetics & Chromatin, 2019. **12**.
142. Mallick, B.N. and A. Singh, *REM sleep loss increases brain excitability: role of noradrenaline and its mechanism of action*. Sleep Med Rev, 2011. **15**(3): p. 165-78.
143. Takahashi, K. and S. Yamanaka, *Induction of pluripotent stem cells from mouse embryonic and adult fibroblast cultures by defined factors*. Cell, 2006. **126**(4): p. 663-76.
144. Zeineddine, D., et al., *The Oct4 protein: more than a magic stemness marker*. (2160-4150 (Print)).
145. Ghaleb, A.M. and V.W. Yang, *Kruppel-like factor 4 (KLF4): What we currently know*. Gene, 2017. **611**: p. 27-37.
146. Schaefer, T. and C. Lengerke, *SOX2 protein biochemistry in stemness, reprogramming, and cancer: the PI3K/AKT/SOX2 axis and beyond*. Oncogene, 2020. **39**(2): p. 278-292.
147. Miller, D.M., et al., *c-Myc and cancer metabolism*. Clin Cancer Res, 2012. **18**(20): p. 5546-53.
148. Jack, J., D. Rotroff, and A. Motsinger-Reif, *Lymphoblastoid Cell Lines Models of Drug Response: Successes and Lessons from this Pharmacogenomic Model*. Current Molecular Medicine, 2014. **14**(7): p. 833-840.
149. Omi, N., et al., *Efficient and reliable establishment of lymphoblastoid cell lines by Epstein-Barr virus transformation from a limited amount of peripheral blood*. Scientific Reports, 2017. **7**.
150. Auburger, G., et al., *Primary Skin Fibroblasts as a Model of Parkinson's Disease*. Molecular Neurobiology, 2012. **46**(1): p. 20-27.
151. Thomson, J.A., et al., *Embryonic stem cell lines derived from human blastocysts*. Science, 1998. **282**(5391): p. 1145-7.
152. Rowe, R.G. and G.Q. Daley, *Induced pluripotent stem cells in disease modelling and drug discovery*. Nature Reviews Genetics, 2019. **20**(7): p. 377-388.
153. Raab, S., et al., *A Comparative View on Human Somatic Cell Sources for iPSC Generation*. Stem Cells Int, 2014. **2014**: p. 768391.
154. Hu, S., et al., *Effects of cellular origin on differentiation of human induced pluripotent stem cell-derived endothelial cells*. JCI Insight, 2016. **1**(8).
155. Scesa, G., R. Adami, and D. Bottai, *iPSC Preparation and Epigenetic Memory: Does the Tissue Origin Matter?* Cells, 2021. **10**(6).
156. Poetsch, M.S., A. Strano, and K. Guan, *Human Induced Pluripotent Stem Cells: From Cell Origin, Genomic Stability, and Epigenetic Memory to Translational Medicine*. Stem Cells, 2022. **40**(6): p. 546-555.
157. Diecke, S., et al., *Recent technological updates and clinical applications of induced pluripotent stem cells*. Korean J Intern Med, 2014. **29**(5): p. 547-57.

158. Huang, C.Y., et al., *Human iPSC banking: barriers and opportunities*. J Biomed Sci, 2019. **26**(1): p. 87.
159. Terhune, A.H., et al., *Stem cell-based models of early mammalian development*. Development, 2022. **149**(20).
160. Sthijns, M.M.J.P.E., V.L.S. LaPointe, and C.A. van Blitterswijk, *Building Complex Life Through Self-Organization*. Tissue Engineering Part A, 2019. **25**(19-20): p. 1341-1346.
161. De Masi, C., et al., *Application of CRISPR/Cas9 to human-induced pluripotent stem cells: from gene editing to drug discovery*. Hum Genomics, 2020. **14**(1): p. 25.
162. Sen, T. and R.P. Thummer, *CRISPR and iPSCs: Recent Developments and Future Perspectives in Neurodegenerative Disease Modelling, Research, and Therapeutics*. Neurotox Res, 2022. **40**(5): p. 1597-1623.
163. Brouwer, M., H.Q. Zhou, and N.N. Kasri, *Choices for Induction of Pluripotency: Recent Developments in Human Induced Pluripotent Stem Cell Reprogramming Strategies*. Stem Cell Reviews and Reports, 2016. **12**(1): p. 54-72.
164. Lister, R., et al., *Hotspots of aberrant epigenomic reprogramming in human induced pluripotent stem cells*. Nature, 2011. **471**(7336): p. 68-U84.
165. Shi, Y., et al., *Induced pluripotent stem cell technology: a decade of progress*. Nat Rev Drug Discov, 2017. **16**(2): p. 115-130.
166. Bongso, A., et al., *Isolation and culture of inner cell mass cells from human blastocysts*. Hum Reprod, 1994. **9**(11): p. 2110-7.
167. Kaufmann, M., et al., *High-Throughput Screening Using iPSC-Derived Neuronal Progenitors to Identify Compounds Counteracting Epigenetic Gene Silencing in Fragile X Syndrome*. J Biomol Screen, 2015. **20**(9): p. 1101-11.
168. Lancaster, M.A. and J.A. Knoblich, *Generation of cerebral organoids from human pluripotent stem cells*. Nature protocols, 2014. **9**(10): p. 2329-2340.
169. Qian, X., H. Song, and G.-I. Ming, *Brain organoids: advances, applications and challenges*. Development, 2019. **146**(8).
170. Arlotta, P. and S.P. Pasca, *Cell diversity in the human cerebral cortex: from the embryo to brain organoids*. Current Opinion in Neurobiology, 2019. **56**: p. 194-198.
171. Bekhite, M.M. and P.C. Schulze, *Human Induced Pluripotent Stem Cell as a Disease Modeling and Drug Development Platform-A Cardiac Perspective*. Cells, 2021. **10**(12).
172. Bystron, I., C. Blakemore, and P. Rakic, *Development of the human cerebral cortex: Boulder Committee revisited*. Nat Rev Neurosci, 2008. **9**(2): p. 110-22.
173. Rakic, P., *Specification of Cerebral Cortical Areas*. Science, 1988. **241**(4862): p. 170-176.
174. Sidman, R.L. and P. Rakic, *Neuronal migration, with special reference to developing human brain: a review*. Brain Res, 1973. **62**(1): p. 1-35.
175. Lui, J.H., D.V. Hansen, and A.R. Kriegstein, *Development and evolution of the human neocortex*. Cell, 2011. **146**(1): p. 18-36.
176. Smart, I.H., *Proliferative characteristics of the ependymal layer during the early development of the mouse neocortex: a pilot study based on recording the number, location and plane of cleavage of mitotic figures*. J Anat, 1973. **116**(Pt 1): p. 67-91.
177. Miller, D.J., et al., *Shared and derived features of cellular diversity in the human cerebral cortex*. Curr Opin Neurobiol, 2019. **56**: p. 117-124.
178. Haubensak, W., et al., *Neurons arise in the basal neuroepithelium of the early mammalian telencephalon: A major site of neurogenesis*. Proceedings of the National Academy of Sciences of the United States of America, 2004. **101**(9): p. 3196-3201.
179. Hansen, D.V., et al., *Neurogenic radial glia in the outer subventricular zone of human neocortex*. Nature, 2010. **464**(7288): p. 554-U110.
180. Haldipur, P., et al., *Spatiotemporal expansion of primary progenitor zones in the developing human cerebellum*. Science, 2019. **366**(6464): p. 454-460.
181. Florio, M. and W.B. Huttner, *Neural progenitors, neurogenesis and the evolution of the neocortex*. Development, 2014. **141**(11): p. 2182-2194.

182. Liu, J., et al., *The Primate-Specific Gene Marks Outer Radial Glia Cells and Promotes Cortical Expansion and Folding*. *Cell Stem Cell*, 2017. **21**(5): p. 635-+.
183. Nowakowski, T.J., et al., *Transformation of the Radial Glia Scaffold Demarcates Two Stages of Human Cerebral Cortex Development*. *Neuron*, 2016. **91**(6): p. 1219-1227.
184. Silbereis, J.C., et al., *The Cellular and Molecular Landscapes of the Developing Human Central Nervous System*. *Neuron*, 2016. **89**(2): p. 248-68.
185. Vanderhaeghen, P. and F. Polleux, *Developmental mechanisms underlying the evolution of human cortical circuits*. *Nat Rev Neurosci*, 2023. **24**(4): p. 213-232.
186. Carletti, B. and F. Rossi, *Neurogenesis in the cerebellum*. *Neuroscientist*, 2008. **14**(1): p. 91-100.
187. Chédotal, A., *Roles of axon guidance molecules in neuronal wiring in the developing spinal cord*. *Nature Reviews Neuroscience*, 2019. **20**(7): p. 380-396.
188. Aida, T. and G.P. Feng, *The dawn of non-human primate models for neurodevelopmental disorders*. *Current Opinion in Genetics & Development*, 2020. **65**: p. 160-168.
189. Dehay, C., H. Kennedy, and K.S. Kosik, *The Outer Subventricular Zone and Primate-Specific Cortical Complexification*. *Neuron*, 2015. **85**(4): p. 683-694.
190. Bystron, I., et al., *The first neurons of the human cerebral cortex*. *Nature Neuroscience*, 2006. **9**(7): p. 880-886.
191. García-Moreno, F., L. López-Mascaraque, and J.A. De Carlos, *Origins and migratory routes of murine Cajal-Retzius cells*. *Journal of Comparative Neurology*, 2007. **500**(3): p. 419-432.
192. Marín-Padilla, M., *The mammalian neocortex new pyramidal neuron: a new conception*. *Frontiers in Neuroanatomy*, 2014. **7**.
193. Bystron, I., C. Blakemore, and P. Rakic, *Development of the human cerebral cortex: Boulder Committee revisited*. *Nature Reviews Neuroscience*, 2008. **9**(2): p. 110-122.
194. Iacopetti, P., et al., *Expression of the antiproliferative gene TIS21 at the onset of neurogenesis identifies single neuroepithelial cells that switch from proliferative to neuron-generating division*. *Proceedings of the National Academy of Sciences of the United States of America*, 1999. **96**(8): p. 4639-4644.
195. Li, J., et al., *Integrative genomic analysis of early neurogenesis reveals a temporal genetic program for differentiation and specification of preplate and Cajal-Retzius neurons*. *PLoS Genet*, 2021. **17**(3): p. e1009355.
196. Takahashi, T., et al., *Sequence of neuron origin and neocortical laminar fate: Relation to cell cycle of origin in the developing murine cerebral wall*. *Journal of Neuroscience*, 1999. **19**(23): p. 10357-10371.
197. Andrews, M.G., et al., *How mechanisms of stem cell polarity shape the human cerebral cortex*. *Nature Reviews Neuroscience*, 2022. **23**(12): p. 711-724.
198. Molnár, Z., H.J. Luhmann, and P.O. Kanold, *Transient cortical circuits match spontaneous and sensory-driven activity during development*. *Science*, 2020. **370**(6514): p. 308-+.
199. Hoerder-Suabedissen, A. and Z. Molnár, *Development, evolution and pathology of neocortical subplate neurons*. *Nature Reviews Neuroscience*, 2015. **16**(3): p. 133-146.
200. Duque, A., et al., *Secondary expansion of the transient subplate zone in the developing cerebrum of human and nonhuman primates*. *Proceedings of the National Academy of Sciences of the United States of America*, 2016. **113**(35): p. 9892-9897.
201. Silbereis, J.C., et al., *The Cellular and Molecular Landscapes of the Developing Human Central Nervous System*. *Neuron*, 2016. **89**(2): p. 248-268.
202. Cadwell, C.R., et al., *Development and Arealization of the Cerebral Cortex*. *Neuron*, 2019. **103**(6): p. 980-1004.
203. Balaram, P., N.A. Young, and J.H. Kaas, *Histological features of layers and sublayers in cortical visual areas V1 and V2 of chimpanzees, macaque monkeys, and humans*. *Eye Brain*, 2014. **2014**(6 Suppl 1): p. 5-18.

204. Telley, L. and D. Jabaudon, *A mixed model of neuronal diversity*. Nature, 2018. **555**(7697): p. 452-454.
205. Idova, G.V., et al., *Cytokine Content in the Hypothalamus and Hippocampus of C57Bl/6J Mice with Depressive-Like Behavior*. Bull Exp Biol Med, 2019. **167**(1): p. 11-16.
206. Sasai, Y., *Next-Generation Regenerative Medicine: Organogenesis from Stem Cells in 3D Culture*. Cell Stem Cell, 2013. **12**(5): p. 520-530.
207. Kretzschmar, K. and H. Clevers, *Organoids: Modeling Development and the Stem Cell Niche in a Dish*. Developmental Cell, 2016. **38**(6): p. 590-600.
208. Fathi, A., et al., *Discovery of Novel Cell Surface Markers for Purification of Embryonic Dopamine Progenitors for Transplantation in Parkinson's Disease Animal Models*. Molecular & Cellular Proteomics, 2018. **17**(9): p. 1670-1684.
209. Garber, B.B. and A.A. Moscona, *Reconstruction of Brain-Tissue from Cell Suspensions .2. Specific Enhancement of Aggregation of Embryonic Cerebral Cells by Supernatant from Homologous Cell-Cultures*. Developmental Biology, 1972. **27**(2): p. 235-&.
210. Crain, S.M., L. Alfei, and E.R. Peterson, *Neuromuscular Transmission in Cultures of Adult Human and Rodent Skeletal Muscle after Innervation in-Vitro by Fetal Rodent Spinal Cord*. Federation Proceedings, 1970. **29**(2): p. A715-+.
211. Thomson, J.A., et al., *Embryonic stem cell lines derived from human blastocysts*. Science, 1998. **282**(5391): p. 1145-1147.
212. Takahashi, K. and S. Yamanaka, *Induction of pluripotent stem cells from mouse embryonic and adult fibroblast cultures by defined factors*. Cell, 2006. **126**(4): p. 663-676.
213. Chambers, S.M., et al., *Highly efficient neural conversion of human ES and iPS cells by dual inhibition of SMAD signaling*. Nature Biotechnology, 2009. **27**(3): p. 275-280.
214. Chambers, I. and S.R. Tomlinson, *The transcriptional foundation of pluripotency*. Development, 2009. **136**(14): p. 2311-2322.
215. Mertens, J., et al., *Evaluating cell reprogramming, differentiation and conversion technologies in neuroscience*. Nature Reviews Neuroscience, 2016. **17**(7): p. 424-437.
216. Wang, M., et al., *Scalable Production of Mechanically Robust Antireflection Film for Omnidirectional Enhanced Flexible Thin Film Solar Cells*. Advanced Science, 2017. **4**(9).
217. Pasca, S.P., *The rise of three-dimensional human brain cultures*. Nature, 2018. **553**(7689): p. 437-445.
218. Eiraku, M., et al., *Self-organizing optic-cup morphogenesis in three-dimensional culture*. Nature, 2011. **472**(7341): p. 51-U73.
219. Camp, J.G., et al., *Human cerebral organoids recapitulate gene expression programs of fetal neocortex development*. Proceedings of the National Academy of Sciences of the United States of America, 2015. **112**(51): p. 15672-15677.
220. Guidotti, S., et al., *GSK3 $\beta$ : a key regulator of oxidative stress in 3D-cultures of osteoarthritic chondrocytes*. Febs Journal, 2015. **282**: p. 396-397.
221. Pasca, A.M., et al., *Functional cortical neurons and astrocytes from human pluripotent stem cells in 3D culture*. Nature Methods, 2015. **12**(7): p. 671-+.
222. Yoon, S.J., et al., *Reliability of human cortical organoid generation*. Nature Methods, 2019. **16**(1): p. 75-+.
223. Gordon, A., et al., *Long-term maturation of human cortical organoids matches key early postnatal transitions*. Nat Neurosci, 2021. **24**(3): p. 331-342.
224. Trevino, A.E., et al., *Chromatin accessibility dynamics in a model of human forebrain development*. Science, 2020. **367**(6476).
225. Jinek, M., et al., *A Programmable Dual-RNA-Guided DNA Endonuclease in Adaptive Bacterial Immunity*. Science, 2012. **337**(6096): p. 816-821.
226. Barrangou, R., et al., *CRISPR provides acquired resistance against viruses in prokaryotes*. Science, 2007. **315**(5819): p. 1709-1712.
227. Waddington, S.N., et al., *A Broad Overview and Review of CRISPR-Cas Technology and Stem Cells*. Curr Stem Cell Rep, 2016. **2**(1): p. 9-20.

228. Cong, L., et al., *Multiplex Genome Engineering Using CRISPR/Cas Systems*. Science, 2013. **339**(6121): p. 819-823.
229. Ledford, H., *CRISPR: gene editing is just the beginning*. Nature, 2016. **531**(7593): p. 156-159.
230. Ben Jehuda, R., Y. Shemer, and O. Binah, *Genome Editing in Induced Pluripotent Stem Cells using CRISPR/Cas9*. Stem Cell Reviews and Reports, 2018. **14**(3): p. 323-336.
231. Guirouilh-Barbat, J., et al., *Impact of the KU80 pathway on NHEJ-induced genome rearrangements in mammalian cells*. Molecular Cell, 2004. **14**(5): p. 611-623.
232. Iyama, T. and D.M. Wilson, *DNA repair mechanisms in dividing and non-dividing cells*. DNA Repair, 2013. **12**(8): p. 620-636.
233. Wan, L.L., et al., *CRISPR-Cas9 Gene Editing for Fruit and Vegetable Crops: Strategies and Prospects*. Horticulturae, 2021. **7**(7).
234. Vangipuram, M., et al., *Skin Punch Biopsy Explant Culture for Derivation of Primary Human Fibroblasts*. Jove-Journal of Visualized Experiments, 2013(77).
235. Mali, P., et al., *RNA-guided human genome engineering via Cas9*. Science, 2013. **339**(6121): p. 823-6.
236. Yumlu, S., et al., *Efficient Gene Editing of Human Induced Pluripotent Stem Cells Using CRISPR/Cas9*. Methods Mol Biol, 2019. **1961**: p. 137-151.
237. Havlicek, S., et al., *Gene dosage-dependent rescue of HSP neurite defects in SPG4 patients' neurons*. Hum Mol Genet, 2014. **23**(10): p. 2527-41.
238. Zhou, S.L., et al., *Neurosphere Based Differentiation of Human iPSC Improves Astrocyte Differentiation*. Stem Cells International, 2016. **2016**.
239. Sasaki, R., et al., *A protocol for immunofluorescence staining of floating neurospheres*. Neurosci Lett, 2010. **479**(2): p. 126-7.
240. Taylor, S.C., et al., *The Ultimate qPCR Experiment: Producing Publication Quality, Reproducible Data the First Time*. Trends Biotechnol, 2019. **37**(7): p. 761-774.
241. Firsanov, D., et al., *Rapid Detection of gamma-H2AX by Flow Cytometry in Cultured Mammalian Cells*. Methods Mol Biol, 2017. **1644**: p. 129-138.
242. Burke, E.E., et al., *Dissecting transcriptomic signatures of neuronal differentiation and maturation using iPSCs*. Nat Commun, 2020. **11**(1): p. 462.
243. Kaya-Okur, H.S., et al., *Efficient low-cost chromatin profiling with CUT&Tag*. Nat Protoc, 2020. **15**(10): p. 3264-3283.
244. Matsumura, K., et al., *De novo POGZ mutations in sporadic autism disrupt the DNA-binding activity of POGZ*. J Mol Psychiatry, 2016. **4**: p. 1.
245. D'Antoni, C., et al., *Unlocking Neural Function with 3D In Vitro Models: A Technical Review of Self-Assembled, Guided, and Bioprinted Brain Organoids and Their Applications in the Study of Neurodevelopmental and Neurodegenerative Disorders*. International Journal of Molecular Sciences, 2023. **24**(13).
246. Lancaster, M.A., et al., *Cerebral organoids model human brain development and microcephaly*. Nature, 2013. **501**(7467): p. 373-9.
247. Nava, C., et al., *De novo mutations in HCN1 cause early infantile epileptic encephalopathy*. Nat Genet, 2014. **46**(6): p. 640-5.
248. Yuen, R.K.C., et al., *Whole genome sequencing resource identifies 18 new candidate genes for autism spectrum disorder*. Nature Neuroscience, 2017. **20**(4): p. 602-+.
249. Linhoff, M.W., et al., *An Unbiased Expression Screen for Synaptogenic Proteins Identifies the LRRTM Protein Family as Synaptic Organizers*. Neuron, 2009. **61**(5): p. 734-749.
250. Aruga, J. and K. Mikoshiba, *Identification and characterization of Slitrk, a novel neuronal transmembrane protein family controlling neurite outgrowth*. Molecular and Cellular Neuroscience, 2003. **24**(1): p. 117-129.
251. Ebstein, F., et al., *Neurodevelopmental Disorders (NDD) Caused by Genomic Alterations of the Ubiquitin-Proteasome System (UPS): the Possible Contribution of Immune Dysregulation to Disease Pathogenesis*. Frontiers in Molecular Neuroscience, 2021. **14**.

252. Nussbacher, J.K., et al., *Disruption of RNA Metabolism in Neurological Diseases and Emerging Therapeutic Interventions*. *Neuron*, 2019. **102**(2): p. 294-320.
253. Lisowski, P., et al., *Mutant huntingtin impairs neurodevelopment in human brain organoids through CHCHD2-mediated neurometabolic failure*. *Nature Communications*, 2024. **15**(1): p. 7027.
254. Shimojima, K., et al., *CHCHD2 is down-regulated in neuronal cells differentiated from iPSC cells derived from patients with lissencephaly*. *Genomics*, 2015. **106**(4): p. 196-203.
255. Fregeau, B., et al., *De Novo Mutations of Cause a Genetic Syndrome with Features that Overlap Those Associated with Proximal 1p36 Deletions*. *American Journal of Human Genetics*, 2016. **98**(5): p. 963-970.
256. Niehaus, A.D., J. Kim, and M.A. Manning, *Phenotypic variability in RERE-related disorders and the first report of an inherited variant*. *Am J Med Genet A*, 2022. **188**(11): p. 3358-3363.
257. Petersen, A.K., et al., *Deletion 1q43 encompassing only in a patient with autistic disorder*. *European Journal of Medical Genetics*, 2013. **56**(2): p. 118-122.
258. Hirano, S. and M. Takeichi, *Cadherins in brain morphogenesis and wiring*. *Physiol Rev*, 2012. **92**(2): p. 597-634.
259. Huang, W., et al., *Origins and Proliferative States of Human Oligodendrocyte Precursor Cells*. *Cell*, 2020. **182**(3): p. 594-608 e11.
260. Ahmed, Z.M., et al., *Mutations of the protocadherin gene PCDH15 cause Usher syndrome type 1F*. *Am J Hum Genet*, 2001. **69**(1): p. 25-34.
261. Ishizuka, K., et al., *Investigation of Rare Single-Nucleotide PCDH15 Variants in Schizophrenia and Autism Spectrum Disorders*. *PLoS One*, 2016. **11**(4): p. e0153224.
262. Takahashi, K., et al., *Induction of pluripotent stem cells from adult human fibroblasts by defined factors*. *Cell*, 2007. **131**(5): p. 861-72.
263. Dafforn, T.R., M. Della, and A.D. Miller, *The molecular interactions of heat shock protein 47 (Hsp47) and their implications for collagen biosynthesis*. *Journal of Biological Chemistry*, 2001. **276**(52): p. 49310-49319.
264. Kuroda, K. and S. Tajima, *HSP47 is a useful marker for skin fibroblasts in formalin-fixed, paraffin-embedded tissue specimens*. *Journal of Cutaneous Pathology*, 2004. **31**(3): p. 241-246.
265. Ravikanth, M., et al., *Heterogeneity of fibroblasts*. *J Oral Maxillofac Pathol*, 2011. **15**(2): p. 247-50.
266. Wakui, T., et al., *Method for evaluation of human induced pluripotent stem cell quality using image analysis based on the biological morphology of cells*. *J Med Imaging (Bellingham)*, 2017. **4**(4): p. 044003.
267. Hussein, S.M., et al., *Copy number variation and selection during reprogramming to pluripotency*. *Nature*, 2011. **471**(7336): p. 58-62.
268. Sobol, M., et al., *Methods of Reprogramming to Induced Pluripotent Stem Cell Associated with Chromosomal Integrity and Delineation of a Chromosome 5q Candidate Region for Growth Advantage*. *Stem Cells Dev*, 2015. **24**(17): p. 2032-40.
269. Altieri, F., et al., *Production and characterization of human induced pluripotent stem cells (iPSC) CSSi007-A (4383) from Joubert Syndrome*. *Stem Cell Res*, 2019. **38**: p. 101480.
270. Segre, J.A., C. Bauer, and E. Fuchs, *Klf4 is a transcription factor required for establishing the barrier function of the skin*. *Nature Genetics*, 1999. **22**(4): p. 356-360.
271. Jaubert, J., J. Cheng, and J.A. Segre, *Ectopic expression of kruppel like factor 4 (Klf4) accelerates formation of the epidermal permeability barrier*. *Development*, 2003. **130**(12): p. 2767-77.
272. Havlicek, S., et al., *Gene dosage-dependent rescue of HSP neurite defects in SPG4 patients neurons*. *Human Molecular Genetics*, 2014. **23**(10): p. 2527-2541.

273. Baghbaderani, B.A., et al., *Detailed Characterization of Human Induced Pluripotent Stem Cells Manufactured for Therapeutic Applications*. Stem Cell Rev Rep, 2016. **12**(4): p. 394-420.
274. Li, H.L., et al., *Precise correction of the dystrophin gene in duchenne muscular dystrophy patient induced pluripotent stem cells by TALEN and CRISPR-Cas9*. Stem Cell Reports, 2015. **4**(1): p. 143-154.
275. Dever, D.P., et al., *CRISPR/Cas9 beta-globin gene targeting in human haematopoietic stem cells*. Nature, 2016. **539**(7629): p. 384-389.
276. Sternberg, S.H. and J.A. Doudna, *Expanding the Biologist's Toolkit with CRISPR-Cas9*. Mol Cell, 2015. **58**(4): p. 568-74.
277. Fu, J., et al., *Improved and Flexible HDR Editing by Targeting Introns in iPSCs*. Stem Cell Reviews and Reports, 2022. **18**(5): p. 1822-1833.
278. Yang, H., et al., *Methods Favoring Homology-Directed Repair Choice in Response to CRISPR/Cas9 Induced-Double Strand Breaks*. International Journal of Molecular Sciences, 2020. **21**(18).
279. Sander, J.D. and J.K. Joung, *CRISPR-Cas systems for editing, regulating and targeting genomes*. Nature Biotechnology, 2014. **32**(4): p. 347-355.
280. Liang, X., et al., *Enhanced CRISPR/Cas9-mediated precise genome editing by improved design and delivery of gRNA, Cas9 nuclease, and donor DNA*. J Biotechnol, 2017. **241**: p. 136-146.
281. Lotfi, M., et al., *Recent Advances in CRISPR/Cas9 Delivery Approaches for Therapeutic Gene Editing of Stem Cells*. Stem Cell Rev Rep, 2023. **19**(8): p. 2576-2596.
282. Yang, D., et al., *Enrichment of G2/M cell cycle phase in human pluripotent stem cells enhances HDR-mediated gene repair with customizable endonucleases*. Scientific Reports, 2016. **6**.
283. Smirnikhina, S.A., et al., *Improving Homology-Directed Repair in Genome Editing Experiments by Influencing the Cell Cycle*. Int J Mol Sci, 2022. **23**(11).
284. Pauklin, S. and L. Vallier, *The Cell-Cycle State of Stem Cells Determines Cell Fate Propensity (vol 155, pg 135, 2013)*. Cell, 2014. **156**(6): p. 1338-1338.
285. Yiangou, L., et al., *Method to Synchronize Cell Cycle of Human Pluripotent Stem Cells without Affecting Their Fundamental Characteristics*. Stem Cell Reports, 2019. **12**(1): p. 165-179.
286. Rao, S., et al., *Lovastatin-mediated G arrest is through inhibition of the proteasome, independent of hydroxymethyl glutaryl-CoA reductase*. Proceedings of the National Academy of Sciences of the United States of America, 1999. **96**(14): p. 7797-7802.
287. Chung, L.C., et al., *L-Mimosine blocks cell proliferation via upregulation of B-cell translocation gene 2 and N-downstream regulated gene 1 in prostate carcinoma cells*. American Journal of Physiology-Cell Physiology, 2012. **302**(4): p. C676-C685.
288. Denes, C.E., et al., *Approaches to Enhance Precise CRISPR/Cas9-Mediated Genome Editing*. Int J Mol Sci, 2021. **22**(16).
289. Pawelczak, K.S., et al., *Modulating DNA Repair Pathways to Improve Precision Genome Engineering*. ACS Chem Biol, 2018. **13**(2): p. 389-396.
290. Maurissen, T.L. and K. Woltjen, *Synergistic gene editing in human iPSC cells via cell cycle and DNA repair modulation*. Nature Communications, 2020. **11**(1).
291. Guo, C., et al., *Off-target effects in CRISPR/Cas9 gene editing*. Frontiers in Bioengineering and Biotechnology, 2023. **11**.
292. Aljabali, A.A.A., M. El-Tanani, and M.M. Tambuwala, *Principles of CRISPR-Cas9 technology: Advancements in genome editing and emerging trends in drug delivery*. Journal of Drug Delivery Science and Technology, 2024. **92**: p. 105338.

293. Chambers, S.M., et al., *Highly efficient neural conversion of human ES and iPS cells by dual inhibition of SMAD signaling*. Nat Biotechnol, 2009. **27**(3): p. 275-80.
294. Heldin, C.H., K. Miyazono, and P. tenDijke, *TGF-beta signalling from cell membrane to nucleus through SMAD proteins*. Nature, 1997. **390**(6659): p. 465-471.
295. Chandrasekaran, A., et al., *Comparison of 2D and 3D neural induction methods for the generation of neural progenitor cells from human induced pluripotent stem cells*. Stem Cell Res, 2017. **25**: p. 139-151.
296. Duval, K., et al., *Modeling Physiological Events in 2D vs. 3D Cell Culture*. Physiology (Bethesda), 2017. **32**(4): p. 266-277.
297. Griesi-Oliveira, K., et al., *Modeling non-syndromic autism and the impact of TRPC6 disruption in human neurons*. Mol Psychiatry, 2015. **20**(11): p. 1350-65.
298. Kilpatrick, S., C. Irwin, and K.K. Singh, *Human pluripotent stem cell (hPSC) and organoid models of autism: opportunities and limitations*. Transl Psychiatry, 2023. **13**(1): p. 217.
299. Amin, N.D. and S.P. Pasca, *Building Models of Brain Disorders with Three-Dimensional Organoids*. Neuron, 2018. **100**(2): p. 389-405.
300. Koch, K., et al., *Scientific Validation of Human Neurosphere Assays for Developmental Neurotoxicity Evaluation*. Front Toxicol, 2022. **4**: p. 816370.
301. Forster, N., et al., *Reliable identification and quantification of neural cells in microscopic images of neurospheres*. Cytometry A, 2022. **101**(5): p. 411-422.
302. Drydale, E., et al., *Stem-cell derived neurosphere assay highlights the effects of viral infection on human cortical development*. Brain Behav Immun, 2024. **115**: p. 718-726.
303. Gordon, A. and D.H. Geschwind, *Human in vitro models for understanding mechanisms of autism spectrum disorder*. Mol Autism, 2020. **11**(1): p. 26.
304. Oliveira, M.S., et al., *The Connection between Autism Spectrum Disorder and the Scn2a and Renl Genes*. Cytotherapy, 2021. **23**(4): p. 35-35.
305. Saorin, G., I. Caligiuri, and F. Rizzolio, *Microfluidic organoids-on-a-chip: The future of human models*. Seminars in Cell & Developmental Biology, 2023. **144**: p. 41-54.
306. Hetzel, L.A., et al., *Microfluidics and Organoids, the Power Couple of Developmental Biology and Oncology Studies*. International Journal of Molecular Sciences, 2023. **24**(13).
307. Cho, A.N., et al., *Microfluidic device with brain extracellular matrix promotes structural and functional maturation of human brain organoids*. Nature Communications, 2021. **12**(1).
308. Jalilian, E. and S.R. Shin, *Novel model of cortical-meningeal organoid co-culture system improves human cortical brain organoid cytoarchitecture*. Scientific Reports, 2023. **13**(1).
309. Chukwurah, E., et al., *All Together Now: Modeling the Interaction of Neural With Non-neura Systems Using Organoid Models*. Frontiers in Neuroscience, 2019. **13**.
310. Del Dosso, A., et al., *Upgrading the Physiological Relevance of Human Brain Organoids*. Neuron, 2020. **107**(6): p. 1014-1028.
311. Le Hir, H., et al., *The spliceosome deposits multiple proteins 20-24 nucleotides upstream of mRNA exon-exon junctions*. EMBO J, 2000. **19**(24): p. 6860-9.
312. Nagy, E. and L.E. Maquat, *A rule for termination-codon position within intron-containing genes: when nonsense affects RNA abundance*. Trends in Biochemical Sciences, 1998. **23**(6): p. 198-199.
313. Supek, F., B. Lehner, and R.G.H. Lindeboom, *To NMD or Not To NMD: Nonsense-Mediated mRNA Decay in Cancer and Other Genetic Diseases*. Trends Genet, 2021. **37**(7): p. 657-668.
314. Lindeboom, R.G.H., F. Supek, and B. Lehner, *The rules and impact of nonsense-mediated mRNA decay in human cancers*. Nature Genetics, 2016. **48**(10): p. 1112-1118.
315. Singh, G., I. Rebbapragada, and J. Lykke-Andersen, *A competition between stimulators and antagonists of Upf complex recruitment governs human nonsense-mediated mRNA decay*. Plos Biology, 2008. **6**(4): p. 860-871.
316. Dyle, M.C., et al., *How to get away with nonsense: Mechanisms and consequences of escape from nonsense-mediated RNA decay*. Wiley Interdisciplinary Reviews-Rna, 2020. **11**(1).

317. Qi, Y., M. Wang, and Q. Jiang, *PABPC1--mRNA stability, protein translation and tumorigenesis*. *Front Oncol*, 2022. **12**: p. 1025291.
318. Eberle, A.B., et al., *SMG6 promotes endonucleolytic cleavage of nonsense mRNA in human cells*. *Nature Structural & Molecular Biology*, 2009. **16**(1): p. 49-55.
319. Llabata, P. and P. Llinàs-Arias, *How the West(ern) Was Won: Solutions for Immunoblotting Large and Small Proteins*. *bioRxiv*, 2022: p. 2022.03.23.485494.
320. Scholzen, T. and J. Gerdes, *The Ki-67 protein: from the known and the unknown*. *J Cell Physiol*, 2000. **182**(3): p. 311-22.
321. Lombardi, D., F. Becherucci, and P. Romagnani, *How much can the tubule regenerate and who does it? An open question*. *Nephrology Dialysis Transplantation*, 2016. **31**(8): p. 1243-1250.
322. Miller, I., et al., *Ki67 is a Graded Rather than a Binary Marker of Proliferation versus Quiescence*. *Cell Reports*, 2018. **24**(5): p. 1105-+.
323. Ladstein, R.G., et al., *Ki-67 expression is superior to mitotic count and novel proliferation markers PHH3, MCM4 and mitotin as a prognostic factor in thick cutaneous melanoma*. *Bmc Cancer*, 2010. **10**.
324. O'Hara, R.E., et al., *Three Optimized Methods for In Situ Quantification of Progenitor Cell Proliferation in Embryonic Kidneys Using BrdU, EdU, and PCNA*. *Canadian Journal of Kidney Health and Disease*, 2019. **6**.
325. Hesse, M., et al., *Direct visualization of cell division using high-resolution imaging of M-phase of the cell cycle*. *Nature Communications*, 2012. **3**.
326. Bolgioni, A.F., M.A. Vittoria, and N.J. Ganem, *Long-term Live-cell Imaging to Assess Cell Fate in Response to Paclitaxel*. *Jove-Journal of Visualized Experiments*, 2018(135).
327. Lukasik, P., M. Zaluski, and I. Gutowska, *Cyclin-Dependent Kinases (CDK) and Their Role in Diseases Development-Review*. *International Journal of Molecular Sciences*, 2021. **22**(6).
328. Mirzaa, G., et al., *De novo CCND2 mutations leading to stabilization of cyclin D2 cause megalencephaly-polymicrogyria-polydactyly-hydrocephalus syndrome*. *Nat Genet*, 2014. **46**(5): p. 510-515.
329. Tsunekawa, Y., T. Kikkawa, and N. Osumi, *Asymmetric inheritance of Cyclin D2 maintains proliferative neural stem/progenitor cells: a critical event in brain development and evolution*. *Dev Growth Differ*, 2014. **56**(5): p. 349-57.
330. Mirzaa, G., *MPPH Syndrome*, in *GeneReviews((R))*, M.P. Adam, et al., Editors. 1993: Seattle (WA).
331. Shcheglova, E., K. Blaszczyk, and M. Borowiak, *Mitogen Synergy: An Emerging Route to Boosting Human Beta Cell Proliferation*. *Front Cell Dev Biol*, 2021. **9**: p. 734597.
332. Malumbres, M. and M. Barbacid, *To cycle or not to cycle: a critical decision in cancer*. *Nat Rev Cancer*, 2001. **1**(3): p. 222-31.
333. Malumbres, M., *Cyclin-dependent kinases*. *Genome Biol*, 2014. **15**(6): p. 122.
334. Miller, F.D. and A.S. Gauthier, *Timing is everything: Making neurons versus glia in the developing cortex*. *Neuron*, 2007. **54**(3): p. 357-369.
335. Yoo, Y.E., et al., *Brain region and gene dosage-differential transcriptomic changes in -mutant mice*. *Frontiers in Molecular Neuroscience*, 2022. **15**.
336. Lee, S., et al., *Gene Dosage- and Age-Dependent Differential Transcriptomic Changes in the Prefrontal Cortex of -Mutant Mice*. *Frontiers in Molecular Neuroscience*, 2021. **14**.
337. Higgins, D., et al., *Mechanisms of neuronal polarity*. *Current Opinion in Neurobiology*, 1997. **7**(5): p. 599-604.
338. Gu, X., C.H. Jia, and J.H. Wang, *Advances in Understanding the Molecular Mechanisms of Neuronal Polarity*. *Molecular Neurobiology*, 2023. **60**(5): p. 2851-2870.
339. Liu, J.S., *Molecular Genetics of Neuronal Migration Disorders*. *Current Neurology and Neuroscience Reports*, 2011. **11**(2): p. 171-178.

340. Friocourt, G., et al., *Role of cytoskeletal abnormalities in the neuropathology and pathophysiology of type I lissencephaly*. *Acta Neuropathologica*, 2011. **121**(2): p. 149-170.
341. Friocourt, G., et al., *Doublecortin functions at the extremities of growing neuronal processes*. *Cerebral Cortex*, 2003. **13**(6): p. 620-626.
342. Goldberg, A.L., *Protein degradation and protection against misfolded or damaged proteins*. *Nature*, 2003. **426**(6968): p. 895-9.
343. Balchin, D., M. Hayer-Hartl, and F.U. Hartl, *In vivo aspects of protein folding and quality control*. *Science*, 2016. **353**(6294): p. aac4354.
344. Manzini, P., et al., *Validation of an automated cell counting method for cGMP manufacturing of human induced pluripotent stem cells*. *Biotechnol Rep (Amst)*, 2022. **33**: p. e00708.
345. Biggs, R. and R.L. Macmillan, *The Errors of Some Haematological Methods as They Are Used in a Routine Laboratory*. *Journal of Clinical Pathology*, 1948. **1**(5): p. 269-287.
346. Wang, T.Y., et al., *Dynamic behavior of cells within neurospheres in expanding populations of neural precursors*. *Brain Research*, 2006. **1107**: p. 82-96.
347. Ladiwala, U., H. Basu, and D. Mathur, *Assembling neurospheres: dynamics of neural progenitor/stem cell aggregation probed using an optical trap*. *PLoS One*, 2012. **7**(6): p. e38613.
348. Siqueira, L.D., et al., *Neurospheres: a potential in vitro model for the study of central nervous system disorders*. *Molecular Biology Reports*, 2021. **48**(4): p. 3649-3663.
349. Gage, F.H. and S. Temple, *Neural stem cells: generating and regenerating the brain*. *Neuron*, 2013. **80**(3): p. 588-601.
350. Falk, S. and M. Götz, *Glial control of neurogenesis*. *Current Opinion in Neurobiology*, 2017. **47**: p. 188-195.
351. Borrell, V. and M. Götz, *Role of radial glial cells in cerebral cortex folding*. *Current Opinion in Neurobiology*, 2014. **27**: p. 39-46.
352. Ferent, J., D. Zaidi, and F. Francis, *Extracellular Control of Radial Glia Proliferation and Scaffolding During Cortical Development and Pathology*. *Front Cell Dev Biol*, 2020. **8**: p. 578341.
353. Barkovich, A.J., et al., *A developmental and genetic classification for malformations of cortical development: update 2012*. *Brain*, 2012. **135**: p. 1348-1369.
354. Ziv, O., et al., *Quantitative Live Imaging of Human Embryonic Stem Cell Derived Neural Rosettes Reveals Structure-Function Dynamics Coupled to Cortical Development*. *PLoS Comput Biol*, 2015. **11**(10): p. e1004453.
355. Bagley, J.A., et al., *Fused cerebral organoids model interactions between brain regions*. *Nature Methods*, 2017. **14**(7): p. 743-+.
356. Suliman-Lavie, R., et al., *deficiency leads to transcription dysregulation and impaired cerebellar activity underlying autism-like behavior in mice (vol 11, 5836, 2020)*. *Nature Communications*, 2021. **12**(1).
357. DiFrancesco, J.C. and D. DiFrancesco, *Dysfunctional HCN ion channels in neurological diseases*. *Front Cell Neurosci*, 2015. **6**: p. 174.
358. Santoro, B. and M.M. Shah, *Hyperpolarization-Activated Cyclic Nucleotide-Gated Channels as Drug Targets for Neurological Disorders*. *Annual Review of Pharmacology and Toxicology*, Vol 60, 2020. **60**: p. 109-131.
359. Nie, Z. and P.A. Randazzo, *Arf GAPs and membrane traffic*. *J Cell Sci*, 2006. **119**(Pt 7): p. 1203-11.
360. Dwane, S., et al., *RACK1 promotes neurite outgrowth by scaffolding AGAP2 to FAK*. *Cellular Signalling*, 2014. **26**(1): p. 9-18.
361. Ma, D.Q., et al., *Identification of significant association and gene-gene interaction of GABA receptor subunit genes in autism*. *Am J Hum Genet*, 2005. **77**(3): p. 377-88.

362. Piton, A., et al., *Analysis of the effects of rare variants on splicing identifies alterations in GABAA receptor genes in autism spectrum disorder individuals*. Eur J Hum Genet, 2013. **21**(7): p. 749-56.
363. Dikow, N., et al., *3p25.3 microdeletion of GABA transporters SLC6A1 and SLC6A11 results in intellectual disability, epilepsy and stereotypic behavior*. Am J Med Genet A, 2014. **164A**(12): p. 3061-8.
364. Abelson, J.F., et al., *Sequence variants in SLITRK1 are associated with Tourette's syndrome*. Science, 2005. **310**(5746): p. 317-20.
365. Beaubien, F., et al., *Slitrk1 is localized to excitatory synapses and promotes their development*. Scientific Reports, 2016. **6**.
366. Sando, R., X. Jiang, and T.C. Südhof, *Latrophilin GPCRs direct synapse specificity by coincident binding of FLRTs and teneurins*. Science, 2019. **363**(6429): p. 837-+.
367. Cediël, L., et al., *GABBR1 monoallelic de novo variants linked to neurodevelopmental delay and epilepsy*. European Journal of Human Genetics, 2023. **31**: p. 477-477.
368. Satterstrom, F.K., et al., *Large-Scale Exome Sequencing Study Implicates Both Developmental and Functional Changes in the Neurobiology of Autism*. Cell, 2020. **180**(3): p. 568-+.
369. Heyne, H.O., et al., *De novo variants in neurodevelopmental disorders with epilepsy*. Nat Genet, 2018. **50**(7): p. 1048-1053.
370. Lampada, A. and V. Taylor, *Notch signaling as a master regulator of adult neurogenesis*. Frontiers in Neuroscience, 2023. **17**.
371. Yeh, E., et al., *Patient-derived iPSCs show premature neural differentiation and neuron type-specific phenotypes relevant to neurodevelopment*. Molecular Psychiatry, 2018. **23**(8): p. 1687-1698.
372. Scott, D.A. and E.H. Sherr, *RERE-Related Disorders*, in *GeneReviews((R))*, M.P. Adam, et al., Editors. 1993: Seattle (WA).
373. Sabaie, H., et al., *Long non-coding RNA-associated competing endogenous RNA axes in the olfactory epithelium in schizophrenia: a bioinformatics analysis*. Scientific Reports, 2021. **11**(1).
374. Regard, J.B., et al., *Verge: a novel vascular early response gene*. J Neurosci, 2004. **24**(16): p. 4092-103.
375. Stritt, S., et al., *APOLD1 loss causes endothelial dysfunction involving cell junctions, cytoskeletal architecture, and Weibel-Palade bodies, while disrupting hemostasis*. Haematologica, 2023. **108**(3): p. 772-784.
376. Roszkowski, M., *The effects of acute stress on Apold1 gene expression and blood-brain barrier permeability*. 2014.
377. Fan, Z., et al., *The vascular gene is dispensable for normal development but controls angiogenesis under pathological conditions*. Angiogenesis, 2023. **26**(3): p. 385-407.
378. Aragón-González, A., P.J. Shaw, and L. Ferraiuolo, *Blood-Brain Barrier Disruption and Its Involvement in Neurodevelopmental and Neurodegenerative Disorders*. International Journal of Molecular Sciences, 2022. **23**(23).
379. Kealy, J., C. Greene, and M. Campbell, *Blood-brain barrier regulation in psychiatric disorders*. Neurosci Lett, 2020. **726**: p. 133664.
380. Wang, Y., S. Yu, and M. Li, *Corrigendum: Neurovascular crosstalk and cerebrovascular alterations: an underestimated therapeutic target in autism spectrum disorders*. Front Cell Neurosci, 2024. **18**: p. 1435981.
381. Usui, N., H. Kobayashi, and S. Shimada, *Neuroinflammation and Oxidative Stress in the Pathogenesis of Autism Spectrum Disorder*. Int J Mol Sci, 2023. **24**(6).

382. Eissa, N., et al., *Role of Neuroinflammation in Autism Spectrum Disorder and the Emergence of Brain Histaminergic System. Lessons Also for BPSD?* *Frontiers in Pharmacology*, 2020. **11**.
383. Nakagawa, Y. and K. Chiba, *Involvement of Neuroinflammation during Brain Development in Social Cognitive Deficits in Autism Spectrum Disorder and Schizophrenia*. *Journal of Pharmacology and Experimental Therapeutics*, 2016. **358**(3): p. 504-515.
384. Missler, M. and T.C. Südhof, *Neurexophilins form a conserved family of neuropeptide-like glycoproteins*. *Journal of Neuroscience*, 1998. **18**(10): p. 3630-3638.
385. Yan, J., et al., *Neurexin 1 $\alpha$  structural variants associated with autism*. *Neuroscience Letters*, 2008. **438**(3): p. 368-370.
386. Zoghbi, H.Y. and M.F. Bear, *Synaptic Dysfunction in Neurodevelopmental Disorders Associated with Autism and Intellectual Disabilities*. *Cold Spring Harbor Perspectives in Biology*, 2012. **4**(3).
387. Born, G., et al., *Modulation of synaptic function through the  $\alpha$ -neurexin-specific ligand neurexophilin-1*. *Proceedings of the National Academy of Sciences of the United States of America*, 2014. **111**(13): p. E1274-E1283.
388. Zhao, K., et al., *The Impact of Altered HCN1 Expression on Brain Function and Its Relationship with Epileptogenesis*. *Current Neuropharmacology*, 2023. **21**(10): p. 2070-2078.
389. Xie, C., et al., *Novel HCN1 Mutations Associated With Epilepsy and Impacts on Neuronal Excitability*. *Front Mol Neurosci*, 2022. **15**: p. 870182.
390. Nisar, S., et al., *Association of genes with phenotype in autism spectrum disorder*. *Aging-Us*, 2019. **11**(22): p. 10742-10770.
391. Montanari, M., et al., *Autism Spectrum Disorder: Focus on Glutamatergic Neurotransmission*. *International Journal of Molecular Sciences*, 2022. **23**(7).
392. Yadav, R., et al., *Deletion of Glutamate Delta-1 Receptor in Mouse Leads to Aberrant Emotional and Social Behaviors*. *Plos One*, 2012. **7**(3).
393. Li, Z.Z., et al., *contributes to cognitive deficits in chronic patients with schizophrenia*. *Schizophrenia Research*, 2020. **215**: p. 134-139.
394. Bartolini, G., et al., *Neuregulin 3 Mediates Cortical Plate Invasion and Laminar Allocation of GABAergic Interneurons*. *Cell Reports*, 2017. **18**(5): p. 1157-1170.
395. Avramopoulos, D., *Neuregulin 3 and its roles in schizophrenia risk and presentation*. *Am J Med Genet B Neuropsychiatr Genet*, 2018. **177**(2): p. 257-266.
396. Kao, W.-T., et al., *Common genetic variation in Neuregulin 3 (*NRG3*) influences risk for schizophrenia and impacts *NRG3* expression in human brain*. *Proceedings of the National Academy of Sciences*, 2010. **107**(35): p. 15619-15624.
397. Longart, M., et al., *Neuregulins: subcellular localization, signaling pathways and their relationship with neuroplasticity and neurological diseases*. *Exploration of Neuroscience*, 2022. **1**(1): p. 31-53.
398. Taylor, J., et al., *Expanding the phenotype of HNRNPU-related neurodevelopmental disorder with emphasis on seizure phenotype and review of literature*. *Am J Med Genet A*, 2022. **188**(5): p. 1497-1514.
399. Sapir, T. and O. Reiner, *HNRNPU's multi-tasking is essential for proper cortical development*. *Bioessays*, 2023. **45**(9).
400. Rooney, K., et al., *DNA methylation epsignature and comparative epigenomic profiling of HNRNPU-related neurodevelopmental disorder*. *Genet Med*, 2023. **25**(8): p. 100871.
401. Mastropasqua, F., et al., *Deficiency of the Heterogeneous Nuclear Ribonucleoprotein U locus leads to delayed hindbrain neurogenesis*. *Biol Open*, 2023. **12**(10).
402. Dreikorn, E.N., et al., *Case report: Early use of whole exome sequencing unveils HNRNPU-related neurodevelopmental disorder and answers additional clinical questions through reanalysis*. *Front Genet*, 2024. **15**: p. 1380552.

403. Bramswig, N.C., et al., *Heterozygous HNRNPU variants cause early onset epilepsy and severe intellectual disability*. Hum Genet, 2017. **136**(7): p. 821-834.
404. Balasubramanian, M., *HNRNPU-Related Neurodevelopmental Disorder*, in *GeneReviews((R))*, M.P. Adam, et al., Editors. 1993: Seattle (WA).
405. Hadjebi, O., et al., *The RCC1 superfamily: From genes, to function, to disease*. Biochimica Et Biophysica Acta-Molecular Cell Research, 2008. **1783**(8): p. 1467-1479.
406. Furuta, M., T. Hori, and T. Fukagawa, *Chromatin binding of RCC1 during mitosis is important for its nuclear localization in interphase*. Molecular Biology of the Cell, 2016. **27**(2): p. 371-381.
407. Ranieri, A., et al., *Genetic Alterations in a Large Population of Italian Patients Affected by Neurodevelopmental Disorders*. Genes (Basel), 2024. **15**(4).
408. Carbonell, A.U., et al., *Haploinsufficiency in the ANKS1B gene encoding AIDA-1 leads to a neurodevelopmental syndrome*. Nat Commun, 2019. **10**(1): p. 3529.
409. Moon, A.L., et al., *CACNA1C: Association With Psychiatric Disorders, Behavior, and Neurogenesis*. Schizophr Bull, 2018. **44**(5): p. 958-965.
410. Herold, K.G., J.W. Hussey, and I.E. Dick, *CACNA1C-Related Channelopathies*. Handb Exp Pharmacol, 2023. **279**: p. 159-181.
411. Cipriano, L., et al., *Expanding the Phenotype of the CACNA1C-Associated Neurological Disorders in Children: Systematic Literature Review and Description of a Novel Mutation*. Children (Basel), 2024. **11**(5).
412. Petersen, A.K., et al., *Deletion 1q43 encompassing only CHRM3 in a patient with autistic disorder*. Eur J Med Genet, 2013. **56**(2): p. 118-22.
413. Dean, B. and E. Scarr, *Possible involvement of muscarinic receptors in psychiatric disorders: a focus on schizophrenia and mood disorders*. Curr Mol Med, 2015. **15**(3): p. 253-64.
414. Sauer, A.V., et al., *Autoimmune dysregulation and purine metabolism in adenosine deaminase deficiency*. Front Immunol, 2012. **3**: p. 265.
415. Rogers, M.H., et al., *Cognitive and behavioral abnormalities in adenosine deaminase deficient severe combined immunodeficiency*. J Pediatr, 2001. **139**(1): p. 44-50.
416. Ivarola, P., et al., *A Clinical Neurological Approach to the Child With Adenosine Deaminase Deficiency*. Pediatr Neurol, 2024. **158**: p. 49-56.
417. Cagdas, D., et al., *ADA Deficiency: Evaluation of the Clinical and Laboratory Features and the Outcome*. J Clin Immunol, 2018. **38**(4): p. 484-493.
418. Roy, B., et al., *Role of miRNAs in Neurodegeneration: From Disease Cause to Tools of Biomarker Discovery and Therapeutics*. Genes (Basel), 2022. **13**(3).
419. Nawalpuri, B., S. Ravindran, and R.S. Muddashetty, *The Role of Dynamic miRISC During Neuronal Development*. Front Mol Biosci, 2020. **7**: p. 8.
420. Lessel, D., et al., *Germline AGO2 mutations impair RNA interference and human neurological development*. Nat Commun, 2020. **11**(1): p. 5797.
421. Hong, S.F., et al., *Development of an assay system for the analysis of host RISC activity in the presence of a potyvirus RNA silencing suppressor, HC-Pro*. Virol J, 2023. **20**(1): p. 10.
422. Nfonsam, L.E., et al., *expression correlates with epithelial mesenchymal transition-linked genes and poor overall survival in colon cancer patients*. World Journal of Gastrointestinal Oncology, 2019. **11**(8): p. 589-598.
423. Freese, J.L., D. Pino, and S.J. Pleasure, *Wnt signaling in development and disease*. Neurobiology of Disease, 2010. **38**(2): p. 148-153.
424. Scruggs, B.A., M.Q. Reding, and L.A. Schimmenti, *NDP-Related Retinopathies*, in *GeneReviews((R))*, M.P. Adam, et al., Editors. 1993: Seattle (WA).
425. Jiang, K., et al., *Novel mutation in the NDP gene associated with Norrie disease in a Chinese pedigree*. Mol Genet Genomic Med, 2024. **12**(1): p. e2345.
426. Farhy-Tselnicker, I., et al., *Astrocyte-Secreted Glypican 4 Regulates Release of Neuronal Pentraxin 1 from Axons to Induce Functional Synapse Formation*. Neuron, 2017. **96**(2): p. 428-445 e13.

427. Dowling, C. and N.J. Allen, *Mice Lacking Glypican 4 Display Juvenile Hyperactivity and Adult Social Interaction Deficits*. *Brain Plast*, 2018. **4**(2): p. 197-209.
428. Moore, D.L., A. Aprara, and J.L. Goldberg, *Kruppel-like transcription factors in the nervous system: novel players in neurite outgrowth and axon regeneration*. *Mol Cell Neurosci*, 2011. **47**(4): p. 233-43.
429. Kennedy, C.L.M., et al., *Genomic regulation of Krüppel-like-factor family members by corticosteroid receptors in the rat brain*. *Neurobiology of Stress*, 2023. **23**: p. 100532.
430. Miao, H., et al., *Glia-specific expression of neuropeptide receptor Lgr4 regulates development and adult physiology in Drosophila*. *J Neurosci Res*, 2024. **102**(1): p. e25271.
431. Brafman, D. and K. Willert, *Wnt/ $\beta$ -Catenin Signaling during Early Vertebrate Neural Development*. *Developmental Neurobiology*, 2017. **77**(11): p. 1239-1259.
432. Weissberg, O. and E. Elliott, *The Mechanisms of CHD8 in Neurodevelopment and Autism Spectrum Disorders*. *Genes (Basel)*, 2021. **12**(8).
433. Sugathan, A., et al., *CHD8 regulates neurodevelopmental pathways associated with autism spectrum disorder in neural progenitors*. *Proc Natl Acad Sci U S A*, 2014. **111**(42): p. E4468-77.
434. Derafshi, B.H., et al., *The autism risk factor CHD8 is a chromatin activator in human neurons and functionally dependent on the ERK-MAPK pathway effector ELK1*. *Scientific Reports*, 2022. **12**(1).
435. Gordon, C.T., et al., *Identification of Novel Craniofacial Regulatory Domains Located far Upstream of*  
*and Disrupted in Pierre Robin Sequence*. *Human Mutation*, 2014. **35**(8): p. 1011-1020.
436. Al-Qattan, M.M. and S.A. Almohrij, *The Pathogenesis of Pierre Robin Sequence through a Review of SOX9 and Its Interactions*. *Plastic and Reconstructive Surgery-Global Open*, 2022. **10**(4).
437. Turner, C.A., et al., *Dysregulated fibroblast growth factor (FGF) signaling in neurological and psychiatric disorders*. *Semin Cell Dev Biol*, 2016. **53**: p. 136-43.
438. Prochazkova, M., et al., *Bones, Glands, Ears and More: The Multiple Roles of FGF10 in Craniofacial Development*. *Front Genet*, 2018. **9**: p. 542.
439. Bzdega, K. and J.A. Karolak, *Phenotypic spectrum of FGF10-related disorders: a systematic review*. *PeerJ*, 2022. **10**: p. e14003.

# Azza Soliman

## PhD Candidate

- ✉ a.soliman@uni-mainz.de
- ☎ +49 17675864111
- 📍 Max-Hufschmidt St.13, 55130 Mainz, Germany



Date of Birth: 31<sup>th</sup>. January 1989, Birth Place: Giza, Egypt

## Professional Experience

- 10/2024 - Present **Postdoctoral Researcher**  
**Computational Systems Genetics Group, Institute of Human genetics, University Medical Center Mainz • Mainz, Germany.**
- 12/2018 – Present **PhD Candidate**  
**Institute of Human genetics, University Medical Center Mainz • Mainz, Germany.**  
Investigation of the molecular mechanisms through which mutations in POGZ gene are associated with autism spectrum disorders (ASDs) using neural progenitor cells (NPCs) and neurons derived from induced pluripotent stem cells (iPSCs) in in 2D culture and 3D organoids.
- 8/2012 - Present **Microbiological quality control specialist**  
**National Organization of Drug control and research (NODCAR), Cairo, Egypt.**  
My work includes antibiotics assays using Agar diffusion and turbidimetry methods. Besides that, research work is required so I was master student at Cairo university and volunteer researcher in different research work of professors at NODCAR.
- 12/2017 - 7/2018 **Research Intern**  
**Stress Neurobiology & Neurogenetics, Max-Planck-Institute of Psychiatry, Munich, Germany**  
Studying dynamic changes in BDNF secretion in freely moving mice using a modified microdialysis-Western blot method, with a focus on the effects of novel antidepressants like ketamine and HNK, and their interaction with FKBP5, a co-chaperone linked to psychopathology susceptibility and therapy response
- 1/2017 - 7/2017 **Research Intern**  
**Human Genetics department, Radboud University Nijmegen Medical Center, Netherlands.**  
Investigating the pathogenicity of novel spindle assembly checkpoints (SAC) mutations (BUB1B and MAD2L1) introduced via CRISPR/Cas9 with ssODN in cell models, focusing on their impact on checkpoint activity, chromosome instability, and protein localization.
- 8/2012 - 7/2016 **Community Pharmacist "Part time"**  
**Ahmed Nashaat Pharmacy, Cairo, Egypt.**  
I was responsible for dispensing prescription medicines to the public, ensuring that different treatments are compatible, checking dosage and introducing counselling to the public.
- 8/2013 - 8/2013 **Research assistant**  
**Genetic engineering and biotechnology research institute, Menoufia University, Egypt.**

## Education

---

2024	<b>PhD Student</b> Johannes Gutenberg-Universität, Institute of Molecular Biology, Mainz, Germany. Human Genetics and Biology
2018	<b>Master Degree</b> Radboud University Nijmegen, Faculty of medical science, Netherlands. Molecular mechanisms of disease (MMD) research master's program.
2014	<b>Pre-master Diploma</b> Cairo University, Faculty of pharmacy, Egypt Microbiology and Immunology
2011	<b>Bachelor Degree</b> Ain Shams University, Faculty of pharmacy, Egypt. Pharmaceutical Sciences

## Languages

---

<b>Arabic</b>	Mother tongue
<b>English</b>	Professional proficiency
<b>German</b>	Basic proficiency

## Awards & Scholarships

---

**2020:** FTN/TransMed scholarship  
**2017:** Radboud Max Planck Internship grant  
**2017:** ERASMUS+ traineeship Radboud University grant  
**2016:** Radboud Scholarship Programme 2016: Radboud University Medical Center Study Fund  
**2011:** Certificate of appreciation from Nobel Prize Simulation for a pharmaceutical chemistry and drug design project "Fibroblast growth factor receptor inhibition by molecular modeling".  
**2009 – 2011:** Summers: Certificate of appreciation for my participation in medical caravans. (leader of health awareness team of medical caravan of faculty of pharmacy, Ain shams University, Cairo).

## Certificates

---

**2017, Oct.:** Laboratory animals license (article 9) & FELASA (EU Function B) Certificate of animal experiments (Species -Specific Certificate).  
**2014-2015:** Systems Biology and Biotechnology Specialization; Icahn School of Medicine, Mount Sinai; Coursera platform.

## Extracurricular courses

---

**2018, 12<sup>th</sup>-23<sup>rd</sup> Mar.:** Radiation-induced effects with particular emphasis on genetics, development, teratology, cognition; SCK•CEN Academy for Nuclear Science and Technology; Mol; Belgium.  
**2014-2015:** Systems Biology and Biotechnology Specialization; Icahn School of Medicine at Mount Sinai; Coursera Platform.  
**2014, 1<sup>st</sup> Sept.- 5<sup>th</sup> Nov.:** Writing in the Sciences, Kristin Sainani; Assistant Professor; Stanford University; Stanford ONLINE.

## Conferences & Workshops

---

- 2024, 1-4 June:** European society of Human Genetics (ESHG) (Poster Presentation), Berlin, Germany.
- 2023, 25-28 April:** Brain Genome symposium, (Oral Presentation), EMBL, Heidelberg, Germany.
- 2023, 15-17 Mar.:** German society of Human Genetics (GfH) (Oral Presentation), Kassel, Germany.
- 2022, 5-9 June:** EMBO Workshop: Neural Stem Cells: From Basic Understanding to Translational Application (Poster Presentation), Kyllini, Greece.
- 2022, 16-18 March:** Annual Meeting of the German Society for Human Genetics (GfH) (Poster Presentation), Würzburg, Germany.
- 2022, 15 March:** 1st Scotland - Rhineland-Palatinate Conference on Life Sciences and Biotechnology (Poster Presentation), online, Germany.
- 2018, 25 January:** Mini-Symposium at the Max Planck Institute of Neurobiology, Martinsried, Germany.
- 2017, 26 December:** Second Egyptian Bioinformatics Workshop, Nile University, Egypt.
- 2016, 24-25 November:** Radboud New Frontiers 2016 in Cancer Research, Radboud Institute for Health Sciences, Nijmegen, Netherlands.
- 2016, 9 September:** Radboud Institute for Molecular Life Sciences (RIMLS) Symposium, Nijmegen, Netherlands.

## Publications

---

- 2020, Nov.:** The stress susceptibility factor FKBP51 controls S-ketamine-evoked release of mBDNF in the prefrontal cortex of mice. Elmira Anderzhanova, Kathrin Hafner, Andreas J. Genewsky, Azza Soliman, Max L. Pöhlmann, Mathias V. Schmidt, Robert Blum, Carsten T. Wotjak, Nils C. Gassen, *Neurobiology of Stress*, Volume 13, 2020, 100239, ISSN 2352 2895, <https://doi.org/10.1016/j.ynstr.2020.100239>

## Extracurricular activities

---

- 2017, 22<sup>nd</sup> Aug.:** Molecular Mechanisms of disease master program recruitment presentation, Faculty of Pharmacy, Cairo University.
- 2011 1<sup>st</sup> May- 6<sup>th</sup> Sept.:** Researcher delegate; Nobel Prize Simulation organization (NPS), American University of Cairo (AUC), Egypt.

## Interests

---

- Reading: Sciences, Religion and Philosophy.  
Music, Sports (Yoga, Running).

## References

---

- Available upon request





